High Spatial Resolution Millimeter VLBI Studies of the Nearby Radio Galaxies M 87 and 3C 84

INAUGURAL-DISSERTATION

zur
Erlangung des Doktorgrades
der Mathematisch-Naturwissenschaftlichen Fakultät
der Universität zu Köln

vorgelegt von
Jae-Young Kim
aus Ulsan, Republik Korea

Köln 2018

Berichterstatter: Prof. Dr. Andreas Eckart
Prof. Dr. J. Anton Zensus

Tag der letzten mündlichen Prüfung: 11 September 2018

To my beloved parents and sister
사랑하는 부모님과 동생에게

Abstract

Active galactic nuclei (AGN) are believed to be powered by accretion of gas onto a central supermassive black hole (SMBH). In particular, a certain fraction of AGN show unusual, dramatic outflows of ionized plasma – relativistic jets – which are extended from the compact central engine region up to millions of light years from the host galaxies. The jets are observationally characterized by superluminal propagation speeds and a highly collimated structure. Recent theoretical studies suggest physical models to explain the origin and evolution of the jets. In spite of the recent progress, however, the extremely small spatial scale of the base of the jet (a few to hundreds of Schwarzschild radii R_s) poses almost unsurmountable difficulties to observe the regions directly.

This thesis presents my work attempting to understand the physics and test observationally the existing theoretical models of the central regions based on high spatial resolution observations of selected nearest radio galaxies Messier 87 (M 87, Virgo A, NGC 4486, 3C 274) and 3C 84 (NGC 1275). For this, I employ the technique of very-long-baseline interferometry (VLBI), which allows to resolve the vicinity of the central engine at an ultra-high angular resolution of 50 micro-arcseconds at the high observing radio frequency of 86 GHz (providing a spatial resolution of only $7R_s$ for M 87).

In Chapter 1, I present a brief review of the historical and astrophysical backgrounds of AGN and their relativistic jets. Basics of radio astronomical observations and theoretical/practical aspects of VLBI are given in Chapter 2. The main results and conclusions from our studies of M 87 and 3C 84 based on the Global Millimeter VLBI Array (GMVA) observations at 86 GHz are presented in Chapters 3 and 4, respectively.

GMVA observations of M 87 performed between 2004 and 2015 reveal the fine-scale structure of the innermost jet at the highest resolution and sensitivity to date. The following main results are presented in the thesis based on the high-resolution high-fidelity images and other VLBI data of M 87: (i) the substantially low brightness temperature of the compact VLBI core region (whose size is only $\sim 10R_s$ at 86 GHz), suggesting a magnetic energy dominated jet launching region, (ii) the wide diameter of the jet base ($\sim (4-6)R_s$) inferred from the collimation profile of the edge-brightened jet and the slow propagation speed of the inner jet (apparent speed $\lesssim 1.0\,c$), indicating that the bright edges of the outflow may originate from the inner accretion disk, (iii) the rapidly increasing brightness temperature of the VLBI core at low observing frequencies (by an order of magnitude from 230 GHz down to 1.6 GHz), which could be a signature of internal microscopic particle accelerations, and (iv) the presence of a faint central lane between the bright edges of the jet, which may correspond to an ultra-relativistic "spine" of the outflow with a different physical origin.

The GMVA observations of 3C 84 in May 2015 resolve the complicated inner jet structure at a spatial resolution of $250R_s$ at 86 GHz (at the highest image dynamic range of ~ 3400 at this frequency to date). Other intensive multi-frequency VLBI observations during 2015 also reveal highly time-variable flux density in the VLBI core region. In this thesis, I particularly focus on the spectral and linear polarization properties and present the following results: (1) a significant detection of linearly polarized features in the VLBI core region at 86 and 43 GHz, whose morphology appears to be highly time-variable on monthly timescales (at 43 GHz), (2) a significant detection of large Faraday rotations in the core region (typical values of rotation measure$\sim 10^{(5-6)}\,\mathrm{rad/m^2}$) and the rotation measure sign change in time, (3) comparisons of the Faraday depolarization models and the observed linear polarization spectrum, which suggests the boundary layer of the jet threaded by ordered magnetic fields as the external Faraday screen, and (4) an estimate of the magnetic field strength and the electron number density in the jet by a joint analysis of the observed Faraday rotation and the synchrotron self-absorption in the core region.

These findings provide a lot of valuable information about the inner structure of M 87 and 3C 84 which was not available before, and these observational data will be served as a paramount morphological description of the total intensity and polarized emission of these sources for theoreticians to tune their models. I summarize our main conclusions and suggest future work in Chapter 5.

Zusammenfassung

Es wird angenommen, das Aktive Galaktische Kerne (AGN) durch Akkretion von Gas auf ein zentrales supermassereiches schwarzes Loch (SMBH) angetrieben werden. Im Besonderen zeigt ein bestimmter Teil von AGNs ungewöhnliche, dramatische Ausströmungen von ionisiertem Plasma - relativistische Jets - welche sich von dem kompakten, zentralen Motor bis zu Entfernungen von Millionen von Lichtjahren von der Heimatgalaxie erstrecken. Beobachtungen von Jets sind durch Überlichtgeschwindigkeiten und einer sehr kollimierten Struktur gekennzeichnet. Aus jüngste theoretische Studien folgen physikalische Modelle, welche den Ursprung und die Evolution von Jets erklären. Trotz der aktuellen Fortschritte stellt die unglaublich kleine räumliche Ausdehnung der Jetbasis (einige hundert Schwarzschild-Radien R_s) dennoch eine nahezu unüberwindliche Hürde dar diese Regionen direkt zu beobachten.

Diese Doktorarbeit präsentiert meine Bemühungen die Physik zu verstehen und bestehende theoretische Modelle der zentralen Region durch Beobachtungen mit hoher räumlicher Auflösung anhand einer Auswahl der uns am nächsten gelegenen Radiogalaxien Messier 87 (M 87, Virgo A, NGC 4486, 3C 274) und 3C 84 (NGC 1275) zu überprüfen. Hierfür verwende ich die Technik der Very long Baseline Interferometry (VLBI), welche es mir erlaubt die Umgebung des zentralen Motors mit einer ultra-hohen Winkelauflösung von 50 Mikrobogensekunden bei einer hohen Radiofrequenz von 86 GHz aufzulösen (dies resultiert in einer räumlichen Auflösung von nunmehr $7\,R_s$ für M 87).

In Kapitel 1 präsentiere ich einen kurzen überblick über die historischen und astrophysikalischen Hintergründe von AGNs und deren relativistischen Jets. Grundlagen von radioastronomischen Beobachtungen und theoretische sowie praktische Aspekte von VLBI sind in Kapitel 2 erläutert. Die wichtigsten Ergebnisse und Schlussfolgerungen unserer Studien von M 87 und 3C 84, anhand von Global Millimeter VLBI Array (GMVA) Beobachtungen bei 86 GHz, sind jeweils in den Kapitel 3 und 4 präsentiert.

GMVA Beobachtungen von M 87, durchgeführt in dem Zeitraum zwischen 2004 und 2015, offenbaren die Feinstruktur des innersten Jets bei der bisher höchsten Auflösung und Sensitivität. Die folgenden wichtigsten Ergebnisse, wie sie in dieser Arbeit präsentiert sind, basieren auf den hoch-aufgelösten Karten mit hoher Genauigkeit und anderen VLBI Daten von M 87: (i) Die erheblich niedrige Helligkeitstemperatur der kompakten VLBI Kernregion (deren Größe gerade einmal $\sim 10R_s$ bei 86 GHz beträgt), welche nahelegt, dass die Entstehungsregion des Jets von magnetischer Energie dominiert wird; (ii) der große Durchmesser der Jetbasis ($\sim$ (4-6) R_s), abgeleitet von dem Kollimationsprofil des an den Rändern helleren Jets und der langsamen Ausbreitungsgeschwindigkeit des inneren Jets (scheinbare Geschwindigkeit $\lesssim 1.0\,$c). Dies gibt Hinweise darauf, dass die hellen Ränder des Jets wahrscheinlich von der inneren Akkretionsscheibe hervorgehen; (iii) die rapide ansteigende Helligkeitstemperatur des VLBI

Kernes bei niedrigen Beobachtungsfrequenzen (eine Größenordnung von 230 GHz zu 1.6 GHz). Dies könnte ein Hinweis auf interne mikroskopische Teilchenbeschleunigung sein; und (iv) das Vorhandensein einer schwachen, zentralen Spur zwischen den hellen Rändern des Jets, welche mit einem ultra-relativistischen inneren Teil der Ausströmung übereinstimmt, welche einen anderen physikalischen Ursprung hat.

Die GMVA Beobachtungen von 3C 84 von Mai 2015 bilden die komplizierte innere Struktur des Jets mit einer Auflösung von $250 R_s$ bei 86 GHz ab (mit dem bisher höchsten Kontrast eines Bildes von ~ 3400 bei dieser Frequenz). Andere intensive Multi-Frequenz VLBI Beobachtungen im Laufe des Jahres 2015 haben ebenfalls eine mit der Zeit sehr variable Flussdichte in der VLBI Kernregion offenbart. In dieser Doktorarbeit habe ich meinen Schwerpunkt speziell auf die spektralen Eigenschaften und die der linearen Polarisation gesetzt und präsentiere folgende Ergebnisse: (1) Eine signifikante Detektion von linear polarisierten Strukturen in der VLBI Kernregion bei 86 GHz und 43 GHz, deren Morphologie auf Zeitskalen von Monaten sehr variabel ist (bei 43 GHz); (2) eine signifikante Detektion von Faraday-Rotation in der Kernregion (typische Werte des rotation measure (RM) sind $\sim 10^{(5-6)}\mathrm{rad/m^2}$) und einer änderung des Vorzeichens des RM im Laufe der Zeit; (3) Vergleich der Faraday-Depolarisations-Modelle und des beobachteten linearen Polarisations-Spektrums, welches eine Grenzfläche des Jets suggeriert. Diese wird durch geordnete magnetische Felder aufgefädelt wie der externe Faraday-Schirm; (4) eine Abschätzung der magnetischen Feldstärke und der Teilchendichte der Elektronen im Jet mithilfe einer gemeinsamen Analyse der beobachteten Faraday-Rotation und der Synchrotron-Selbst-Absorption in der Kernregion.

Diese Erkenntnisse stellen neue, sehr wertvolle Informationen über die innere Struktur von M 87 und 3C 84 zur Verfügung. Diese Beobachtungen fungieren als hervorragende, morphologische Beschreibung der totalen und polarisierten Intensität dieser Quellen, mit welchen Theoretiker ihre Modelle anpassen können. Eine Zusammenfassung meiner wichtigsten Schlussfolgerungen und vorgeschlagenen zukünftigen Arbeiten gebe ich in Kapitel 5.

Table of contents

List of figures xiii

List of tables xvii

1 Introduction 1

1.1 Brief history of active galactic nuclei . . . 1

1.1.1 Modern understanding of AGN . . . 2

1.2 The central engine . . . 3

1.2.1 The supermassive black holes . . . 4

1.2.2 Accretion flow . . . 5

1.2.3 X-ray corona . . . 8

1.3 Broad- and narrow-line emission regions . . . 9

1.4 Dusty torus . . . 11

1.5 Jets and outflows . . . 13

1.5.1 Relativistic AGN jet . . . 14

1.5.2 Non-relativistic disk winds . . . 23

1.6 Radiation from AGN jets . . . 24

1.6.1 Synchrotron spectrum . . . 24

1.6.2 Brightness temperature . . . 27

1.6.3 Polarization . . . 27

1.6.4 Relativistic effects . . . 30

1.6.5 Inverse Compton scattering . . . 34

1.7 Summary – unification of (nearly all) AGNs . . . 36

1.8 Main scope of this thesis . . . 38

2 Radio interferometric observations 41

2.1 Concepts of radio astronomy . . . 41

2.1.1 Antenna . . . 42

2.1.2 Feed horns . . . 43
2.1.3 Receivers and further data processing . . . 44
2.1.4 Practical calibration procedure . . . 45
2.2 Radio interferometry . . . 47
2.2.1 Interferometric response – fringes . . . 48
2.2.2 Image⇔Visibility – 2D Fourier transform . . . 51
2.2.3 Practicalities of interferometric observations . . . 54
2.2.4 VLBI polarimetry . . . 64

3 Millimeter VLBI observations of the radio galaxy M 87 67
3.1 Introduction . . . 67
3.1.1 Previous studies and motivation . . . 68
3.2 GMVA 86 GHz observations of M 87 . . . 72
3.2.1 Observations and data reduction . . . 72
3.2.2 Results and analysis . . . 73
3.2.3 Discussions . . . 83
3.2.4 Conclusions from the GMVA observations . . . 95
3.3 Multi-frequency VLBI observations . . . 96
3.3.1 Quasi-simultaneous multi-frequency VLBI observations in 2009 . . . 96
3.3.2 Frequency dependence of the brightness temperature in the M 87 core 108
3.4 KVN multi-frequency VLBI monitoring of M 87 . . . 113
3.4.1 Observations and data processing . . . 116
3.4.2 Results and analysis . . . 118
3.4.3 Discussion . . . 122
3.5 Summary of the multi-frequency VLBI observations . . . 123

4 Millimeter VLBI polarimetry of 3C 84 125
4.1 Introduction . . . 125
4.2 Observations and data reduction . . . 128
4.2.1 GMVA 86 GHz data . . . 128
4.2.2 Contemporaneous 43 GHz and 15 GHz VLBA data . . . 134
4.2.3 Other VLBA 43 GHz data . . . 135
4.2.4 Contemporaneous ALMA data . . . 135
4.2.5 Model-fitting, polarization measurements, and their uncertainties . . . 136
4.3 Results . . . 137
4.3.1 Total intensity structure and the core flux density . . . 137
4.3.2 Linear polarization in the core region . . . 140

4.3.3 Rotation measure between 43 GHz and 343.5 GHz in May 2015 . . . 142
4.3.4 Rotation measure within the 43 GHz band 145
4.4 Discussions 149
4.4.1 Polarization structure 149
4.4.2 Polarization spectrum and the origin of the large EVPA rotation . . . 150
4.4.3 Faraday depolarization models 152
4.4.4 Estimation of the jet magnetic field strength and electron density . . . 157
4.5 Summary of conclusions 159

5 Summary **161**

References **167**

Appendix A Model-fit parameters of the VLBI core of the M 87 jet obtained by KVN observations **179**

Appendix B GMVA polarization images of the other sources in May 2015 **185**

Appendix C Multi-epoch VLBA 43 GHz total and linear polarization measurements of 3C 84 **195**

List of figures

1.1 Schematic diagram of AGN unification model 3
1.2 A sketch of the spacetime around a Kerr BH 5
1.3 Different types of accretion flows versus Eddington ratio 7
1.4 Illustration of a broad emission line profile in a BH-disk system 10
1.5 Median quasar composite spectrum in the optical band 11
1.6 Geometry of AGN torus 12
1.7 Illustration of jet phenomena in compact astrophysical systems 13
1.8 Example of structure of an extragalactic jet in M 87 16
1.9 Example of jet formation from BH and disk in numerical simulation 18
1.10 Conversion of magnetic energy into kinetic power in jets 19
1.11 Example of kpc-scale jet structure in Cygnus A 21
1.12 Synchrotron spectrum of a partially self-absorpbed plasma 26
1.13 Schematic illustration of a typical AGN jet polarization morphology 29
1.14 Relativistic beaming 31
1.15 Doppler boosting effect 32
1.16 Geometry of relativistic beaming in a bipolar jet 33
1.17 Flux density ratio of the jet and counter-jet 33
1.18 Apparent superluminal jet speed versus viewing angle 34
1.19 Example of apparent superluminal motion 35
1.20 Example of broadband SED variabilities of a blazar 3C 454.3 36
1.21 Summary of the AGN categories 37

2.1 Diagram of data acquisition and analysis 42
2.2 Beam pattern of an antenna 43
2.3 Block diagram of data acquisition and process 45
2.4 A photo of ALMA band-8 receiver box 46
2.5 Illustration of the fundamental idea of interferometry 49
2.6 Two element interferometer 50

2.7 Definition of the coordinates (l,m,n) in the sky and (u,v,w) for the baseline . 52
2.8 Example of FFT fringe fitting 57
2.9 Incomplete (u,v) sampling and the corresponding synthetic beam 59
2.10 Example visibility distribution and dirty map 60
2.11 Final dirty and CLEAN maps 62

3.1 Hubble Space Telescope image of M 87 69
3.2 Proper motions of bright components in the inner jet of M 87 70
3.3 Illustration of Global Millimeter VLBI Array 71
3.5 Radial dependence of the visibility amplitude of the 2015 data 75
3.6 GMVA images of M 87 76
3.7 Stacked M 87 jet images and transverse intensity profiles 79
3.8 Averaged transverse jet intensity profile 80
3.9 M 87 jet base collimation profile 81
3.10 Illustration of the central engine and the 86 GHz core geometry 82
3.11 Gradient of the jet to counter-jet intensity ratio (R) 84
3.12 Diameter of the jet base at a distance of $1R_s$ from the BH center as a function of positional offset ε 88
3.13 Possible range of M 87 jet viewing angles and jet speeds 92
3.14 Bulk Lorentz factor of the inner jet of M 87 93
3.15 Doppler factor versus Lorentz factor for the spine 94
3.16 VLBA 43 GHz and 15 GHz images of the jet of M 87 in 2009 98
3.17 GMVA 86 GHz image of the jet of M 87 recovered by the model-fitting . . . 101
3.18 The same as Fig. 3.17 but for the VLBA 43 GHz data 102
3.19 The same as Fig. 3.17 but for the VLBA 15 GHz data 103
3.20 Arc-second scale ALMA flux measurements of the M 87 core synchrotron spectrum between 221 GHz and 635 GHz in 2012 105
3.21 The VLBI core synchrotron spectrum between 43 GHz and 230 GHz in 2009 106
3.22 Kinematics of the inner M 87 jet in 2009 109
3.23 Apparent inner M 87 jet velocity versus the core separation 110
3.24 Brightness temperature of the core of M 87 at different frequencies 114
3.25 Doppler factor versus bulk Lorentz factor 114
3.26 Multi-frequency core flux density light curves obtained by the KVN observations 119
3.27 KVN visibility amplitudes of M 87 as a function of (u,v) distance at 43 GHz . 119
3.28 Spectral index light curve of the core of M 87 ($S \propto \nu^{+\alpha}$). 120
3.29 Radio spectrum of the M 87 core region in log-log scale 121

4.1 Hubble Space Telescope and VLBI images of the host galaxy NGC 1275 and the radio source 3C 84 . . . 126
4.2 Stokes I visibilities of the GMVA 86 GHz data of 3C 84 . . . 131
4.3 Polarimetric VLBI images of 3C 84 at 15 GHz and 43 GHz . . . 138
4.4 GMVA 86 GHz images of 3C 84 . . . 139
4.5 Transverse jet intensity profiles at 43 GHz and 86 GHz . . . 140
4.6 Total intensity spectrum of the VLBI core region between 15 GHz and 86 GHz. 140
4.7 VLBA 43 GHz core flux density and the peak values of 3C 84 during 2015 . . 141
4.8 Comparison of the total intensity, the polarized intensity, and the polarization angle in the nuclear region at 43 GHz and 86 GHz . . . 141
4.9 VLBA 43 GHz polarization images of 3C 84 zoomed into the core . . . 143
4.10 Spatially integrated EVPA versus the squared wavelength and the best λ^2 fit in May 2015 . . . 145
4.11 43-86 GHz RM distributions of 3C 84 . . . 146
4.12 Variation of the measured EVPA in 4 sub-bands of the VLBA 43 GHz observing band at different observing epochs . . . 147
4.13 EVPAs of 3C 84 versus the squared wavelength λ^2 within the VLBA 43 GHz band . . . 148
4.14 Slice profiles of the total intensity, linear polarization intensity, and degree of linear polarization at 86 GHz . . . 150
4.15 Degrees of linear polarization of 3C 84 from this work, previous VLBA observations, and spatially integrated single-dish or connected-interferometer observations from the literature . . . 151
4.16 Upper limits for m_L for external (Case I and II) and internal (Case III) Faraday depolarization and the VLBI polarization from observations . . . 154
4.17 Illustration of the geometry discussed throughout Sect. 4.3.3 and 4.4.3 . . . 156

B.1 0716+714. . . . 186
B.2 3C 111. . . . 187
B.3 3C 120. . . . 188
B.4 3C 273. . . . 189
B.5 3C 279. . . . 190
B.6 3C 454.3. . . . 191
B.7 BL Lac. . . . 192
B.8 CTA 102. . . . 193
B.9 OJ 287. . . . 194

List of tables

3.1 Summary of the GMVA 86 GHz observations of M 87 74

3.2 VLBI core model-fit parameters at 86 GHz 77

3.3 Brightness temperature ratio and the magnetic field strength 86

3.4 M 87 jet component parameters obtained by the multi-Gaussian model-fitting 104

3.5 Synchrotron spectrum model-fit parameters 107

3.6 A summary of the jet component kinematics 110

3.7 Gaussian modelfit properties of the VLBI core of M 87 at different frequencies 115

4.1 Summary of the polarimetric VLBI observations of 3C 84 in May 2015. . . . 130

4.2 Summary of the GMVA antenna D-terms at 86 GHz 133

4.3 Summary of the ALMA archival data 136

4.4 VLBI model-fit core properties of 3C 84 in May 2015 138

4.5 Properties of the polarized components of 3C 84 in May 2015 144

4.6 Rotation measure within the VLBA 43 GHz band 147

A.1 KVN observing epochs and M 87 core model-fit parameters 180

A.1 Continued. 181

A.1 Continued. 182

A.1 Continued. 183

C.1 Properties of the polarized components of 3C 84 obtained for the four different IFs of the VLBA 43 GHz data 196

C.2 Stokes I core flux density, the peak, and the core FWHM size during 2015 measured from the VLBA 43 GHz data of 3C 84 196

Chapter 1

Introduction

1.1 Brief history of active galactic nuclei

Active galaxies are, like normal galaxies, systems of stars, gases, and dust that are bound to each other by self gravity. However, active galaxies contain peculiar nuclei (active galactic nuclei; hereafter AGN), which are characterized by their extreme luminosity and compact size. A brief history about pioneering studies of AGN is outlined below to illustrate basic properties of AGN.

One of the first systematic observations towards AGN was made by Seyfert (1943) when extragalactic objects were still often called as *nebulae* due to their nebulous aspect. The author reported that the velocity dispersion of the observed galaxy optical emission lines is ~ 8500 km/s. Such a large velocity dispersion was later interpreted as extreme motion of ionized gas in the galactic nuclei (Burbidge et al., 1959). Woltjer (1959) also pointed out that bright galactic nuclei emitting the broad emission lines are spatially extended only over ~ 100 parsec scales. This implies a large dynamical mass of 100 million solar masses to hold the ionized gases moving at high speed. Galaxies showing such optical emission lines were later named as *Seyfert galaxies*. Independently, novel techniques were developed to observe celestial sources at radio wavelengths in the 1930s. Karl G. Jansky detected the serendipitous radio emission from outside our solar system for the first time (Jansky, 1933). Its origin was later identified as the center of our galaxy. In the 1950s, a number of extragalactic objects were identified in radio wavelengths by the Third Cambridge Catalogue of Radio Sources (3CR) survey. However, the origin of extragalactic radio emission remained elusive because it was difficult to match their poorly determined radio positions with photographic images. This occasionally confused astronomers (see, e.g., Baade & Minkowski 1954 for the case of Cygnus A). It was 1963 when Maarten Schmidt discovered that the radio source 3C 273 was associated with an optically unresolved, star-like bright object (Quasi-Stellar Object; *QSO*) (Schmidt, 1963). The source was emitting highly red-shifted optical emission lines. The high red-shift suggested that the star-like object (and the radio counter-part) is located at a cosmological distance. Another interesting aspect of this finding was that the star-like object was nearly 100 times brighter than typical host galaxies of similar radio sources. Thus, it became clear that both the QSO and the quasi-stellar radio source 3C 273 (*Quasar*) were associated with an ultra-luminous nucleus in a distant extra galaxy, i.e., an AGN. Indeed, AGNs are typically ultra-luminous so that they can easily outshine their host galaxies in the distant universe and appear to the observer in the optical just like starts. New observational studies followed. Sandage (1965) found a large number of AGNs at even higher redshifts. It was also found that a large fraction of QSOs do not have radio counterparts. This implies that AGNs do not always produce radio emission. Later, this idea led to the classification of *radio-loud* and *radio-quiet* AGN.

Based on observational progress, new theoretical questions were posed. The most intriguing question among them was the possible source of the extraordinary high luminosity observed. Several explanations were suggested. Burbidge (1961) proposed a chain reaction of supernovae explosions in a dense star cluster in a galactic nucleus. Spitzer & Saslaw (1966) also suggested frequent stellar collisions and tidal encounters in a dense star cluster and release of large amount of gases and energies. Notably, Hoyle & Fowler (1963) proposed the possibility of powering AGN by gravitational potential energy via mass accretion onto a stellar-type object of large mass. It was soon realized that mass accretion is a highly efficient process for a given small volume. Later, researchers suggested more specific scenarios such as mass accretion onto supermassive black holes (SMBHs) in the center of active galaxies because SMBHs were able to hold large amount of mass in a small volume (Salpeter, 1964; Zel'dovich & Novikov, 1964; Lynden-Bell, 1969; Lynden-Bell & Rees, 1971). A model of an accretion disk around a SMBH successfully explained the non-stellar origin of radiation in nearby Seyfert galaxies (e.g., Lynden-Bell 1969) and their X-ray emission observed by early astronomical X-ray observations as well (see Beckmann & Shrader 2012 and references therein).

A more detailed review about the history of AGN research can be found in the following literature; Urry & Padovani (1995); Shields (1999). In the next sections, I will provide additional, more recent physical explanations about AGNs based on the present understanding of their astrophysical processes.

1.1.1 Modern understanding of AGN

Since the early discoveries of AGNs, our knowledge has evolved significantly by cutting-edge observations and state-of-the-art theories. Figure 1.1 provides a schematic illustration of how we understand an AGN and its sub-components. The current paradigm of AGN is largely based on this picture, which is the so-called *AGN Unification Model* (Urry & Padovani, 1995).

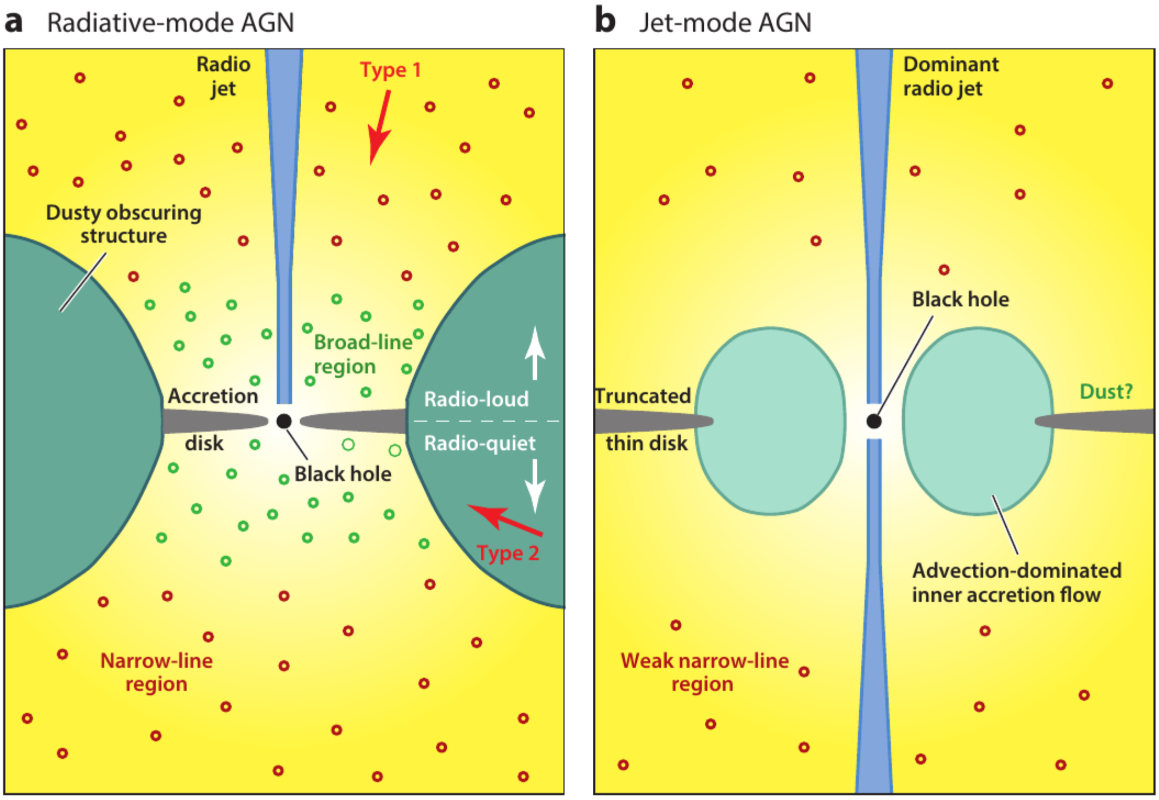
a Radiative-mode AGN
Radio jet
Type 1
Dusty obscuring structure
Broad-line region
Accretion disk
Black hole
Radio-loud
Radio-quiet
Type 2
Narrow-line region
b Jet-mode AGN
Dominant radio jet
Black hole
Truncated thin disk
Dust?
Advection-dominated inner accretion flow
Weak narrow-line region

Fig. 1.1 A schematic diagram showing the geometry of several elements that constitute a typical AGN. **(a)** : For a radiative-mode AGN with weak or no radio jet. **(b)** : For a jet-mode AGN with a prominent radio jet but weak or no line emissions. The figure is not drawn to scale. Figure taken from Heckman & Best (2014).

The model explains variety of AGN properties by adopting intrinsically the same AGN but viewed at different angles by observers. From §1.2 to §1.5 we describe the basic properties of each individual component in more detail. In §1.6 we discuss the radiation processes in AGN, particularly focusing on emission mechanisms related to AGN jets. Then, we discuss in §1.7 how different viewing angles give rise to different AGN classes (and what are still not clearly understood).

1.2 The central engine

The central engine converts the gravitational energy of accreting gas into radiation and triggers outflows of plasma. The central engine is the main source of the deep gravitational potential which attracts gas spiralling around and falling onto the central supermassive black hole.

1.2.1 The supermassive black holes

Supermassive black holes (SMBHs) are a scaled-up version of typical astrophysical black holes such as stellar mass black holes. As the name implies, SMBHs have extraordinarily large mass ranging between $10^6 - 10^{10} M_\odot$ where $M_\odot \approx 2 \times 10^{33} g$ is the solar mass. It is also remarkable that SMBHs are supposed to reside not only exclusively in AGNs but also in many other types of galaxies. One of the best examples is the Milky Way. A massive BH named as Sagittarius A* resides at the center of our galaxy and its mass is accurately measured ($M_{\rm BH} \sim 4.3 \times 10^6 M_\odot$ based on Keplerian motions of stars orbiting the BH; see, e.g., Gillessen et al. 2009). It is still not fully understood how SMBHs were able to accumulate such a large mass over the cosmic time. However, several evolutionary pathways to produce SMBHs have been proposed during the last decades. The scenarios basically suggest that SMBHs and/or their seeds were formed in the early universe when primordial cold gases in proto-galaxies condensated due to gravity of dark matter halo (see, e.g., Volonteri 2012). An observationally found strong correlation between mass of the SMBHs and the host galaxy stellar mass also indicate that there have been strong interplay between the SMBH and host galaxies during their evolution over cosmic time (see Heckman & Best 2014 for a review).

SMBHs can be characterized by two main parameters – their mass ($M_{\rm BH}$) and spin (a)[1]. The mass is a dominant factor in determining the size of the event horizon. The event horizon of a non-rotating BH is characterized by the Schwarzschild radius R_s which is the radius of a spherical BH sphere. R_s is given by $R_s = 2GM_{\rm BH}/c^2 \approx 3(M_{\rm BH}/M_\odot)$ km where G is the gravitational constant and c is the speed of light. This implies that more massive BHs are simply larger, being the radius directly proportional to the mass. It is also useful to define the gravitational radius $R_g = GM_{\rm BH}/c^2$ and express R_s by $R_s = 2R_g$ because R_g is independent of the BH spin. On the other hand, SMBHs in galaxies presumably have non-zero spin because of their astrophysical origin. The BH spin a is expressed in a normalized form by $a = (Jc)/(GM_{BH}^2)$ where J is the BH angular momentum (i.e., $0 \leq a \leq 1$). A non-zero BH spin has an important implication because it changes the structure of the spacetime near the event horizon as well as the size of the event horizon itself. A sketch of the spacetime near a spinning black hole is presented in Fig. 1.2. The radius of the event horizon of a spinning BH R_k is smaller than that of the non-spinning BH:

$$R_k = 2GM/c^2 \times (1 - \sqrt{1-a^2}) = 2R_g(1 - \sqrt{1-a^2}) \quad . \tag{1.1}$$

---

[1] In theory, BHs can have certain non-zero net electric charge Q. However, astrophysical BHs have $Q \approx 0$ because they form out of stars, compact objects, and gaseous interstellar medium, all of which have no net electric charge.

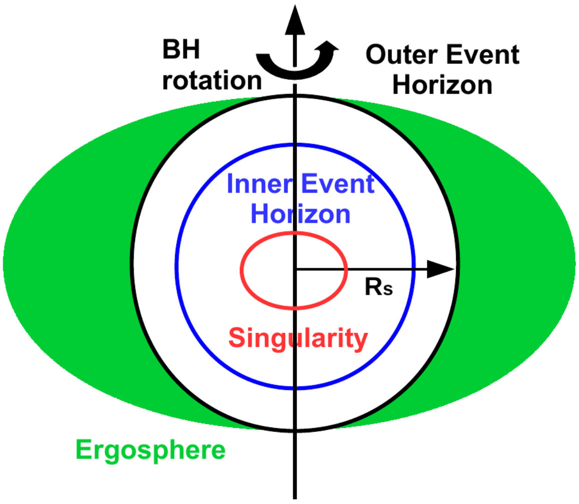

Fig. 1.2 A sketch of the spacetime around a Kerr BH.

Outside the event horizon is a region in which BH rotation causes the inertial frame to be dragged in the direction of the BH spin (thus accelerating a test particle in this region). This phenomenon is called Lense-Thirring effect and also known as frame-dragging (see, e.g., Misner et al. 1973). This region is called ergosphere and has a radius of

$$R_e = R_g(1 - \sqrt{1 - a^2 \cos\theta}) \tag{1.2}$$

where θ is the angle measured from the pole of the rotation. We note that R_e is always greater than R_k. This implies that matter falling towards BH can enter this region and also escape to outside if sufficient escape energy is provided. This is indeed possible because matter orbiting around the BH within the ergosphere can extract rotation energy of the BH via the Blandford-Znajek mechanism (Blandford & Znajek, 1977). This has important implications for the physics of the mass accretion (§1.2.2) and outflows (§1.5) in the central engine of AGN.

1.2.2 Accretion flow

Gas in the vicinity of the central engine falls towards central BH due to the strong gravitational potential. In astrophysical circumstances, the gas has non-negligible angular momentum with respect to the central BH. Therefore, the gas forms a rotating flow. The rotating flow has different rotation speeds at different radial distances as a consequence of the Keplerian motion. Therefore, various kinds of viscosities are naturally developed between different layers. The viscosity gradually transports the angular momentum in the inner region to outward. This helps the gas finally plunge into the BH. Such kind of inflow is broadly called accretion flow.

Observational evidence for the presence of accretion flows in AGNs includes the large bolometric luminosity of AGN and shape of the spectral energy distribution (SED) in the optical and ultraviolet wavelengths (e.g., Malkan & Sargent 1982). Broadband SEDs of AGNs typically show a big bump of continuum emission in the form of the so-called *Big Blue Bump*. The optical continuum SED of BH accretion flow can be understood as following. Near the BH, the rotation velocity of accretion flow becomes very high and the viscosity effect is also strong. This makes the gas temperature high (e.g., $\gtrsim 10^4$ K) and the exact flow temperature depends on the distance from the BH. Given that the accretion disk is optically thick, the emission spectrum of a local region in the disk can be approximated by that of a black body with the disk temperature. The sum of the black body spectra with different disk temperature gives rise to the excess ultraviolet emission from the entire accretion disk. Similarly, the SEDs of accretion disks can be decomposed into several black body spectra with typical temperatures of 10^{4-7} K or even higher.

There are several macroscopic, phenomenological parameters describing accretion flows in AGNs. The first parameter is the mass accretion rate $\dot{M}$ which is also simply called accretion rate. For spherical mass accretion, the total amount of gas captured by the central engine is predominantly determined by the total mass within a critical radial distance where the velocity of a test particle v (or the sound speed of environmental gas c_s when $v < c_s$) is equal to the escape velocity. Bondi (1952) shows that the mass accretion rate is then

$$\dot{M} = \frac{4\pi\rho G^2 M_{\rm BH}^2}{c_s^3} \tag{1.3}$$

where ρ is the ambient gas density. The second parameter is the bolometric luminosity of the accretion flow L. Accretion flows produce radiation and the radiation energy primarily comes from the gravitational potential energy of the accreting gas. It is therefore useful to express the luminosity in terms of the rest mass energy of the accretion rate $\dot{M}$ such that $L = \eta\dot{M}c^2$ where η is the efficiency of the energy conversion process. Although the exact value of η depends on a number of details, typical values are $\eta \sim 0.1$ for the geometry of BH accretion systems. This is far greater than that of the nuclear fusion of hydrogen into helium, $\eta \sim 0.007$. Thus, mass accretion is a very efficient mechanism to power AGN. The third parameter is a characteristic upper limit of the luminosity of the accretion. The luminosity upper limit and the accretion rate are closely related because the disk radiation produces an outward pressure against the gravitational force acting on the infalling gas. For an accretion flow with spherical geometry, this upper limit is called *Eddington luminosity* and is given by

$$L_{\rm Edd} = \frac{4\pi G c M_{\rm BH}}{\kappa_{es}} \tag{1.4}$$

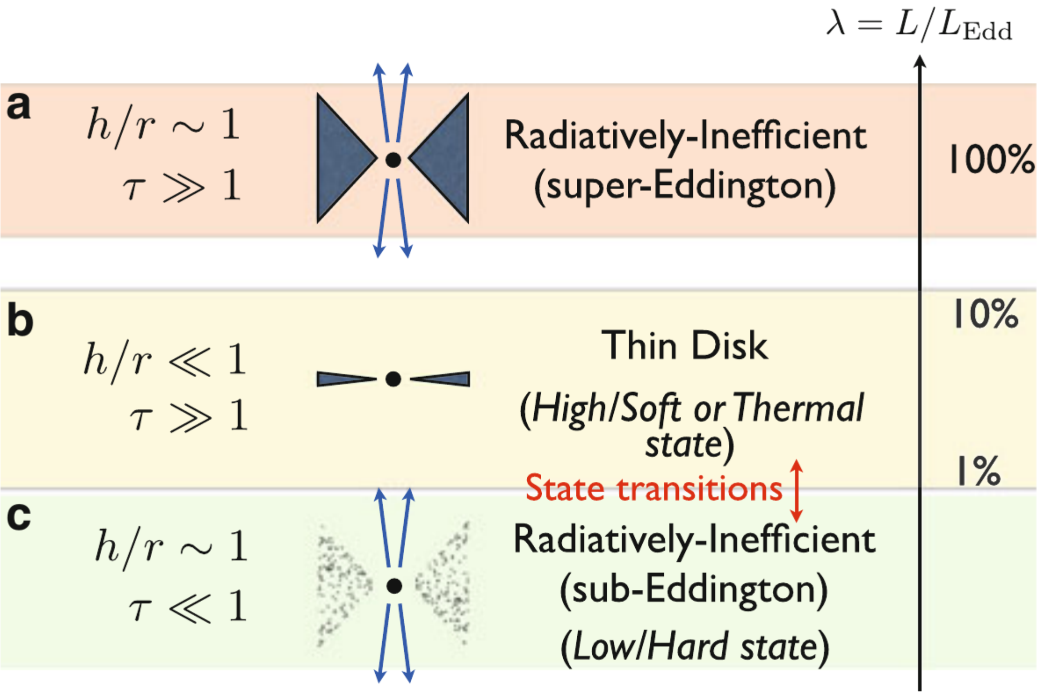
$\lambda = L/L_{\rm Edd}$
a
$h/r \sim 1$
$\tau \gg 1$
Radiatively-Inefficient
(super-Eddington)
100%
b
$h/r \ll 1$
$\tau \gg 1$
Thin Disk
(High/Soft or Thermal state)
10%
1%
State transitions
c
$h/r \sim 1$
$\tau \ll 1$
Radiatively-Inefficient
(sub-Eddington)
(Low/Hard state)

Fig. 1.3 Different types of accretion flows depending on the Eddington ratio. The figure taken from Tchekhovskoy (2015).

where $\kappa_{\rm es} \sim 0.4$ cm^2 g^{-1} is the electron scattering opacity. If the BH mass is known a priori, one can compare the observed disk luminosity with $L_{\rm Edd}$ and compute the *Eddington ratio* by $\lambda = L/L_{\rm Edd}$. Similarly, one could also define the corresponding mass accretion rate, *the Eddington accretion rate*, $\dot{M}_{\rm Edd} = L_{\rm Edd}/\eta c^2$. The Eddington ratio and accretion rate are useful to understand the state of the mass accretion (see 1.3).

Finally, the innermost stable circular orbit (ISCO) distinguishes BH accretion flow from other similar flows. This is because the effective gravitational potential of BH differs from that of Newtonian cases. When a test particle approaches the BH closer than the ISCO, the particle cannot maintain a stable orbit any more and plunges into the BH. For a continuous flow, this implies a truncated inner edge of the disk. Therefore the ISCO defines the minimum inner radius of a rotating accretion flow. Depending on the BH spin a, the ISCO radius ranges between $(1-6) \times R_g$ for $a = (1-0)$ where R_g is the gravitational radius[2].

The above descriptions are useful to understand the basic properties of the accretion flows. However, it is also important to note that the detailed microphysics of rotating and *magnetized* plasma is highly complicated. For instance, the presumed viscosity in the accretion disk is a complicated process involving a number of different physical mechanisms. So far, the most realistic and dominant process driving the viscosity is considered to be magnetorotational instability (MRI; Balbus & Hawley 1991). Also, in the strong magnetic field case, the accretion flows are not only subject to the gravitational potential of the BH but the fields themselves also become dynamically important (see Zamaninasab et al. 2014 and references therein). The thermodynamics of the accretion flow is also important. It is possible that the viscously dissipated energy is not converted into radiation but rather heats the particles by advection (Ichimaru, 1977). Other microphysical processes such as magnetrohydrodynamic (MHD) turbulence, magnetic reconnection, and pressure anisotropy in a collisionless plasma are also able to do so. In fact, observations often find a large X-ray to optical bolometric luminosity ratio and frequent absence of the excess of ultraviolet emission (i.e., the big blue bump). They suggest that non-standard disk-like accretion flows do exist in a number of AGNs. Such accretion flows are often called advection dominated accretion flows (ADAFs) (Narayan & Yi, 1994) or more broadly *hot accretion flows* (see Yuan & Narayan 2014 for a review).

---

[2] This is for the case of a prograde black hole and accretion disk system. In the retrograde case, the ISCO radius is $(6-9) \times R_g$ for $a = -(1-0)$.

To summarize, there exist two main types of accretion flows : (i) relatively cold plasma with thin and disk-like geometry (electron temperature $T_e \sim 10^4$ K; Shakura & Sunyaev 1973 and see also Blaes 2014 for a brief review) and (ii) hot plasma with thick disk with large disk height to disk radius ratio ($T_e \sim 10^{10}$ K; see Yuan & Narayan 2014). Those models are successful in explaining various types of AGNs which are believed to be in different phases of their evolution. In particular, the hot accretion flow appears to be crucial for the formation and propagation of jets and outflows (§1.5).

1.2.3 X-ray corona

Based on the existence of ubiquitous hard X-ray continuum emission in AGN (i.e., photon energy $\gtrsim 10$ keV), astronomers have suggested the existence of a coronal medium on top of the AGN accretion disk (see Uttley et al. 2014 for a review). The corona most likely contains energetic electrons and produces X-ray radiation by inverse Compton scattering of seed photons from accretion disks. In addition, the continuum X-ray photons ionize gas in the accretion disk. This results in highly ionized iron and other emission lines, which are frequently observed at X-ray energy spectrum. It is unclear if the corona is just a part of the hot accretion flow or it is a group of clouds floating above the disk. However, studies suggest that the X-ray corona is often located very close to the BH ($\sim 10 R_g$).

One of the important merits of observing the X-ray corona emission is that it allows us to indirectly probe geometry and properties of the inner BH accretion disk. For instance, as explained above, the observed X-ray emission originates not only from the corona itself (which emits a power-law continuum) but also from the inner accretion disk (which emits highly ionized emission lines). The latter lags behind the former because of additional geometric pathlengths. This time lag depends on the spatial extension of the highly ionized regions in the disk (e.g., located within a few to tens of R_g from the BH). Thus, the time-series analysis of the X-ray continuum and line emission can constrain the geometry of the inner accretion disk. This technique is called the X-ray reverberation mapping (see Uttley et al. 2014 for technical details). On the other hand, detailed shape of the line emission profile also contains a lot of information. The line profiles are influenced by (i) Doppler shift from the relativistic beaming due to the fast disk rotation and (ii) gravitational redshift due to the deep gravitational potential of the central BH. Therefore, it is possible to build a model of the line profiles based on the above effects. An example of the resulting line emission is shown in Fig. 1.4. Observational studies measure the time lags and model the disk geometry including the BH spin effect (Brenneman & Reynolds, 2009). Now the X-ray reverberation phenomena are found in $\sim 50\%$ of all X-ray detected Seyfert galaxies (Kara et al., 2016). It is also important to note that such measurements are not possible at longer observing wavelengths because of heavy obscuration of the inner accretion disk by the presumed dusty torus (see §1.4).

1.3 Broad- and narrow-line emission regions

The gravitational potential of the central engine is strong enough to hold ambient gas at even larger distances from the central BH. The gases are strongly bound to the system and move at high speed. They can be also photo-ionized by the strong continuum radiation from the accretion disk. Therefore, the gases produce unique emission lines with very large line widths. Typical full-width-half-maximum (FWHM) widths of observed hydrogen Balmer lines are typically $\Delta v \gtrsim 1000$ km s^{-1} (see Fig. 1.5). Because of the broad widths of such lines, a region containing these gases is called broad line region (BLR). It is unclear if the gases are a group of randomly moving clouds or if they form an organized stream surrounding the central engine. But it is remarkable to note that thermal Doppler broadening cannot reproduce the observed Hα or Hβ line widths because the corresponding kinetic temperature of $T \sim 10^7$ K to 10^8 K should ionize almost all hydrogen in the gas. This indicates that the broad lines are produced by bulk, Keplerian random motions of the gases under strong gravity.

Another interesting feature of the BLR is that the broad line luminosity is time-variable and the variability is correlated with the variable continuum radiation from the disk. The line variabilities lag behind the disk luminosity by usually a few weeks to several months (or even years). This provides an estimate of the distance of the gas from the BH. The mass of the central BH responsible for the gravitational potential can be estimated from the observed Keplerian velocities based on the Virial theorem by $M_{\rm BH} \approx \frac{\tau c}{G} f \Delta v^2$ where τ is the time lag and f is a scaling factor that depends on the geometry. This technique is called *Reverberation mapping*

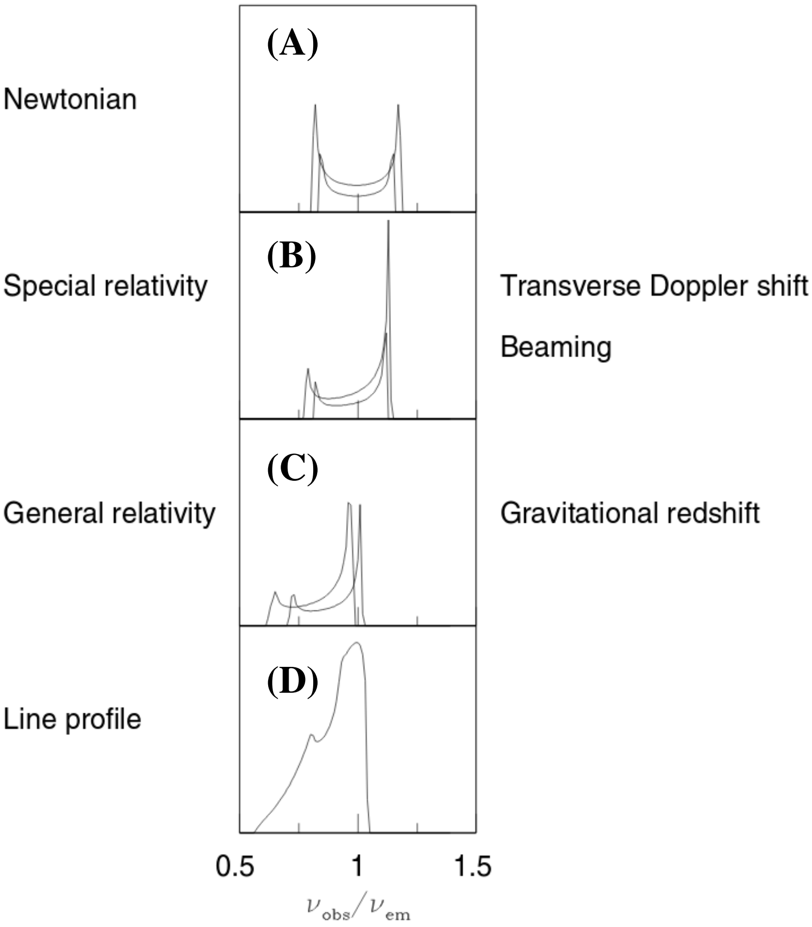

Fig. 1.4 Illustration of a broad iron line profile in a BH-disk system. **(A)** The line profile of one annulus in the disk without relativistic effects, **(B)** The same line profile affected by relativistic Doppler boosting. **(C)** The same profile as (B) after accounting for the gravitational redshift. **(D)** A synthetic line profile of a disk ring generated by the sum of many orbits. The figure has been taken from Fabian (2008).

and gives a good estimate of the BH mass. Studies based on this method reveal wide range of the BH masses with $M_{\rm BH} \sim 10^6 - 10^9 M_\odot$ (see, e.g., Bentz et al. 2009).

In addition, some lines have relatively narrower widths (Δv of hundreds of km $\rm s^{-1}$). Interestingly, the narrow lines are much less time-variabile. The gas responsible for this emission is considered to be located in the so-called narrow line region (NLR). The narrower widths and smaller velocities suggest the NLR is located farther from the BH than the BLR. Lack of the time variability also indicates that the gas in the NLR is kinetically separated from the BLR. An example of a quasar line spectrum showing the BLR and NLR signatures is displayed in Fig. 1.5.

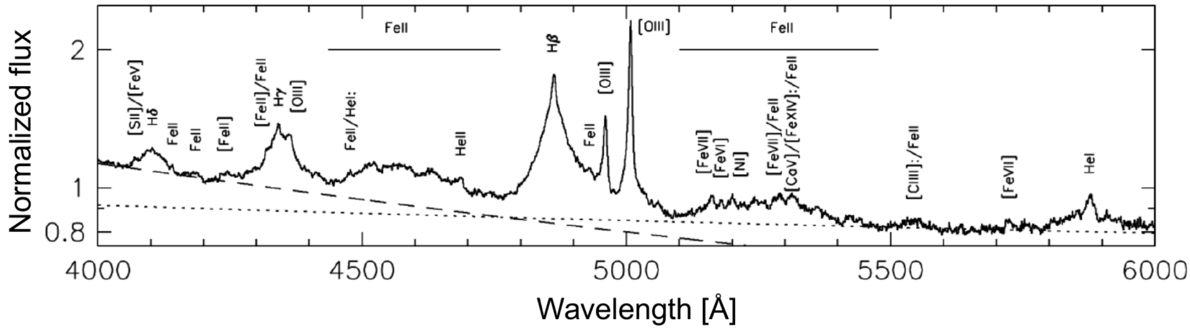

Fig. 1.5 Median quasar composite spectrum derived from the Sloan Digital Sky Survey. Note the broad Hβ and narrow [OIII] emission lines. The figure has been taken from Vanden Berk et al. (2001).

The different spatial extension of BLR and NLR makes another crucial observational difference. The broad lines are often missing in the observed spectrum in contrast to the narrow lines, which are observed in a number of Seyfert galaxies. The former and latter types of AGN are called type 1 and type 2, respectively. It is assumed that this difference is due to dusty torus whose thickness is sufficient to obscure the BLR cloud emission from close to the central engine. This difference leads to the development of the unified scheme.

1.4 Dusty torus

The torus is a key element in the unified model of AGN (Urry & Padovani, 1995). It mainly consists of dust and gas with different temperatures. As the name implies, the torus has a toroidal structure and surrounds the central engine (see Fig. 1.6 for an illustration). AGN tori are considered to have a finite thickness and obscure emission from the BLR, when the AGN is observed at a large inclination with respect to the line of sight (i.e., close to edge-on view). Statistical studies of type 1 and 2 sources suggest that a torus thickness-to-radius ratio $H/R \sim 1$ (and the corresponding viewing angle $i \sim 45°$) can explain the observed AGN population ratio (Schmitt et al., 2001). The torus obscuration is also seen in the soft X-ray band ($\sim$ 1 keV), implying that the column density of the dust is sufficiently large to scatter soft X-ray photons produced by inner accretion disk and corona away. For hard X-rays, the torus generally appears transparent and the obscuration is very weak (e.g., Gilli et al. 2001). However, very large torus column density of $N_H \gtrsim 10^{24}$ cm^{-2} could obscure even hard X-ray emissions (i.e., “Compton-thick” torus; see Comastri 2004).

It is also important to note that the internal structure of the torus could be complex. Several observational evidences – e.g., presence of cold dust ($\sim 200 - 300$ K) close to the central

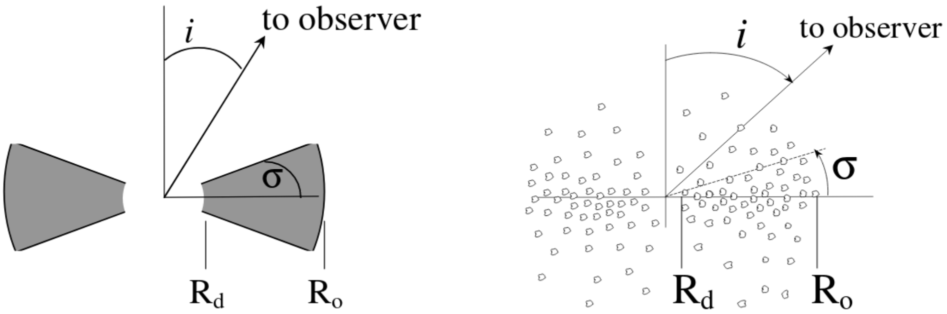

Fig. 1.6 Geometry of AGN torus. **Left** : a torus with smooth density. **Right** : a torus with clumped gases. Figure from Elitzur (2007).

engine, isotropic infrared emission from the torus, and peculiar X-ray absorption properties – suggest that the torus dusts and gases may be clumpy (Fig. 1.6, right; see Elitzur 2007). The luminosity of inner accretion disk also affects the obscuration geometry because the disk radiation sublimates dust in the inner edge of the torus. For higher-luminosity AGN, the inner wall recedes away from the central BH and the obscuration effect is weaker (i.e., larger fraction of type 1 sources; Simpson 2005).

A crucial evidence for the existence of the torus and its obscuration was obtained by detection of linearly polarized broad emission lines in type 2 Seyfert galaxies. Even though the broad optical lines are heavily obscured by the dust and thus not directly observed, electron scattering by molecules in the dust and gas can reflect the emission without absorbing them. Eventually, the scattered broad lines can escape from the central engine region and be observed. An important observational signature of the scattering is that it induces linear polarization in the broad line emission. In fact, Antonucci & Miller (1985) first discovered linearly polarized broad lines in the Seyfert 2 galaxy NGC 1068 and suggested unification of type 1 and 2 sources following the ideas discussed above. We also note that strong free-free absorptions in the counter-jet regions of several AGNs suggest a disk-like geometry of the screening medium (e.g., see §1.5 of this thesis and Krichbaum et al. 1998; Walker et al. 2000).

Last but not least, it is worth noting that the origin of dusty tori in AGNs is still not yet fully understood. Theories suggest that the formation of the torus involves gas and dust transported from the outer accretion disk, direct feeding of molecular gas from the host galaxy, and/or molecular clouds vertically outflowing from the outer accretion disk (see Beckmann & Shrader 2012 for a brief review). In spite of theoretical challenges in understanding the origin of the torus, recent millimeter/sub-millimeter observations with sensitive telescopes such as the Atacama Large Millimeter/submillimeter Array (ALMA) started to directly resolve the torus structure in nearby AGNs and reveal complex, dynamical evolution of the toroidal gas structure (see, e.g., García-Burillo et al. 2016).

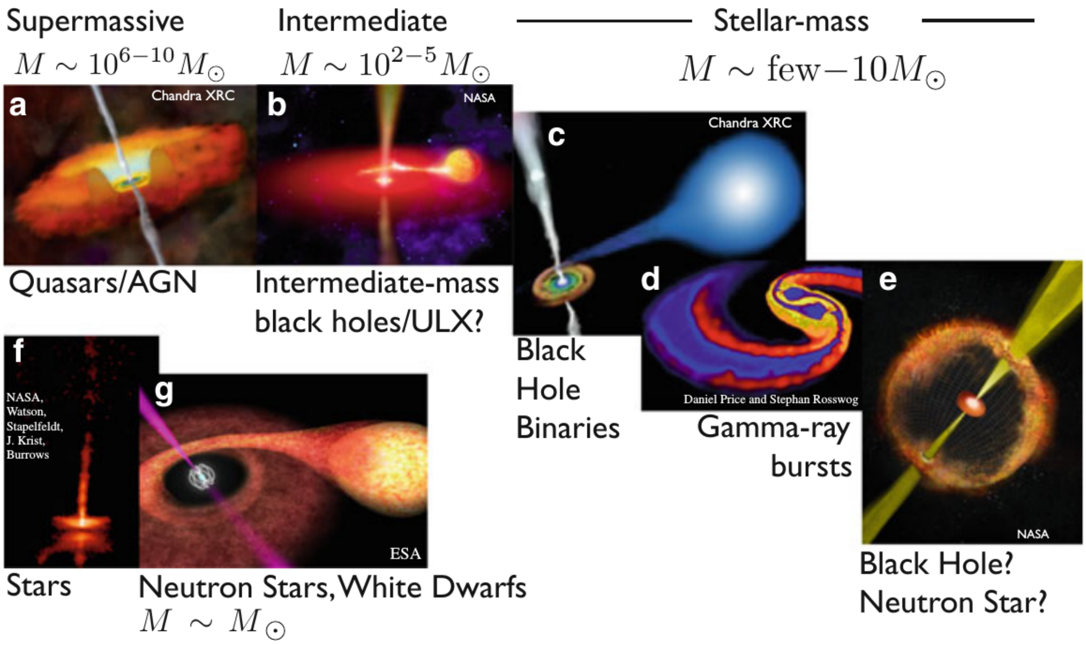
Supermassive
$M \sim 10^{6-10} M_\odot$
Intermediate
$M \sim 10^{2-5} M_\odot$
Stellar-mass
$M \sim$ few$-10 M_\odot$
a
Chandra XRC
b
NASA
c
Chandra XRC
Quasars/AGN
Intermediate-mass black holes/ULX?
d
e
Black Hole Binaries
Daniel Price and Stephan Rosswog
Gamma-ray bursts
f
NASA, Watson, Stapelfeldt, J. Krist, Burrows
g
ESA
NASA
Stars
Neutron Stars, White Dwarfs
$M \sim M_\odot$
Black Hole? Neutron Star?

Fig. 1.7 Illustration of jet phenomena in compact astrophysical systems over a wide range of central masses. The figure has been taken from Tchekhovskoy (2015).

1.5 Jets and outflows

Bipolar outflow phenomena are commonly seen in compact astrophysical systems across all ranges of central masses. Typical examples are young and protostellar objects (typical central mass $\sim 1M_\odot$), evolved stellar binaries and massive stars associated with gamma-ray bursts (a few to $10M_\odot$), and most remarkably the centers of active galaxies ($\sim 10^6 M_\odot$ to $10^{10} M_\odot$). Figure 1.7 provides an illustration of the astrophysical jets and outflows, including those in the still poorly understood intermediate-mass BH systems whose typical BH mass is in the range of $\sim 10^{(2-5)} M_\odot$. Certainly, these systems differ in many aspects. However, they have a similarity in that the outflow phenomena commonly involve accretion of mass onto central compact object. For instance, observations reveal that the jet radio luminosity, the disk X-ray luminosity, and the BH mass strongly correlate over many orders of magnitude of BH masses (from $M_{\rm BH} \lesssim 10^2 M_\odot$ to $M_{\rm BH} \gtrsim 10^9 M_\odot$; Merloni et al. 2003). The correlation implies a tight connection between the BH, accretion disk, and relativistic jet, suggesting that the fundamental physics of the jet phenomena might be the same in all the compact objects. In this section, let us particularly focus on the phenomenology and physics of jets and outflows in AGNs, since those are deeply associated to the main focus of this thesis.

1.5.1 Relativistic AGN jet

A relativistic jet is an outflow of ionized plasma concentrated in a narrow beam (opening angle $\lesssim$ a few degrees on kpc-scales). In particular, jets in AGN are characterized by their highly collimated structure and relativistic propagation speeds (close to the speed of light). The typical kinetic power of the jet ranges between $10^{43} - 10^{49}$ erg s^{-1} (e.g., Ghisellini et al. 2014), which corresponds to $\sim 10^9 - 10^{15} L_\odot$ where $L_\odot \sim 3.8 \times 10^{33}$ erg s^{-1} is the solar luminosity. This is comparable to or even larger than the luminosity of most massive host galaxies of AGNs. Figure 1.8 shows an example of an extragalactic jet in the nearby radio galaxy M 87, which is one of the first discovered jets (Curtis, 1918). The figure shows a jet originating from the central engine within $\ll 1$ pc from the BH and propagating up to kpc-scales without disruption. The jet emits radiation from radio to optical and X-ray wavelengths. The jet also produces photons even up to GeV and TeV energies by the inverse Compton scattering or by intrinsic hadronic processes within the jet. In the nearby Universe, jets are found in approximately 10% of AGNs (e.g., Heckman & Best 2014). This small fraction is intriguing and suggests that (i) relativistic jets are a universal phenomenon in active galaxies, but (ii) their formation requires certain conditions. Indeed, jets are found in AGNs with quite low Eddington ratios ($L/L_{\mathrm{Edd}} < 0.01$) and very massive central BHs. One clear difference between low- and high-Eddington ratio AGNs is that the geometry and physical properties of the accretion flow are substantially different (see §1.2.2). This indicates that ADAF-like hot accretion flows may play an important role in the jet formation. Relativistic AGN jets contain large amount of kinetic energy and the jets can affect the phase of the interstellar medium in the host galaxy. For instance, the typically observed temperature of the diffuse hot gas in a galaxy cluster is $T \sim 10^7 - 10^8$ K. For such a high temperature, the gas quickly looses its internal kinetic energy by emitting bright X-ray radiation and falls towards the center of the galaxy cluster due to the gravity. The cooling time of the hot intracluster medium, i.e., a typical timescale needed for the gas to loose its internal energy by radiation, is $\lesssim 10^8$ yr. However, this is extremely short compared to the age of the Universe ($\sim 10^{10}$ yr). The large discrepancy between the two timescales makes it difficult to understand why many galaxy clusters still host the hot intracluster medium and how the clusters maintain the high temperature of the ambient gas against the high cooling rate. This is known as the cooling flow problem (see Fabian 1994). Interestingly, jets of AGNs in the centers of the galaxy clusters could interact with the ambient gas and convert the bulk kinetic jet power into random and thermal energy of ambient gas, for example by propagation of sound waves. Such a mechanical feedback heats the ambient medium efficiently and could be a possible solution for the cooling flow problem (see, e.g., Vernaleo & Reynolds 2006). The importance of mechanical AGN feedback through relativistic jet is also importantly recognized in galaxy formation in cosmological context (Croton et al., 2006).

In the following, I describe different main stages of AGN jet evolution in more detail, i.e., launching, collimation and acceleration, and its final disruption and energy dissipation (see also other review articles; Zensus 1997; Boccardi et al. 2017).

Launching the jet

A relativistic jet requires matter in the outer accretion disk to fall towards the vicinity of the central BH and to escape from the deep gravitational potential. This is not a trivial process and requires special physical mechanisms. Different models were suggested during the last decades (see Lynden-Bell 2015 for a historical review). An immediate candidate is the magnetic field which emerges naturally in astrophysical plasmas. Magnetic fields also work efficiently, especially for rotating and turbulent plasma (like accretion flows near the BH).

Currently, two most favored scenarios of jet launching involve the central SMBH (Blandford & Znajek, 1977) and the inner accretion disk (Blandford & Payne, 1982). We recall that astrophysical BHs are presumably rotating with nonzero spin (i.e., $a > 0$), thus they have an ergosphere. As explained in §1.2.1, the BH rotation forces plasma trapped within the ergosphere to rotate in the direction of the BH spin. This rotation is faster than the pure Keplerian rotation and thus leads to a differential rotation in the vicinity of the BH. Magnetic fields frozen in the plasma rotate in the same way. Eventually, the differential rotation develops a number of magnetic loops around the BH. The growing magnetic pressure then starts to push away the “ceiling” (i.e., the ambient medium) vertically and creates the pathway of the jet (see also Tchekhovskoy 2015). In this regard, the ergosphere is also called BH magnetosphere. At the same time, the rotating plasma extracts the spin energy of the BH via the Lense-Thirring or Penrose mechanism (Penrose & Floyd, 1971) and becomes able to escape from the ergosphere with sufficient energy. This is the basic idea of the Blandford-Znajek mechanism (BZ; Blandford & Znajek 1977). Several arguments suggest that the central SMBHs do power relativistic jets in AGN. For instance, a statistical comparison of the jet power and the accretion disk luminosity reveals that the jet power usually exceeds the power provided by gravitational potential energy of the disk (Ghisellini et al., 2014). Based on this, Ghisellini et al. (2014) suggest that additional energy from the BH magnetosphere is involved in powering the jet. Similar phenomena are also observed in numerical simulations of BH accretion with strong magnetic fields (e.g., Tchekhovskoy et al. 2011). They show that the jet power $P_{\rm Jet}$ could exceed the mass accretion power (e.g., $\eta \equiv P_{\rm Jet}/\dot{M}c^2 > 1$). It is important to recall that typical values of η corresponding to the gravitational energy of accretion flow is ~ 0.1 (see §1.2.2). Recent theoretical studies show that the process of energy extraction from the central spinning BH is particularly efficient when the magnetic field flux threading the inner accretion disk – which is eventually transported to the central BH – is large. Such an accretion flow is often referred to as the magnetically

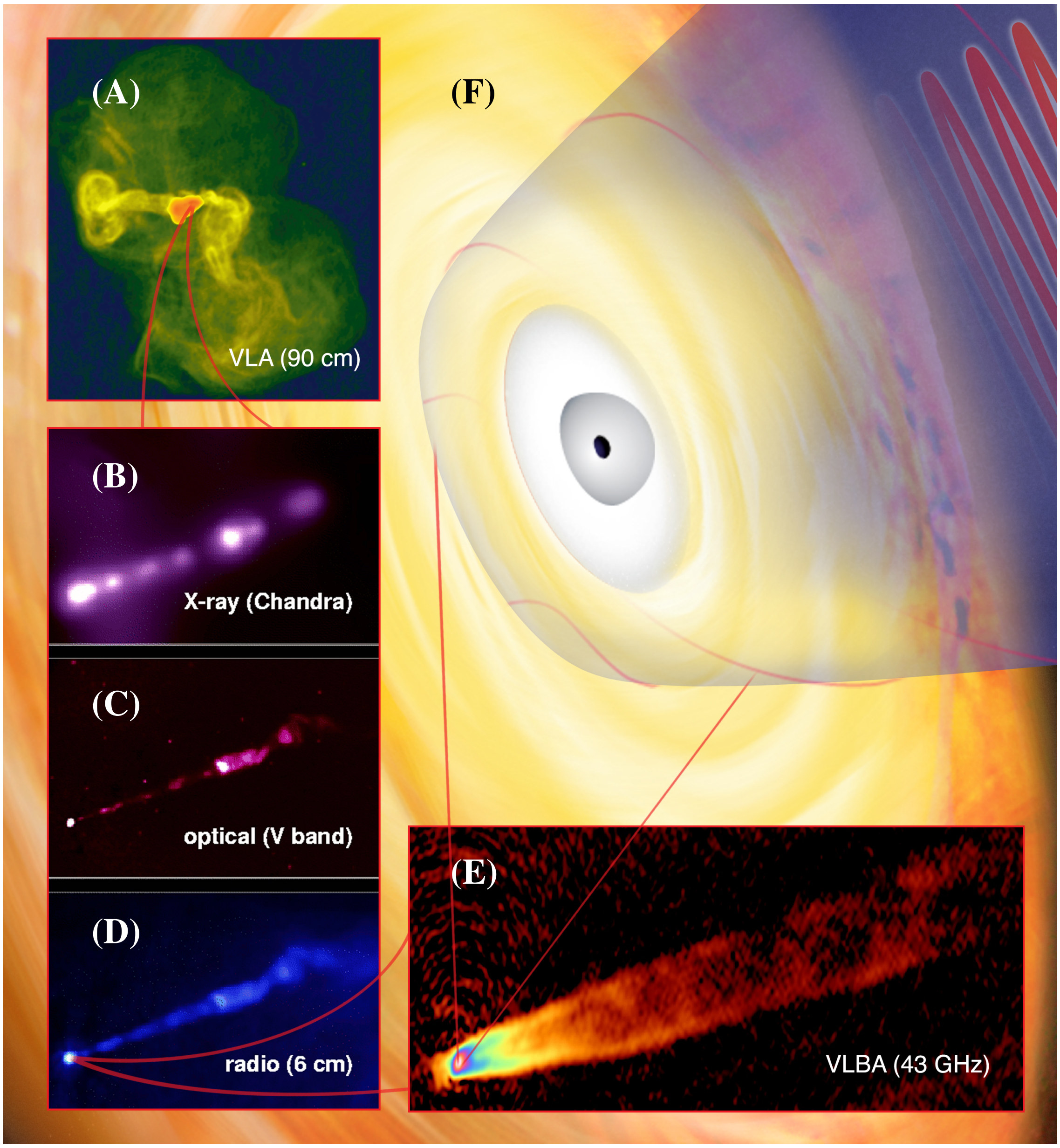

Fig. 1.8 Example of structure of an extragalactic jet in the radio galaxy M 87 on different spatial scales. From the top left panel and in counter-clockwise direction: **(A)** : The jet and halo structure. The image covers ~ 60 kpc projected distance. **(B-D)** : Zoom into the inner jet structure on ~ 1 kpc scale. The kpc-scale jet structure observed at X-ray (B), optical (C), and radio (D) are displayed. **(E)** : The innermost jet structure observed by very long baseline interferometry technique. The displayed jet structure extends $\lesssim 2$ pc. **(F)** : An artistic view of the central engine launching the jet (blue). The central dark point is the central SMBH surrounded by ergosphere (gray sphere) and accretion disk (yellow). Red lines show wrapped magnetic fields. Image credit : Bill Saxton, NRAO/AUI/NSF.

dominated accretion disk (MAD; Igumenshchev et al. 2003; Narayan et al. 2003). The MAD models are widely investigated in recent theoretical works because the resulting jet power is usually very large (see §3.2.3 of Yuan & Narayan 2014 for a brief review). In summary, the BH magnetosphere launches the relativistic jet efficiently, in particular in presence of strong magnetic field and fast BH spin. The resulting jet also has high speed, although the exact value of the asymptotic speed seems to depend strongly on the initial conditions assumed in the numerical simulations[3].

On the other hand, the accretion disk can launch less relativistic, but still strong outflows via the Blandford-Payne mechanism (BP; Blandford & Payne 1982) in which magnetocentrifugal acceleration of the inner accretion disk plasma leads to rather relativistic MHD winds (see also Camenzind 1986). Also, Blandford & Begelman (1999) point out that accreting gases may not easily plunge into the central BHs if the accretion flows are hot, radiatively inefficient, and geometrically thick. In this case, the viscous energy dissipation is used to heat the ions and electrons and causes advection. Such accretion flow is usually gravitationally unbound and produces an outflow from the surface. This substantially lowers the mass accretion rate closer to the BH in comparison to the rate defined at much larger Bondi radius (see Yuan & Narayan 2014 and references therein). Differential rotation in accretion disks can also build up loops of magnetic fields. The magnetic loops eventually generate a magnetic "tower", which also launches a jet from the disk via magnetic pressure (Lynden-Bell, 2003; Hawley & Krolik, 2006; Contopoulos et al., 2009). Anyhow, recent studies suggest that the power of the jet from the disk is considered to be $\sim \dot{M}c^2$ and is less dependent on the BH spin and magnetic flux in the BH magnetosphere (see §3.3.2 of Yuan & Narayan 2014). However, the jet originating from the very inner accretion disk might not be clearly distinguishable from the jet from the BH itself in terms of the total jet power (e.g., De Villiers et al. 2005; Sądowski et al. 2013).

Because of the two distinct origins, the jets from the BH and the disk have several different characteristics. First of all, the jet originating from the BH ("BH jet") is narrow, highly magnetized, less mass-loaded, and easily achieves high velocity. Therefore it plays a central role in transporting energy outward in the form of magnetic fields (in other words magnetic energy dominated). On the other hand, the jet launched from the disk ("disk jet") is wider, more mass dominated, and is considered to have lower velocity than the jet from the BH. Thus it is believed that the jet from the disk mainly carries mass and momentum of the whole outflow. For this reason, the disk jet separates the BH jet from the geometrically thick mass accretion flow and help the latter maintain its own properties (see discussions in Hawley & Krolik 2006). From this perspective, it is crucial to note that the jets from the BH and the disk are not mutually

---

[3] One of the main reasons responsible for the discrepancy is that the detailed physical processes related to the mass loading onto the magnetic fields of the jet are poorly understood. See §3.3.1 of Yuan & Narayan (2014) for more discussions.

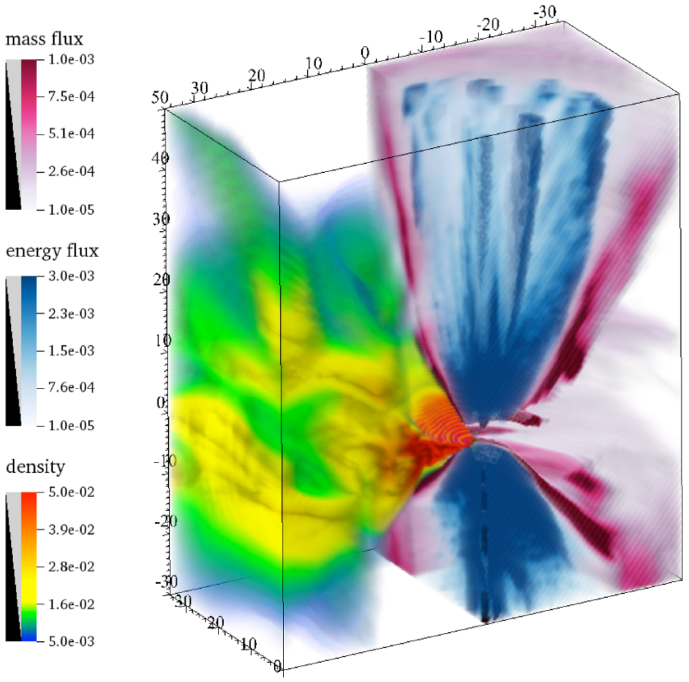

Fig. 1.9 An example of a 3D general relativistic magnetohydrodynamic simulation showing jet formation from the BH and disk. The coordinate values of the simulation box are in units of the gravitational radius ($R_g = GM_{\rm BH}/c^2$). Figure taken from Sądowski et al. (2013).

exclusive. Instead, they may co-exist in the same system as a natural consequence of the mass accretion and BH physics (e.g., Hawley & Krolik 2006; Hardee et al. 2007; Sądowski et al. 2013; see Fig. 1.9).

Acceleration

The acceleration of the relativistic jet requires additional mechanisms. Many studies have widely investigated different ideas involving gas-dynamic acceleration, acceleration by radiation pressure, gas and magnetic pressure gradient due to overpressure, and magnetic acceleration by magnetohydrodynamic (MHD) processes (see §1 of Singh et al. 2016 and references therein). Currently, the magnetic acceleration scenario appears to have several advantages over the other models because (i) it is able to provide acceleration over long distances for highly magnetized flow and (ii) the MHD acceleration can occur as a natural consequence of jet expansion under external pressure confinement (e.g., Komissarov et al. 2007; Lyubarsky 2009).

Details of the magnetic acceleration scenario are different from model to model. But many different models are based on the same root, which is the conversion of the magnetic energy to the kinetic power. Theoretical works have mainly explored the magnetic acceleration scenario for rather cold plasma with strong toroidal magnetic field (i.e., negligible internal energy of the

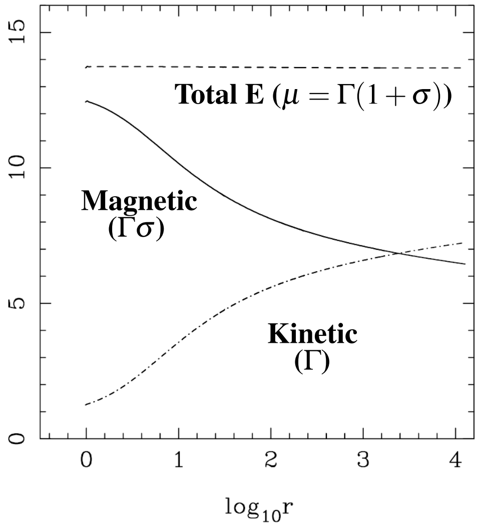

Fig. 1.10 Conversion of magnetic energy into kinetic power in a numerical simulation of MHD jet. The abscissa corresponds to the logarithm of the jet radius in units of gravitational radius. The figure has been taken from Komissarov et al. (2007).

gas and poloidal component of the magnetic field [4]). This condition is usually reasonable for magnetically launched, *supermagnetosonic* jet (i.e., the bulk speed faster than the sound speed of the magnetic plasma). When such a jet expands under the pressure of ambient atmosphere, the flow maintains a parabolic shape and the inner layers of the quasi-cylindrical jet expand slower than the outer layers (i.e., *differential collimation*). This leads to an overall decrease of the magnetic energy density and invokes bulk acceleration the jet plasma (see Komissarov 2012 for a quantitative analysis based on the relativistic Bernoulli equation). Figure 1.10 shows an example of evolution of the magnetic and kinetic power versus the expanding jet radius as obtained by numerical simulations. There is a number of observational evidence showing acceleration of the jets. Homan et al. (2015) find significant, parallel acceleration of jets in ~ 100 blazars within projected linear distances of $\sim 10-20$ pc (de-projected distances of order of ~ 100 pc). In individual nearby sources such as M 87, the jet acceleration is observed in greater detail. The source shows significant acceleration from projected distances of initial ~ 0.1 pc from the central engine (Mertens et al., 2016; Walker et al., 2018) up to kpc (Asada et al., 2014), followed by significant deceleration (Biretta et al., 1999). Similar jet acceleration patterns are also found in Cygnus A (Krichbaum et al., 1998; Bach et al., 2003; Boccardi et al., 2016b).

---

[4] The magnetic field fluxes decay proportionally to the inverse of the jet cross-section for the poloidal components but proportionally to the inverse of jet radius for the toroidal components. Therefore, the poloidal components become less important at longer distances from the central engine.

The magnetic acceleration by differential collimation applies to relativistic flows. In the immediate vicinity of the central engine (e.g., $\lesssim 100R_g$), the launched outflow has to overcome the gravity before its speed reaches the fast magnetosonic point. Only then, the aforementioned mechanisms start to work. Theoretical studies suggest several diverging scenarios about the very initial jet acceleration (e.g., see McKinney 2006 and also Pu et al. 2017 and Contopoulos 2018).

Collimation

Once the jet is triggered from the BH and/or the disk and gets accelerated, it propagates up to pc and kpc scales without disruption and significant loss of speed. The central engine occupies only a tiny volume and cannot affect the jet evolution over such large distances. In this perspective, the jet can in principle be disrupted by a number of processes. One example is the current-driven kink instability (CDI). For a magnetic energy dominated jet, the nonuniform magnetic force of a toroidal field can produce a pinch by magnetic instabilities. The pinch can easily grow up and make the force gradient larger. This makes a curved jet and produces a kink which amplifies the gradient even larger. Eventually, the jet curvature becomes so large that the jet may be disrupted already near the central engine (see Perucho et al. 2012 for a brief review). For sufficiently accelerated gas dynamic jet, the shear instability driven by the viscosity on the surface of the flow is also important (e.g., Hardee 2000). Hence, additional mechanisms should help the outflow to be focused in a narrow beam.

The collimation mechanism of outflows has been extensively studied. It is generally understood that "self-confinement" of a hydrodynamic jet is not easy. For a magnetically launched jet, the outward magnetic pressure overcomes the other inward forces (see Komissarov et al. 2007 and references therein). A non-relativistic jet with a toroidal magnetic field can "self-collimate" by magnetic hoop stress produced by the field and the jet current. However, the magnetic hoop mechanism also becomes inefficient when the flow approaches relativistic speed. The outward electric force by charges in the plasma becomes significant in relativistic case, causing the two forces to nearly cancel each other. Currently, there is consensus that the external confinement of the outflow by an ambient plasma "atmosphere" works efficiently. This idea has been broadly investigated by analytical and numerical studies (e.g., Begelman & Li 1994; Spruit et al. 1997; Vlahakis & Königl 2003; Komissarov et al. 2007; Lyubarsky 2009; see also Komissarov 2012 for a review).

The composition of the plasma atmosphere is unclear. Nonetheless, the fact that most of AGN jets are found in low-accretion-rate systems hints that the geometrically thick accretion flow or the non-relativistic "wind" from the outer accretion disk (see Yuan & Narayan 2014) are important for the jet collimation. Observationally, the transverse expansion rate of the

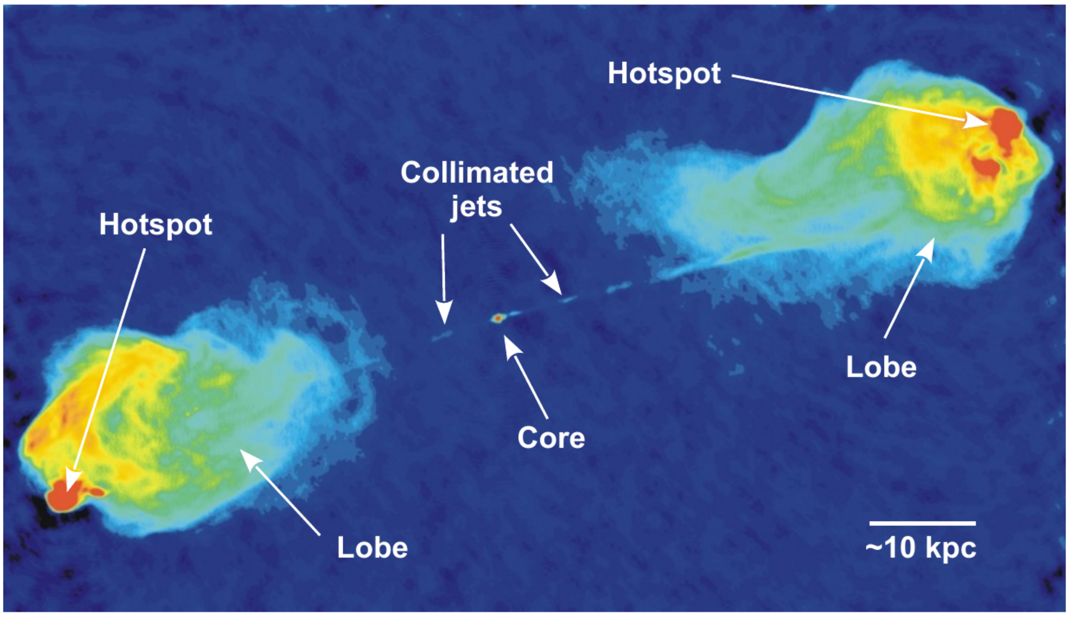

Fig. 1.11 A false color image of kpc-scale radio jet structure in the radio galaxy Cygnus A. Note highly collimated twin jet structure followed by two nebulous lobes and hotspots at the end. Image courtesy of NRAO/AUI.

parsec-scale jet is generally slower than a conically expanding flow (e.g., Pushkarev et al. 2017). Furthermore, the collimation of the jets significantly changes near their Bondi radius, where the ambient gas starts to accrete toward the central engine from all directions (e.g., Asada & Nakamura 2012; Tseng et al. 2016). A less extreme but similar jet structure transition is also observed in a number of sources (Pushkarev et al., 2017). Therefore, a halo-like accretion flow of spherical shape may provide the required ambient pressure as well. Similarly, stellar-mass binary BH systems show signatures of relativistic outflows only when the inner accretion disk enters a geometrically thick phase (Fender et al., 2004). On the other hand, it is also important to note that a number of quasars presumably have slim disks but they show collimated jets (Pushkarev et al. 2017; see also Akiyama et al. 2018). In such case, the external confinement pressure may be provided by very wide wind of non-relativistic speed cocooning the relativistic central flow (see §1.5.2).

Termination of jet propagation and energy dissipation

It is evident from observations that neither jet acceleration nor collimation continue infinitely (see Fig. 1.11). Instead, the collimated bipolar jet looses its kinetic energy in several different forms and there are several different processes that lead to termination of the pc-scale jet on larger scales.

It is important to note that the magnetic energy in the jet is gradually depleted over long distances by accelerating the outflow. When the ratio of the magnetic to kinetic energy σ becomes $\sigma \lesssim 1$, the jet interacts with the surrounding medium by ordinary hydrodynamic processes. The jet is already supersonic at this stage so that it has little time to adjust itself to small pressure perturbations in the environment. As a result, the jet is over-expanded/collimated several times during the propagation. Such type of perturbation may begin to occur on scales of tens of pc. One important outcome of the over-collimation and *recollimation* is that it overpressurizes the jet plasma, producing shock(s). Shocks can convert the bulk (i.e., macroscopic) kinetic jet power into random and turbulent (i.e., microscopic) particle energies. Particle acceleration in the turbulent zone provides a good explanation for the bright, flaring radiation observed in the compact AGN jet across all photon energy ranges from radio to GeV and TeV (see Chapter 7 of Belloni 2010 and Marscher 2016 for a review).

Furthermore, when the jet is kinetic-energy dominated, the velocity shear between the flow and the ambient medium becomes larger and induces significant viscosity in the interface. This excites a hydrodynamic instability; the well-known *Kelvin-Helmholtz instability* (KHI; see Birkinshaw 1991 for a brief review and also Hardee 2000). KHI plays a central role in developing turbulences in the jet flow and allows for partial dissipation of its kinetic energy into the ambient medium. In addition, the KHI induces different kinds of oscillations in the plasma flow such as axial displacement of the flow (i.e., helical mode) or elliptical oscillations of the jet cross-section. High angular resolution observations of jets in some nearby sources reveal remarkable helical "patterns" (Lobanov & Zensus, 2001; Hardee & Eilek, 2011). Depending on the spatial growth of the oscillations, the KHI might even disrupt a collimated jet before it reaches the kpc scale (e.g., Perucho et al. 2012).

Alternatively, the jet may be still so powerful that it propagates further downstream against the energy dissipation and/or instabilities and can be strongly disrupted, forming a termination shock on kpc-scale. This kind of jet termination could provide a significant feedback to the environment of its host galaxy (see Fabian 2012 for a review). The termination region on each side of the bipolar jet is a complex region of "hot spot", sharp bow shock, and bright lobe filled by hot electrons. Intriguingly, Fanaroff & Riley (1974) find that the sharp termination shock features are observed particularly often in high-power jet systems (Fanaroff-Riley class II sources; FR II) while in contrast low-power sources mostly show diffuse lobes with smooth edges (FR I).

The environment which surrounds the jet can suddenly and significantly change as well. As discussed in §1.2.2, the Bondi radius has a finite spatial scale and thus the jet collimation can be supported efficiently up to only limited distances. The same would be true for the acceleration. For nearby sources such as M 87, the Bondi radius can be directly measured from high resolution X-ray observations of hot electrons in the galactic halo. High resolution imaging and monitoring of radio jets in such sources reveal that, around the Bondi radius, the jet width changes from a parabolic to conical shape and the jet starts to significantly decelerate (e.g., Asada & Nakamura 2012; Asada et al. 2014; Tseng et al. 2016). Such jets will be eventually mixed with the diffuse interstellar medium. The sudden pressure change in the environment can induce a strong recollimation shock at the end of the collimation and acceleration zone. In this case, the jet may dissipate energy into radiation efficiently as discussed above (e.g., Stawarz et al. 2006; Cheung et al. 2007). The different jet environments might be responsible for the FR I/II dichotomy as well (e.g., Gopal-Krishna & Wiita 2002; see discussions in Boccardi et al. 2016b and references therein).

1.5.2 Non-relativistic disk winds

There are not only fully and mildly relativistic jets but also non-relativistic outflows ("winds") originating from the central engine region. They may be driven from the outer accretion disks in low-accretion-rate systems, as a natural consequence of the force balance between the self-gravity, radiation, and the advection/convection. We recall that this picture is similar to the launching of the disk jet (see §3.4 of Yuan & Narayan 2014). In this regard, the disk jets and winds follow a similar physics with a smooth transition between the two types of outflows. For instance, ultra-fast disk winds can reach even mildly relativistic speeds ($\sim 0.1c$; e.g., Tombesi et al. 2015). Except for some extreme cases, however, the winds are generally characterized by much lower, non-relativistic speeds, and a larger solid angle coverage.

The wind is therefore important in AGNs in two perspectives: it can (1) reduce the net mass inflow rate and (2) provide sufficient momentum-driven feedback to the interstellar medium with a large collisional cross-section. The former is important to understand decreasing mass accretion rate near the central engine of low Eddington ratio systems. For instance, X-ray observations of Sgr A* suggest a mass inflow rate of $\sim 10^{-6} M_\odot$ yr^{-1} near the Bondi radius (Baganoff et al., 2003), while radio polarimetric observations suggest much lower value of $\sim 10^{-7} M_\odot$ yr^{-1} near the event horizon (Marrone et al., 2006, 2007). Decrease in the net mass inflow rate of one order of magnitude can be well explained by the disk wind model (e.g., Yuan et al. 2012a,b). The latter is associated with suppression of the mass accretion onto the host galaxy on much larger kilo-parsec scales, which may turn off the star formation in the galaxy. Signatures of the wind feedback are observed in form of large Doppler-broadening and/or shifts of optical and molecular lines (e.g., Bae & Woo 2014; Cicone et al. 2014). Typical velocities of the winds measured by the lines are $\lesssim 1{,}000$ km s^{-1}. While relativistic jets could equally release large amounts of energy to the interstellar medium, theories invoking narrow jets often encounter problems because the jet could produce only a small tunnel in the system.

The momentum-driven wind, on the other hand, easily pushes interstellar gas away from the host galaxy. Therefore, the winds may have a significant impact on the growth of the SMBHs, the host galaxies, and their co-evolution over cosmic timescales (see Kormendy & Ho 2013).

1.6 Radiation from AGN jets

We continue the review of AGN jets, but we change our view now to the radiation theory and emission mechanisms. Descriptions provided in this section are based mainly on Ghisellini (2013). See also Pacholczyk 1970 and Rybicki & Lightman 1979 for a deeper review.

1.6.1 Synchrotron spectrum

When a charged particle is moving at a non-relativistic speed around a magnetic field, the particle is centrifugally accelerated by the field and gyrates with a specific period. A sinusoidal radiation is produced as a result. The radiation spectrum can be characterized by a well-defined single electromagnetic frequency, which is roughly inversely proportional to the gyration period of the particle. When the particle moves at a relativistic speed, however, the resulting radiation is significantly beamed parallel to the particle velocity vector and the observed electromagnetic pulses result in a broader radiation spectrum. This is the mechanism producing the synchrotron radiation. Its spectrum is peaked around a critical radiation frequency

$$\nu_c \sim \gamma^2 \frac{qB}{2\pi m} \tag{1.5}$$

where γ is the particle Lorentz factor, q is the charge of the particle, B is the magnetic field strength in Gauss, and m is the particle mass in gram. The synchrotron spectrum of a single electron $P(\nu)$ is $P(\nu) \propto \nu^{1/3}$ when $\nu \ll \nu_c$ and $P(\nu) \propto \exp(-(\nu/\nu_c))$ for $\nu \gg \nu_c$, respectively. For an electron, Eq. 1.5 is simply $\nu_c \sim 2.8B\gamma^2$ MHz. For $B \gtrsim 1$ G, it is clear that most of the synchrotron radiation is emitted at radio wavelengths.

By integrating the synchrotron emission over the solid angle and frequency, the synchrotron power of an electron is given by

$$\langle P_e \rangle = \frac{4}{3}\sigma_T c U_B \gamma^2 \tag{1.6}$$

where e in the subscript indicates a single electron, σ_T is the Thompson scattering cross-section, and $U_B = B^2/8\pi$ is the magnetic energy density. The protons are heavier than the electrons and proton synchrotron radiation power is scaled down by a large factor of $\sim (m_e/m_p)^2 \sim 3 \times 10^{-7}$ where m_p and m_e are the mass of the proton and electron, respectively. Therefore, we could ignore proton-synchrotron radiation in the following. We can also calculate a synchrotron cooling timescale $t_{\rm syn} \equiv E/\langle P \rangle$ where $E = \gamma m_e c^2$ is the relativistic electron energy. This gives

$$t_{\rm syn} \sim \frac{7.75 \times 10^8}{B^2 \gamma}\,{\rm s} \sim \frac{25}{B^2 \gamma}\,{\rm yr} \quad . \tag{1.7}$$

Therefore, we can estimate the "lifetime" of electrons in different environments of AGN. For example, for an electron with $\gamma \sim 10^3$ and a strong field strength of $B \sim 10^3$ G (e.g., near the BH) , the lifetime is only ~ 1 s while for much lower $B \sim 10^{-5}$ G (e.g., in the radio lobe) the lifetime is ~ 2 Myr.

In real AGN jets, the number density of particles usually follows a power-law energy distribution. The power-law particle energy distribution is generally produced as a result of particle acceleration in a shock [5]. The number density of the non-thermal particles $n(\gamma)$ per unit particle Lorentz factor interval $[\gamma, \gamma + d\gamma]$ can be expressed by

$$n(\gamma) = n_0 \gamma^{-p}, \quad \gamma_{\rm min} \leq \gamma \leq \gamma_{\rm max} \tag{1.8}$$

where $n_0 = N/(\int_{\gamma_{\rm min}}^{\gamma_{\rm max}} \gamma^{-p} d\gamma)$, N is the total number of the particles, p is the particle spectral index, and $\gamma_{\rm min}$ and $\gamma_{\rm max}$ are the low and high energy cutoff of the energy distribution, respectively. We note that recent numerical simulations show that the resulting particle energy distribution is not only power-law like but also presents other features such as breaks and cutoffs at certain critical particle energies (e.g., Baring 2012). For the purpose of this section, however, it is sufficient to assume a power-law with the two energy cutoffs. The synchrotron radiation spectrum $F(\nu)$ of an ensemble of electrons in the jet plasma is obtained by integrating $P(\nu)n(\gamma)$ over $[\gamma_{\rm min}, \gamma_{\rm max}]$. In the optically thin case (i.e., no self-absorption), the spectrum is given by

$$F(\nu) \propto N B^{(p+1)/2} \nu^{-(p-1)/2} = N B^{1+\alpha} \nu^{-\alpha}, \quad \alpha = \frac{p-1}{2} \tag{1.9}$$

where α is the *synchrotron radiation spectral index* (i.e., not the particle spectral index p). Determining observationally the slope of the synchrotron spectrum also determines the particle energy distribution. On the other hand, the spectrum is expected to change its shape due to larger number of low energy particles and increased synchrotron opacity at low observing frequencies. The spectrum in the *synchrotron self-absorbed* regime can be obtained by calculating an equivalent thermodynamic temperature T of relativistic electrons with the corresponding

---

[5] In many astrophysical cases, gas densities are low and shocks often involve magnetic fields. This causes a so-called *collisionless shock*, in which charged particles are reflected between magnetic walls and the particles pass the shock front multiple times and gain more energy. This mechanism is called *Fermi acceleration* (see, e.g., Baring 2012).

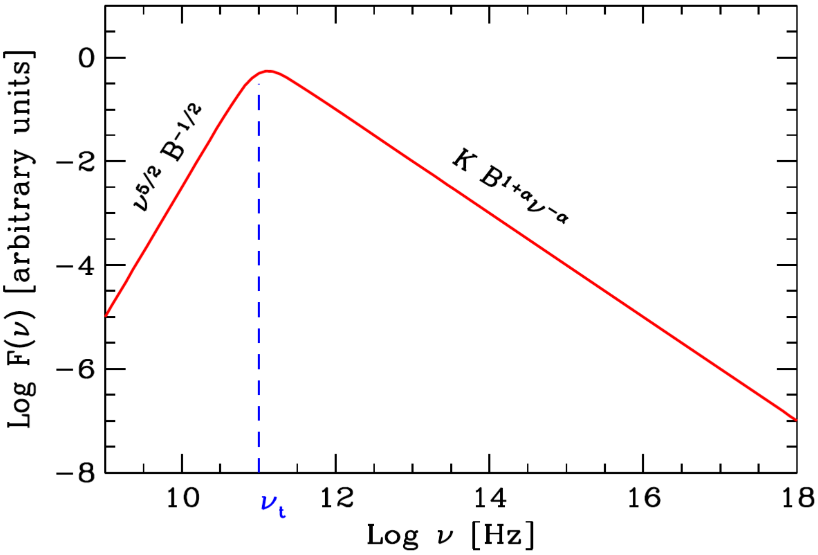

Fig. 1.12 Synchrotron spectrum of a partially self-absorbed plasma. Note a turn-over of the spectrum around ν_t. Figure taken from Ghisellini (2013).

Lorentz factor γ (e.g., $T = \gamma m_e c^2/k_B$ where k_B is the Boltzmann's constant) and comparing it with the brightness temperature of a black body (see §1.6.2). This results in

$$F(\nu) \propto \nu^{5/2}\, B^{-1/2} \quad . \tag{1.10}$$

The transition from the optically thick to thin regime occurs at a frequency ν_t when the synchrotron opacity is $\tau(\nu) = \alpha(\nu)R \approx 1$ where $\alpha(\nu)$ is the microscopic synchrotron absorption coefficient and R is the light travel distance (e.g., macroscopic plasma size). The transition frequency, or *turn-over frequency*, is given by

$$\nu_t \propto \left[R\, N\, B^{(p+2)/2}\right]^{2/(p+4)} \quad . \tag{1.11}$$

An example of $F(\nu)$ of a partially self-absorbed plasma is shown in Fig. 1.12. The synchrotron turn-over frequency is a crucial parameter to link observations with theory. It provides a good estimation of the magnetic field strength of a synchrotron-emitting plasma without large number of assumptions, once the size of the plasma blob is measured. For instance, Marscher (1983) provides an estimation of the synchrotron self-absorption (SSA) magnetic field strength B_{SSA} by

$$B_{\mathrm{SSA}} = 10^{-5} b(\alpha)\theta^4 \nu_m^5 S_m^{-2} \frac{\delta}{1+z} \quad \text{Gauss} \tag{1.12}$$

where the parameter $b(\alpha)$ is a function of the spectral index α tabulated in Marscher (1983), θ is the angular size of the source in milli-arcsecond, ν_m is the turn-over frequency in GHz, S_m is the flux density at the turn-over in Jy, δ is the Doppler factor of a moving plasma at relativistic speed (see §1.6.4), and z is the redshift of the source.

1.6.2 Brightness temperature

The surface brightness of synchrotron radiation in AGN jets can be also represented by the *brightness temperature*. The brightness temperature T_B of a plasma in the radio frequencies is defined by

$$T_B = \frac{c^2 I(\nu)}{2k_B \nu^2} \tag{1.13}$$

where $I(\nu)$ is the intensity, k_B is the Boltzmann constant, and ν is the observing frequency. This definition apparently originated from the Rayleigh-Jeans law because photon energies in the radio bands are typically much lower than the particle energies ($h\nu/k_B T \ll 1$ where h is the Planck constant). In many astrophysical contexts and especially for thermal radiation, T_B provides a good estimation of the true gas temperature. For non-thermal radiation such as synchrotron radiation in AGN jets, however, T_B does not necessarily mean the physical thermodynamic temperature corresponding to the particle energy distribution. This is simply because the particle energies are not Maxwellian distributed. Nevertheless, the concept of temperature is still applicable to a portion of non-thermal particles having a characteristic energy E because such particles emit and absorb most of energies by radiation around the critical radiation frequency $\nu \sim \nu_c$ (Eq. 1.5). For instance, brightness temperature in the milli-arcsecond scale core of AGNs is typically $T_B \gtrsim 10^{10}$ K and much larger values of $T_B \sim 10^{11} - 10^{12}$ K are also common (e.g., Kovalev et al. 2005). Remarkably, even higher brightness temperatures of $> 10^{13}$ K are found by recent space-VLBI observations (e.g., Gómez et al. 2016; Kovalev et al. 2016). We recall that a characteristic temperature corresponding to the rest-mass energy of an electron is $T_e = m_e c^2/k_B \sim 6 \times 10^9$ K. This indicates that the radio-emitting electrons are indeed relativistic.

1.6.3 Polarization

Descriptions provided in this section are largely based on Gabuzda (2015). See Pacholczyk 1970 for a deeper review and also Trippe 2014 and references therein.

Linear polarization

Synchrotron radiation is intrinsically linearly polarized because electrons responsible for the emission are accelerated perpendicular to the magnetic field. If all the electrons move at exactly the same pitch angle with respect to uniform magnetic fields in the jet plasma, the resulting emission will be linearly polarized by 100% and have polarization angle oriented perpendicular to the magnetic fields. However, the real particle motions are mostly randomly oriented on microscopic scales. Thus they have random pitch angles and produce *incoherent* synchrotron emission. The degree of linear polarization is defined by $m_L = I_{\rm pol}/I_{\rm tot}$ where $I_{\rm pol}$ and $I_{\rm tot}$ are the linear polarized and total (thus polarized + unpolarized) intensities, respectively. Following Pacholczyk (1970), m_L of incoherent synchrotron emission produced by a uniform magnetic field configuration is expressed by

$$m_L = \begin{cases} (3p+3)/(3p+7) & \text{if optically thin} \\ 3/(6p+13) & \text{if optically thick} \end{cases} \tag{1.14}$$

where p is the spectral index of the particle energy distribution. For an optically thin synchrotron spectrum $\alpha = (p-1)/2 \sim (0.5-1.0)$, the polarization fraction is $m_L \sim 0.70-0.75$. The orientation of the observed linear polarization (*electric vector position angle*; EVPA) is still perpendicular to the magnetic field. On the other hand, the same plasma has a much lower polarization degree $m_L \sim (0.10-0.12)$ if it is observed at the optically thick regime. In this case the EVPA is parallel to the magnetic field. The transition occurs when the synchrotron optical depth becomes ~ 1 (i.e., around $\nu \sim \nu_t$; see Fig. 1.12). The change of polarization behavior for the optically thick case can be qualitatively understood as follows. When the opacity is high, synchrotron radiation emitted by a single electron has a high chance of being absorbed by nearby electrons spiraling around magnetic fields. We note that any polarized light can be decomposed into two orthogonal components, e.g., perpendicular and parallel to the magnetic fields (the prior more dominant over the latter). The chance of the absorption is higher for the perpendicular polarization because of the nearby electrons gyrating in the same direction. In the large opacity case, therefore, the net linear polarization is decreased and the net EVPA becomes parallel to the magnetic fields.

We also note that the observed linear polarization can be much lower if the magnetic field configuration is disordered (e.g., Jorstad et al. 2007). If the plasma consists of N cells of randomly oriented magnetic fields, the integrated linear polarization will be decreased by $m_L \rightarrow m_L/\sqrt{N}$. On the other hand, shocks in AGN jets can work as pistons and compress initially disordered magnetic fields, thus increasing m_L and making EVPA perpendicular to the shock front (Laing, 1980; Hughes et al., 1985).

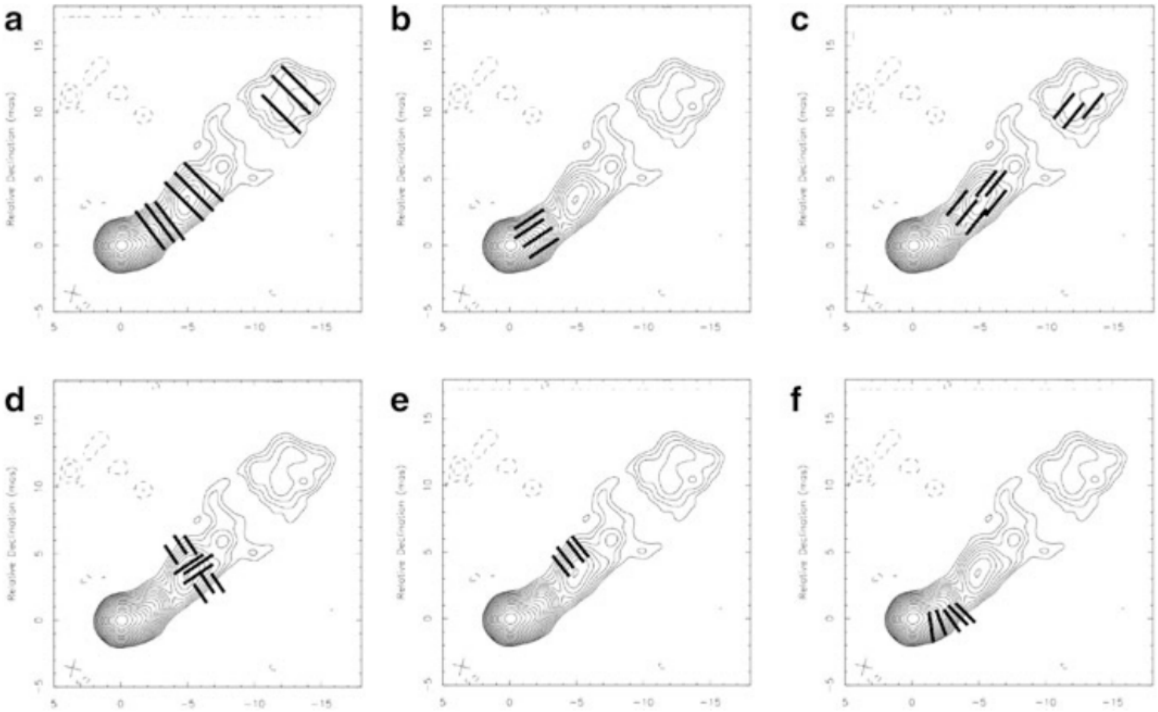

Fig. 1.13 Schematic illustration of a typical AGN jet morphology in linear polarization. Each panel shows the polarization in different situations. Sticks represent the EVPAs in the corresponding regions. **(A)** : optically thin plasma with globally longitudinal magnetic fields. **(B)** and **(C)** : optically thin, compact and extended plasma with magnetic fields perpendicular to the jets, respectively. **(D)** : mixed, optically thin plasma with the perpendicular (jet center) and longitudinal (edges) magnetic fields. **(E)** : one-sided polarization offset from the jet axis. **(F)** : polarization along the curved jet with longitudinal magnetic fields. The figure has been taken from Gabuzda (2015).

A schematic illustration of various polarization distributions in AGN jets and their descriptions are provided in Fig. 1.13.

Circular polarization

A substantial fraction of synchrotron radiation is linearly polarized by the sky-projected magnetic field components. But there is a weak, intrinsic circular polarization produced by the line-of-sight magnetic field component as well (see Pacholczyk 1970). The intrinsic circular polarization m_C decreases with increasing observing frequency as $m_C \propto \nu^{-0.5}$. For $m_L \approx 0.1$ and typical magnetic field strength of $B \sim 0.1$ G, the resulting m_C is of order of 10^{-3} (see, e.g., Gabuzda 2015). However, observations often find much larger $m_C \sim 0.01$ (i.e., 1%) in AGN jets (Homan & Wardle 2004; see also Thum et al. 2018; Agudo et al. 2018b). This implies that additional processes take place in AGN jets to produce larger circular polarization (e.g., Jones & O'Dell 1977).

Faraday rotation

In addition to the in-situ emission and self-absorption processes, the polarized radiation can be further affected by electrons and magnetic fields embedded in external ionized gas. When a polarized light passes through a magnetized medium, the resulting polarization angle χ changes from the intrinsic angle χ_0 by

$$\chi = \chi_0 + \mathrm{RM} \times \lambda^2, \quad \frac{\mathrm{RM}}{\mathrm{rad/m^2}} = 8.1 \times 10^5 \int_{\mathrm{source}}^{\mathrm{telescope}} \left(\frac{n_e}{\mathrm{cm^{-3}}}\right) \left(\frac{B_{||}}{\mathrm{G}}\right) \left(\frac{dl}{\mathrm{pc}}\right) \tag{1.15}$$

where λ is the wavelength, RM is the rotation measure, n_e is the electron density, $B_{||}$ is the line of sight magnetic field strength, and dl is the line element from the source to the telescope. One can determine RM and χ_0 simultaneously if the observed EVPA shows significant wavelength dependences (e.g., $\chi(\lambda) \propto \lambda^2$). One of useful applications of the Faraday rotation analysis is to understand the nature of the foreground in front of AGN jets. Such foregrounds – the *Faraday screens* – could be accretion flows, disk winds, or any interstellar medium between the background source and observer (e.g., Taylor et al. 2006; Marrone et al. 2006; Plambeck et al. 2014).

The external Faraday rotation not only changes the apparent EVPA but also decreases the fractional linear polarization. An inhomogeneous RM distribution in the foreground induces different amount of EVPA rotations for different light rays of the same intrinsic linear polarization but passing through the screen in slightly different directions. Therefore, if the spatial RM structure in the screen is unresolved by the finite observing resolution, the net polarization is decreased (thus larger depolarization for larger inhomogeneity and poorer angular resolution).

In addition, it is important to note that source-intrinsic Faraday rotation can occur within the jet plasma. Also, the geometry of the external screens could be complex. In this case, the observed EVPAs may not follow the λ^2 dependence in Eq. 4.8 and the resulting polarization patterns are generally complicated (see, e.g., Sokoloff et al. 1998; Brentjens & de Bruyn 2005).

1.6.4 Relativistic effects

At this point, it is useful to review several important consequences of the relativistic bulk plasma motions on their observed radiation. First, we define the bulk Lorentz factor $\Gamma = 1/\sqrt{1-\beta_\Gamma^2}$ where β_Γ is the speed of the moving bulk emission region normalized by the speed of light.

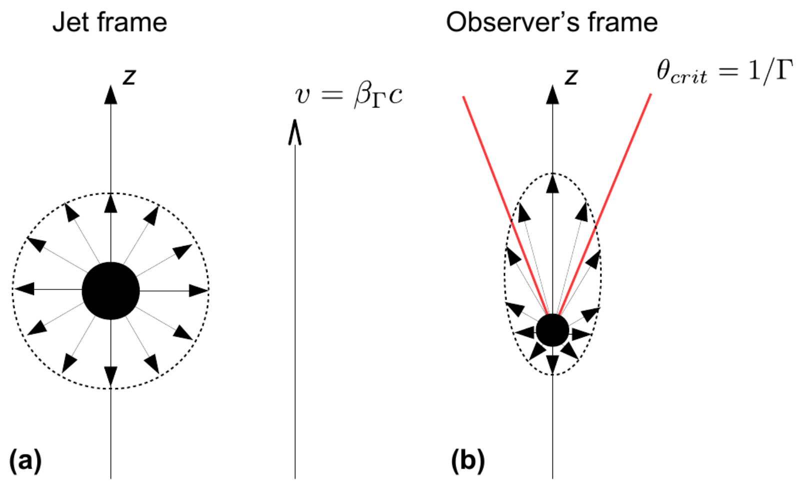

Fig. 1.14 Illustration of relativistic beaming. **(a)** : The radiation seen in the jet frame. **(b)** : The same radiation seen from observer's frame. Note the beaming within critical angle θ_{crit}. This figure was created based on the sketch of Böttcher (2012).

Because of the special relativistic time dilation and length contraction, the isotropic radiation in the jet frame appears anisotropic in the observer's frame. The radiation is therefore preferentially beamed along the moving direction and focused within a critical angle $\theta_{\text{crit}} \approx 1/\Gamma$ (see Fig. 1.14).

The beaming effect and the relativistic Doppler shift change the power-law spectrum in the jet frame $F'(\nu') \propto (\nu')^{-\alpha}$ into the observed flux $F(\nu)$ by

$$F(\nu) = F'(\nu)\delta^{3+\alpha}, \quad \delta = \frac{1}{\Gamma(1-\beta_\Gamma \cos\theta)} \tag{1.16}$$

where δ is the Doppler factor and θ is the angle between the moving direction and the line of sight[6]. Figure 1.15 shows δ values versus various β_Γ and θ. It is clear that the flux density can be greatly amplified depending on the speed and the viewing angle.

Relativistic effect also boosts the observed brightness temperature T_B. If T_B in the observer's frame is calculated from a direct plasma flux density and size measurement, then the observed temperature is Doppler-boosted by $T_B = T'_B\delta$ where T'_B is the intrinsic brightness temperature. The boosting effect is larger, $T_B = T'_B\delta^3$, if the source size is indirectly estimated by the flux variability timescale Δt because additional Doppler boosting of δ^2 is added due to the special relativistic time transformation. For instance, AGN jets showing intrinsic flux density variabilities on intra-day timescales suggest values of $\delta > 10$ in the jet. This results in extremely high observed brightness temperatures of $T_B \gtrsim 10^{14}$ (e.g., Fuhrmann et al. 2008).

---

[6] The exponent for the Doppler factor becomes $2+\alpha$ for a continuous jet (see Blandford & Königl 1979).

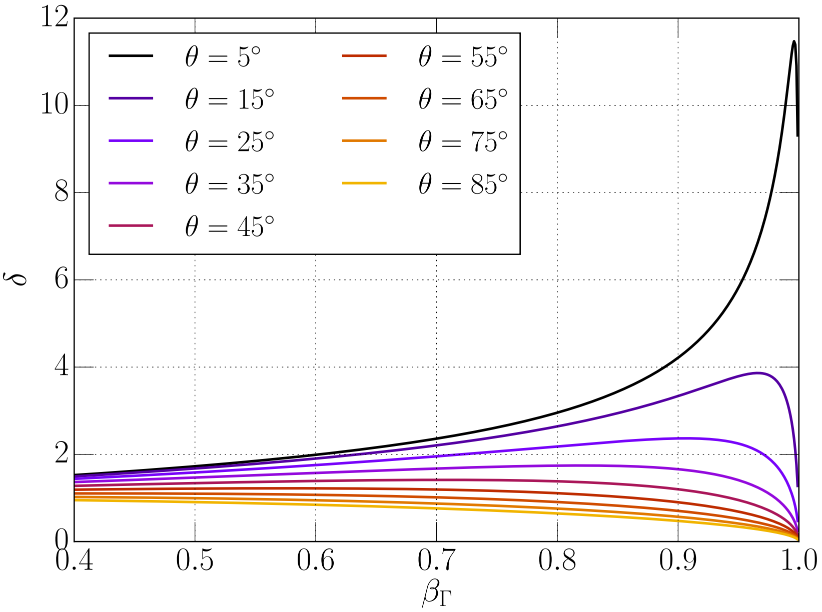

Fig. 1.15 Doppler factor (δ) versus various bulk motion speeds (β_Γ) and the viewing angle (θ). Note strong boosting manifests for small θ and also de-boosting for large θ.

The beaming also affects the apparent brightness ratio between the forward and receding plasma in a bipolar jet. A geometry of a bipolar jet is shown in Fig. 1.16. The flux densities of both approaching and receding jet plasmas $F_{a,r}$ are Doppler boosted/de-boosted by factor $\delta_{a,r}^{3+\alpha}$ where the subscripts a and r indicate the approaching and receding flows, respectively. The Doppler factors are given by

$$\delta_a = \frac{1}{\Gamma(1-\beta\cos\theta)} \quad , \tag{1.17}$$

$$\delta_r = \frac{1}{\Gamma(1+\beta\cos\theta)} \quad , \tag{1.18}$$

and their observed flux density ratio is given by

$$\frac{F_a}{F_r} = \left(\frac{1+\beta\cos\theta}{1-\beta\cos\theta}\right)^{3+\alpha} \quad . \tag{1.19}$$

Figure 1.17 shows the brightness ratio as a function of the viewing angle and the jet speed. Depending on the intrinsic speed and the viewing angle, the de-boosting can be very large (e.g., $F_a/F_r \gtrsim 100$). This explains why most of relativistic jets with fast speed appear to be one-sided (e.g., see Homan et al. 2015).

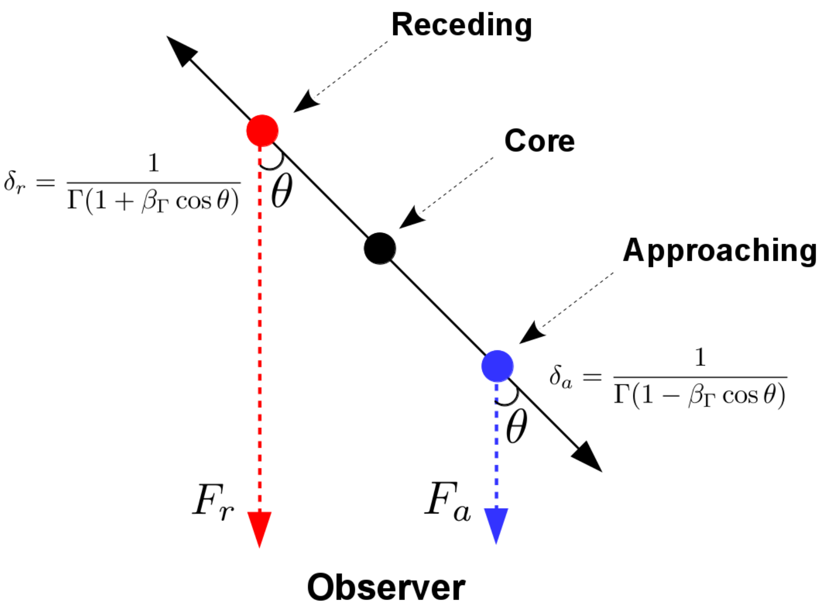
Receding
Core
Approaching
$\delta_r = \frac{1}{\Gamma(1+\beta_\Gamma \cos\theta)}$
θ
$\delta_a = \frac{1}{\Gamma(1-\beta_\Gamma \cos\theta)}$
θ
F_r
F_a
Observer

Fig. 1.16 Geometry of relativistic beaming in a bipolar jet. The figure was created based on the sketch of Böttcher (2012).

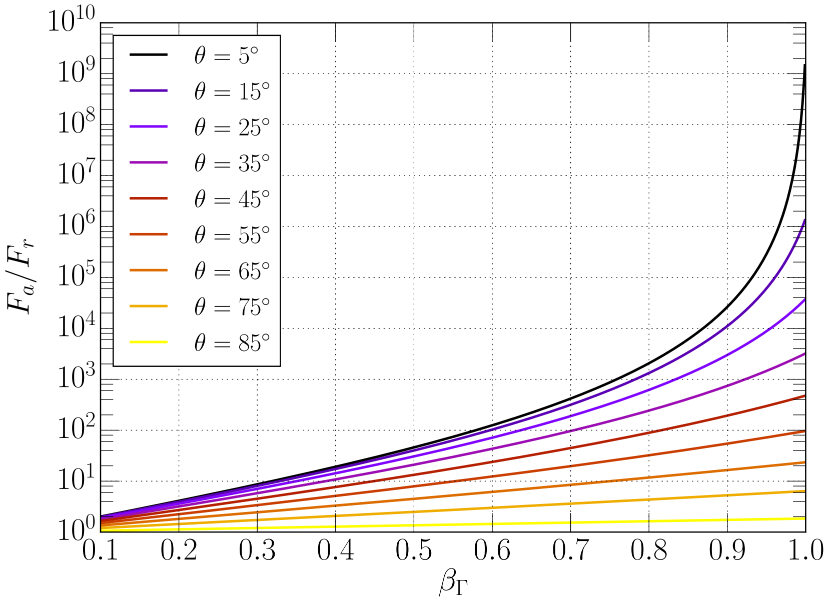

Fig. 1.17 Flux density ratio of the approaching and receding jet plasma (F_a/F_r) versus the viewing angle (θ) and the jet speed (β_Γ) for a single component.

Finally, the relativistic time dilation and length contraction can significantly change the sky-projected observed bulk speed of a moving plasma and the plasma could move apparently faster than the speed of light. The apparent projected speed β_{app} normalized by the speed of light c is given by

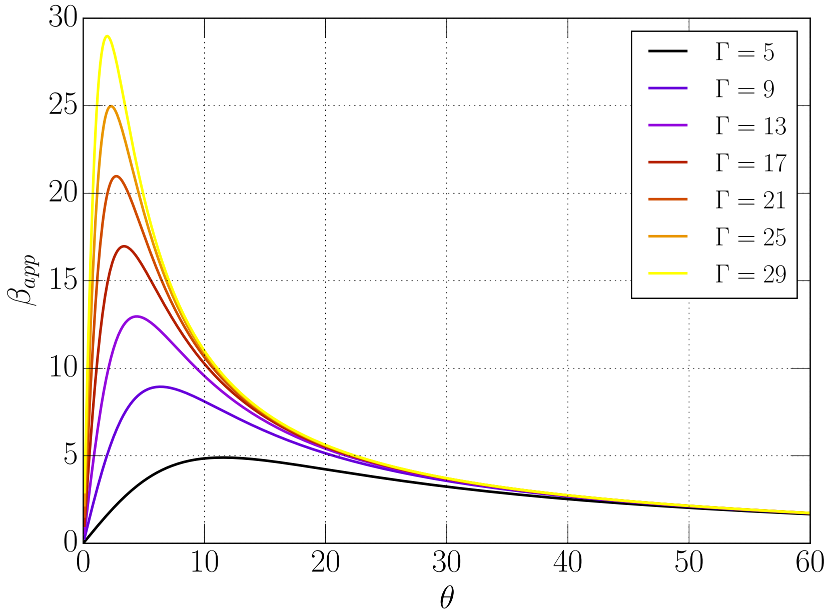

Fig. 1.18 The apparent jet speed ($\beta_{\rm app}$) versus the viewing angle (θ) and bulk Lorentz factor (Γ).

$$\beta_{\rm app} = \frac{\beta_\Gamma \sin\theta}{1 - \beta_\Gamma \cos\theta} \quad . \tag{1.20}$$

An example of the apparent speed versus the viewing angle and bulk Lorentz factor Γ is shown in Fig. 1.18. It can bee seen that the observed jet speed can easily exceed the speed of light ($\beta_{\rm app} \gg 1$). Rees (1966) suggested for the first time the possibility of observing a *superluminal motion* in astronomical objects due to special relativistic effects. Indeed, superluminal motions are routinely observed in parsec-scale AGN jets nowadays after they were discovered by Whitney et al. (1971) and Cohen et al. (1971) (see Fig. 1.19).

1.6.5 Inverse Compton scattering

In non-relativistic cases, photons can transfer additional momentum and energy to slowly moving particles by the Compton scattering process. In relativistic cases when the energy of a particle can be much greater than the incident photon energy, particles can instead boost up the energy of the photons by factor $\sim \gamma^2$ where γ is the characteristic Lorentz factor of the particles. This is called *inverse Compton scattering* (IC) process. We recall that a background radiation field can be produced in the surroundings of relativistic AGN jets by the accretion disk, the broad/narrow line region clouds, and the torus. If electrons in the jet plasma have high internal energy due to several physical mechanisms (e.g., shocks), the IC process can

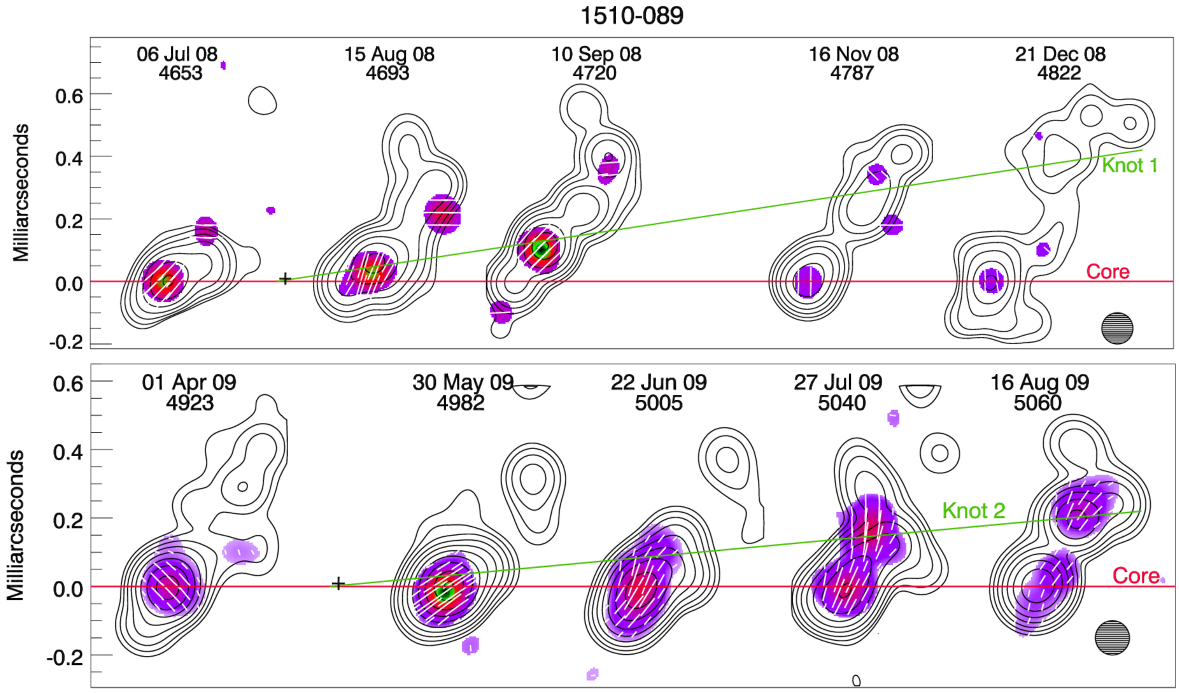

Fig. 1.19 Example of apparent superluminal motions in the jet of AGN PKS 1510–089. Jet components labelled Knot 1 and 2 move at apparent speeds of $\approx 22c$. The figure has been taken from Marscher et al. (2010).

easily occur. In addition, a homogeneous background field is Doppler-boosted within the jet frame by factor $\sim \Gamma^2$ along its propagation where Γ is the bulk Lorentz factor of the flow (i.e., $\Gamma \neq \gamma$). The resulting IC radiation is therefore even stronger along the jet propagation. Thus the inverse Compton mechanism is quite relevant for many AGN jets, especially for jets with small viewing angles with respect to the observers.

One of the important applications of the IC scattering is the modeling of the broadband spectral energy distribution (SED) of AGNs, which in particular have jets and show correlated flux density variabilities across different wavelengths (see Fig. 1.20). Broadband observations of many blazars often reveal a two-humped SED with the γ-ray emission coherently varying with the radio emission. Therefore, the peak in the radio band can be interpreted as direct synchrotron emission from relativistic jets while the peak in the γ-ray may originate from the radiation of the IC-scattered particles. The origin of the seed photons needed for the IC scattering is however often controversial (see Madejski & Sikora 2016 for a review).

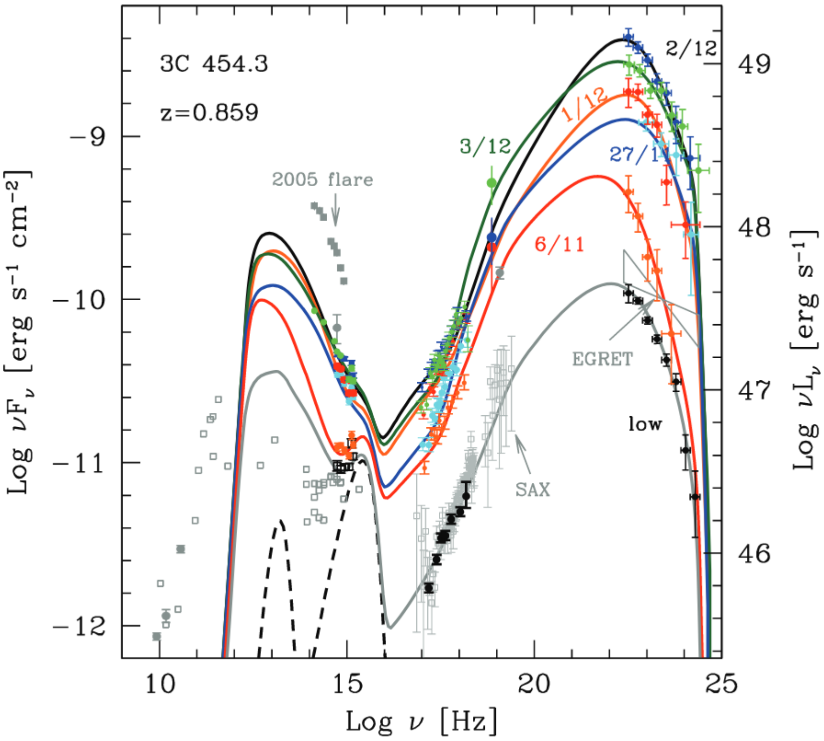

Fig. 1.20 Example of broadband SED variabilities of a blazar 3C 454.3 Date labels of different colors indicate their corresponding observing epochs (day/month) in the year 2009. The figure has been taken from Bonnoli et al. (2011).

1.7 Summary – unification of (nearly all) AGNs

We have reviewed the current understanding of AGNs focusing on the properties of their sub-components and phenomenology. We did not make an explicit attempt to introduce a number of different names of AGNs based on their phenomenology (see Urry & Padovani 1995 for details). However, it is helpful to summarize several classification schemes here for a better understanding of various AGN phenomena from an observational perspective.

Figure 1.21 briefly summarizes a possible categorization of AGN based on a few important criteria. Three main criteria are (1) viewing angle θ, (2) the Eddington ratio $\lambda = L/L_{\rm Edd}$, and (3) the radio loudness R which was classically defined as the ratio of the bolometric luminosity between the radio (at 5 GHz) and the optical (at B-band). More in detail: The inclination determines the fraction of the AGN light from the central engine region which can be directly observed against torus obscuration (critical $\theta \sim 45^\circ$ for a thickness-to-radius ratio ~ 1 of a solid torus). Smaller inclination angles also cause larger Doppler boosting of the emission from the jet. The Eddington ratio characterizes the mass accretion rate and geometry of the accretion flow. The radio loudness represents the relative strength of the jet emission (classically

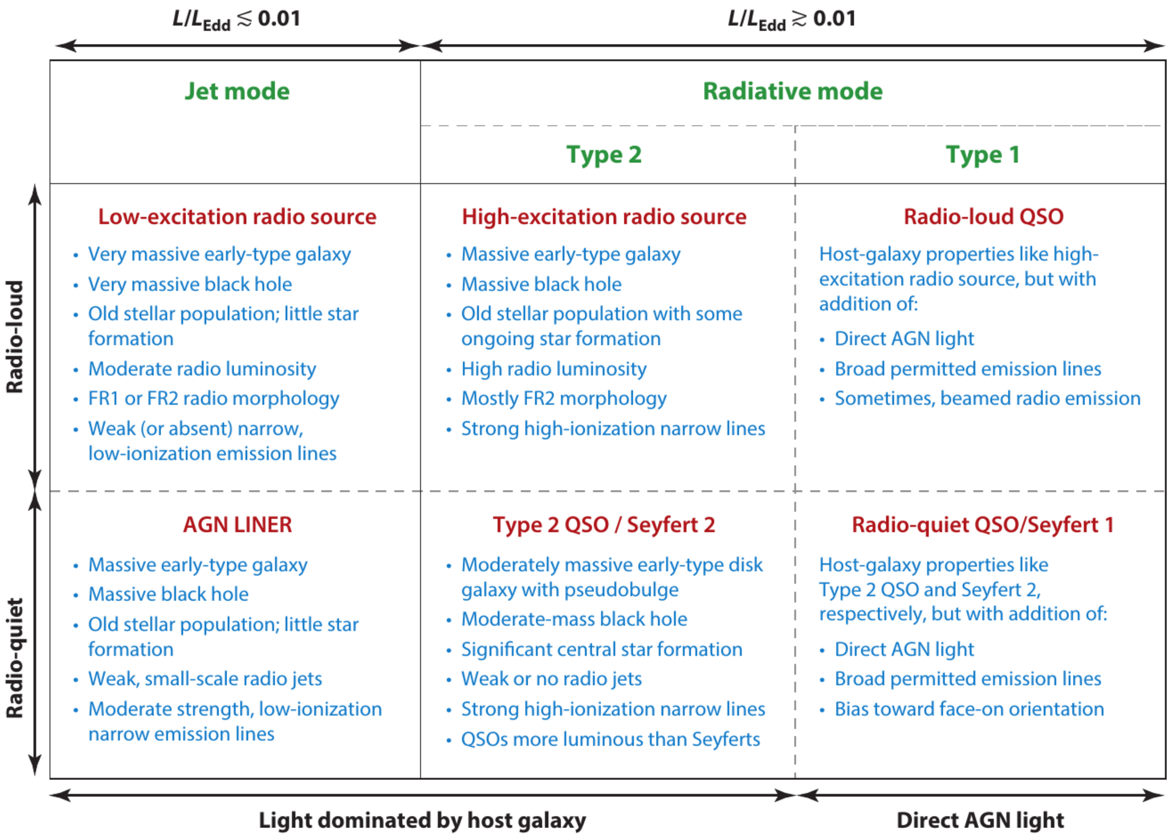

	$L/L_{\rm Edd} \lesssim 0.01$	$L/L_{\rm Edd} \gtrsim 0.01$	
	Jet mode	**Radiative mode**	
		Type 2	**Type 1**
Radio-loud	**Low-excitation radio source** • Very massive early-type galaxy • Very massive black hole • Old stellar population; little star formation • Moderate radio luminosity • FR1 or FR2 radio morphology • Weak (or absent) narrow, low-ionization emission lines	**High-excitation radio source** • Massive early-type galaxy • Massive black hole • Old stellar population with some ongoing star formation • High radio luminosity • Mostly FR2 morphology • Strong high-ionization narrow lines	**Radio-loud QSO** Host-galaxy properties like high-excitation radio source, but with addition of: • Direct AGN light • Broad permitted emission lines • Sometimes, beamed radio emission
Radio-quiet	**AGN LINER** • Massive early-type galaxy • Massive black hole • Old stellar population; little star formation • Weak, small-scale radio jets • Moderate strength, low-ionization narrow emission lines	**Type 2 QSO / Seyfert 2** • Moderately massive early-type disk galaxy with pseudobulge • Moderate-mass black hole • Significant central star formation • Weak or no radio jets • Strong high-ionization narrow lines • QSOs more luminous than Seyferts	**Radio-quiet QSO/Seyfert 1** Host-galaxy properties like Type 2 QSO and Seyfert 2, respectively, but with addition of: • Direct AGN light • Broad permitted emission lines • Bias toward face-on orientation
	Light dominated by host galaxy		Direct AGN light

Fig. 1.21 A table summarizing categories of AGNs and their characteristics depending on the radio loudness and viewing angle. Figure taken from Heckman & Best (2014).

the ratio of radio to optical flux density $R \gtrsim 10 - 1000$ for radio-loud and $R \lesssim 0.1 - 1.0$ for radio-quiet; see Kellermann et al. 1994). For radio-quiet AGNs, this categorization gives rise to three different AGN classes as follows:

- **Radio-quiet type 1/2** or **Seyfert 1/2** : The geometry of type 1 sources is close to the face-on case. The broad emission lines and the bluish continuum emission from the accretion disk are directly observed. On the other hand, type 2 sources are more edge-on and thus the broad lines and disk continuum are not directly seen. It is crucial to note that these two systems are found mostly in spiral galaxies (with a relatively small mass and disk-like geometry of the host).

- **Low-ionization nuclear emission-line region (LINER)** : This class is rather controversial because AGN activity signatures are generally weak (e.g., lack of highly ionized atomic emissions and direct disk emission features). Near-infrared observations often find that the high star formation rate of LINER's host galaxies produce signatures similar to those of AGN. On the other hand, LINERs are found in rather massive elliptical galaxies and associated with compact radio emission feature in the centers of the galaxies. The compact radio emission is believed to originate from the hot BH accretion flows or weak radio jets, which are AGN signatures. Therefore LINERs are also referred to as **low luminosity AGNs** (LLAGNs). See Ho (2008) for a review.

The other AGNs are radio-loud and show more pronounced jet emission. First of all, it is remarkable that radio-loud AGNs are found almost always in massive elliptical galaxies. Their specific characteristics are as follows:

- **Radio-loud QSO** or **Quasar** : They are basically the same as type 1 AGNs, but their bolometric luminosity is often dominated by the jet emission. In extreme cases, the broad emission lines and disk continuum are hidden by the jet emission if the jet is sharply aligned to the line of sight and thus relativistically boosted. Such systems are specifically called **blazars** (see Madejski & Sikora 2016 for a review).
- **Radio galaxy** : Radio galaxies include the other classical radio-loud AGNs seen at large viewing angles. They are often further classified into **high-excitation** and **low-excitation radio galaxies** depending on the level of ionization of atomic lines. It is intriguing that their jet morphologies are quite different on kpc-scales (FR II morphologies for the high-excitation systems but both FR I and II in the low-excitation systems). It is also known that the two sub-classes differ in their Eddington ratios, which suggests that the difference may originate from different mass accretion and jet physics (e.g., Tchekhovskoy & Bromberg 2016).

In summary, the AGN unification scheme can explain different kinds of AGN phenomena with a quite small number of free parameters such as the viewing angle, which relies on a purely observational bias. In spite of the success of the AGN unification scheme, however, it should be noted that several important questions are not clearly answered yet. Especially, the importance of relativistic jets and outflows have been addressed in various context of AGNs from dynamics of the central engine region to the co-evolution of SMBHs and host galaxies. However, it is still unclear why some AGNs launch powerful relativistic jets successfully while the others fail to do so. The dichotomy of radio loudness might require a certain level of intrinsic differences in different AGNs (e.g., see Kellermann et al. 2016 and references therein).

1.8 Main scope of this thesis

As we have reviewed, the importance of jet and outflow activities in AGNs has been recognized in various astrophysical contexts over the last decades. This has stimulated a number of theoretical studies focused on different aspects of jet physics; particularly the physics of mass accretion, initial jet launching, and the jet collimation and acceleration. Many of them, in particular those involving magnetohydrodynamic flows, successfully explain basic characteristics of jets observed on parsec scales and beyond (see §1.5). Theoretical studies now deeply focus on the jet production in the immediate vicinity of the SMBHs and many of them can reproduce jet phenomena in numerical simulations (e.g., $\lesssim 100R_s$ from the BH; see Meier 2012).

However, it is worth noting that many different theories are degenerated because different dynamical models reproduce similar observational parameters on large spatial scales and are thus not clearly distinguished from each other (see Boccardi et al. 2017 for a recent review). Furthermore, several fundamental questions such as why jets are launched only in a limited fraction of AGNs and why jets show a dichotomy of FR I/II are not yet clearly answered. One of the causes of this unsolved question is the finite computing power in numerical simulations because it is still not possible to run a fully self-consistent simulation of the complete physical picture including mass accretion, jet launching, and propagation from the BH accretion zone ($\sim 1R_s$) to the host galaxy scale (e.g., $\gtrsim 10^5 R_s$). However, another fundamental issue is the lack of robust constraints provided by direct observations of the compact BH accretion/ejection region.

In this regard, **the main aim of this thesis is to provide better observational constraints on the present theories by direct ultra-high spatial resolution imaging observations of two the nearest, more conspicuous AGN jets.** Recent technical improvements in radio astronomy now allow us to resolve the central engine region at an extremely high angular resolution. Especially, the global network of radio telescopes operating at millimeter wavelengths allows for routine very-long-baseline interferometry (VLBI) observations of AGN sources at ~ 50 micro-arcseconds resolution. For the nearest radio galaxies, such as the giant radio galaxy M 87, millimeter-VLBI observations can resolve the jet down to $\sim 7R_s$ from the BH (e.g., Lu et al. 2014; Kim et al. 2016). Therefore, millimeter VLBI observations can reach the jet base region and directly reveal the jet structure, the outflow speed, and magnetic field characteristics.

The rest of this thesis is structured as follows. In Chap. 2, the basic principles of radio astronomical observations and particularly relevant details of radio interferometry are provided. Chapter 3 is dedicated to the high spatial resolution study of the radio jet in the nearby giant radio galaxy M 87. Additional studies of another nearby, but more peculiar radio galaxy NGC 1275 (3C 84) is provided in Chap. 4. In Chap. 5, I close the thesis by providing a summary of the main conclusions and suggesting future work.

Chapter 2

Radio interferometric observations

As we have discussed in the previous chapter, the power-law energy distributions of non-thermal electrons in an optically thin plasma results in synchrotron radiation with a steep power-law spectrum. This makes it easier to observe AGN jets at radio wavelengths. In addition, the low frequencies of radio waves allow radio telescopes to directly record and preserve the phase of the incoming waves coherently. Therefore, remote stations separated by distances B much longer than the antenna diameter D can coherently synthesize observed signals of wavelength λ to image the source morphology at extreme angular resolution of $\sim \lambda/B \ll \lambda/D$ radian. Such a procedure is called interferometry. Radio interferometry is applied to resolve compact regions in the nuclei of active galaxies. In this chapter, we review the basic concepts of radio astronomy, the fundamental theory of radio interferometry and aperture synthesis, and several technical details. Special emphasis is made on VLBI observations. In this chapter, we follow the classical overview provided by Taylor et al. (1999); Wilson et al. (2012); Thompson et al. (2017).

2.1 Concepts of radio astronomy

A brief sketch of data acquisition and processing steps in a radio astronomical telescope used for VLBI is shown in Fig. 2.1. First, the incoming radio waves are collected and concentrated on the focus by primary and secondary reflectors. The radio signal is then captured and amplified by specific receivers which are designed to be sensitive to specific wavelengths of interest. The analog data are further electronically processed and transferred to the observatory building for final processing and digital recording. A more detailed descriptions of each component are given in the following sections.

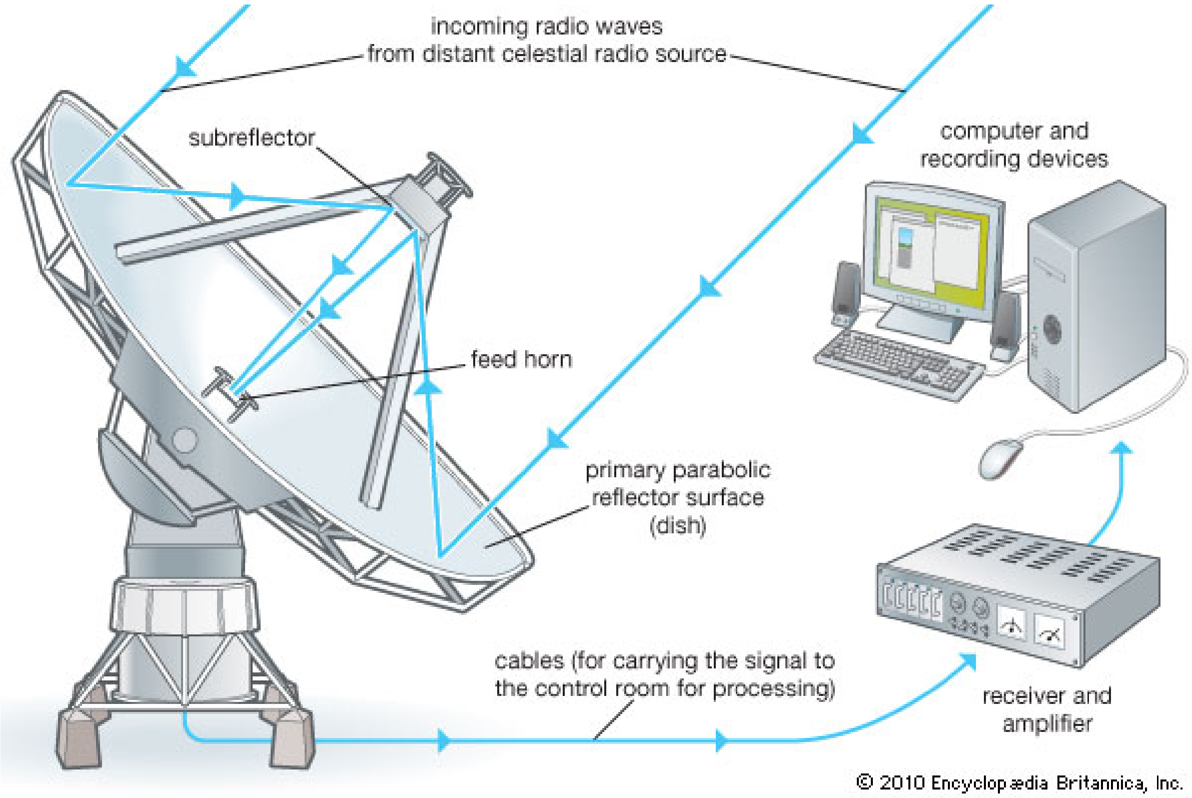
incoming radio waves
from distant celestial radio source
subreflector
computer and
recording devices
feed horn
primary parabolic
reflector surface
(dish)
cables (for carrying the signal to
the control room for processing)
receiver and
amplifier
© 2010 Encyclopædia Britannica, Inc.

Fig. 2.1 Diagram showing data acquisition and processing pipeline in a radio observatory. We additionally note that the receivers and amplifiers are typically placed in the primary or secondary focus of the antenna. Figure courtesy of Encyclopedia Britanica (https://www.britannica.com/science/radio-astronomy).

2.1.1 Antenna

Similarly to astronomical telescopes observing at other wavelengths, the faint radiation from astronomical objects is collected and amplified by the antenna. The antenna surface is designed to be sensitive to only a certain direction so that signals of only the target can be collected. The directional sensitivity, *the beam pattern*, is optimized by designing the antenna surface in usually a parabolic shape. For many antennas with circular apertures, the sensitivity is maximized within certain solid angle, *the main beam* (see Fig. 2.2). Similar to the full width half maximum (FWHM) of a Gaussian function, the angular size of the main beam θ is defined by the angle between two points where the beam efficiency drops by half of the maximum. This angular size is called the half-power beam width (HPBW). The beam size θ is inversely proportional to the diameter of the aperture D and proportional to the observing wavelength λ, i.e., $\theta = a \times \lambda / D$. The constant a is nearly unity and varies depending on the detailed aperture geometry. For example, the 100 m radio telescope in the Effelsberg observatory has typical beam size of $\theta \approx 41$ arcsec at the observing frequency of 15 GHz ($\lambda \approx 20$ mm). In contrast, a

10 m class telescope operating at the same frequency would have a much larger beam size of $\theta \approx 410$ arcsec. In theory, a smaller beam size is always desired. It is good to note, however, that the small beam practically requires more accurate pointing of the telescope towards the source. This is often demanding for big antennas because the mechanical precision is poorer for heavier telescopes. In this regard, the smaller dishes have some advantages over the big antennas, especially at short mm-wavelengths.

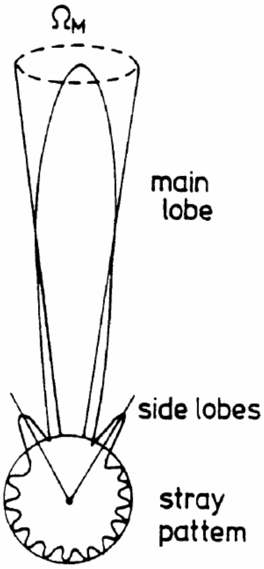

Fig. 2.2 A qualitative polar diagram of the angle dependence of the antenna beam. Figure taken from Wilson et al. (2012)

The light collecting power is largely determined by the diameter D of the aperture, but its efficiency also depends on the surface accuracy. The antenna efficiency η can be expressed by the Ruze equation; $\eta = \eta_0 \exp(-(4\pi\sigma/\lambda)^2)$ where η_0 is the ideal antenna efficiency in the absence of design errors and σ is the rms of the surface panel deviation from the ideal design (Wilson et al., 2012). A rule of thumb is that a surface accuracy of at least $\sigma \lesssim \lambda/4$ is required to observe at a wavelength λ. For example, a telescope with $\sigma \sim 0.3$ mm has $\eta \sim 0.75$ at 43 GHz (7 mm) but η drops quickly to ~ 0.31 at 86 GHz (3.5 mm) and even $\eta \ll 0.01$ at 230 GHz (1.3 mm). It is practically difficult to reduce the surface error for big telescopes. Thus, many radio telescopes operating at mm and sub-mm bands choose relatively small diameter (e.g., $D \sim$ 10-30m). However, recent technology allows to actively adjust individual surface panels during the observation to maintain good surface accuracy at high frequencies. Examples include the 100 m telescope at the Green Bank Observatory in the US, the 50 m Large Millimeter Telescope in Mexico, the 64 m Sardinia Radio Telescope in Italy, and the 65 m Tianma Radio Telescope in China.

2.1.2 Feed horns

Once the incoming radiation is collected and well focused by the telescope, it is led to the receiver through waveguides, which are also called *feed horns*. The main role of the feed horn system is to filter only the radiation of desired wavelength and specific polarization. The specific sampling capability is necessary in order to study spectral and polarization properties of radio emission from astronomical sources. The spectral sampling can be done by optimizing the shape of the feed horn to the observing wavelength. As for the polarization, we recall that electromagnetic waves can be decomposed into any set of two orthogonal polarizations (e.g., vertical/horizontal or left/right circular vectors). Both linear and circular basis have their own merits and the receivers are generally built on the linear basis for several practical reasons. While the linear basis is more intuitive, astronomers often prefer the circular basis more for a tracking observation of a linearly polarized source because the side-effect of sky rotation on the linear polarization of the source can be minimized. In such a case, the linearly polarized signals can be recorded on the circular basis using a quater-wave plate, which introduces additional $\lambda/4$ pathlength delay in one of the two linear polarizations (see Wilson et al. 2012 for more details)[1].

2.1.3 Receivers and further data processing

Radio telescopes can use both bolometers and heterodyne receivers to detect the radio signal. Bolometers measure only the intensity and are used for specific purposes such as fast, wide field total intensity mapping. On the other hand, heterodyne receivers measure both intensity and phase of the incoming wave. Therefore, heterodyne receivers are used in radio interferometers. Typical data acquisition and processing procedures are performed in several steps as follows.

- First, the front-end of the receivers consisting of two orthogonal dipole detectors convert incoming waves into electronic voltages consisting of the phase and the amplitude.
- Second, once the conversion is done, artificial signals of similar but slightly different oscillation frequencies are generated by local oscillators (LOs) and mixed with the incident voltage pattern. Because of slight differences in the frequencies, the net voltage is a beating pattern consisting of rapidly and slowly varying components. The frequency of the LO can be set to any arbitrary value and is known a priori. Therefore, the frequency of the sky emission can be effectively down-converted (e.g., down to GHz or MHz level). This makes it possible to identify and record the sky emission by proper samplers in the back-end, which are equipped with intermediate bandpass filters.
- Third, it is important to note that the raw signals from astronomical sources are very weak compared to laboratory voltages. Therefore, the frequency down-converted data are amplified by standard digital/analog signal processing instruments. The amplification is done at the expense of additional noises generated by the individual amplifiers.

---

[1] For ulterior calibration of linear polarization observations, other details such as the mount of the telescope (e.g., Alt-Azimuth or Equatorial) are also important.

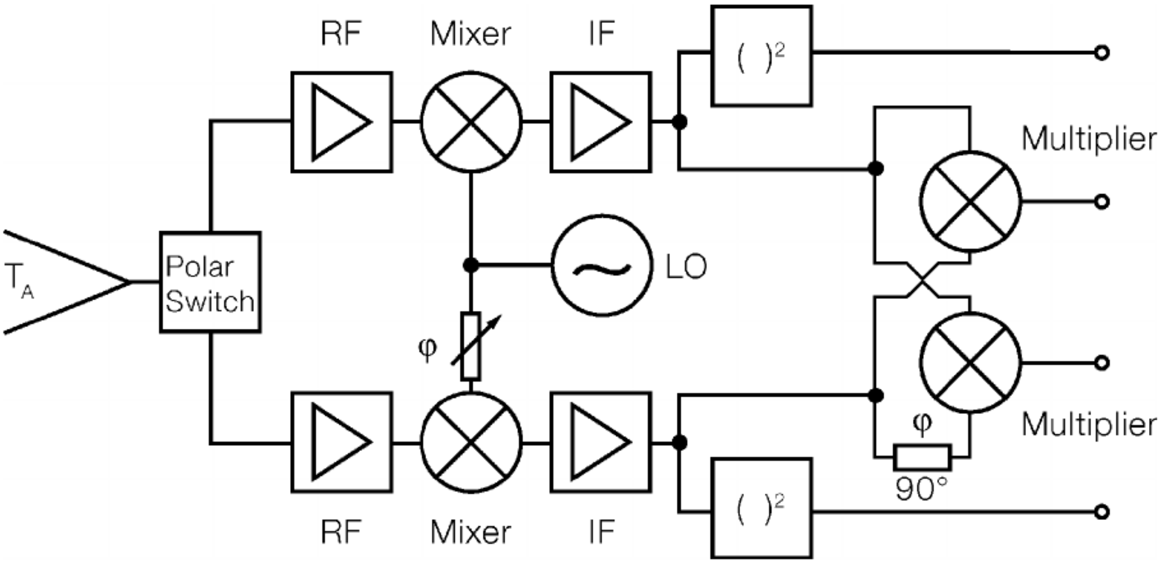

Fig. 2.3 A block diagram of data acquisition and processing from the front-end to the back-end of a polarization-sensitive receiving system with four polarization outputs. Figure taken from Wilson et al. (2012).

- Finally, an autocorrelation spectrometer (or simply correlator) is used to digitize and obtain the final source spectrum by fast Fourier transform[2].

Further details such as the number of intermediate frequencies (IFs) and sub-channels can be optimized depending on the purpose of the experiment. A schematic illustration provided in Fig. 2.3 summarizes the aforementioned processes. A photo of a real heterodyne receiver box is shown in Fig. 2.4.

2.1.4 Practical calibration procedure

The characteristics of the radio emission such as source brightness, spectrum, and polarization can be analyzed for scientific purposes only after proper calibration of the raw data. For a radio telescope, it is convenient to represent the source brightness in units of temperature (i.e., in K) rather than in units of radio sky flux density Jansky ($1\,\mathrm{Jy} = 10^{-26}\,\mathrm{W\,m^{-2}\,Hz^{-1}} = 10^{-23}\,\mathrm{erg\,s^{-1}\,cm^{-2}\,Hz^{-1}}$) because the noise power of electronic systems can be expressed in temperature units. For a source with astronomical flux of density $S_{\rm sou}$, we can write a scalar measurement equation by

---

[2] The autocorrelation is used for single dish observations while for interferometers this is replaced by cross correlation.

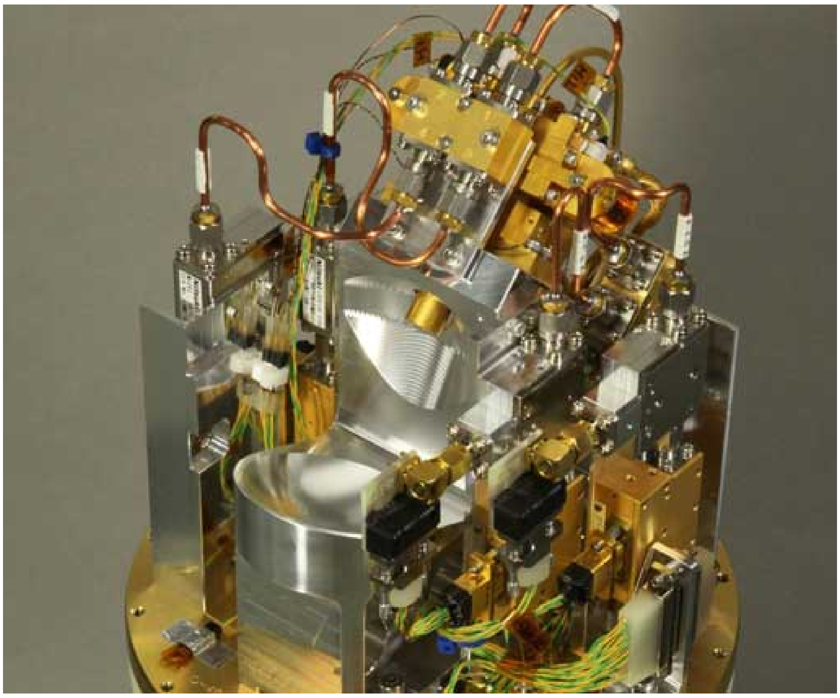

Fig. 2.4 A photo of a heterodyne receiver box developed for the Atacama Large Millimeter/submillimeter Array band-8 observations at ∼500 GHz. Image courtesy of NAOJ.

$$S_{\mathrm{sou}} = G \times \frac{T_{\mathrm{sou}}}{T_{\mathrm{sys}}} \times T_{\mathrm{sys}} = G \times \frac{C_{\mathrm{sou}}}{C_{\mathrm{sys}}} \times T_{\mathrm{sys}} \tag{2.1}$$

where G is the characteristic Kelvin-to-Jansky conversion factor of the system (in units of Jy/K), T_{sou} is the receiver temperature enhancement due to the source, T_{sys} is the system temperature representing sum of powers of all but the source, and C_{sou} and C_{sys} are uncalibrated counts for the source and the system, respectively (in arbitrary system count units). The antenna gain G can be well determined by observing a flux calibrator with known flux. At mm-wavelengths, planets are ideal flux calibrators because their brightness temperature can be accurately calculated prior to the observation (e.g., Perley & Butler 2013). The system count C_{sys} can be obtained by flux measurements towards a blank sky. Since the count towards the source is $C_{\mathrm{sou}} + C_{\mathrm{sys}}$, the source count can be obtained by $(C_{\mathrm{sou}} + C_{\mathrm{sys}}) - (C_{\mathrm{sys}})$ [3]. One remaining term is the system temperature T_{sys}, which is necessary to convert the count to Kelvin. Because the noise power is additive, T_{sys} is sum of the temperature of all components except the source. We can model T_{sys} as

---

[3] For a spectral line observation, the source and noise can be separated from a single measurement towards the source by making use of noisy continuum signals outside the line frequencies.

$$T_{\rm sys} = T_{\rm rx} + (1-\varepsilon) \times T_{\rm atm}(1-\exp(-\tau)) + \varepsilon T_{\rm amb} \tag{2.2}$$

where $T_{\rm rx}$ is the receiver temperature, ε is the receiver spill-over of the antenna, $T_{\rm atm}$ is the atmospheric temperature, τ is the opacity of the atmosphere, and $T_{\rm amb}$ is the ambient temperature (e.g., the receiver cabin temperature). The system temperature can be estimated in various ways. Typically, $T_{\rm rx}$ is known a-priori from lab measurements or can be also determined by cold/hot load systems (e.g., liquid helium). $T_{\rm atm}$ and $T_{\rm amb}$ can be directly measured from the observatory site. The opacity term is usually solved by assuming a plane-parallel atmosphere and fitting the baseline of the $T_{\rm sys}$ versus the airmass $\sec z$ where z is the zenith angle.

Astronomical sources are faint and the blank sky counts also fluctuate with time. Therefore, one needs to know about the signal-to-noise ratio (SNR) of the observation. For autocorrelation measurement devices, random noises are uncorrelated with themselves. Thus the noise can be suppressed with longer integration time and wider electronic bandwidth. The source intrinsic signal however correlates with itself and remains the same regardless of the integration time. Hence, the SNR can be expressed by

$$\mathrm{SNR} = \frac{\mathrm{Signal}}{\mathrm{Noise}} = A\frac{T_{\rm sou}}{T_{\rm sys}/\sqrt{\Delta\nu\Delta t}} = A\frac{T_{\rm sou}}{T_{\rm sys}}\sqrt{\Delta\nu\Delta t} \tag{2.3}$$

(Thompson et al., 2017) where A is a constant greater than unity and depends on the system design, $\Delta\nu$ is the bandwidth, and Δt is the integration time.

2.2 Radio interferometry

One problem in radio observations is that the angular resolution of a radio telescope is quite poor simply because of the long observing wavelengths. For instance, the angular resolutions of the Effelsberg telescope at 2 cm and of the human pupil at optical wavelengths are comparable. Improving the angular resolution has been therefore one of central quests in radio astronomy. The resolution may be substantially improved by making an artificial large aperture consisting of largely separated but electronically connected smaller radio telescopes. Radio interferometry (or aperture synthesis[4]; see Ryle 1962) is such a technique. Radio interferometers collect the signals from remote telescopes, produce synthetic data by cross correlation, and provide high resolution images after proper imaging process, which involves Fourier transformation.

Interferometry was first used in astronomy by Michelson in the late 19th century when he measured the diameters of several nearest stars using a two-element optical interferometer. The idea of radio interferometry started with the beginning of radio astronomy when Karl G. Jansky developed an adding radio interferometer, a prototype of modern cross-product inteferometers. Since then, a lot of progress have been made in the field ranging from fundamental theories of aperture synthesis to electronic technologies and signal processing. Nowadays, physically disconnected antennas distributed over the globe or even space radio telescopes can be used to form an array. Interferometers consisting of physically disconnected antennas are used in VLBI. Typical angular resolutions achieved by VLBI observations can exceed that of a single telescope of same type by a factor of a million. A review about the history of astronomical interferometers and aperture synthesis can be found in §1.3 of Thompson et al. (2017). In this section, we focus on the fundamental principles of radio interferometry and other practical aspects, which are especially relevant for VLBI.

---

[4] https://www.nobelprize.org/nobel_prizes/physics/laureates/1974/

2.2.1 Interferometric response – fringes

The basic idea of radio interferometry is to synthesize the desired large antenna surface by a number of smaller antennas. The individual antennas have a small diameter and are distributed at various sites. The key point is to form a virtual focus of the array in a virtual focal plane by adding the signals of different array elements coherently. The synthesized observable in the virtual plane[5] is called visibility and the angular response of a series of the small antennas is called interferometric beam pattern. The visibility function is the key product of an interferometer and is used to map the sky intensity distribution. Figure 2.5 provides an illustration of the similarities and differences between a large single dish and an interferometer.

In order to demonstrate the mathematical principles of a basic interferometer, let us consider a monochromatic observation of a point source located at a large astronomical distance by using a one-dimensional two antenna interferometer (see Fig. 2.6). If we ignore the individual antenna beam pattern, the voltage outputs V from each element in response to the far-field radiation are $V_1 = E\cos[\omega(t-\tau_g)]$ and $V_2 = E\cos(\omega t)$ where E is the amplitude of the radiation, ω is the angular frequency of the radiation, and τ_g is the time delay of the wave detection in antenna 1 due to geometry. Assuming that the two antennas are connected to a signal multiplier by cables of exactly the same length, the cross product of the two voltages is given by $V_1V_2 = E^2/2 \times [\cos(\omega\tau_g) + \cos(2\omega t - \omega\tau_g)]$ [6]. Integrating V_1V_2 over a sufficiently long period, the final response of the system R_C becomes

$$R_C \equiv < V_1V_2 > = P\cos(\omega\tau_g) \tag{2.4}$$

---

[5] Strictly speaking, this plane is the Fourier counterpart of the projected sky plane. The coherently added synthetic data in this plane are the Fourier transform of the sky brightness distribution. See §2.2.2 for details.

[6] In contrast to the adding interferometer, the voltages are multiplied and averaged in modern interferometers because the cross-product scheme results in lower noises. See Thompson et al. (2017) for an analysis of the difference between the two types of interferometers.

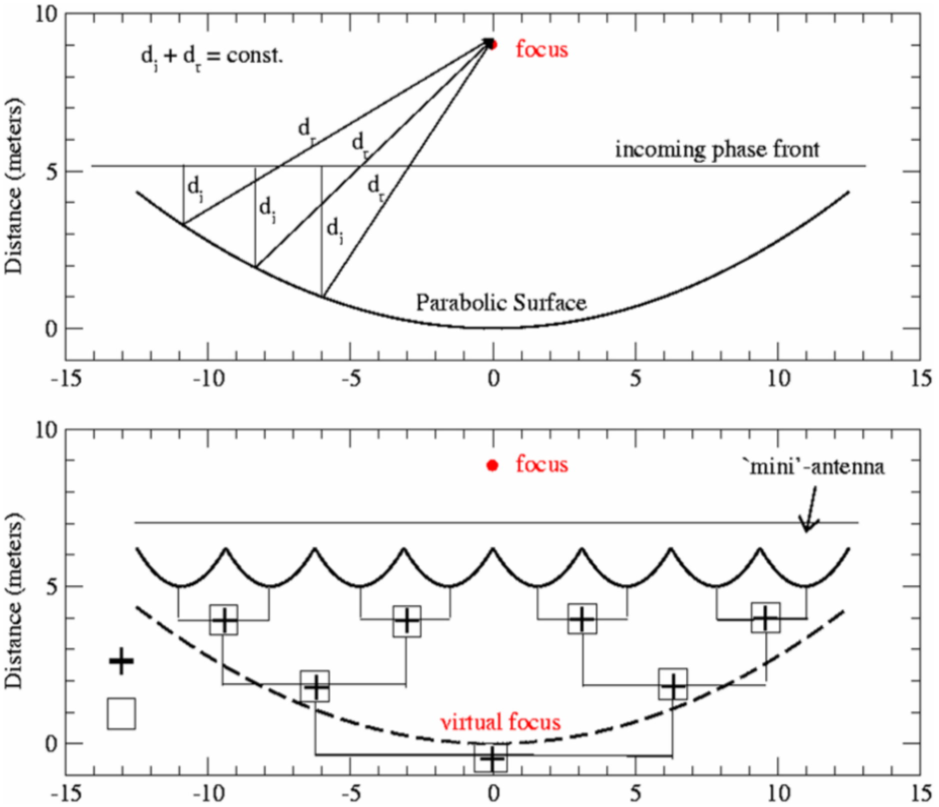

Fig. 2.5 An illustration showing the fundamental idea of radio interferometry. **Top** : optical paths of an incoming wavefront reflected by a parabolic surface of a filled aperture. The amplitude of sum of the reflected wavefront is maximum at the focus and decreases following the telescope beam pattern. **Bottom** : an interferometer equivalent to a virtual telescope. Individual little antennas have dishes smaller than the filled aperture. In this case, the wavefront received by each small antennas are electronically guided to a virtual focus to produce a maximum amplitude. Figure courtesy of Rick Perley (https://science.nrao.edu/science/meetings/2014/14th-synthesis-imaging-workshop).

where P is a constant for the amplitude and the $\cos(2\omega t)$ term has been removed by time-averaging. The geometrical time delay τ_g can be written in terms of a source direction vector $\vec{s}$ ($|\vec{s}| \equiv 1$) and the baseline vector $\vec{b}$ where $|\vec{b}| = b$ is the distance between the two antennas. Then, the response function R_C can be written as

$$R_C = P\cos(\omega\tau_g) = P\cos\left(2\pi\frac{\vec{b}\cdot\vec{s}}{\lambda}\right) \tag{2.5}$$

where λ is the wavelength of the radiation. It is important to note that the response R_C has null values when $\vec{b}\cdot\vec{s}/\lambda$ is integer. Thus, R_C is a sensitive function of the source direction $\vec{s}$ when $b/\lambda \gg 1$. The term $(\vec{b}\cdot\vec{s}/\lambda)$ can be specifically written as

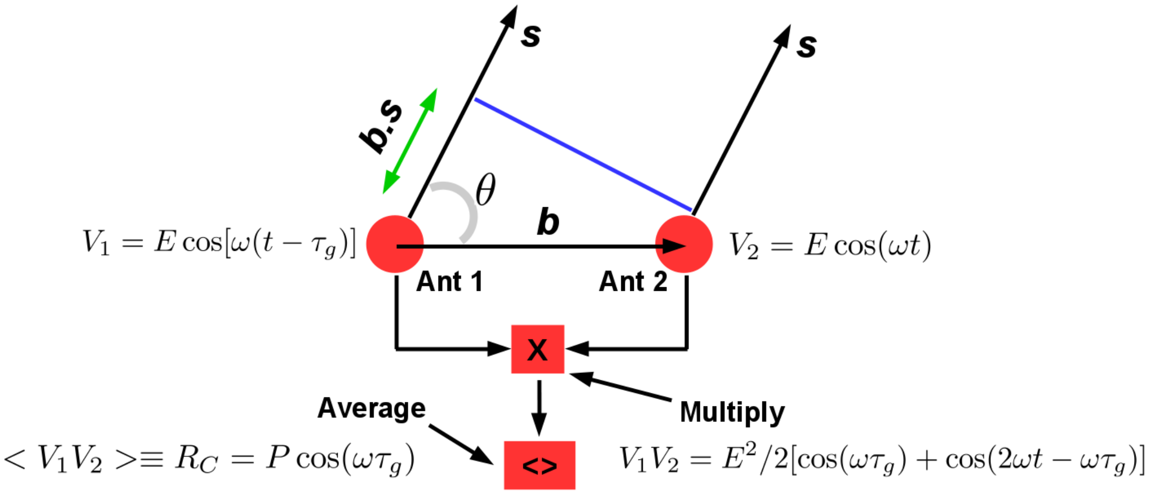
s
s
b.s
θ
b
$V_1 = E\cos[\omega(t-\tau_g)]$
$V_2 = E\cos(\omega t)$
Ant 1
Ant 2
X
Average
Multiply
<>
$< V_1V_2 > \equiv R_C = P\cos(\omega\tau_g)$
$V_1V_2 = E^2/2[\cos(\omega\tau_g)+\cos(2\omega t-\omega\tau_g)]$

Fig. 2.6 Interferometric observation of a far-field source by a two-element interferometer. Bold italic letters denote vectors.

$$\vec{b}\cdot\vec{s}/\lambda = u\cos(\theta) = u\sin(\alpha) = ul \tag{2.6}$$

where $u = b/\lambda$ is the baseline length normalized by the wavelength, $\alpha = 90-\theta$ is the angle between $\vec{s}$ and the zenith, and $l = \cos(\theta) = \sin(\alpha)$. Now we call R_C, which is a synthetic response of the two telescopes, as *fringe*. The fringe pattern has its first maximum at $l = 0$ (i.e., zenith) and the angle separation from every peak to peak is $1/u = \lambda/b$ radian. We note that the constant amplitude term P can be replaced by the beam pattern of the individual antenna. In this case, R_C will begin to be strongly tapered outside λ/D.

Therefore, the resulting fringe has a very sharp angular response compared to that of a single dish beam (e.g., 100 times sharper for $b/D = 100$). The fine angular response of the fringe can be used for several purposes. For example, one can attempt a high-accuracy position determination of a compact radio source by making interferometric measurements at several different sky positions. The interferometric measurements will have non-zero outputs only when the source is within $\sim\lambda/b$ radian from the pointing direction and the response will be nearly zero otherwise. In this way, we can regard the fringe spacing λ/b as *HPBW of the synthetic beam of the array*. While this particular interferometer lacks several considerations which are relevant for more realistic interferometers, this example nicely demonstrates how a radio interferometer achieves a higher angular resolution.

2.2.2 Image⇔Visibility – 2D Fourier transform

Now we consider the interferometric response output from observations of an extended source on the sky. When each antenna points towards a patch of the 2D intensity distribution on the sky and produces voltage outputs $V_{1,2}(\vec{s})$, the interferometric response R_C is

$$R_C(\vec{s}) = \left\langle \int\int V_1(\vec{s})d\Omega_1 \times \int\int V_2(\vec{s})d\Omega_2 \right\rangle \tag{2.7}$$

where $d\Omega$ is the solid angle towards $\vec{s}$ and $\langle\rangle$ denotes time averaging. If the source emission is incoherent – i.e., $I(\vec{s})$ is independent of $d\Omega(\vec{s})$ – the integrals and averaging can be interchanged. If we further ignore the telescope gains and assume ideal calibrations, the product of the two voltages $V_1(\vec{s}) \times V_2(\vec{s})$ is the source brightness $I(\vec{s})$. Using the same notation, we can replace the geometric time delay term in Eq. 2.4 by $\tau_g = \vec{b} \cdot \vec{s}/c$ where c is the speed of light. Therefore, the response function R_C is expressed by

$$R_C = \int\int I(\vec{s})\cos(2\pi\nu\vec{b}\cdot\vec{s}/c)d\Omega\ . \tag{2.8}$$

From Eq. 2.8 it is clear that the response of the correlator is the source sky intensity distribution multiplied by the fringe pattern of the interferometer. The next step is to find an expression which represents $I(\vec{s})$ as function of R_C. Before doing so, it is useful to decompose the arbitrary sky intensity distribution function into odd and even symmetric parts, i.e. $I(\vec{s}) = I_E(\vec{s}) + I_O(\vec{S})$ where I_E and I_O are the even and odd symmetric part, respectively. Since the odd symmetric part is filtered out by the cosine term during the integration, it is straightforward to find

$$R_C = \int\int (I_E + I_O)\cos(2\pi\nu\vec{b}\cdot\vec{s}/c)d\Omega = \int\int I_E\cos(2\pi\nu\vec{b}\cdot\vec{s}/c)d\Omega \equiv R_{C,E} \quad . \tag{2.9}$$

In order to recover the interferometric response from the odd symmetric part, a phase shift by $\pi/2$ can be added in the cosine term. From the practical point of view, the additional phase in the array can be easily controlled either analogically (e.g., making one of the electronic cables longer by $\lambda/4$) or digitally (e.g., adding lag in the data stream during the cross correlation). In this way, Eq. 2.9 can become sensitive to the odd symmetric part:

$$R_C = \int\int (I_E + I_O)\cos\left(2\pi\nu\vec{b}\cdot\vec{s}/c + \pi/2\right)d\Omega = \int\int I_O\sin(2\pi\nu\vec{b}\cdot\vec{s}/c)d\Omega \equiv R_{C,O}\ . \tag{2.10}$$

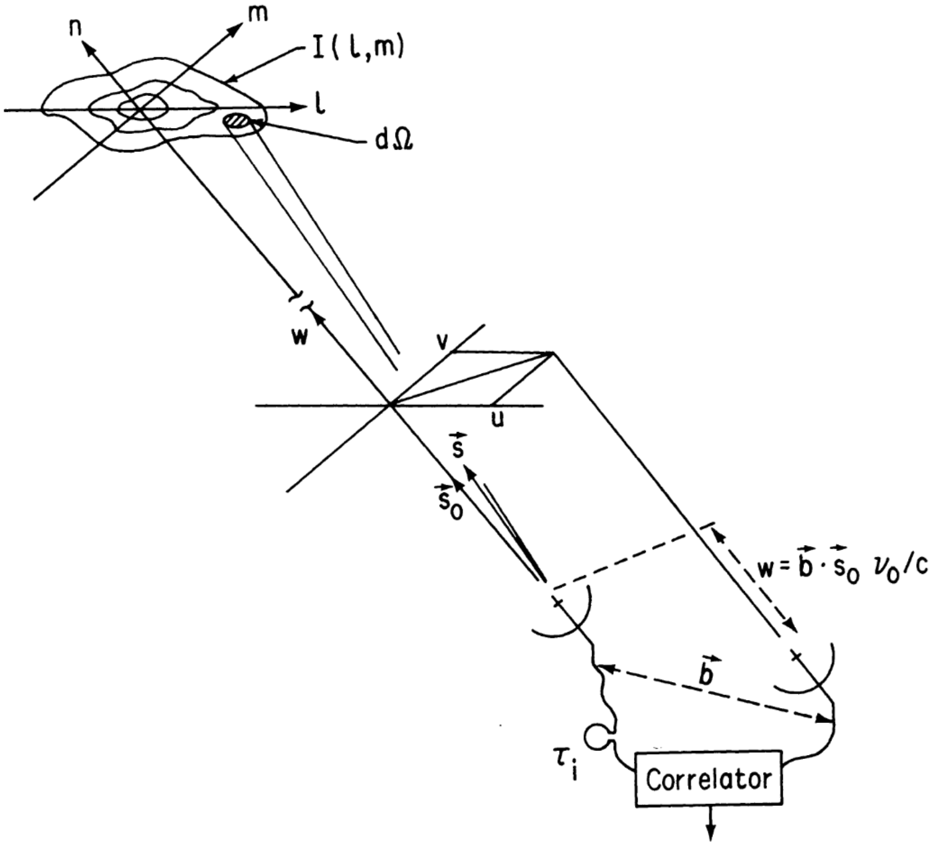

Fig. 2.7 Definition of the coordinates (l,m,n) for the sky and (u,v,w) for the baseline. Figure taken from Taylor et al. (1999).

In order to describe the full sky distribution pattern, we can linearly combine Eq. 2.9 and 2.10 to express the response function R_C in a generalized complex form by

$$R_C \equiv R_{C,E} - \mathrm{i} \times R_{C,O} = \int\int I_E \exp(-2\pi \mathrm{i} \nu \vec{b} \cdot \vec{s}/c) d\Omega \tag{2.11}$$

where i is the imaginary unit. The complex response function can be obtained by performing the voltage multiplication twice with and without the additional $\pi/2$ phase in one of the two stations.

Now we introduce specific coordinate systems for the Earth and the sky in order to obtain an explicit expression for the $\vec{b} \cdot \vec{s}$ term in Eq. 2.11. For the sky, we write the directional vector $\vec{s} = (l,m,n)$ (i.e., $|\vec{s}| = 1$) which is defined with respect to a reference direction $\vec{s_0}$, the *phase tracking center*. For the baselines, we define $\vec{b} = (u,v,w)$ where $u, v,$ and w are measured in units of λ. Geometry of this coordinate system is shown in Fig. 2.7. Following Taylor et al. (1999), we can write

$$\begin{aligned} \nu\frac{\vec{b}\cdot\vec{s}}{c} &= ul+vm+wn && (2.12)\\ \nu\frac{\vec{b}\cdot\vec{s}_0}{c} &= w && (2.13)\\ d\Omega = \frac{dl\,dm}{n} &= \frac{dl\,dm}{\sqrt{1-l^2-m^2}}\,. && (2.14) \end{aligned}$$

Therefore,

$$R_C \equiv V(u,v,w) = \int\int \frac{I(l,m)}{\sqrt{1-l^2-m^2}} \exp\left(-2\pi\mathrm{i}\left(ul+vm+w\left(\sqrt{1-l^2-m^2}-1\right)\right)\right) dldm \tag{2.15}$$

where now we call R_C the *visibility function* $V(u,v,w)$. When $|l|$ and $|m|$ are sufficiently small (e.g., $\vec{s}$ being sufficiently close to the phase center), we can reasonably assume $\sqrt{1-l^2-m^2} \approx 1$ and $w(\sqrt{1-l^2-m^2}-1) \approx 0$ [7]. This simplifies Eq. 2.15 as

$$V(u,v) = \int\int I(l,m)\exp\left(-2\pi\mathrm{i}\left(ul+vm\right)\right) dldm\,. \tag{2.16}$$

By inspecting Eq. 2.16, we can notice that $V(u,v)$ is a two-dimensional Fourier transform of $I(l,m)$. Therefore, we can express $I(l,m)$ as inverse Fourier transform of $V(u,v)$:

$$I(l,m) = \int\int V(u,v)\exp\left(2\pi\mathrm{i}\left(ul+vm\right)\right) dudv \quad . \tag{2.17}$$

While we have assumed a two-element interferometer, this principle should hold for any pair of antennas in other radio interferometers with larger number of antennas. Thus, it should be emphasized that **for any interferometer, the sky intensity distribution is obtained by the inverse Fourier transform of the interferometric visibility function.** This principle is the *Van Cittert–Zernike theorem* (van Cittert, 1934; Zernike, 1938).

As an additional remark, we also notice that the brightness pattern of the object is a continuous function while its Fourier counterpart (i.e., the visibility function) is sparsely sampled in the (u,v) space. The problem of obtaining a good image therefore depends on how to improve the visibility sampling in the (u,v) domain. One particular solution is to add a large number of antennas in the array so that $V(u,v)$ are measured for many $\vec{b}$. However, this option is practically expensive and contradicts the motivation of interferometric technique. Thus, a special observing technique is desired. In fact, Ryle (1962) pointed out that the Earth rotation accompanies elevation and hour angle change of a celestial source and this also changes the source direction vector $\vec{s}$ for a fixed baseline vector $\vec{b}$. Therefore, a baseline tracking the source over long time can sample the source visibilities at many different (u,v) points. Ryle (1962) formulated its mathematical description and named this principle as *Earth-rotation aperture synthesis* (for the formulas see also Taylor et al. 1999; Thompson et al. 2017). For modern radio interferometers, the Earth-rotation synthesis technique is used on a daily basis for radio imaging.

---

[7] For a wide-field interferometry, however, the w term cannot be dropped out and must be properly accounted for. Thus special considerations are needed (see Thompson et al. 2017 for details).

2.2.3 Practicalities of interferometric observations

In §2.2.1 and §2.2.2 we have examined the fundamental principles of radio interferometry and how a sky intensity distribution can be obtained from the visibility. In reality, however, interferometric observations involve a large number of further technical considerations from data acquisition to analysis. For instance, we have considered only monochromatic and noise-free radio waves in §2.2.1. However, real radio signals are observed over finite electronic bandwidths and observations always suffer from incoherent noises. Therefore the data integration time is quite limited by the finite coherence time and the signal-to-noise ratio becomes lower. For VLBI where the antennas are not physically connected, data recording and correlation is another issue. Additional issues include uncertainties in the VLBI station positions and the clock, and residual errors from the receiver/cable systematics. At short mm-wavelengths, the characteristics of the turbulent atmosphere vary from each VLBI station to station and fast phase variations are unavoidable[8]. How to best image the source structure against limited (u,v) sampling is another issue. Therefore, VLBI observations require high-precision data recording, timing analysis, and dedicated efforts for calibration/imaging. These practical issues are briefly covered in the rest of this chapter.

Data acquisition

The front-end of VLBI stations observe incoming waves in the same manner as single-dish observations. However, the physical separations between the antennas are large, often reaching thousands of kilometers. This prevents a straightforward data correlation. Therefore, the raw signals (amplitudes and phases) and precise time stamp information are properly recorded using dedicated digital back-end systems. This requires spacious data storages (usually hundreds of TB for one-night long observation at 2 Gbps data recording) and a precise time standard such as the hydrogen maser, which provides timestamps on pico-second accuracy level. In the past, different observatories used to have different data recording formats, which made a straightforward and routine VLBI observations challenging. Nowadays, most observatories use the same standard format maintained by a worldwide VLBI community. After each observing run, the disk packs from each of the stations are shipped to specific places for data correlation (e.g., to the Socorro correlation center in the US for the Very Long Baseline Array (VLBA), the JIVE correlator in Dwingeloo for the European VLBI Network (EVN), and the MPIfR correlation center for the Global mm-VLBI Array (GMVA)). Dedicated computing facilities installed at the data correlation center play back the data stream into the correlator and carry out the multiplication and time averaging.

---

[8] For small arrays, the antennas share the same atmosphere and relative phase differences between each antenna pairs are small even though the atmosphere is still turbulent.

Data correlation

The main role of the correlator is to simply cross-correlate the data and average them over finite time in order to generate the complex visibilities (see Fig. 2.6). Even though it sounds simple, the procedure is in practice complicated because correct visibilities can be obtained only when the geometric and other instrumental effects – which cause timing errors – are properly compensated for (see Whitney 2000 for a comprehensive review). A priori correlator model accounts for predictable effects such as the antenna positions, radio source positions, clocks, and the thickness of the atmosphere. After the initial correlation, residual errors affecting the timing and the temporal alignment of the data streams from independent telescopes are further calibrated by the so-called fringe fitting which is described below.

Fringe fitting

The main causes of the residual timing errors are various. Examples are wrong clock models, poorly known electric cable lengths, and the weather. If the residuals are reasonably small compared to the model prediction, the residual parameters can be empirically estimated by dedicated fitting procedures and the side-effects can be removed. As a result, the visibility data become more coherent in both frequency and time. The process of estimating the residuals and calibrating the interferometric phase is called *fringe fitting*. A nice review on the basic principles of fringe fitting is given by Cotton (1995). Here, I shortly describe fundamental aspects of the fringe fitting after the major steps are performed in the correlator.

As we have seen earlier, an interferometric phase ϕ can be written as $\phi = 2\pi\nu t$ where t is the measurement time. Using a first-order approximation, the phase error $\Delta\phi$ can be expressed by

$$\Delta\phi = \phi_0 + \left(\frac{\partial\phi}{\partial\nu}\Delta\nu + \frac{\partial\phi}{\partial t}\Delta t\right) \tag{2.18}$$

where $\partial\phi/\partial\nu$ is called *delay* and describes the variation of the residual phase in frequency, and $\partial\phi/\partial t$ is called fringe rate or simply *rate* and describes variation of the residual phase in time. Different signal pathlengths for different frequency bands are one of the origins of the residual delay. This can happen if electronic cable lengths are different for different spectral channels. At low radio frequencies, the ionosphere also causes a dispersive pathlength differences in the atmosphere and induces frequency-dependent phase changes in the interferometer data. The rate describes the time variation of the phase and could originate from several different effects such as drifts in the station clock. Thus, delays and rates can be reasonably assumed as characteristics of each station. Another reason of modeling the phase error based on the antenna basis, especially in astronomical VLBI, is that the number of baselines of an array $N(N-1)/2$ is usually much larger than the total number of antennas N. The antenna-based calibration approach therefore employs the over-determined boundary conditions to improve the calibration accuracy (see Cotton 1995).

When the source or calibrator structure is known a priori (e.g., for slightly resolved or unresolved source), observed complex visibilities can be divided by that of the source model to remove the source phase from the data. Then the residual error parameters can be estimated for each baseline and corrected for each antenna after parameter optimization. There are several algorithms to estimate the delays and rates (see Cotton 1995 and references therein). For integer n, there is $2n\pi$ radian angle ambiguities in the phase. Thus, modern radio interferometry softwares perform so-called fast Fourier-transform (FFT) fringe search. That is, the phase of each baseline is 2D Fourier-transformed in order to find the best delay and rate values which give the highest signal-to-noise in the delay and rate domain. Examples of the FFT fringe fitting are shown in Fig. 2.8.

Practically, the delay values are rather stationary in time if they have an instrumental origin (e.g., cable length differences in different spectral channels which do not change a lot over day timescales). Therefore, the *instrumental* delay is solved in the first step of the fringe fitting manually by making use of highest signal-to-noise scans on bright calibrators of (hopefully) simple structures. After the phase is aligned in frequency, the time-dependent rate and (relatively smaller) residual multi-band delay can be solved by the fringe-fitting over the entire observing run (see, e.g., the AIPS Cookbook[9])

Amplitude calibration

The amplitude calibration is necessary in order to obtain the visibilities in units of astronomical flux densities. Specifically, the amplitude calibration converts the cross-correlation coefficients

---

[9] http://www.aips.nrao.edu/cook.html

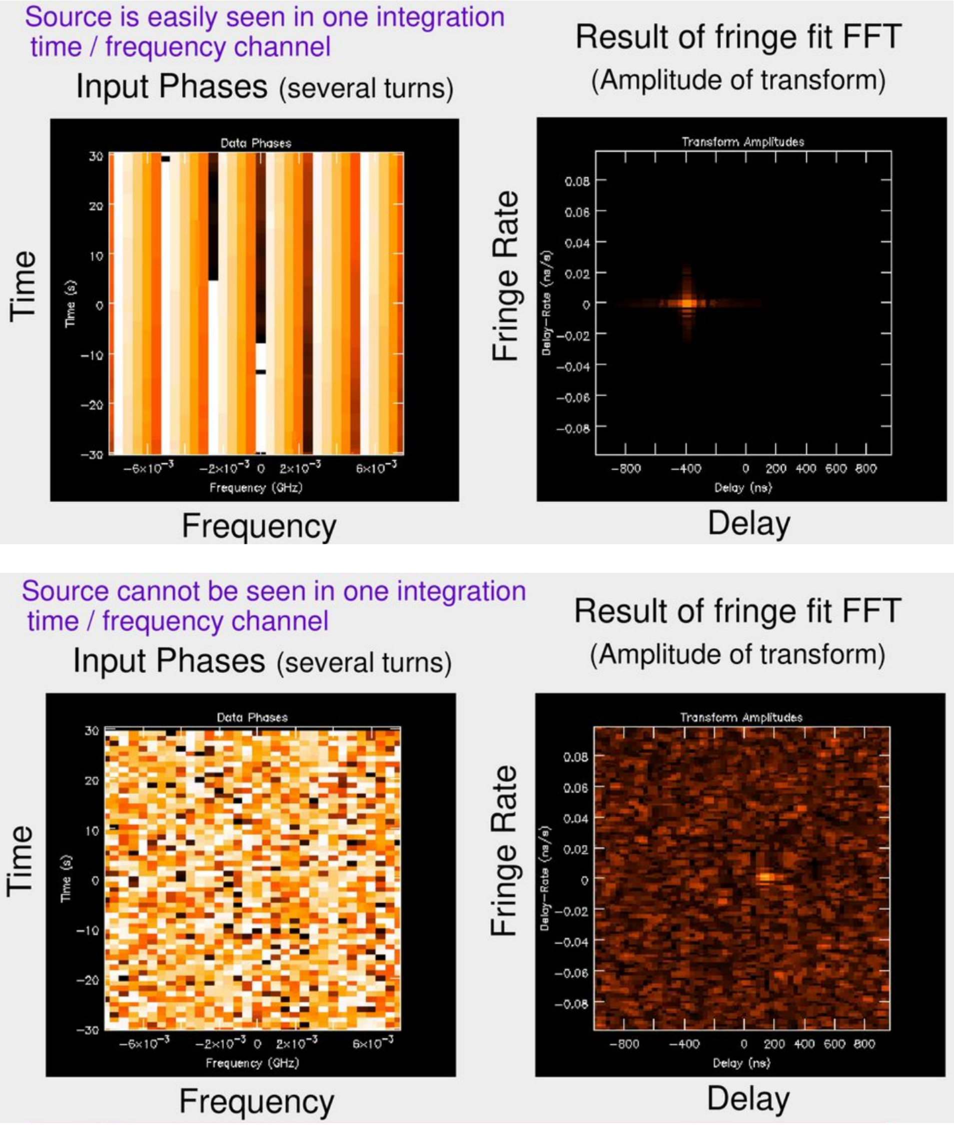

Fig. 2.8 Examples of FFT fringe fitting on two baselines of different signal-to-noise ratios. In the left and right columns, the color indicates values of the phase and their Fourier transform amplitude, respectively. **Top** : The input phase in frequency and time domain (left) and its Fourier transform amplitude in the rate and delay space (right). In both panels, characteristics delay and rate are clearly seen. **Bottom** : The same plot but for a lower signal-to-noise baseline. The noisy phases in the frequency and time domain show a more clear signature of a fringe solution in its Fourier transform. Figure courtesy of George Moellenbrock and R. Craig Walker (http://www.aoc.nrao.edu/events/synthesis/2002/)

obtained by the correlator into the Jansky unit. Similar to the single-dish observations, amplitude of a baseline between stations i and j can be calibrated by

$$S_{ij} = \rho_{ij} A \sqrt{SEFD_i\ SEFD_j} = \rho_{ij} A \sqrt{\frac{T_{\mathrm{sys},i}\ T_{\mathrm{sys},j}}{G_i G_j\ \exp(-\tau_i)\exp(-\tau_j)}} \tag{2.19}$$

(Thompson et al., 2017) where ρ_{ij} is the raw cross-correlation coefficient of the baseline ij, A is a constant close to unity and corrects side effects from the data digitization and the correlator characteristics (e.g., A=0.88 and 0.64 for 2-bit and 1-bit digitization, respectively), $SEFD$ is the system equivalent flux density (in Jy), T_{sys} is the system temperature (in K), G is the elevation dependent antenna gain (in K/Jy), and τ is the atmospheric opacity. Unlike single dish observations, VLBI observations are usually performed in source tracking mode. Therefore T_{sys} is frequently measured close to the source between VLBI scans or it is measured in real time during the VLBI scan on the source (e.g., using a secondary off-axis weather measurement feed).

Imaging process

After the data correlation and proper calibrations, the source can be finally imaged using the resulting visibility data. As we discussed, however, the incomplete (u,v) sampling leads to undesired artifacts in the image since discrete $V(u,v)$ data points create oscillation patterns in its Fourier transform. Let us have a look at a realistic example. Figure 2.9 shows examples of the (u,v) coverage from a real Very Long Baseline Array (VLBA) observation of a radio galaxy jet at 15 GHz and its corresponding interferometric beam pattern. Apparently, the beam response is maximized at the center, but the beam also has other positive and negative responses around the center (i.e., sidelobe interferences). The sidelobe becomes a significant issue for a source with complex structure. In Fig. 2.10 we show an example of radial distribution of the visibilities of the same data set as function of radial (u,v) distances $\sqrt{u^2+v^2}$ and a direct Fourier transform of $V(u,v)$, the *dirty map*. Decreasing visibility amplitudes at longer (u,v) distances and complex visibility structure in the inner (u,v) spacings ($\lesssim 100M\lambda$) suggest that the source is clearly resolved and has complicated structure on a larger scale. But the dirty map shows no hint of such structure.

Therefore, the source structure has to be carefully recovered against the interference even if the visibility is free from noise and any calibration errors. Unfortunately, there is no unique solution because interferometric imaging is by nature an ill-posed, highly non-linear problem. Nevertheless, several empirical and mathematical methods have been proposed and they have been proved to be working successfully under certain conditions. One of the most popular, intuitive, and successful image deconvolution algorithms is CLEAN (Högbom, 1974). The basic idea is to model a continuous, smooth intensity distribution as sum of many discrete components. In practice, a CLEANing run is performed as follows:

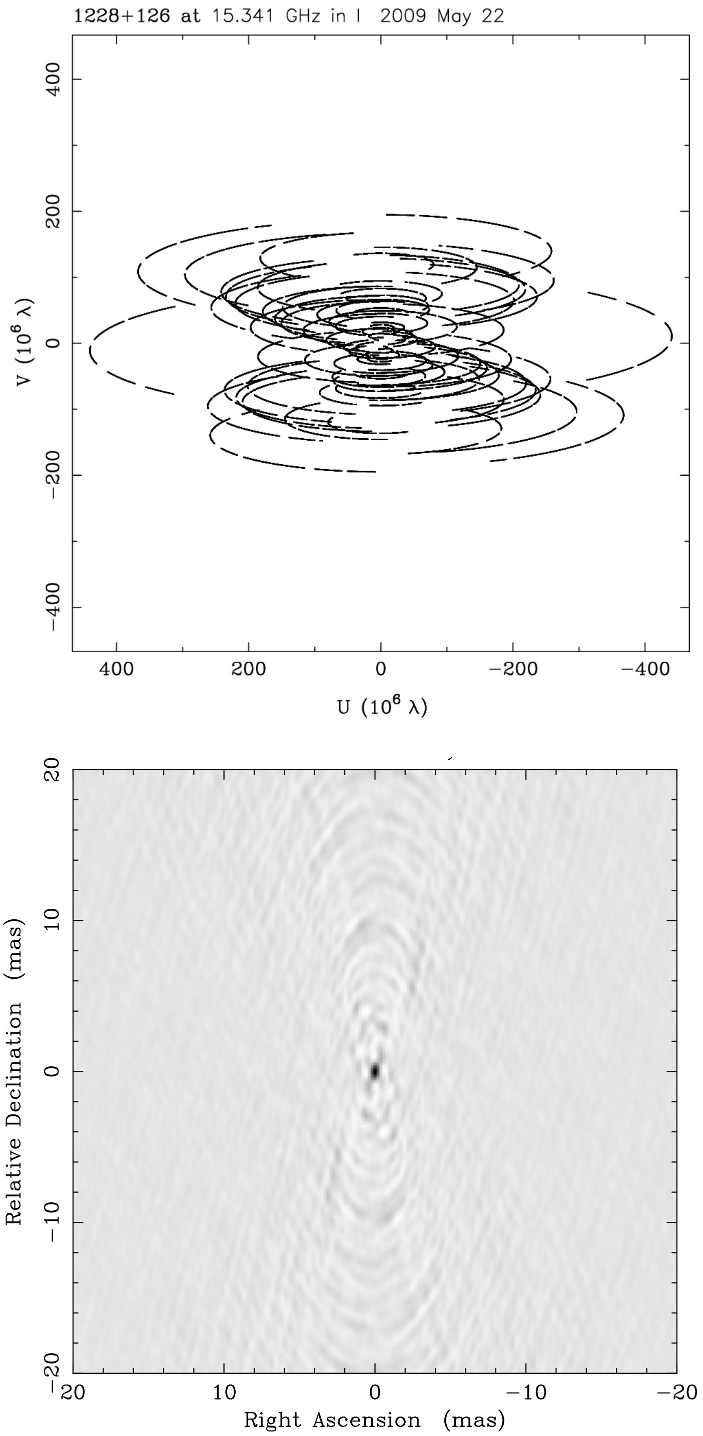

Fig. 2.9 **Top** : Example of (u,v) sampling for a real, full-track VLBA observation at 15 GHz. **Bottom** : The interferometric beam of the corresponding (u,v) coverage. The beam response is higher for darker color. The data have been taken from the MOJAVE program database (Lister & Homan, 2005).

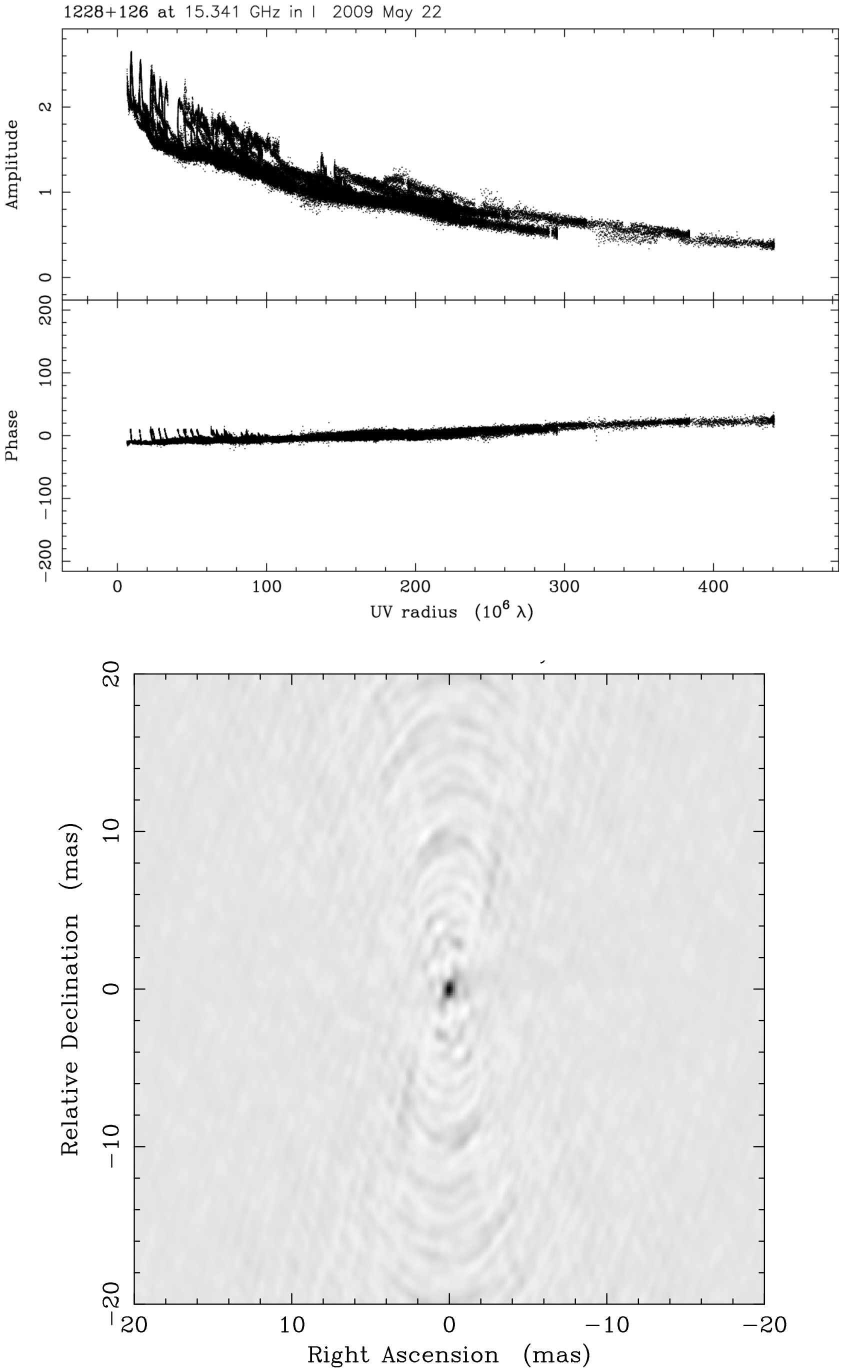

Fig. 2.10 **Top** : Example of radial visibility amplitude and phase distribution for a real VLBA 15 GHz data set of the radio galaxy M 87. **Bottom** : Direct Fourier transform of the visibility distribution, i.e. the dirty map. The image is dominated by the sidelobe interference shown in the bottom panel of Fig. 2.9. The data have been taken from the MOJAVE program database (Lister & Homan, 2005).

1. In the dirty map, set a support region (CLEAN box) around bright, significant emission features manually. Note that this procedure is somewhat subjective.

2. Find the position of a peak in the box. Then subtract the peak value multiplied by the interferometric beam profile from the dirty map (i.e., deconvolve the peak). The resulting dirty map is called *residual map*.

3. Record the peak information (i.e., the coordinates and the peak value) into a model table. A model for a single peak is called CLEAN component.

4. Calculate a *restoring beam* by fitting an elliptical Gaussian to the center of the interferometric beam. This is to estimate the interferometric resolution of the interferometric data. Then multiply the CLEAN component(s) in the table by the restoring beam and add the resulting Gaussian(s) to a blank image. This image is an initial CLEAN map.

5. Find a second peak in the CLEAN box and continue steps 1-4 to update the model table. The next version of the CLEAN image is a sum of all the Gaussians obtained by the step 4.

6. Continue the procedure until no significant emission feature is found in the first CLEAN box. Then set another CLEAN box to extract the features and repeat the procedure. Note that this decision is also subjective.

7. Repeat steps 1-6 until no significant peaks are found in the entire residual map. Finally, add the latest residual map to the latest CLEAN map to obtain a final one. Note that the decision to stop CLEAN is also subjective. However one could estimate a theoretically expected image noise level in the residual image to determine the time to stop the CLEAN procedure.

As illustrated above, CLEAN is a highly subjective procedure and the steps depend on human biases. However, experiences show that it is a powerful, computationally efficient method and works successfully on different source morphologies if the source is reasonably bright and compact (see §11 of Thompson et al. 2017). In Fig. 2.11 we show an example of the final residual and CLEAN maps obtained by iterative CLEAN of the same data presented in Fig. 2.9 and 2.10.

Overcoming unpredictable residual errors

The fringe fitting and a-priori amplitude calibration get rid of many known effects that contaminate the data. Even after rigorous data calibration, however, some systematic effects are

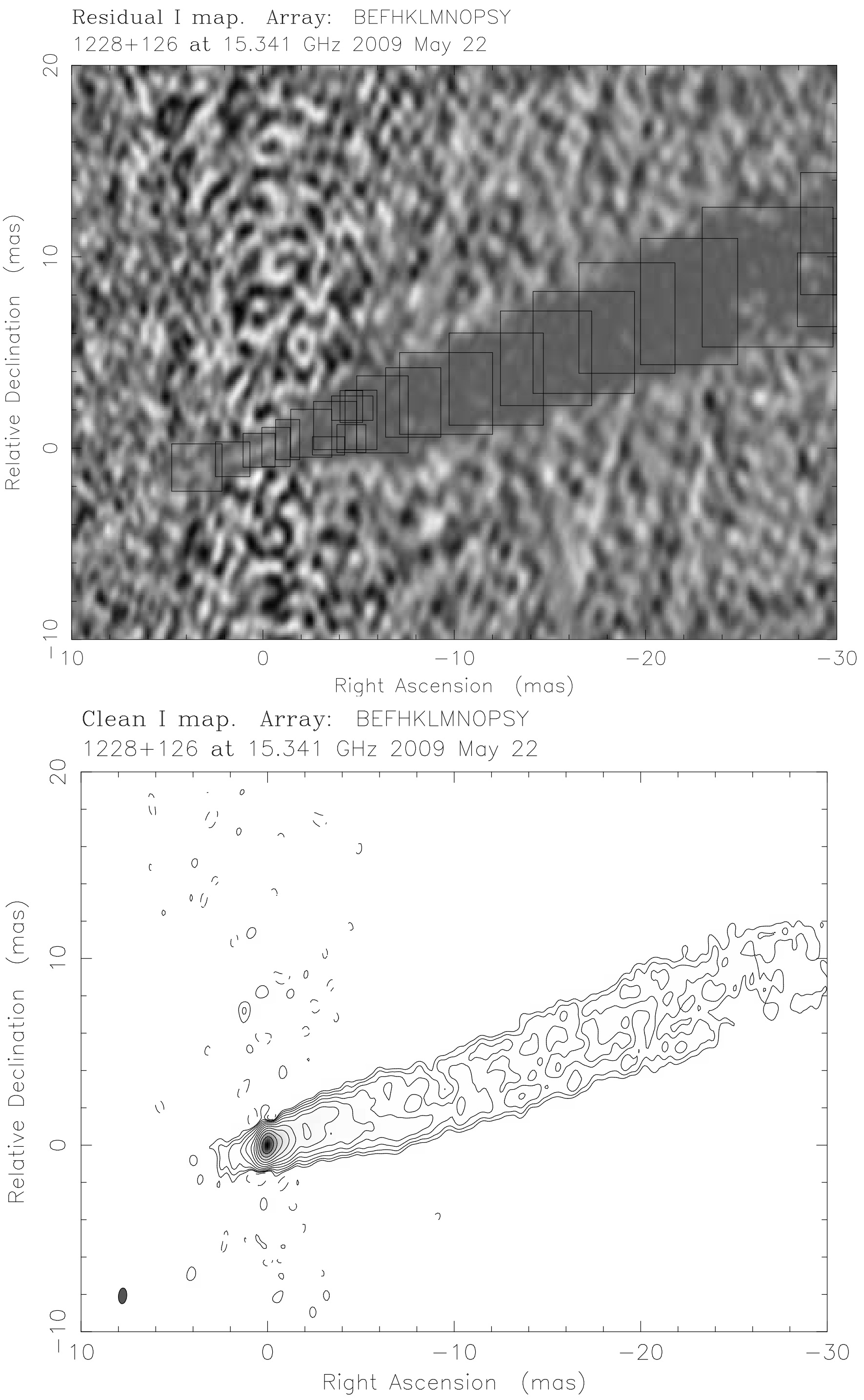

Fig. 2.11 **Top** : Final residual map of the same data presented in Fig. 2.9 and 2.10 after iterative CLEAN procedures with the black CLEAN boxes. The intensity is higher for darker color. **Bottom** : Final CLEAN map. The image is displayed using contours for better illustration.

hard to be incorporated during the a-priori calibration stage. One typical example is an antenna pointing error. For instance, a pointing error of a VLBI station by half of the single-dish beam size causes a factor 2 amplitude decrease in the corresponding baselines. Another example are turbulent phase variations caused by the water vapor in the atmosphere, which absorbs and re-radiates radio waves. This results in a significant VLBI phase change on short timescales (e.g., ~ 1 radian phase rotation within tens of seconds at short mm-wavelengths). Apparently, these effects are unpredictable. A clever data flagging is helpful to improve the data quality.

Several approaches are possible to estimate and remove the unpredictable errors. For instance, measuring the source visibility $V(u,v)$ using multiple baselines at the same (u,v) points provide additional redundancy in the data. If the source has no time-variability during the observing run, any difference in the measured $V(u,v)$ can be referred to as residual errors. Thus, the differences can be calibrated away by applying additional amplitude and phase corrections to each station. Alternatively, observations of a point-like calibrator near the science target help estimate and remove the errors, especially for the phase. A point-like source has a simple interferometric phase distribution and any deviation of the observed phases from the model can be referred to as residual errors. The atmospheric phase model derived from the calibrator may be applied to the nearby science target assuming the same atmosphere.

On the other hand, when the science target is sufficiently bright, the most basic structure of the source – e.g., cores of AGN jets – can be modeled and imaged even under the presence of the unpredictable noises. Then it is possible to adopt this structure as a "calibrator" and estimate station gain correction factors to calibrate certain fraction of the data (i.e., phases of long baselines). As the initial model is incomplete, this procedure can be repeated iteratively until the model and the data agree. This strategy is called *self-calibration*. In a general self-calibration loop, the station gain correction factors are estimated so that they minimize the sum of the difference between the model and the corrected data. It is worth noting that a poor source model would require more calibration loops and could develop artifacts in the image. Furthermore, it is impossible to correct the data if the data suffer from very large errors or even the first preliminary model is not suitable for its purpose. In this regard, the success of self-calibration depends on the total number of independent, "robust" measurements. In order to boost the number of robust independent constraints, special observable quantities immune to station-based errors can be calculated from the raw visibilities. Such observables are *closure phases* and *closure amplitudes* (see, e.g., Cornwell & Fomalont 1999). The closure phases are calculated by summing the visibility phases of three baselines in a station triangle (i.e., three stations involved). Similarly, the closure amplitudes are calculated by the ratio of the visibility amplitude of four baselines in a square (i.e., four stations involved). For N antennas, the number of *independent* closure phases and amplitudes are $(N-1)(N-2)/2$ and

$N(N-3)/2$, respectively. Analysis shows that the fraction of phase and amplitude information that can be recovered for each antenna are then $(N-2)/N$ and $(N-3)/(N-1)$, respectively (see §10 and §11 of Thompson et al. 2017). A large number of antennas therefore ensures that self-calibration can recover the true source information successfully.

Nowadays, self-calibration is a broadly adapted technique and iteratively used with CLEAN. We refer to Cornwell & Fomalont (1999) and references therein for deeper discussions about the closure quantities and full mathematical descriptions of the self-calibration algorithms. Furthermore, it is interesting to note that recent advances in the computing power now allow us to use the closure quantities to image the source directly (e.g., Lu et al. 2014; Chael et al. 2016, 2018).

2.2.4 VLBI polarimetry

The linear and circular polarizations of electromagnetic waves can be parameterized by different combinations of orthogonal electric vectors. In optics, polarization is parametrized by Stokes parameters I, Q, U, and V. Stokes I is used for total intensity while different combinations of Q, U, and V represent linear and circular polarization. Principles and practicalities of radio interferometry that we have discussed can be naturally extended to interferometric measurements and analysis of Stokes Q, U, and V as well. Similar to single-dish polarimetry, however, interferometric polarimetry requires a couple of extra calibrations. Here I briefly discuss additional considerations necessary for VLBI polarimetry. For a general review about Stokes parameterization and radio polarimetry, see Wilson et al. (2012); Thompson et al. (2017). A deeper review about the polarization measurements and error analysis is given by the following articles and references therein; Wardle & Kronberg (1974); Montier et al. (2015a,b).

The fundamental reason why the additional calibration is needed is that each receiver feed is designed to be sensitive to only one polarization, but no receivers are ideal and they somehow record the other orthogonal polarization as well. This is called polarization leakage. In order to provide a more quantitative picture, let us describe four complex visibilities of a single baseline assuming that both antennas are equipped with right and left hand circular polarization feeds (RCP and LCP, respectively). For a VLBI station, the complex signal can be written by (Roberts et al., 1994)

$$v_L = G_L\left(E_L \exp(i\phi) + D_L E_R \exp(-i\phi)\right) \tag{2.20}$$

$$v_R = G_R\left(E_R \exp(-i\phi) + D_R E_L \exp(i\phi)\right) \tag{2.21}$$

where L and R respectively denote the left and right circular polarization, v is the voltage, E is the complex electric field of the observed radiation (i.e., both amplitude and phase), ϕ is the parallactic angle, and D is the complex polarization leakage of the observing feed (i.e., D-terms). If the leakage is reasonably small (e.g., $|D| \lesssim 0.1$), all the four possible cross-correlations of the baseline can be expressed by (Roberts et al., 1994)

$$\begin{aligned}
R_1R_2 &= G_{R1}G^*_{R2} I \exp(-i(\phi_1-\phi_2)) \\
L_1L_2 &= G_{L1}G^*_{L2} I \exp(i(\phi_1-\phi_2)) \\
R_1L_2 &= G_{R1}G^*_{L2}\{P\exp(-i(\phi_1+\phi_2)) + I\,[D^*_{L2}\exp(-i(\phi_1-\phi_2)) + D_{R1}\exp(i(\phi_1-\phi_2))]\} \\
L_1R_2 &= G_{L1}G^*_{R2}\{P^*\exp(i(\phi_1+\phi_2)) + I\,[D^*_{R2}\exp(i(\phi_1-\phi_2)) + D_{L1}\exp(-i(\phi_1-\phi_2))]\}
\end{aligned} \tag{2.22}$$

where the subscripts 1 and 2 denote different antenna numbers, G is the complex receiver gain, I is the total intensity, P is the complex linear polarization intensity of the incident radiation, and the superscript * denotes the complex conjugate. Note that we have ignored second and higher order leakage terms (i.e., D^2, D^3, etc). In an ideal case (e.g., $|D| = 0$), the cross-hand terms contain only the linear polarization information. However, we can see that even a small D-terms can mimic the behaviour of an intrinsic linear polarization of a weakly polarized source if $|P| \sim |D| \times I$.

If $|G_R/G_L|$ does not vary a lot during an observing run, the D-terms can be best estimated by observing an unpolarized, point-like calibrator source. In such case, any polarization signature in the uncalibrated LR and RL visibilities can be associated with the polarization leakage effect. Therefore, the leakage modeling is straightforward (see Roberts et al. 1994). For relatively low angular resolution observations at long wavelengths (e.g., $\lambda \gtrsim 1\,\mathrm{cm}$), several well known calibrators are available for such purposes. However, most of the AGN sources are somehow resolved by much higher angular resolution for mm-VLBI observations. The calibrators also show larger intrinsic linear polarization at shorter wavelengths. Therefore, VLBI polarimetric calibration algorithms divide the total intensity and unknown polarization structure of the calibrator into several discrete components and solve the D-terms and the source polarization simultaneously by the least square minimization (Leppanen et al. 1995; see also VLBA Scientific Memo 30[10]). Also, solving the unknown polarization structure requires the calibrator source to be observed with a larger parallactic angle coverage (see Hales 2017).

Another issue in polarimetric VLBI observations arises from the fact that the absolute value of the phase offsets between the RCP and LCP receivers are poorly known. We note that the unknown R-L phase offset can be absorbed by the complex source polarization P (see Eq. 2.22). Therefore, the polarization angle of the main science target can be determined only when the instrumental R-L phase offset is known. We recall that large instrumental phase offset *between* different VLBI stations are already solved by the fringe fitting procedure. In this procedure, the interferometric phase of one particular station (i.e., reference antenna) is set to zero and all phases of all the other antennas are linked to the reference antenna. Therefore, one can estimate the instrumental R-L phase offset of the array by estimating the value *within* only the reference antenna. However, the absolute phase between the two receivers *within* the reference antenna is still unknown. It is worth noting that fringe-fitting or self-calibration deals with the two orthogonal polarizations independently. Thus, the R-L phase offset can be solved only by observing suitable sky calibrators or using other external information. A couple of suitable calibrators are known to have stable polarization angles at long wavelengths (e.g., $\lambda \gtrsim 1\,\mathrm{cm}$). Once they are observed, their apparent polarization angles can be compared with the known values to compute the R-L phase offset. In mm-wavelengths, however, the linear polarization of most of bright AGN is unstable in time (e.g., Agudo et al. 2018b). It is therefore essential to know the linear polarization of several bright sources close enough in time to the VLBI observations. This requires additional observational resources (e.g., observations by single dishes or connected interferometers whose calibrations can be performed independently using different methods).

---

[10] https://science.nrao.edu/facilities/vlba/publications/memos/sci/sci30memo.ps

Therefore, the success of polarimetric VLBI observations depends a lot on the careful choice of calibrators and on an adequate coverage of the parallactic angle during observations.

Chapter 3

Millimeter VLBI observations of the radio galaxy M 87

Parts of this chapter have been published in the following journal articles; Kim et al. 2016, 2018a,b. Credit : Kim et al., A&A, 610, L5, 2018 and Kim et al., A&A, 616, 188, 2018, reproduced with permission © ESO.

3.1 Introduction

Messier 87 (M 87, 1228+126, 3C 274, Virgo A) is a supergiant elliptical galaxy in the center of Virgo cluster. M 87 contains the first discovered extragalactic jet (Curtis 1918; see Fig. 3.1). The jet of M 87 has been extensively investigated by a number of pioneering studies for two obvious reasons. First, the distance to the source is only $d \sim 16.7$ Mpc (Bird et al., 2010). This yields a conversion from angular to linear scale of only 1 mas$\sim$ 0.081 pc. This is a very high spatial resolution in contrast to an object at the redshift $z = 1$ (1 mas$\sim$ 2.23 pc) [1]. Second, M 87 hosts a central supermassive black hole (SMBH) of extraordinary large mass $M_{\rm BH} \sim 6 \times 10^9 M_\odot$ (Gebhardt et al., 2011) [2]. The combination of the two makes the apparent angular size of one Schwarzschild radius of the system equivalent to $1 R_s \sim 7 \mu$as. This allows typical very-long-baseline interferometry (VLBI) observations to resolve a 1 mas-scale inner jet structure of M 87 at a spatial resolution of $\sim 140 R_s$ (c.f. 1 mas$\sim 2.3 \times 10^5 R_s$ or 0.6μas$\sim 140 R_s$ for $z = 1$ and $M_{\rm BH} = 10^8 M_\odot$). Typical global VLBI observations at 86 GHz can achieve an angular resolution of 50μas. Thus, millimeter VLBI imaging of the jet of M 87 allows us to study the base of the relativistic outflow at a spatial resolution of $\sim 7R_s$. In addition, the inner jet of M 87 can be resolved in the transverse direction (e.g., Walker et al. 2018). Therefore, M 87 is the best source to directly image an extragalactic jet at very high spatial resolution and constrain theoretical models of jet launching, collimation, and propagation.

---

[1] In this calculation we adopt a cosmology of $H_0 = 71$ km s^{-1} Mpc^{-1}, $\Omega_\Lambda = 0.73$, and $\Omega_M = 0.27$.

[2] We note that some studies suggest a factor two lower $M_{\rm BH}$ depending on the BH mass estimators (e.g., Walsh et al. 2013). In order to have a consistent black hole mass as the other recent studies, we adopt the larger $M_{\rm BH}$ in this study.

3.1.1 Previous studies and motivation

High resolution radio interferometric observations reveal a complex structure of the M 87 jet. On kpc-scale, the jet consists of several distinct, bright knots and smooth helical filaments. The jet is sharply collimated within a small jet opening angle of $\sim 7^\circ$ on kpc-scale, while the outflow becomes much broader and shows a larger opening angle of $\sim 60^\circ$ at $\lesssim 0.1$ pc from the core (see Junor et al. 1999 and references therein). Later studies analyzed the inner jet structure more systematically and confirm a similar structure but at greater detail (e.g., Asada & Nakamura 2012; Hada et al. 2013). The "core-shift" measurements of M 87 indicate that at 43 GHz the VLBI core is located at $\sim (15-25)R_s$ from the central BH (Hada et al., 2011), unlike the other blazars (see Marscher 2011; Boccardi et al. 2017). In this context, the expanding jet of M 87 can be understood as an active magnetohydrodynamic (MHD) collimation process near the BH (e.g., Komissarov et al. 2007).

Kinematic studies of the jet have revealed complex motions in the flow. Early VLBI observations suggested an apparent jet speed of $\approx 0.3c$ at $\sim$20 mas (projected ~ 1.7 pc) from the radio VLBI core (Reid et al., 1989). Other low cadence VLBI observations with $\gtrsim 2$ months interval also reported comparable speeds in the sub-pc scale jet (Ly et al., 2007; Kovalev et al., 2007). In contrast, the compact jet feature HST-1, which is located at ~ 800 mas from the VLBI core, shows superluminal motion with a typical speed of $\sim (4-6)c$ (Biretta et al., 1999; Cheung et al., 2007; Giroletti et al., 2012). The large discrepancy between the fast and the slow jet speeds remained problematic for several years. Later, Walker et al. (2008) performed a monitoring of the jet at higher cadence and reported a much faster apparent speed of $\sim 2c$ in the sub-pc scale jet. This suggested that the lack of fast motions was partly due to the slow cadence in the previous monitoring (e.g., a motion speed $1c$ corresponds to $\approx 4\,\mathrm{mas\,yr^{-1}}$ for M 87). This led to the M87 Very Long Baseline Array (VLBA) "movie" observations at 43 GHz, which revealed the detailed velocity field of the M 87 jet (Mertens et al., 2016; Walker et al., 2018). The jet showed significant acceleration from $\sim 0.5c$ to $\sim 2c$ in the sub-pc scale region and the co-existence of fast and other slower motion as well (see Fig. 3.2). The acceleration pattern appears to be in good agreement with the MHD jet acceleration scenario in which the magnetic field energy is gradually converted to the jet kinetic power and accelerates the bulk jet plasma (e.g., Komissarov et al. 2007; Lyubarsky 2009). Other monitoring observations performed in

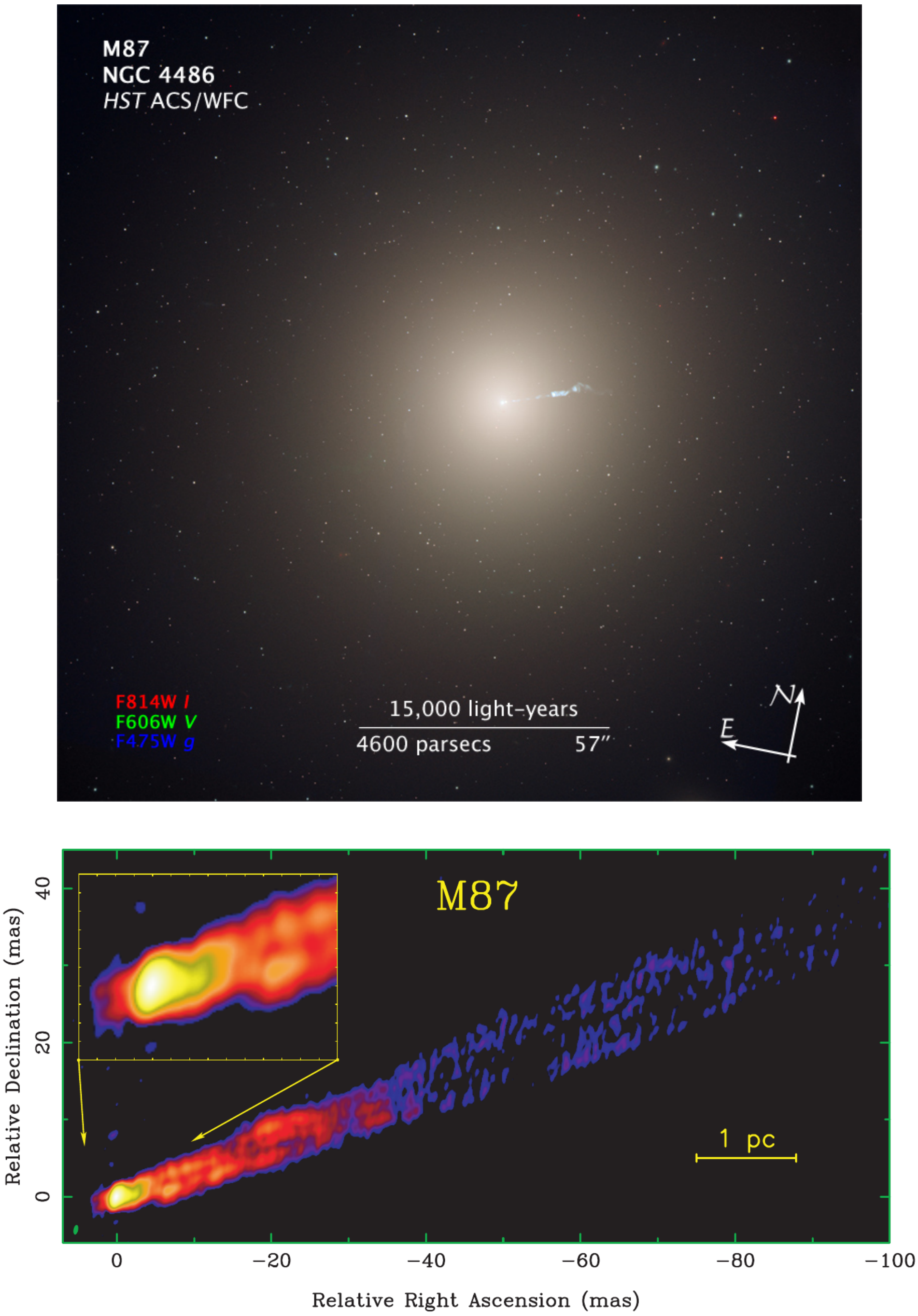
M87
NGC 4486
HST ACS/WFC
F814W I
F606W V
F475W g
15,000 light-years
4600 parsecs
57″
N
E
M87
1 pc
Relative Declination (mas)
0
20
40
Relative Right Ascension (mas)
0
−20
−40
−60
−80
−100

Fig. 3.1 **Top** : Hubble Space Telescope image of M 87. Note the bluish stray ray near the center of the galaxy. Figure courtesy of Hubble Heritage Team. **Bottom** : Very Long Baseline Array (VLBA) 15 GHz image of the inner M 87 jet. The inset shows the core region with an E-W angular (spatial) resolution of 0.6 mas ($86R_s$). Figure taken from Kovalev et al. (2007).

different observing epochs with independent arrays (e.g., KaVA) also confirm the superluminal motion in the inner M 87 jet (Hada et al., 2017).

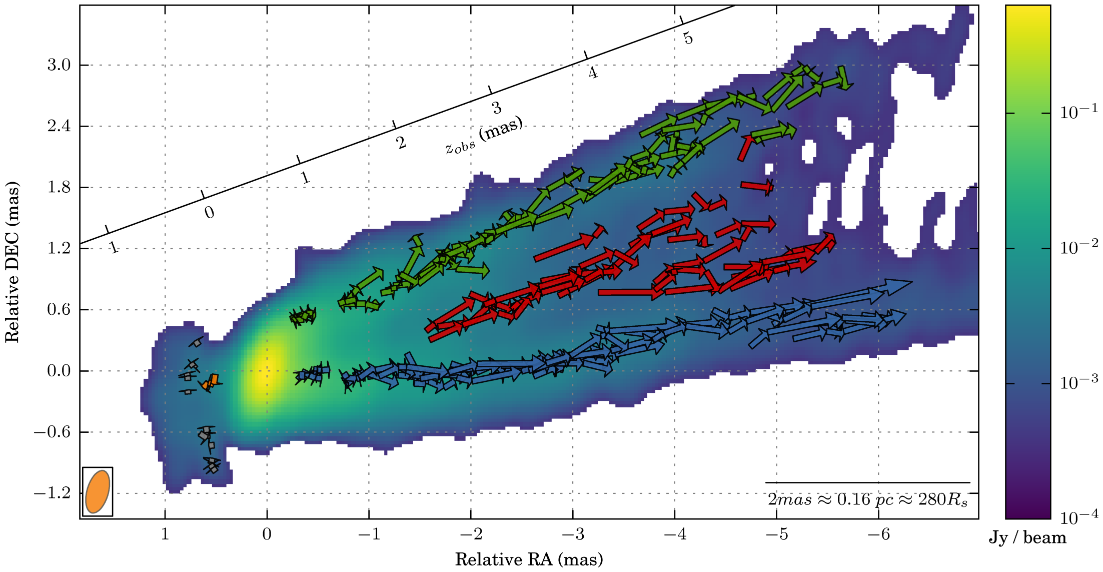

Fig. 3.2 Proper motions of bright components in the inner jet of M 87. The motions are shown by arrows, which are overplotted on a stacked VLBA 43 GHz image of the jet. The figure has been taken from Mertens et al. (2016).

In order to study a finer scale structure in the base of the jet of M 87, global VLBI observations were made at 230 GHz by the Event Horizon Telescope (EHT) array with three VLBI stations by Doeleman et al. (2012). They found the presence of a bright ($\sim$ 1 Jy), compact VLBI component whose size is $(5-6)R_s$. M 87 was observed by the EHT array again in 2013 but by including longer baselines. Krichbaum et al. (2014) model-fitted the visibility data and suggested the presence of a more compact component of $\lesssim 3.5R_s$ size. But these EHT observations were not able to map the detailed source structure because of the limited (u,v)-coverage.

In this regard, Global Millimeter VLBI Array (GMVA; e.g., Martí-Vidal et al. 2012; Krichbaum et al. 2014; see Fig. 3.3) observations at 86 GHz, with up to 14 stations, can resolve the jet of M 87 sufficiently close to the central engine at a spatial resolution of $7R_s$. GMVA also allows high dynamic range imaging of the jet because of larger number of the participating stations, the better array sensitivity at this frequency, and the brighter jet emission. Therefore, GMVA observations are crucial to bridge the gap between the 230 GHz EHT observations and lower resolution VLBI observations at frequencies of $\nu \lesssim 43$ GHz. The former aims at

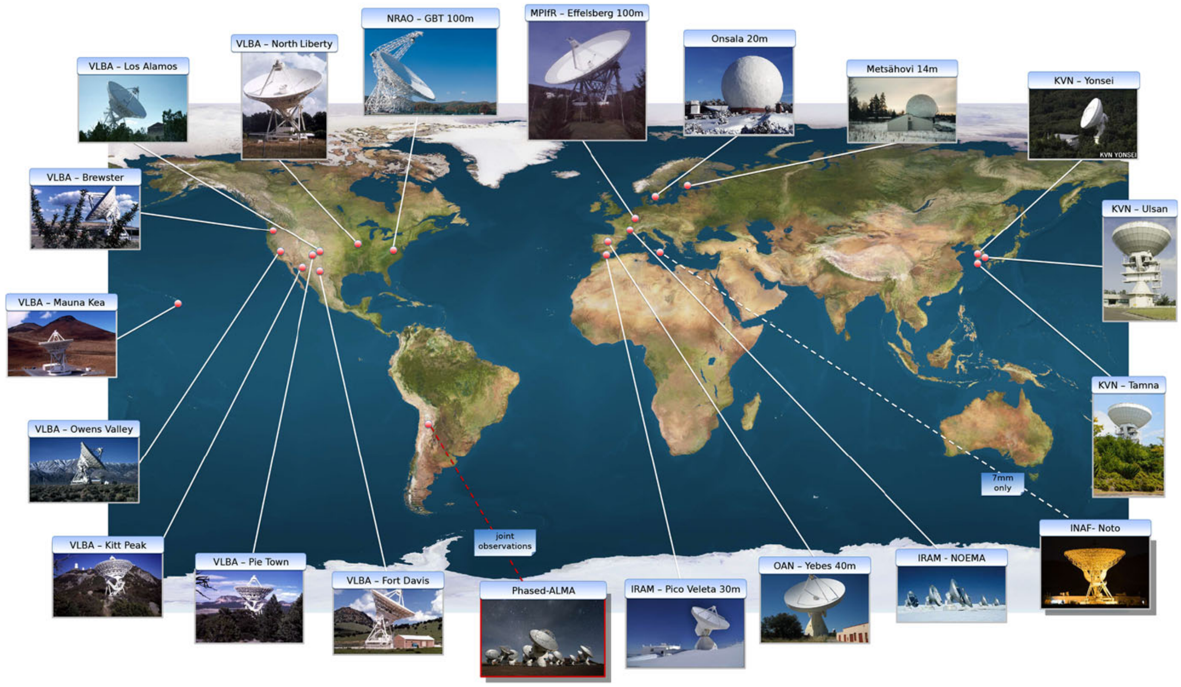
NRAO - GBT 100m
MPIfR - Effelsberg 100m
VLBA - North Liberty
Onsala 20m
VLBA - Los Alamos
Metsähovi 14m
KVN - Yonsei
KVN YONSEI
VLBA - Brewster
KVN - Ulsan
VLBA - Mauna Kea
KVN - Tamna
VLBA - Owens Valley
7mm only
joint observations
INAF- Noto
VLBA - Kitt Peak
VLBA - Pie Town
VLBA - Fort Davis
Phased-ALMA
IRAM - Pico Veleta 30m
OAN - Yebes 40m
IRAM - NOEMA

Fig. 3.3 The GMVA antennas observing at 86 GHz. The figure taken from Boccardi et al. (2017).

resolving the fundamental scale structure of the BH accretion system while the latter allows to study the evolution of the jet on larger scale.

Early GMVA observations of the jet of M 87 revealed a bright, compact core and the edge-brightened jet within $\lesssim$1 mas core distance (Krichbaum et al., 2006, 2014; Kim et al., 2016). Such a basic structure was independently confirmed by follow-up VLBI observations with the VLBA and the Green Bank Telescope (GBT) at 86 GHz (Hada et al., 2016). The authors were able to study the detailed structure and characteristics of the M 87 jet down to $\sim 14 R_s$ from the core. This is however a factor 2 lower angular resolution than the resolution achieved by the GMVA. Participation of sensitive millimeter VLBI telescopes in the GMVA, e.g., the IRAM 30 m telescope (PV), the phased Plateau de Bure interferometer (PdBI), and more recently the GBT, greatly enhance the (u,v) coverage and improve the image sensitivity, allowing high fidelity imaging of the active jet collimation region closer to the BH.

Constraining the physical conditions of the innermost jet of M 87 based on such GMVA observations is the main focus of this chapter. In §3.2, we present details of the previous and new GMVA observations of M 87, the data analysis, and discussions based on the new results. In §3.3, we also analyze other complementary VLBI data sets of M 87 obtained at different frequencies. We provide results from a long-term multi-frequency VLBI flux density monitoring of M 87 performed with the Korean VLBI Network (KVN) in §3.4. In §3.5, we provide a summary of our main conclusions.

3.2 GMVA 86 GHz observations of M 87

3.2.1 Observations and data reduction

M 87 has been often (but not regularly) observed by the GMVA since 2002 (Krichbaum et al., 2006, 2014; Kim et al., 2016). The observations were performed in full track (i.e., from horizon to horizon with $\sim$ 15 hrs of the total array operation time) in order to obtain deep images. Nearby suitable calibrators such as 3C 273 were observed with M 87 in alternating VLBI scans. We mainly focus on the data obtained since 2004 which allow a reliable imaging of the core-jet morphology. The GMVA data before 2009 were recorded at a bit rate of 512 Mbps in left circular polarization (LCP) only (i.e., corresponding to a bandwidth of 128 MHz per polarization with 2 bit digitization). Another observation was performed in 2015 with a higher bit rate of 2 Gbps and the data were recorded in dual circular polarization (LCP and RCP). This setup provided a wider bandwidth of 256 MHz per polarization. We also included another archival 86 GHz data set from the VLBA+GBT observations performed in 2014 (Hada et al., 2016) in order to improve the time baseline of our data sets.

The GMVA data obtained before 2009 were correlated with the Mark IV VLBI hardware correlator at the Max-Planck-Institut für Radioastronomie (MPIfR). The GMVA data obtained in 2015 were correlated by the DiFX software correlator (Deller et al., 2011) at the MPIfR. After the data correlation, further post processing was performed using standard calibration tasks implemented in the Astronomical Image Processing System (AIPS; Greisen 1990). The parallactic angle correction, the bandpass calibration, the manual and global fringe-fitting, and the amplitude a-priori calibration were performed using the relevant AIPS procedures. For the fringe fitting, we first estimated and corrected large sub-band delays and phase offsets between the intermediate frequencies (IFs) by using the scan-averaged power spectra of high signal-to-noise (S/N) scans on bright sources (i.e., manual phase calibration). After removing the large delays and inter-IF phase offsets, we performed a global fringe fitting (e.g., Cotton 1995) for all the scans in order to estimate and remove the effects of the multi-band delays and the fringe rates. In this procedure, we derived the solutions by integrating the data over the full bandwidth (i.e., APARM(5)=1 in the AIPS task FRING) in order to improve the detection rates. We adopted the S/N threshold of 5. The a-priori amplitude calibration was performed based on the system temperature ($T_{\rm sys}$) measurements and the elevation-dependent antenna gain curves provided by each observatory. Atmospheric opacities and receiver temperatures were estimated through the AIPS task APCAL by fitting the lower envelope of T_{sys} versus the airmass. The opacity corrections have been applied using the resulting solutions. The cross-hand delay effect was corrected by the AIPS task RLDLY by choosing proper scans with strong cross-hand power spectra.

After the a-priori calibration, the visibility data were averaged in frequency in order to increase the S/N. Then the data were exported outside AIPS and loaded into the DIFMAP package (Shepherd et al., 1994). The data were further averaged in time for 10 seconds coherently. With such a short time averaging, we estimate that the amplitude loss due to the decoherence is sufficiently small (e.g., $\lesssim 10\%$). We also identified systematically erroneous measurements which could be associated with failures in the antenna pointing and focusing at 86 GHz. We inspected the visibility amplitudes and phases versus time for each baseline and such VLBI scans were flagged in the antenna-based manner. After rigorous flagging, we used the CLEAN algorithm (Högbom, 1974) implemented in the DIFMAP software. CLEAN and phase-only self-calibrations were performed iteratively until the model flux reached the amplitudes of the baselines on short (u,v) distances. Then we started to allow the self-calibration to change the amplitude as well. In order to avoid developing artificial features in the image, we took the whole observing time as the solution interval for the initial amplitude self-calibration and gradually reduced the time interval down to a minute timescale in the subsequent CLEANing and self-calibrations. This scheme was performed until we reached a minimum image noise level in the image. The final image quality was evaluated by calculating the image noise level with those expected from theoretical calculations. The image root-mean-square (rms) noise level was measured by using the AIPS task IMEAN, which fits a Gaussian to the histogram of the pixel values of a CLEAN image. Because of the limited accuracy in the a-priori amplitude calibration, VLBI observations at high frequencies are often subject to systematic amplitude errors in addition to the thermal noises. We examined the station gain corrections made by the amplitude self-calibrations and estimated the systematic flux density error to be $\sim 15\%$ for the data sets presented in this work.

We provide a summary of the GMVA data and the corresponding images in Table 3.1.

3.2.2 Results and analysis

Interferometric visibilities

We show an example of the (u,v) coverage of a GMVA data set in Fig. **??**. Fringes are detected up to maximum (u,v) distances of $\sim 3G\lambda$ thanks to the participation of the sensitive mm-VLBI telescopes. In Fig. 3.5 we plot the radial dependence of the visibility amplitude. The visibility

Table 3.1 Summary of the GMVA 86 GHz observations of M 87. Station abbreviations are as follows: EB–Effelsberg, ON–Onsala, PV–the IRAM 30m Telescope at Pico Veleta, PB–the phased Plateau de Bure interferometer (number of the phased antennas in brackets), GBT–the 100m Green Bank Telescope, and VLBA–8 VLBA stations equipped with 3mm receiver (without Hancock and Saint Croix). The synthetic beam sizes are for natural weighting; angle denotes the position angle of the major axis. Columns denote: (1) observing date; (2) participating stations; (3) beam sizes : major axis, minor axis (in μas) and position angle (in deg); (4) receiver polarization (L=LCP; R=RCP); (5) total bandwidth; (6,7) peak and rms noise level in the resulting images.

Date (yyyy/mm/dd) (1)	Stations (2)	Beam ($b_{\rm min} \times b_{\rm maj}$, $b_{\rm PA}$) (3)	Pol (4)	$\Delta\nu$ (MHz) (5)	Peak (mJy/beam) (6)	RMS (mJy/beam) (7)
2004/04/19	EB, ON, PV, VLBA[a]	71×267, -9.14	L	128	411	0.26
2005/10/15	EB, ON, PV, VLBA	61×214, -5.04	L	128	408	0.27
2009/05/09–10 [b]	EB, ON, PB(6), VLBA	72×272, -10.3	L	128	758	0.24
2014/02/26	GBT, VLBA	116×307, -9.0	L&R	512	496	0.14
2015/05/16	EB, ON, PV, PB(5), GBT, VLBA	59×273, -6.88	L&R	512 [c]	351	0.16

Notes. (a) Brewster was not available; (b) Observations in 2009 were conducted over two consecutive days; (c) PB observed with a reduced bandwidth of 256 MHz (1 Gbps recording rate).

amplitude is ~ 1 Jy for the innermost (u,v) spacings and decreases down to $\sim 50-100$ mJy at the longest baselines.

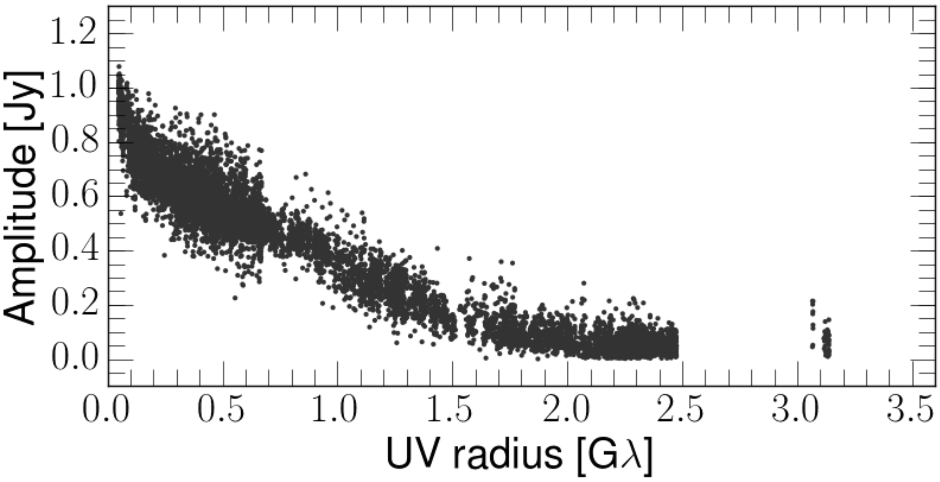

Fig. 3.5 Radial dependence of the visibility amplitude of the 2015 data after the last round of CLEAN and self-calibrations. The data were further averaged in time for 30 sec for a better display.

Final images

We show the GMVA images of M 87 in Fig. 3.6. The images reveal the basic structure of the source such as the bright core and a highly edge-brightened jet, which is similar in all epochs. Besides the bright approaching jet (extending from the core to west), some faint emission features are also present in the east of the VLBI core. Different phase and amplitude self-calibrations during the imaging could not completely remove the faint emission feature. Without CLEANing this feature, the image noise levels were also higher than the minimum values that we achieved (Table 3.1). Therefore, we consider that this feature is real. This feature is most likely related to the counter-jet of M 87 that has been seen at longer wavelengths (Kovalev et al., 2007; Walker et al., 2018). Fine-scale structures such as the brightness and positions of compact knots in the approaching jet also change with time. It is tempting to identify them as slowly moving jet components. However, we note that our time sampling is quite sparse (gaps of at least one year). The inner jet of M 87 is known to have a rather fast speed (e.g., $\sim 2c \sim 8\,\mathrm{mas\,yr^{-1}}$; Walker et al. 2018) and such a high speed could lead to a wrong component identification in our time-series images. Therefore, we do not attempt to cross-identify the bright components across the different epochs. On the other hand, the GMVA observation in 2009 was performed over two consecutive days. Two different images from the different days did not show any significant difference. Therefore, the two visibility data sets were combined into a single one and we used the resulting data set for a higher sensitivity imaging of the source (Fig. 3.6c).

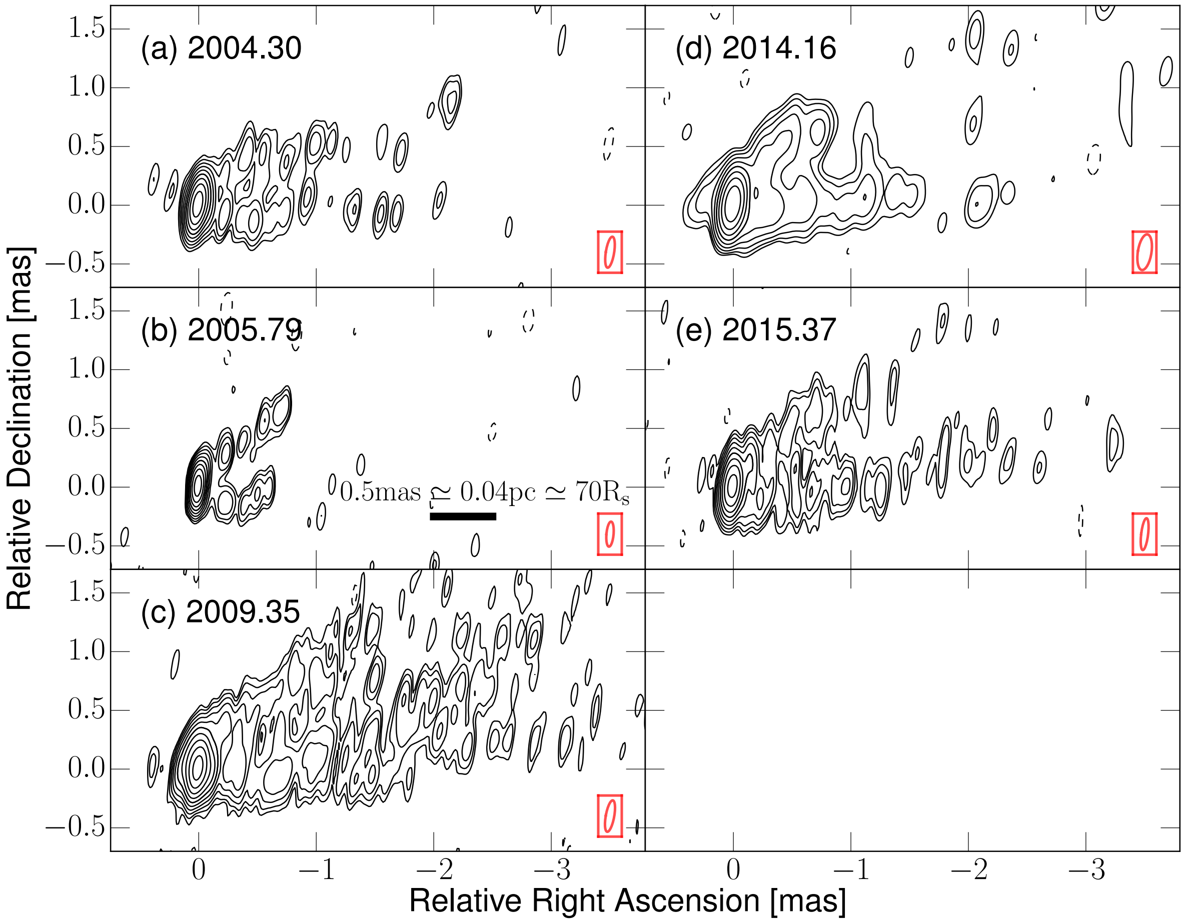

Fig. 3.6 GMVA 86 GHz images of the jet of M 87. Decimal numbers in each panel denote the observing epoch in decimal year format. Red ellipses surrounded by red boxes show the observing beams. The solid thick black bar and the text annotation in panel (b) show the angular to linear scale.

VLBI core

The VLBI core is defined as the most compact and brightest feature located at the upstream end of the approaching flow (thus having the highest brightness temperature; see, e.g., Hodgson et al. 2017). We fitted elliptical Gaussian models to the interferometric visibilities using the DIFMAP task MODELFIT in order to characterize the properties of the core. The task estimates the core flux density $S_{\rm core}$, the FWHM size $\psi_{\rm maj,min}$ along the major and minor axes of the elliptical Gaussian, and the position angle of the major axis $PA_{\rm core}$. The uncertainties of these parameters were estimated following Schinzel et al. (2012), who estimated errors of the model parameters based on the finite signal-to-noise, accounting for strong side-lobe interferences around the bright core. The ratios of the peak and the image rms values near the core were $\gtrsim 71$ in all

Table 3.2 Properties of the VLBI core estimated by elliptical Gaussian model fitting. The column shows (1) the observing epoch (in year/month/day); (2) the core flux (in Jy); (3) and (4) the FWHM core size along the minor and major axis (in μas); (5) and (6) the geometrical mean of the core size (in μas and R_s, respectively); (7) the position angle of the elliptical core (in deg) and (8) the Doppler-boosted apparent brightness temperature (in 10^{10} K).

Epoch	$S_{\rm core}$	$\psi_{\rm min}$	$\psi_{\rm maj}$	$\sqrt{\psi_{\rm maj}\times\psi_{\rm min}}$		PA$_{\rm core}$	$T_{\rm B}\times\delta$
(yyyy/mm/dd)	(Jy)	(μas)	(μas)	(μas)	(R_s)	(deg, N→E)	($\times10^{10}K$)
(1)	(2)	(3)	(4)	(5)	(6)	(7)	(8)
2004/04/19	0.58±0.09	60±12	63±13	62±9	8.7±1.2	29.4	2.5±0.8
2005/10/15	0.53±0.08	38±8	88±18	58±8	8.1±1.1	−11.0	2.6±0.8
2009/05/09	1.39±0.20	75±15	127±30	102±15	13.7±1.9	15.6	2.4±0.8
2014/02/26	0.60±0.09	75±15	80±16	77±11	10.8±1.5	18.6	1.7±0.5
2015/05/16	0.67±0.10	87±18	91±18	89±12	12.5±1.8	48.0	1.4±0.5

epochs. Based on this, we estimated that the uncertainties of the flux density and core size were $\sim 15\%$ and $\sim 20\%$, respectively.

We show the corresponding model-fit parameters in Table 3.2. In all epochs, the FWHM size of the core is $\gtrsim 64\%$ and $\gtrsim 23\%$ of the beam sizes along the minor and major axes, respectively. This size is larger than $1/5$ of the beam, which is widely adopted as an empirical resolution limit of a VLBI array (e.g., Lister & Homan 2005; Jorstad et al. 2017). By taking the signal-to-noise of ~ 70, VLBI components whose FWHM sizes are larger than $\sim 10\%$ of the beam are considered to be spatially resolved (Lobanov 2005; Schinzel et al. 2012; see also Baczko et al. 2016 and references therein). Therefore, we conclude that the core is spatially resolved. The core flux density is in the range of $\sim (0.53-0.67)$ Jy except 2009 when a significantly higher core flux density was measured. We checked the flux density of the calibrator 3C 273 observed in the same observation to examine the calibration errors. By comparing the VLBI flux density of 3C 273 in this epoch with other multi-frequency VLBI and single-dish flux measurements available from the literature (e.g., Chidiac et al. 2016; Jorstad et al. 2017; Lisakov et al. 2017), we could not find signatures of significant amplitude calibration errors. Thus, we infer that the core flux density of M 87 was intrinsically higher in this epoch (see Table 3.2).

Image stacking

As explained above, the sparse time sampling does not allow a robust time-series analysis of motions in the jet. Therefore, we focus on the overall shape and the intensity gradient along and across the jet. Such properties can be reliably studied by time-averaging the variable emission in the jet and increasing the image sensitivity. Hence, we adopt the image stacking technique that has been applied to other AGN jets by other studies (e.g., Fromm et al. 2013; MacDonald et al. 2015; Boccardi et al. 2016a; Pushkarev et al. 2017).

The image stacking was performed as follows. The individual images in Fig. 3.6 were restored with a common restoring beam and aligned by the peaks of their intensities. We adopted two different restoring beams; (i) a rather large beam of 0.1×0.3 mas with the beam position angle 0° (i.e., more elongated in N-S) and (ii) a smaller beam of 0.051×0.123 mas with the same position angle. The former corresponds to the largest beam in Fig. 3.6 and the latter corresponds to 50% of super-resolution in the N-S direction for a typical GMVA beam. By using the intensity peak as the reference position, we also assume that the intensity peak is the dynamical center of the twin-jet system. This is supported by several observational results suggesting that the intensity peak is very close to the central engine location (e.g., Kovalev et al. 2007; Hada et al. 2011). It is also important to note that astrometric VLBI monitoring of the jet of M 87 detected no significant spatial displacement of the peak from its original position even during the phase of the strong radio flare in the core (less than $6R_s$; Acciari et al. 2010).

In Fig. 3.7 we show the results of the image stacking (panel (a) and (b) for the larger and smaller restoring beam, respectively). The rms image noise levels in both images are ~ 0.1 mJy/beam. To our best knowledge, this is the deepest and highest resolution view of the inner jet of M 87 to date.

Transverse emission profile and central emission features

We measure the intensity profiles transverse to the jet in the image plane at different core separations d. By cutting the jet transversely at $d \sim 0.6$ mas and ~ 0.8 mas, we show two example slice profiles in Fig. 3.7c. The emission profile clearly shows two peaks in the outer edges of the jet. We also note that there is another hump between the two prominent edges. The central hump is brighter than the 5σ image noise level. We also obtained another transverse emission profile by averaging many transverse slices made from ~ 0.5 to ~ 1 mas core distances (Fig. 3.8). By this, the presence of the central hump becomes more clear. We measured the spatially integrated flux densities of the bright edges and the central lane of the jet in the image plane in the range of $\sim (0.5-1.0)$ mas core distances. We found ~ 38 mJy and ~ 15 mJy of spatially integrated flux densities for each limb and the central lane, respectively. This results in the center-to-limb brightness ratio $\rho_{\rm CL} \sim 0.4 \pm 0.1$. In the error calculation, the flux density uncertainties of the limb and the center were assumed to be 15% and 30%, respectively.

Ridge line analysis

We measured the jet diameter as a function of the core separation. We took the high-resolution image in Fig. 3.7b and rotated it by 21° clockwise assuming that the overall jet position angle is −69° with respect to north. The jet diameter $W(d)$ at each core separation d was measured by

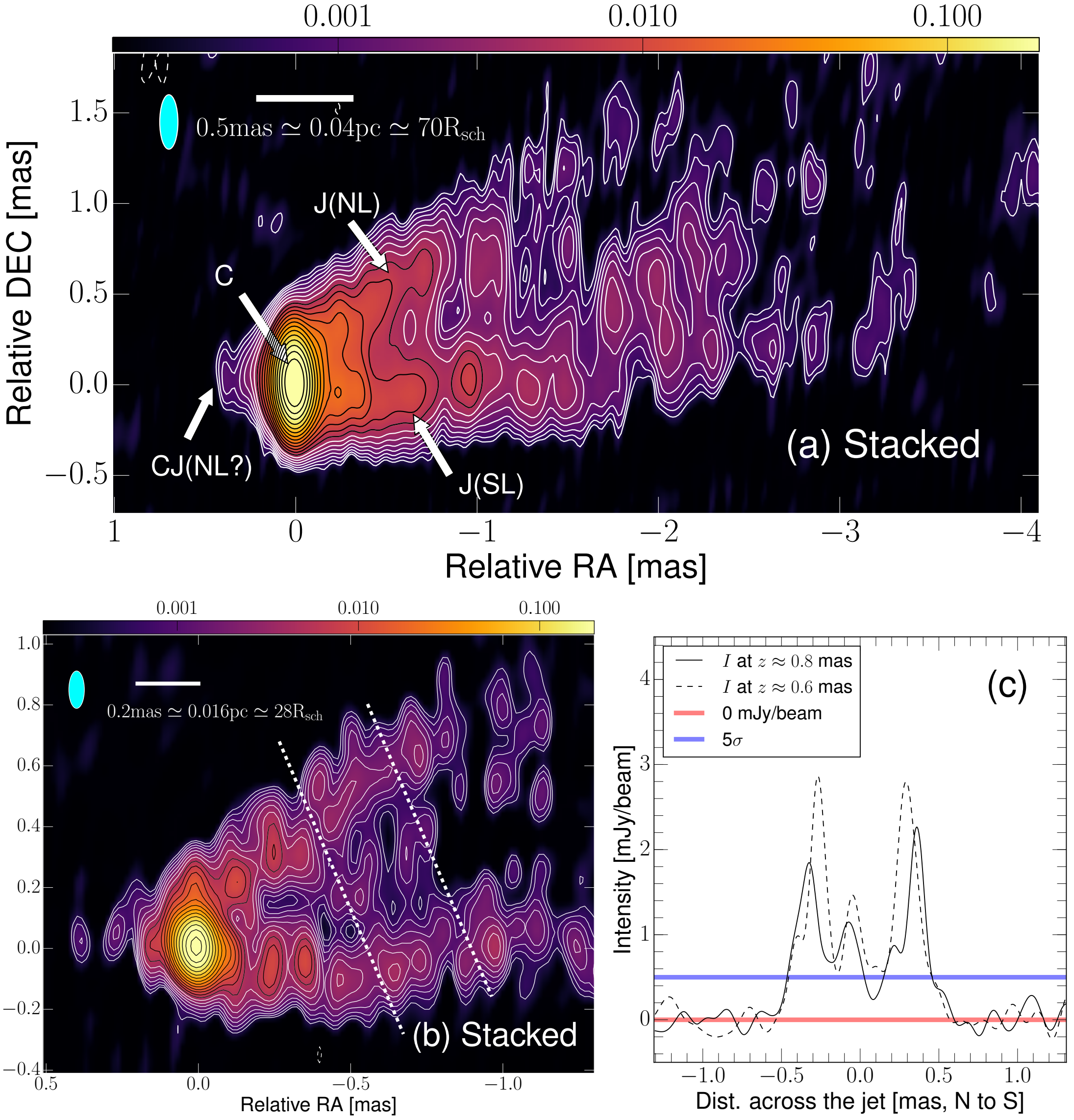

Fig. 3.7 Stacked M 87 jet images and transverse intensity profiles. **Panel (a)**: The image with a restoring beam of 0.3 × 0.1 mas. The core (C), northern/southern limbs (NL/SL) of the jet (J), and the counter jet (CJ) are indicated by white arrows. **Panel (b)**: The same image but restored with a smaller beam of 0.123 × 0.051 mas and zoomed in on the inner region. The colorbars indicate total intensities in units of Jy/beam. Contour levels are $(-1, 1, 1.4, 2, 2.8, ...) \times 0.47$ mJy/beam. The white horizontal bars indicate the projected linear distance scales for M 87. The white dashed lines denote the position of transverse slices through the jet in panel (c). The restoring beams are indicated by the cyan ellipses at the top left corner of each panel. **Panel (c)**: The transverse jet intensity profiles measured by using the higher resolution image in Fig. 3.7b (starting from north to south). The dark solid/broken lines are the measured intensity at $\sim 0.8/0.6$ mas core distance, respectively. The red line is the zero intensity level and the blue line indicates the 5σ noise level.

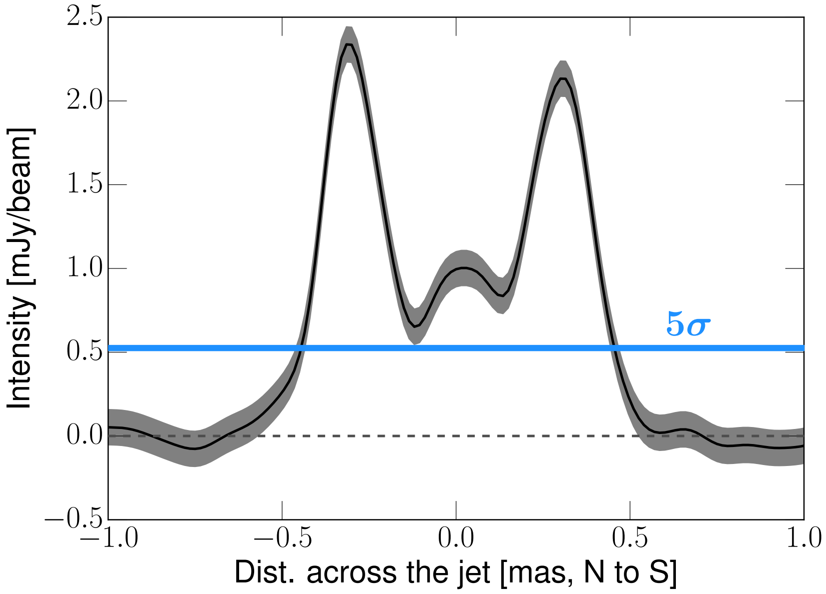

Fig. 3.8 Transverse jet intensity profile obtained by averaging the jet emission over $\sim 0.5-0.9$ mas core distance. The dark solid line is the measured intensity, the shaded region indicates 1σ image rms noise level, and the blue line denotes the corresponding 5σ level.

the separation of the peaks at the edges of the jet. The peak positions were obtained by fitting two Gaussians to the transverse emission profile. We often had to fit another Gaussian in the center in order to improve the fitting accuracy. We started the fitting procedure at $d \sim 1$ mas from the core and continued the measurements down to $d \sim 0.06$ mas, which is one GMVA beam size in the E-W direction. This size is larger than the half of the core FWHM size in the same direction in all epochs ($\lesssim 0.05$ mas). Statistical errors from the Gaussian fitting are often small and we could underestimate the uncertainties of the peak positions. Therefore, we followed Mertens et al. (2016), who took account for different signal-to-noise ratios in different regions of the jet and defined more realistic uncertainties. Similarly, the apparent jet opening angle $\phi_{\text{app}}(d)$ was calculated by computing the angle subtended by the two peaks.

The corresponding jet width profile $W(d)$ is shown in Fig. 3.9. The jet diameter clearly increases with the core distance. At smaller core separations $d \lesssim 0.2$ mas (or equivalently $\lesssim 24R_s$ projected), the jet diameter decreases rather slowly with decreasing d. In the immediate vicinity of the core ($d \leq 0.06$ mas), we find $W(d) = 0.29 \pm 0.09$ mas ($40.8 \pm 12.3R_s$) and a large apparent opening angle $\phi_{\text{app}} = 127^\circ \pm 22^\circ$. If we assume an axially symmetrical jet, the intrinsic opening angle is given by $\phi_{\text{int}} = 2\arctan(\sin\theta \times \tan(\phi_{\text{app}}/2))$ radian where θ is the jet viewing angle (Pushkarev et al., 2017). Using this relationship, we obtain the intrinsic opening angle $\phi_{\text{int}} = 64^\circ \pm 25^\circ$ ($90^\circ \pm 28^\circ$) for the jet viewing angle of $\theta = 18^\circ$ (30°).

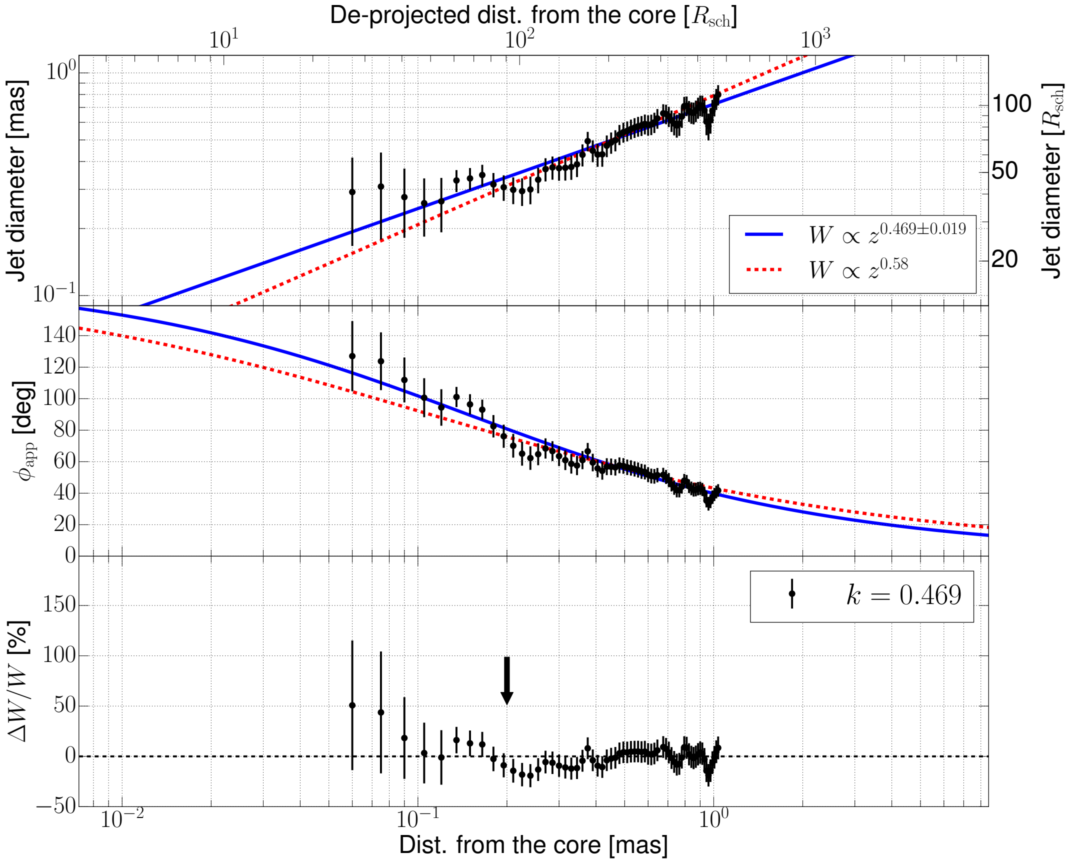

Fig. 3.9 The M 87 jet base collimation profile plotted versus the core separation d. We assume a jet viewing angle of $\theta = 18°$ to calculate the de-projected distances in the top side. **Top** : the jet width and the power-law fit. The black data points are the measurements, the blue solid line is the best power-law fit to the data, and the red broken line is a fit with a fixed slope of $k = 0.58$. **Middle** : the same but for the apparent opening angle. **Bottom** : the fractional difference between the observed diameter and the power-law model with a corresponding slope, $k \approx 0.47$. The arrow marks the core distance from where the fractional difference starts to grow significantly.

The asymptotic structure of the jet can be characterized by using a model $W(z) \propto z^k$ where z is the distance from the central engine and k is a dimensionless parameter that parameterizes the jet expansion and acceleration properties (e.g., Komissarov et al. 2007; Lyubarsky 2009). We note that z is not necessarily the same as d because the intensity peak may be slightly offset from the central engine due to the jet opacity effects (i.e., the core-shift; see Lobanov 1998). Hence, we express $z = d + \varepsilon$ where ε is an unknown separation between the BH and the 86 GHz core (see Fig. 3.10). In this study, we assume $\varepsilon \leq 41\,\mu$as based on the astrometric VLBA observations of Hada et al. (2011), who suggest that the BH of M 87 is located $\sim 41\,\mu$as

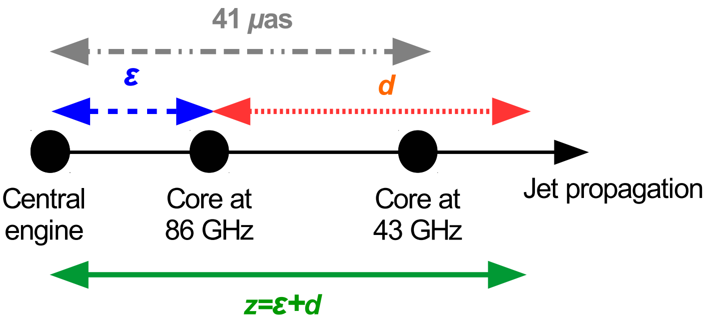

Fig. 3.10 Illustration of the central engine and the 86 GHz core geometry.

east of the intensity peak at 43 GHz. Using this relation, we obtained the jet width W as function of z and performed the power-law fitting for the possible range of ε.

We obtain a power-law index $k = 0.469 \pm 0.019$ when the core-shift is ignored (i.e., $\varepsilon = 0$). Accounting for the core-shift ($\varepsilon \neq 0$), we find k in the range of $\sim 0.47 - 0.51$ with a mean value of $k = 0.498 \pm 0.025$. The error represents uncertainties in both the fitting and the core position. Both fits lead to reduced chi-square values of $\chi_{\rm red} \sim 0.51$. Because of the uncertain absolute position of the 86 GHz core, we take the latter k value for the further analysis. Our value of $k \sim 0.5$ appears to be in agreement with $k = 0.56 - 0.60$ reported by previous studies of larger scale jet structure within a three sigma error (Asada & Nakamura, 2012; Hada et al., 2013; Mertens et al., 2016). In order to more quantitatively illustrate the goodness of the power-law fit, we show in the bottom panel of Fig. 3.9 the fractional difference between the data and the model defined as $\Delta W/W \equiv (W_{\rm obs}/W_{\rm model} - 1)$ where the subscripts indicate the observed and power-law model jet width, respectively. The fractional difference is nearly zero between $d \sim 0.2 - 1.0$ mas, but the difference is somewhat larger at $d \leq 0.2$ mas.

The jet to counter-jet ratio

We measured the time-averaged jet and counter-jet flux densities by spatially integrating the intensities in the image plane at the core separation $d = 0.2 - 0.5$ mas (corresponding to the projected distance of $\sim (28 - 140) R_s$). We used the image with the large convolving beam (i.e., Fig. 3.7a) in order to recover more flux densities from the smooth and extended intensity distribution. On the approaching jet side, we placed a large window covering the two limbs and the central emission feature. Another window of the same size was placed in the counter-jet side. The spatially integrated flux density of the jet and the counter-jet are ~ 95 mJy and ~ 3.5 mJy, respectively. The corresponding jet to counter-jet ratio is $R = 27.1 \pm 9.1$ assuming 15% and 30% of flux density uncertainties for the jet and counter-jet, respectively. It is worth noting that other studies provide some evidence for limb-brightening in the counter-jet (Kovalev et al., 2007; Walker et al., 2018). Such limb-brightening is not clearly seen Fig. 3.7. This is most likely due to the limited imaging sensitivity at the high frequency. Therefore, we reduced the size of the windows such that they cover only the southern limb of the approaching jet and the visible emission of the counter-jet in Fig. 3.7a only. By doing so, we assume that the visible counter-jet emission is associated with the northern edge of the counter-jet (e.g., see Fig. 23 of Walker et al. 2018). This lowers the integrated jet flux density to ~ 60 mJy and results in a lower jet-to-counter jet ratio of $R = 17 \pm 6$.

We also made an attempt to measure the jet to counter-jet ratio in the longitudinal direction by using the pixel values in the image. We cut the counter-jet, the core, and the souther-limb of the approaching jet based on the aforementioned assumption. We used the same jet image in Fig. 3.7a. Because of the faint counter-jet, we clipped out pixels whose intensities were below the 7σ image noise level (0.77 mJy/beam). We also excluded pixels within 0.1 mas from the intensity peak because of the contamination by the core. While this clipping prevents inclusion of unreliable pixel values, we note that the uncertain absolute position of the central engine may cause a systematic bias in the calculation of R and associated physical quantities[3]. Therefore, we made use of the ε parameter in the same manner as before. Specifically, we define the distances along the jet and counter-jet as $z_{\rm jet} = d_{\rm jet} + \varepsilon$ and $z_{\rm cj} = d_{\rm cj} - \varepsilon$, respectively. We note that $d_{\rm cj}$ and $d_{\rm jet}$ are not necessarily the same. Then, we calculate $R(z) = I_{\rm jet}(z)/I_{\rm cj}(z)$ where $I_{\rm jet,cj}(z)$ is the jet and counter-jet intensities as function of $z = z_{\rm jet} = z_{\rm cj}$. This calculation was repeated for a range of ε and we took the average and dispersion of the $R(z)$ profiles (i.e., the standard deviation) in order to define a specific jet to counter-jet ratio value and its uncertainty at each z. The result is shown in Fig. 3.11. The R value within $z \lesssim 0.2$ mas is about 5 but is somewhat uncertain due to the unknown core position ε. However, the result suggests that a single value of R is not suitable to describe the increasing R with the distance ($R \sim 1-10$ near 0.1 mas and increases up to $10-25$ at larger distances).

3.2.3 Discussions

Physical conditions in the VLBI core region

Our accurate measurements of the size and flux density of the core allow to study the energetics within the compact plasma, i.e., the energy density ratio between non-thermal particles and magnetic fields. The VLBI core brightness temperature is a useful parameter to characterize the physical conditions (e.g., Kovalev et al. 2005; Lee et al. 2016). The intrinsic brightness temperature, $T_{\rm B}$, of the partially resolved VLBI core can be calculated by (e.g., Lee et al. 2016)

---

[3] By definition, R should be measured at the same distance from the BH for a bipolar flow.

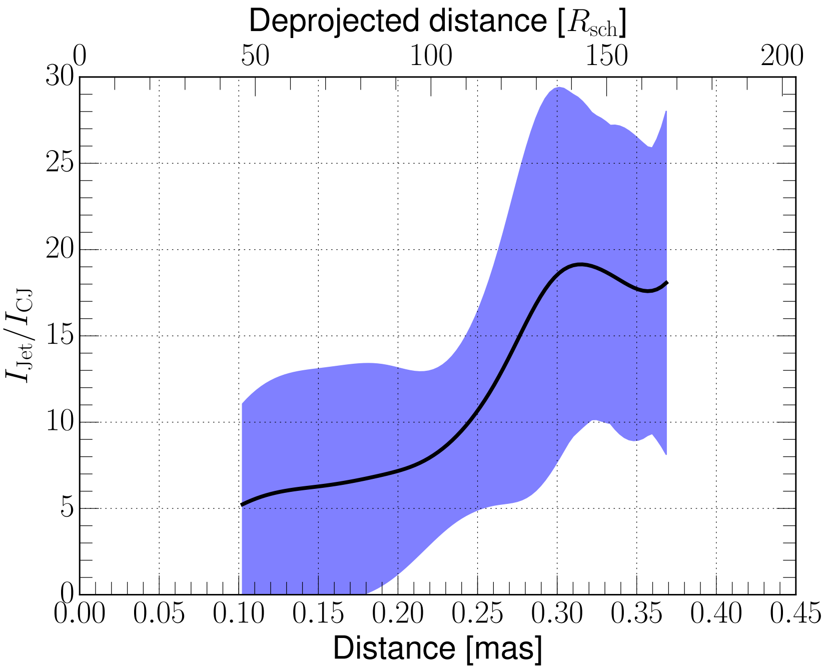

Fig. 3.11 Gradient of the jet to counter-jet intensity ratio (R) measured as described in the text. The solid black line indicates the measured value and the shaded region indicates the error. A viewing angle of $\theta = 18°$ was used to calculate the deprojected distances in the top side.

$$T_\mathrm{B} = 1.22 \times 10^{12} \frac{S_\mathrm{core}}{\nu^2 \psi_\mathrm{maj} \psi_\mathrm{min}} \frac{(1+z)}{\delta} \; K \tag{3.1}$$

where ν is the observing frequency in GHz, S_core is the core flux density in Jy, ψ_maj and ψ_min are the FWHM sizes in mas, $z = 0.00436$ is the redshift of M 87 (Smith et al., 2000), and δ is the Doppler factor. The observed apparent brightness temperature is related to the intrinsic temperature by $T_\mathrm{B,app} = T_\mathrm{B} \times \delta$. We show the $T_\mathrm{B,app}$ values in Table 3.1. We find that the apparent brightness temperature is generally quite low in all epochs ($\lesssim 3 \times 10^{10}$ K). The temperature is even lower than $T_\mathrm{eq} \sim 5 \times 10^{10}$ K, a characteristic brightness temperature of a plasma in which the energy densities of particles and magnetic fields are comparable (i.e., the "equipartition brightness temperature"; Readhead 1994).

In order to make a more quantitative comparison with the equipartition brightness temperature, we calculate the specific value of $T_\mathrm{B,eq}$ for the core of M 87. First, we rewrite Eq. 3 of Singal (2009) by setting the energy densities for particles u_p and magnetic field u_B the same. In this way, the $T_\mathrm{B,eq}$ in the observer's rest frame can be expressed as

$$T_\mathrm{B,eq} = t(\alpha) 10^{11} \left[\left(\frac{s}{\mathrm{pc}} \right) \left(\frac{\nu_\mathrm{turn}}{\mathrm{GHz}} \right) \right]^{1/8} \times \delta \quad \mathrm{K} \tag{3.2}$$

where α is the spectral index ($S \propto \nu^{+\alpha}$; we note that our sign convention is different from Singal 2009), $t(\alpha)$ is a function of α whose numerical values are tabulated in Singal (2009) ($t(\alpha) \sim 0.3-0.7$ for α in the range of -0.3 to -1.5), s is the linear size of the emitting region, and $\nu_{\rm turn}$ is the synchrotron turn-over frequency. In the source frame, $T_{\rm B,eq}$ is lower by a factor δ (e.g., Readhead 1994). For the source size, we adopt $s = \sqrt{\psi_{\rm maj}\psi_{\rm min}} \times 0.08\,{\rm pc\,mas}^{-1}$, which is the mean FWHM size of the core[4]. The exact values of $\nu_{\rm turn}$ and α are poorly determined due to lack of direct multi-frequency observations on scales of $\lesssim 11 R_s$. Nevertheless, the time-averaged core flux densities at 86 GHz (~ 0.5 Jy; this work) and 230 GHz (~ 1.0 Jy; Doeleman et al. 2012; Akiyama et al. 2015) suggest an inverted synchrotron spectrum between 86 GHz and 230 GHz. The VLBI core flux density measurements at 129 GHz by the Korean VLBI Network also supports this (see Kim et al. 2018a and §3.4 of this work). Broadband SED modeling of the core of M 87 by Broderick & Loeb (2009) also suggest a turn-over frequency $\nu_{\rm turn} \sim 230$ GHz and a steep spectral index $\alpha = -1.0$ for the core of M 87. Thus, we adopt these numbers in computing Eq. 3.2. We also remark that the $T_{\rm B,eq}$ value depends weakly on the exact value of $\nu_{\rm turn}$ and α because of the 1/8 power dependence. The Doppler factor is given by $\delta = 1/\Gamma(1-\beta\cos\theta)$ where Γ is the bulk Lorentz factor of the underlying jet flow and β is the corresponding intrinsic speed normalized by the speed of light. So far, no direct jet speed measurements are available on $\lesssim 11 R_s$ scales. Therefore, we assume an apparent jet speed of $\sim 0.5c$, which was obtained at larger core separations ~ 0.5 mas (Mertens et al., 2016). We also adopt a viewing angle of $\theta = 18°$, which yields $\delta \sim 2$. Using these parameters, we compute Eq. 3.2 and obtain $T_{\rm B,eq} \sim 7.7 \times 10^{10}$ K, which is slightly larger than 5×10^{10} K. Because of different underlying assumptions, this value might be somewhat different from other estimates. Therefore we also independently estimate the $T_{\rm B,eq}$ value by computing Eq. 4b of Readhead (1994). This yields $T_{\rm B,eq} \sim 3.5 \times 10^{11}$ K.

Therefore, the brightness temperature of the M 87 core is nearly an order-of-magnitude lower than the equipartition brightness temperature. This is a strong indication that the energy density of the magnetic field is larger than that of the particles. We can estimate the magnetic field strength B in units of the equipartition magnetic field strength $B_{\rm eq}$; $B = B_{\rm eq}(T_{\rm B,eq}/T_{\rm B})^2$ where the brightness temperatures are calculated in the same rest frame (Readhead, 1994). We list values of $T_{\rm B,eq}/T_{\rm B}$ and $B/B_{\rm eq}$ in Table 3.3. If we presume an equipartition magnetic field strength of order of $B_{\rm eq} \sim 1$ G (e.g., Pushkarev & Kovalev 2012), the resulting magnetic field strength is in the range of $\sim 61-210$ G. The field strength might be even higher closer to the BH. We note that Kino et al. (2015) also estimated $B \sim 100$ G based on different constraints and assumptions.

---

[4] If we assume that the VLBI core has a sphere geometry, the Gaussian FWHM value has to be multiplied by a factor 1.8 to account for the geometric correction (e.g., Marscher 1983). This value however changes the $T_{\rm B,eq}$ by a factor of $1.8^{1/8} \sim 1.08$. Therefore we ignore this small correction

Table 3.3 Brightness temperature ratio $T_{\rm B,eq}/T_{\rm B}$ with the equipartition brightness temperature of 2×10^{11} K in the rest frame of the observer and the magnetic field strength in units of $B_{\rm eq}$. Each column shows (1) the observing epoch, (2) the $T_{\rm B}$ ratio, and (3) the magnetic field strength ratio.

Epoch (1)	$T_{\rm B,eq}/T_{\rm B}$ (2)	$B/B_{\rm eq}$ ($\times$10) (3)
2004/04/19	8±3	6.4±4.1
2005/10/15	8±2	6.1±3.9
2009/05/09	8±3	6.9±4.4
2014/02/26	12±4	15±9
2015/05/16	14±5	21±13

We calculate the energy density ratio between the non-thermal particles and magnetic fields $u_p/u_{\rm B}$ by

$$\frac{u_p}{u_{\rm B}} = \left(\frac{T_{\rm B,eq}}{T_{\rm B}}\right)^{-17/2} \tag{3.3}$$

(Readhead, 1994). For $T_{\rm B,eq}$ of $\sim 8\times10^{10}\,K$, we find $-6 \lesssim \log(u_p/u_{\rm B}) \lesssim -4$. This ratio is even lower for the higher equipartition brightness temperature. Therefore, this indicates a magnetic energy dominated jet base. We note that such strong magnetic field seems to be present in other AGN jets as well (Zamaninasab et al., 2014; Martí-Vidal et al., 2015; Baczko et al., 2016).

Another important implication of the low brightness temperature in the M 87 core is that it is much lower than the inverse-Compton limit brightness temperature ($T_{\rm B} \sim 10^{12}$ K; Kellermann & Pauliny-Toth 1969). This makes it difficult to produce high-energy photons by the inverse Compoton process in the compact VLBI core region ($\lesssim 11R_s$) and explain the origin of the γ-ray and TeV radiation correlated with the radio core activities (e.g., Acciari et al. 2010; Abramowski et al. 2012; Hada et al. 2014). Interestingly, these studies constrain the high-energy photon production site to be somewhat larger than the 86 GHz core ($\sim 20-50R_s$). This size is 2-5 times larger than the size of the 86 GHz VLBI core that we measured. This suggests that the γ-ray emission in M 87 may not come from the VLBI core but from the outer jet (e.g., see Hada et al. 2014; Akiyama et al. 2015 and references therein).

Estimating the jet launching region size

Using the ultra-high resolution VLBI image of the jet, it is possible to estimate the size of the jet launching region near the BH. For this, we can reasonably assume a self-similar jet collimation structure (i.e., the same power-law index k) and extrapolate the jet collimation profile down to the BH distance $z \sim 1R_s$.

We show the transverse jet diameter at $z = 1R_s$ obtained by the extrapolation in Fig. 3.12. In this calculation, we accounted for the unknown absolute core position at 86 GHz (i.e., the ε parameter) because larger spatial offsets between the core and the BH would result in a systematically narrower jet base (and vice versa). We find that the jet diameter is as small as $\sim (4.0-5.5)R_s$ for various ε with a statistical fitting uncertainty of $\sim 0.5R_s$. This size is consistent with the upper limit given by the FWHM of the VLBI core ($\sim 11R_s$). We also find that this size is consistent with those independently measured by earlier EHT observations (Doeleman et al., 2012), although, the 230 GHz size measurements can be also model-dependent because of the limited (u,v) coverage.

In terms of the BH-accretion physics, the diameter of the innermost stable circular orbit (ISCO) is $6R_s$ for a non-spinning BH and is as small as $1R_s$ for a maximally spinning BH with an accretion disk with a prograde orbit. In contrast, the diameter of the ergosphere is $(1-2)R_s$ for any BH spin (Komissarov, 2012). This suggests that the relatively wide base of the limb-brightened jet may be anchored in the inner accretion disk. It is interesting to note that comparably wide or even wider jet bases are seen in other AGN jets with limb-brightening (e.g., 3C 84; Giovannini et al. 2018, Cygnus A; Boccardi et al. 2016a).

We also note that Mertens et al. (2016) obtained nearly factor two larger jet base diameter of $(9.6 \pm 1.6)R_s$. The authors estimate the diameter based on the observationally determined angular momentum of the jet at 43 GHz. This momentum is assumed to be conserved and is the same amount in the root of the jet. The diameter of the rotating jet base is then calculated assuming that the accretion disk follows a Keplerian rotation. This method is clearly different from our approach and the factor two difference might originate from the different assumptions.

On the other hand, other physical explanations are also possible. For instance, VLBI observations at different frequencies may see different layers of a transversely stratified jet (e.g., more dominant emission from the inner layers at higher frequencies). Observations of Cygnus A show such a difference at 5 GHz and 86 GHz (Carilli et al., 1991; Boccardi et al., 2016a). An additional effect is related to the jet viewing angle. M 87 has a quite small jet viewing angle ($15^\circ - 30^\circ$; see Walker et al. 2018 and references therein) and any transverse velocity stratification may lead to different level of Doppler boosting at different layers. This could additionally contribute to the aforementioned width difference.

We also remark that our estimation does not account for the thickness of the accretion disk. The multi-wavelength spectral energy distribution of M 87 lacks signatures for a radiatively efficient and geometrically thin accretion disk, suggesting the presence of a geometrically thick and hot accretion flow (e.g., Broderick & Loeb 2009; Prieto et al. 2016). Depending on the scale height of the thick accretion flow, our estimation may be somewhat different from the actual size (e.g., larger diameters with higher scale heights).

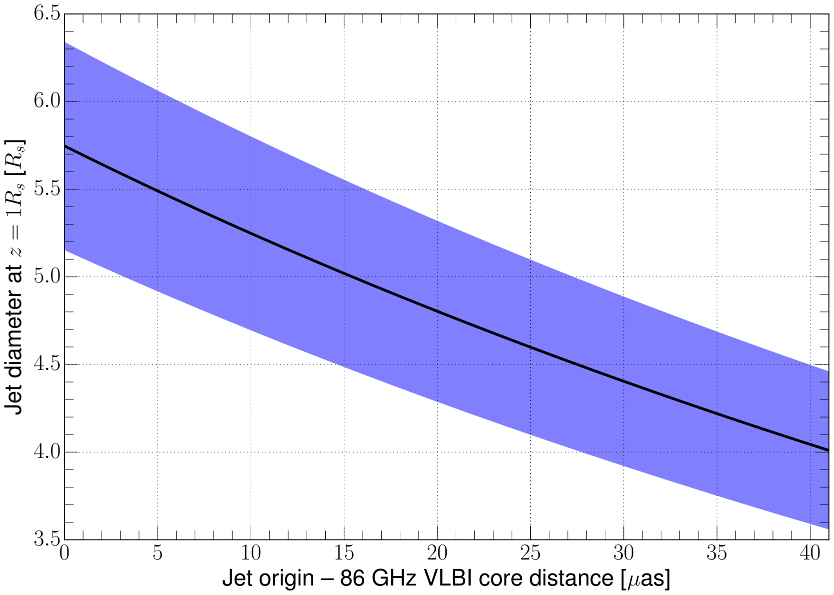

Fig. 3.12 Diameter of the jet base at a distance of $1R_s$ from the BH center as a function of positional offset ε between BH and the 86 GHz VLBI core (larger separation for larger ε). The solid line marks the diameter (width) of the jet base and the shaded area denotes the 1σ uncertainty from the fitting.

At this point, it is important to note that the wide base of the limb-brightened jet (i.e., “sheath”) does not necessarily exclude the presence of a narrower, ultra-relativistic jet from the BH (i.e., a “spine”). General relativistic magnetohydrodynamic (GRMHD) simulations show that the spine component may co-exist within the broader sheath as a natural consequence of the BH-accretion physics (e.g., Hawley & Krolik 2006; Sądowski et al. 2013). Preliminary results from more recent EHT observations of M 87 with longer baselines suggest that a compact Gaussian model with the FWHM size of only $\sim 25-35\,\mu$as could describe the visibilities (Krichbaum et al., 2014). We also note complex transverse jet intensity profiles shown by recent publications, which may support the spine-sheath model (Asada et al., 2016; Hada et al., 2017; Walker et al., 2018).

Implication of the large opening angle

The relationship between the jet opening angle and the jet speed is important to understand the jet dynamics in the collimation and acceleration zone. For instance, Hada et al. (2016) suggested that several nodes of jet reconfinement would form or a jet breakout from a dense atmosphere could occur near the base of the M 87 jet. In such case, the physical evolution of the jet may be significantly different from the gradual acceleration and collimation scenario (e.g., Komissarov et al. 2007; Lyubarsky 2009). Specifically, a sufficiently narrow jet would allow any pressure disturbances from the ambient medium to propagate across the jet within short enough time compared to the dynamical timescale (i.e., causally connected jet). On the other hand, a too wide jet diameter will not allow such a pressure perturbation to propagate across the jet within short enough time. This makes the jet to be less sensitive to the surroundings (i.e., weaker influences of the ambient pressure on the evolution of the internal structure of the expanding jet). In the relativistic cases, this could lead to a different acceleration mechanism such as the rarefaction acceleration (Tchekhovskoy et al. 2010; Komissarov et al. 2010; see also Panaitescu & Kumar 2002).

We study this topic by examining the relationship between the bulk Lorentz factor Γ and the intrinsic opening angle $\phi_{\rm int}$. According to Komissarov et al. (2009), a causally connected jet satisfies the following:

$$\Gamma\phi_{\rm int}/2 \lesssim \sigma^{1/2} \tag{3.4}$$

where the factor 2 on the left hand side indicates the half opening angle of the jet and $\sigma = u_{\rm mag}/u_{\rm kin}$ is the jet magnetization defined by the ratio of the magnetic energy, $u_{\rm mag}$, and the kinetic energy, $u_{\rm kin}$, of the jet (i.e., $\sigma = 1$ for energy equipartition). We compute Eq. 3.4 at the small core separation $d = 60\,\mu$as (equivalently $27R_s$ projected distance). We use the observationally determined intrinsic jet opening angle of $\phi_{\rm int} \sim 64^\circ - 90^\circ$ (a characteristic uncertainty $\sim 28^\circ$) for the range of the viewing angle $\theta = 18^\circ - 30^\circ$. For these parameters, the M 87 jet will be causally connected if $\Gamma \lesssim 2\sigma^{1/2}/\phi_{\rm int} = (1.3-1.8)\sigma^{1/2}$. As we discussed, the inner jet of M 87 is presumably more magnetic energy dominated (i.e., $\sigma \gtrsim 1$). If we take $\sigma \sim 4$ in this region based on the MHD modeling of the M 87 jet (see Fig. 18 of Mertens et al. 2016), Eq. 3.4 becomes $\Gamma \lesssim (5.2-7.2)$. This results in an upper limit of the apparent jet speed of $\sim (2.3-3.4)c$ where the range accounts for the various jet viewing angle. Previous observations suggest much slower apparent jet speeds of $\sim 0.5c$ in this region (Mertens et al., 2016; Hada et al., 2016; Walker et al., 2018). If we instead use this speed in Eq. 3.4, we find that $\Gamma\phi_{\rm int}/2 \sim 0.7-0.9$. Therefore, our calculations support the gradual acceleration and collimation scenario against the rarefaction acceleration which may be accompanied by a jet breakout from a dense atmosphere. It is also interesting to note that typical values of $\Gamma\phi_{\rm int}/2$ are $\sim 0.1-0.2$ in pc-scale jet systems (Jorstad et al., 2005; Pushkarev et al., 2009; Clausen-Brown et al., 2013). This implies that $\Gamma\phi_{\rm int}$ is not constant for the whole AGN jet population.

We extend this analysis to examine if the rapidly expanding jet could suppress several kinds of instabilities or not, especially the current-driven kink instability (CDI). The CDI is considered to play a crucial role in the conversion of the magnetic energy to the kinetic power (e.g., Singh et al. 2016 and references therein). If an instability wave is not quenched by the transverse jet expansion, the jet expansion timescale should be longer than the time needed for an instability wave to propagation across the jet. This leads to the following criterion:

$$\frac{t_{\rm dyn}}{t_{\rm exp}} \approx \frac{\beta\Gamma\phi_{\rm int}/2}{\beta_{\rm s}} \lesssim 1 \tag{3.5}$$

(Clausen-Brown et al., 2013) where $t_{\rm dyn} = (\Gamma\phi_{\rm int}z/2)/(\beta_s c)$ is the jet crossing timescale of the instability wave, $\beta_{\rm s}$ is the signal propagation speed in units of c, $t_{\rm exp} = z/(\beta c)$ is the jet expansion timescale, and β is the intrinsic jet speed in units of c. Inside a highly magnetized jet, $\beta_{\rm s}$ is the azimuthal component of the Alfvén wave and $\beta_{\rm s} \sim 1$ (Giannios & Spruit, 2006). Using the above numbers, we find that Eq. 3.5 is satisfied. This suggests that the CDI could play an important role in spite of the rapid transverse expansion of the innermost M 87 jet.

The inner jet viewing angle and the outflow speed

The viewing angle and the velocity information of the innermost jet of M 87 are crucial to understand the 3D geometry of the outflow and its dynamics. Recent GRMHD simulations show that the projection of the filamentary structure on the sky could make the apparent jet geometry complex (e.g., Mościbrodzka et al. 2016). This can make it difficult to precisely determine the jet viewing angle and the intrinsic jet velocity. However, previous observational studies show that the motions in the jet of M 87 can be decomposed into longitudinal and transverse directions (Mertens et al., 2016; Walker et al., 2018). The former contributes to most of the relativistic Doppler boosting of the jet and counter-jet emission. The latter is inferred as a signature of the internal rotation of the jet and has a smaller boosting effect. In the light of this, we study two possible scenarios of the inner jet kinematics using the observed jet to counter-jet ratio in the vicinity of the core. First, we study a simpler model which corresponds to (1) a stationary jet viewing angle and a constant outflow speed. Then we investigate a more sophisticated scenario (2) in which the viewing angle is still the same but the jet is accelerating at $z \lesssim 1$ mas.

As for the first case, we assume that the approaching and the receding jets have the same intrinsic speeds and brightness. Then the jet to counter-jet brightness ratio R is given by

$$R \equiv I_{\rm jet}/I_{\rm CJ} = \left(\frac{1+\beta\cos\theta}{1-\beta\cos\theta}\right)^{2-\alpha}, \quad \beta = \frac{\beta_{\rm app}}{\sin\theta + \beta_{\rm app}\cos\theta} \tag{3.6}$$

where $I_{\rm Jet}$ and $I_{\rm CJ}$ are respectively the intensities of the jet and the counter-jet, β is the intrinsic jet speed in units of c, θ is the jet viewing angle, α is the spectral index ($S \propto \nu^{+\alpha}$), and $\beta_{\rm app}$ is the apparent jet speed. We note that Eq. 3.6 assumes that the jet velocity is uniform across the outflow. If there is a transverse velocity gradient, the Doppler boosting of the jet and counter-jet emission is more complicated (Komissarov, 1990). This could affect the interpretation of the observed jet to counter-jet ratio. Nevertheless, Mertens et al. (2016) show that the speeds of the jet and counter-jet components are the same within observational uncertainties at distances of $0.5-0.6$ mas from the core. Therefore, we do not include the effect of the velocity stratification in the following analysis.

Due to lack of direct and robust measurements of the jet kinematics at core distances $d \lesssim 0.5$ mas, we assume a certain range of $\beta_{\rm app}$ and attempt to find suitable ranges of θ and β which satisfy Eq. 3.6. Although there is a trend of decreasing jet speed closer to the core, we take a rather broad range of $\beta_{\rm app} = (0.1-0.5)$ based on the results of Mertens et al. (2016), who reported not only fast but also slow motions of $\beta_{\rm app} \sim 0.1$. We also adopt a spectral index $\alpha = -1$ (Hovatta et al., 2014). For the R value, we take those measured at $0.2-0.5$ mas core distances ($R \approx 11-23$). A range of θ and β satisfying Eq. 3.6 is shown in Fig. 3.13. The range of possible viewing angle is wide and not robustly constrained ($\sim 6^\circ - 38^\circ$). This is mainly because of the wide range of apparent jet velocities in our assumption. On the other hand, the M 87 jet is known to accelerate significantly (Mertens et al., 2016; Walker et al., 2018). If this is true in the innermost M 87 jet ($d \lesssim 0.5$ mas), the case (2) could be a more suitable physical scenario.

In the subsequent analysis, we take a viewing angle of 18° which has been estimated from superluminal motions in the M 87 jet at $\sim (1-10)$ mas core separation (Mertens et al., 2016). Then we calculate the intrinsic jet speed, the corresponding apparent speed, and the bulk Lorentz factor using the jet to counter-jet ratio profile $R(z)$ using the following equations:

$$\beta = \frac{1}{\cos\theta}\left(\frac{R^{1/(2-\alpha)}-1}{R^{1/(2-\alpha)}+1}\right) , \tag{3.7}$$

$$\beta_{\rm app} = \frac{\beta\sin\theta}{1-\beta\cos\theta} , \tag{3.8}$$

$$\Gamma = \frac{1}{\sqrt{1-\beta^2}} . \tag{3.9}$$

In Fig. 3.14 we show the resulting bulk Lorentz factor as function of the distance from the central engine. Two main results are noticeable. First, the Lorentz factor in this model is small ($\Gamma \lesssim 1.2$). Second, the model shows a mildly increasing Γ from ~ 1.05 in the vicinity of the central engine (depojrected distance $\sim 50R_s$) to $\Gamma \sim 1.15$ at larger distances (deprojected distance $\sim 150R_s$). The corresponding apparent speed is $\beta_{\rm app} \sim (0.1-0.7)$ at $\lesssim 0.1$ mas and $\beta_{\rm app} \sim (0.6-1.0)$ at $\gtrsim 0.3$ mas, respectively. The latter is comparable to the speed estimated from the VLBA 43 GHz monitoring observations (Mertens et al., 2016; Walker et al., 2018). We

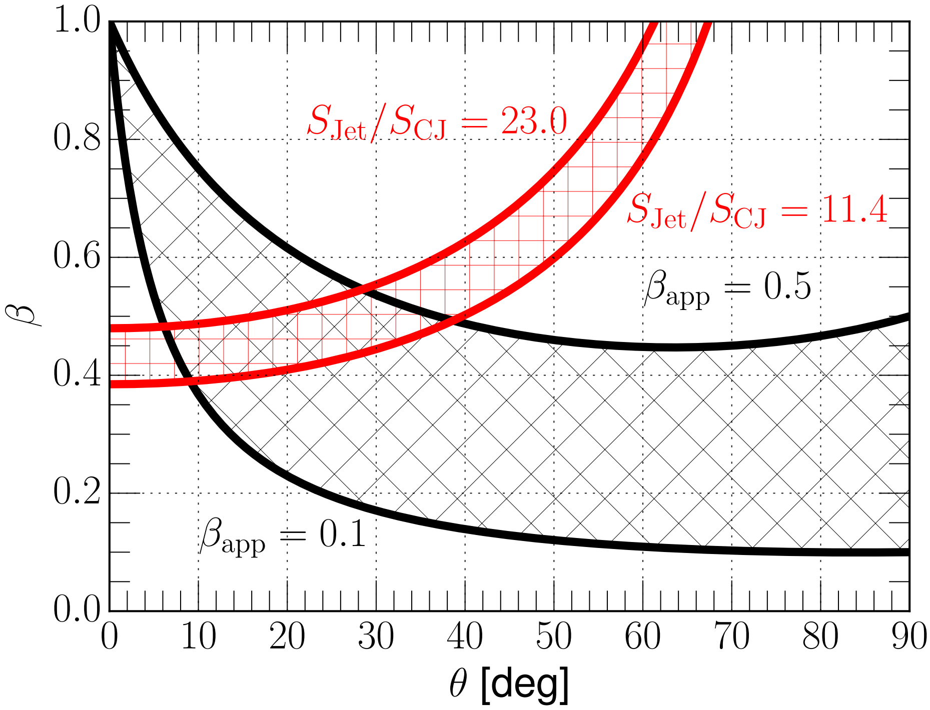

Fig. 3.13 Possible range of M 87 jet viewing angles and jet speeds (in units of c) that satisfy the measured jet to counter-jet ratio R and our assumptions of the value of $\beta_{\rm app}$ at the core separation of 0.2 – 0.5 mas. The black cross and red vertical hatches show allowed ranges of the parameters for R and $\beta_{\rm app}$. Only the overlapping region is physically allowed under the assumptions outlined in the main text.

also note that our two-days long GMVA observations in 2009 showed no significant structural change in the jet on inter-day timescale. If we consider 1/5 of the GMVA beam size in the east-west direction as the marginal angular resolution limit of the array, we derive an upper limit for the apparent motion speed of $0.2 \times 50\,\mu{\rm as\,day}^{-1} \sim 3.65\,{\rm mas\,yr}^{-1} \sim 1c$. This upper limit agrees well with our model prediction. Thus we conclude that the mildly accelerating, slow inner jet model could explain the observed jet to counter-jet ratio close to the central engine.

The spine-sheath scenario in M 87

The M 87 jet is not only highly edge-brightened but also shows a more complicated transverse structure including a faint central lane (see Fig. 3.7 and 3.8). Significant emission features have been found in the jet of M 87 at larger core distances as well (Mertens et al., 2016; Asada et al., 2016; Hada et al., 2017; Walker et al., 2018). The edge-brightened structure can be produced if the flow speed is higher closer to the central axis of the jet and the emission is Doppler

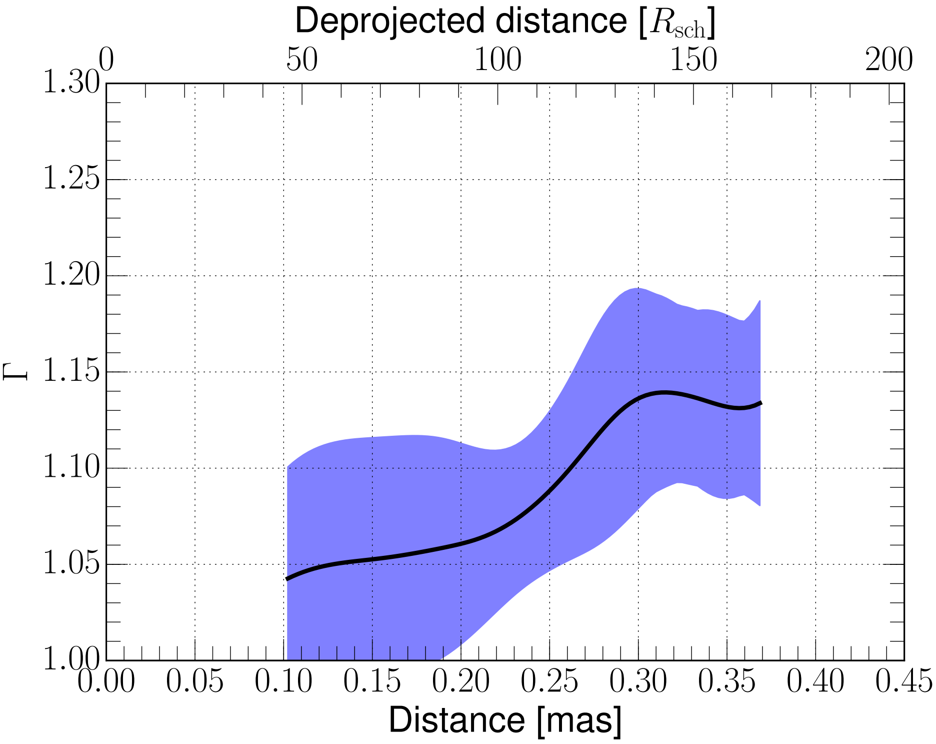

Fig. 3.14 Bulk Lorentz factor of the inner jet of M 87 estimated from the jet to counter-jet ratio versus the distance from the central engine under the assumption of stationary viewing and changing flow speed. The solid lines and the shaded region indicates the mean values and the uncertainties, respectively. The deprojected distance shown in the top side of the figure has been calculated based on the viewing angle of 18°.

de-boosted with respect to the observer (Komissarov, 1990). This configuration corresponds to the so-called spine-sheath structure (e.g., Ghisellini et al. 2005).

If the main reason of the dimming of the central emission is the Doppler de-boosting, we can associate the observed center-to-limb brightness ratio $\rho_{\rm CL}$ measured in the region $d = 0.5 - 1.0$ mas and estimate the required Doppler factor by $\rho_{\rm CL} = (\delta_{\rm spine}/\delta_{\rm sheath})^{2-\alpha}$ where the subscripts "spine" and "sheath" indicate the faster and slower layers of the jet, respectively. We calculate the corresponding spine Lorentz factor $\Gamma_{\rm spine}$ by assuming $\alpha = -1$, the viewing angle of $18^\circ - 30^\circ$, and an apparent speed of the sheath of $\sim 0.5c$ (the corresponding sheath Lorentz factor $\Gamma_{\rm sheath} \sim 1.2 - 1.3$ and $\delta_{\rm sheath} \sim 1.6 - 2.0$). Then we obtain the spine Doppler factor of $\delta_{\rm spine} \sim 1.2 - 1.4$. We show the expected range of the spine Lorentz factor in Fig. 3.15 for two different viewing angles of 18° and 30°, respectively.

For the smaller viewing angle ($\theta \sim 18^\circ$), the inferred $\Gamma_{\rm spine} \sim 13 - 17$ is quite large. This Lorentz factor is comparable to that of HST-1 at optical wavelengths (Biretta et al. 1999; $\Gamma \sim 14$ for $\theta = 18^\circ$). However, it is also worth noting that our estimation was made at the core distance

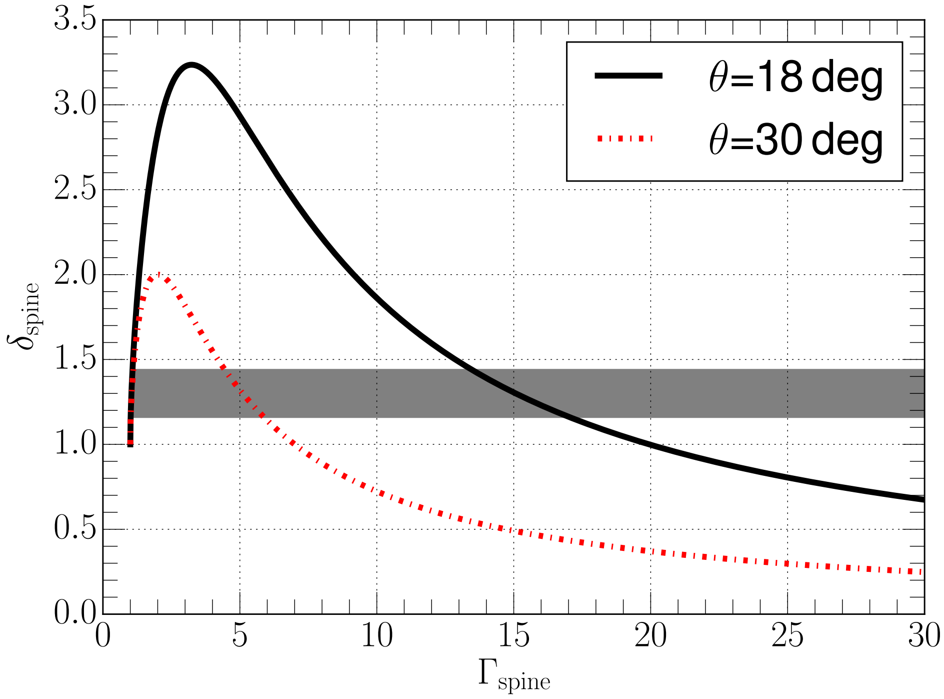

Fig. 3.15 Doppler factor versus Lorentz factor for the spine. The shaded region indicates possible range of the $\delta_{\rm spine}$ derived based on the assumption of the velocity stratification.

$(0.5-1.0)$ mas ($(70-140)R_s$ projected) while HST-1 is located at a much larger distance (~ 900 mas away; $\sim 10^5 R_s$ projected). Therefore, this solution would imply that the spine has a very high speed already near the jet launching region and no significant acceleration or deceleration occurs afterwards. On the other hand, the Lorentz factor is a bit lower for the larger viewing angle case ($\Gamma_{\rm spine} \sim 4.4-5.9$ with $\theta = 30°$).

Recent theoretical studies have shown that accreting BH systems can form both (i) a narrow, relativistic, and magnetic energy dominated beam (i.e., spine) and (ii) a broader, sub-relativistic, and mass-dominated outflow (i.e., sheath) (e.g., Hawley & Krolik 2006; Sądowski et al. 2013). The latter has a large momentum and separates the interior of the jet from the ambient medium. As a result, the spine could propagate without significant mass-loading and deceleration. Such a scenario could qualitatively explain the nearly constant speed of the spine from $\sim 10^2 R_s$ to $\sim 10^5 R_s$ projected distances.

In contrast, Mertens et al. (2016) and Asada et al. (2016) show that the collimation and acceleration of the sheath and the spine may be similar. The gradual MHD acceleration model of the spine presented in Mertens et al. (2016) particularly predicts that the Lorentz factor is much lower than $\Gamma_{\rm spine} \sim 10$. In this regard, the lower $\Gamma_{\rm spine} \sim 4.4-5.9$ with a larger viewing angle $\theta = 30°$ is perhaps a more plausible estimation of the true spine speed.

Although the above calculations provide insights about the internal structure and dynamics of the jet of M 87, it should be noted that the intrinsic synchrotron emissivity is sensitive to the particle energy distribution, the particle number density, and the magnetic field strength. The spine and the sheath may originate from different regions in the central engine (i.e., the spine from the central BH while the sheath from the inner accretion disk). If this is the case, the intrinsic emissivities of the spine and the sheath are not necessarily the same. Therefore, a simply lower intrinsic emissivity of the spine can also produce the limb-brightened morphology as well (see Sect. 4.5 of Mertens et al. 2016). It is also intriguing to note space-VLBI images of the M 87 jet at much lower frequencies (see Asada et al. 2016 for the high resolution jet images at 1.6 – 5 GHz). The images show that the central ridge line has comparably bright or even brighter intensity than the sheath at a few mas downstream of the core (see Fig. 3 and 5 therein). The transverse velocity gradient alone may not be able to reproduce such a profile.

Finally, we remark that the complex transverse emission profiles may be also identified as filamentary emission features. In AGN jets, filamentary and helical trails can be produced by pure hydrodynamic instabilities (e.g., Lobanov et al. 2003). Observations of the M 87 jet suggest that such filamentary structures are present on both kpc- (Lobanov & Zensus, 2001; Hardee & Eilek, 2011) and sub-pc scales (Walker et al., 2018). Therefore, the observed central lane could be a part of helical filaments near the core. More sensitive GMVA observations with improved (u,v)-coverages will be able to image more detailed structure of the jet of M 87 and study these issues more robustly.

3.2.4 Conclusions from the GMVA observations

We arrive at the following conclusions from the GMVA observations of M 87:

- The inner jet of M 87 was successfully imaged at an east-west angular resolution of $50\,\mu as$ (equivalent to $7R_s$ projected spatial resolution) by multi-year GMVA observations at 86 GHz. The jet shows a consistent morphology with the bright and compact VLBI core, the highly edge-brightened approaching jet, and the faint lane of emission between the edges of the jet. The weak counter-jet is also detected east of the core, but our data do not provide a significant evidence for limb-brightening in the counter-jet, most likely due to still insufficient sensitivity.

- The mean FWHM size of the VLBI core is $\sim 11R_s$ at 86 GHz. The apparent brightness temperature of such a compact region is $\sim (1-3) \times 10^{10}$ K. This is nearly an order-of-magnitude lower value than the equipartition brightness temperature ($\sim 2 \times 10^{11}$ K). The low brightness temperature implies that the core is magnetic energy dominated. We infer that the corresponding magnetic field strength would be in the range of $(\sim 61-210)$ G for an equipartition magnetic field strength of ~ 1 G in the core region.

- Assuming a self-similar jet collimation structure, we estimate the diameter of the jet launching region to be $\sim (4.0-5.5)R_s$. This points toward the inner accretion disk as the origin of the sheath, which is responsible for the emission of the bright edges of the jet. This size is also consistent with the results of the previous EHT observations (Doeleman et al., 2012; Akiyama et al., 2015).

- We considered two distinct jet models in order to constrain the jet viewing angle and the speed; one in which the viewing angle and the speed of the jet were fixed, and the other in which the viewing angle was fixed but the jet speed varied with distance from the central engine. We find that the observed jet to counter-jet brightness ratio can be explained with the jet speeds ranging from $(0.1-0.5)c$ for the former and $(0.1-1.0)c$ for the latter.

- We investigated the origin of the faint central emission at 86 GHz by adopting the transverse velocity stratification scenario (i.e., the spine-sheath model). The jet edges were about twice brighter than the central lane. This brightness ratio constrained the Lorentz factor of the spine to be $\Gamma_{\rm spine} \sim 13-17$ $(4-6)$ for the jet viewing angle $\theta = 18^\circ$ (30°). We notice that $\Gamma_{\rm spine} \gtrsim 13$ is comparable to what has been measured from the bulk motion of HST-1 at optical wavelengths ($\Gamma \sim 14$; Biretta et al. 1999). However, we also notice that the central lane appears significantly brighter than the edges of the jet at much lower observing frequencies (e.g., Asada et al. 2016). This may not be explained by the Doppler de-boosting due to the faster speed. Therefore, we consider that the edge-brightening in the jet of M 87 may not be driven only by the pure transverse velocity stratification.

3.3 Multi-frequency VLBI observations

In this section, we extend the analysis of the jet of M 87 by combining the GMVA data with the data from other archival multi-frequency observations.

3.3.1 Quasi-simultaneous multi-frequency VLBI observations in 2009

First, we focus on the GMVA observations performed in May 2009 (day of year (DoY) 129 and 130) and combine the GMVA results with those from close-in-time EHT 230 GHz and VLBA 43 GHz and 15 GHz observations.

EHT and VLBA data

For the EHT observations, Doeleman et al. (2012) observed the source on 2009 Apr 5, 6, and 7 (DoY 95, 96, and 97) and fitted a circular Gaussian model to the visibility data. They obtained a flux density of ~ 1 Jy and size of $\sim 40\,\mu$as, respectively. As explained above, the authors did not perform a direct imaging of the source structure and the absolute position of the compact component is not precisely constrained. Nevertheless, we presume that such a compact and bright feature is most likely spatially coincident with the compact VLBI core of the jet imaged by our contemporaneous GMVA observations (§3.2). We also make use of an archival VLBA data set of M 87 taken as a part of the long-term VLBA 43 GHz monitoring of M 87 (VLBA code BW 092; Walker et al. 2018). The observation was performed on 2009 Mar 13 (DoY 72) and the archival raw data were retrieved from the NRAO data archive [5]. This archival data set was analyzed using the NRAO AIPS software and the DIFMAP package. The corresponding VLBA 43 GHz image of the source is shown in the top panel of Fig. 3.16. We also take an archival VLBA 15 GHz data set of M 87 (VLBA code BK 145; Kovalev et al. 2007) which was independently reduced by the MOJAVE team (Lister et al., 2016) and available from their database[6]. The observation was performed on 2009 May 22 (DoY 142). The visibility data were loaded into the DIFMAP package and the source was re-imaged using the CLEAN algorithm. The corresponding VLBA 15 GHz image of the source is shown in the bottom panel of Fig. 3.16.

Multi-Gaussian model fitting

We decomposed the inner M 87 jet using multiple Gaussian models. We paid extra attention to the different angular resolutions of the multi-frequency VLBI data in order to achieve reasonable fits at all frequencies with comparable total number of Gaussian components. Generally, the elliptical Gaussian model is suitable to measure the brightness temperature with better accuracy (e.g., Kovalev et al. 2005; Jorstad et al. 2017). However, the fine-scale structure in the compact nuclear region is often better represented by circular Gaussians with smaller FWHM sizes and smaller separations from each other. This is especially the case when the fine-scale source structure is known a-priori by other near-in-time higher-resolution observations (see, e.g., Savolainen et al. 2008; Gómez et al. 2016; Hodgson et al. 2017). Bearing this in mind, we fitted multiple circular Gaussians to the visibility data by the DIFMAP task MODELFIT (see §3.2).

To begin with, we applied the model-fitting procedure with the GMVA data in order to identify the jet geometry on the finest scales. Then, for the lower frequency data, we adopted

---

[5] https://archive.nrao.edu/archive/advquery.jsp

[6] https://www.physics.purdue.edu/MOJAVE/

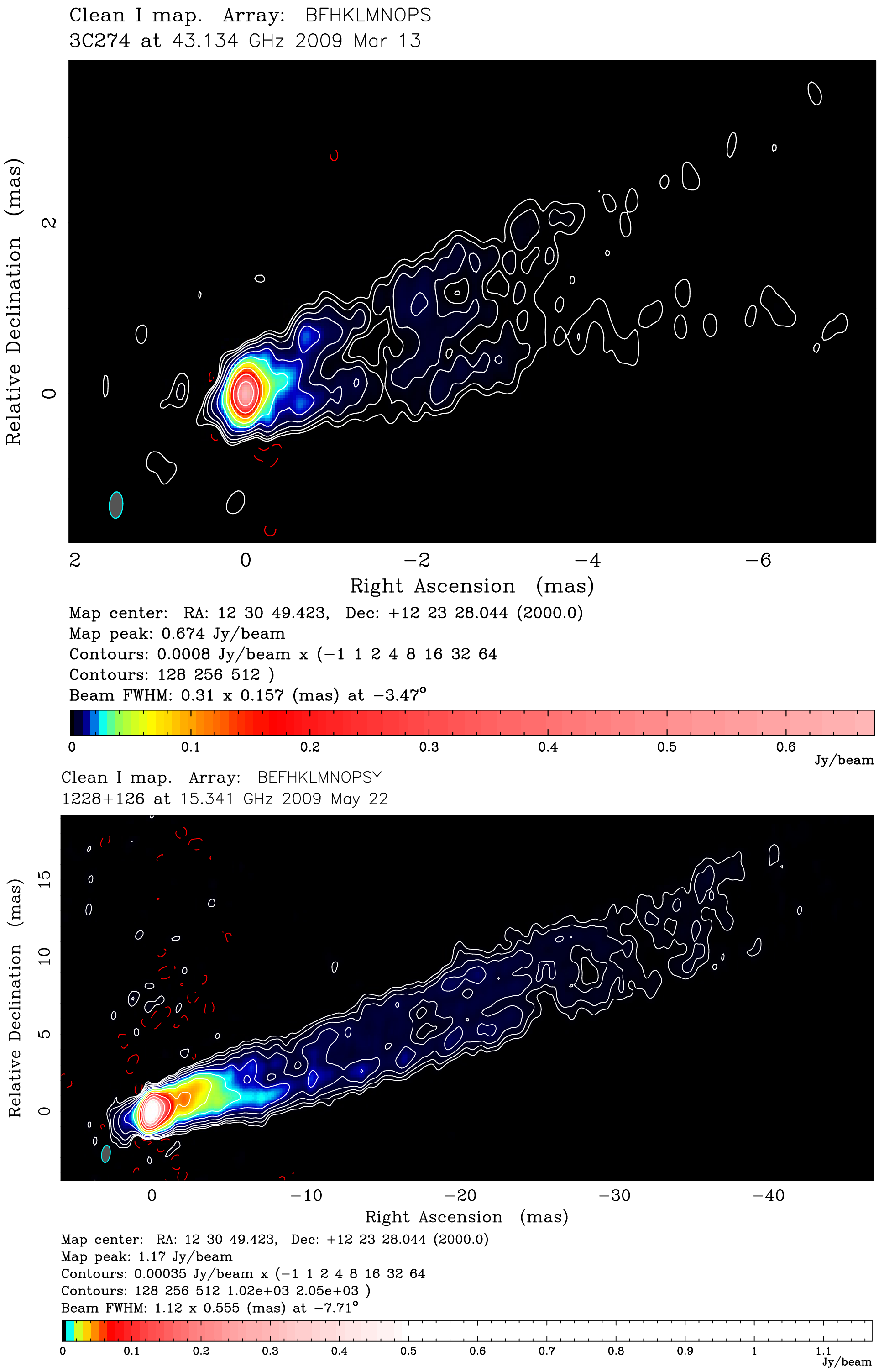

Fig. 3.16 **Top** : VLBA 43 GHz image of the jet of M 87 in Mar 2009. **Bottom** : VLBA 15 GHz image of the jet of M 87 in May 2009. Both images were mapped using the uniform weighting scheme.

only delta components with zero sizes in order to accurately determine the total number of the components and the component positions first. We cross-checked if the total number of components and the component positions at lower frequencies were consistent with those at 86 GHz. When the positions and flux densities converged against additions of new delta components and further model-fitting runs, we allowed the component sizes to vary as free parameters. At this stage, we did not add more Gaussian components. The uncertainties of the model-fit parameters were estimated in the same way as for the GMVA data using the local post-fit rms values of ~ 1.4 mJy/beam (86 GHz), ~ 1.0 mJy/beam (43 GHz), and ~ 0.6 mJy/beam (15 GHz) near the phase center of each frequency image (Schinzel et al. 2012; see §3.2). We scaled the uncertainties of the FWHM sizes by 5% of the FWHM sizes if the size uncertainties were smaller than 5% of the FWHM. For such components, uncertainties of the other geometric parameters were re-calculated based on the modified size errors. We note that these error estimations are primarily based on the thermal noises. The actual errors could be larger, especially for fainter and larger components.

The resulting component properties are shown in Table 3.4. For illustration, we provide slightly super-resolved 86, 43, and 15 GHz model-fit images in Fig. 3.17, 3.18, and 3.19, respectively. The inner jet structure within $\lesssim 0.5$ mas from the phase center is represented by four (J0-J3), three (CJ0-CJ2), and intriguingly two (C0 and C1) compact components in the approaching jet, counter-jet, and the nuclear region ($\lesssim 100\,\mu$as). More details of the results are described in the following. At 86 GHz and 43 GHz, the jet structure within $\lesssim 0.5$ mas core distance can be well fitted with an equal number of the components. The component positions also showed a reasonable agreement, but with slight systematic offsets possibly due to jet motions over the two months time gap. We also check whether the 43 GHz models are reliable against the resolution limit of the array at this frequency. We find that the 43 GHz model components are separated by at least $\sim 80\,\mu$as from each other, which is $\sim 26\%$ and $\sim 51\%$ of the major and minor axis of the VLBA 43 GHz beam, respectively. The beam size is $\sim 310 \times 157\,\mu$as at 43 GHz and therefore the FWHM sizes of the components appear larger than 1/5 of the beam. This suggests that the components are spatially resolved (see, e.g., Homan et al. 2002) and the models are reliable. The angular resolution was however much lower at 15 GHz (the corresponding beam size $\sim 840 \times 440\,\mu$as) and we were not able to obtain comparable Gaussian models especially within $\sim 200\,\mu$as from the phase center. Therefore, we used only a single circular component to represent the bright emission in that region and identified this component as a sum of the three smaller sub-nuclear components found at higher frequencies. At $\gtrsim 200\,\mu$as, the jet was well represented by the same number of Gaussian components with comparable sizes. But the component positions showed similar systematic offsets compared to the positions at 86 and 43 GHz. We find that the 15 GHz components are separated by at least $\sim 120\,\mu$as and their FWHM sizes are also larger than this value. The $120\,\mu$as corresponds to 1/5 of the interferometric beam at this frequency. This suggests that the components are spatially resolved.

Synchrotron spectrum of the core

The spatial distribution of the jet and counter-jet components (J0-J3 and CJ0-CJ2) and the small FWHM sizes of C0 and C1 suggest that either C0 or C1 corresponds to the bona-fide "core" component (i.e., the kinematic center of the system). The exact definition of "core" is however somewhat subjective (e.g., see Hodgson et al. 2017; Boccardi et al. 2017). Therefore, we identify a component with higher brightness temperature and inverted synchrotron spectrum as the true core. At 43 GHz, the brightness temperature of C0 and C1 are $(2.7 \pm 0.3) \times 10^{10}$ K and $(3.7 \times 0.5) \times 10^{10}$ K, respectively. The FWHM size of C1 is slightly smaller. At 86 GHz, the comparison is somewhat ambiguous because C0 is not spatially resolved. However, the C1 component has a factor ~ 6 larger flux compared to C0. This makes the spectral index of C1 much more inverted between 43 GHz and 86 GHz. Based on this, we assume that C1 is associated with the true jet base which may be also coincident with the compact plasma identified at 230 GHz by the near-in-time EHT observations.

Then, we compile the multi-frequency flux density information of C1 and attempt to fit a model synchrotron spectrum. For the model of the synchrotron radiation spectrum we follow Türler et al. (2000). The authors describe the flux density S_ν as function of the frequency ν by

$$S_\nu = S_\mathrm{m} \left(\frac{\nu}{\nu_\mathrm{m}} \right)^{\alpha_\mathrm{t}} \frac{1 - \exp[-\tau_\mathrm{m} (\nu/\nu_\mathrm{m})^{\alpha - \alpha_\mathrm{t}}]}{1 - \exp(-\tau_\mathrm{m})} \tag{3.10}$$

where S_m is the flux density at the synchrotron turn-over (in Jy), ν_m is the turn-over frequency (in GHz), $\tau_\mathrm{m} \approx 3/2(\sqrt{1 - 8\alpha/3\alpha_\mathrm{t}} - 1)$ is the optical depth at ν_m, α_t is the spectral index of the optically thick part of the spectrum ($\alpha_\mathrm{t} \leq 0$), and α is the optically thin spectral index (i.e., $S_\nu \propto \nu^{+\alpha}$ when $\nu \gg \nu_\mathrm{m}$). We set $\alpha_\mathrm{m} = 5/2$ based on the theoretically expected spectrum of an optically thick, homogeneous synchrotron emitter (Pacholczyk, 1970). This leaves three free parameters to be fitted, namely ν_m, S_ν, and α. We cannot fit these three parameters simultaneously since the number of available flux measurements is only three. However, we are mainly interested in estimating the ν_m and S_m values because they are the most critical parameters to compute the synchrotron self-absorption magnetic field strength (Marscher, 1983). Therefore, we fixed the optically thin spectral index to be $-1.0 \leq \alpha \leq -0.3$ and performed the least-square fittings for the remaining two free parameters. We consider that this range of α is a reasonable description of the steep spectral index of the jet base. For instance, quasi-simultaneous (≤ 1 day time offset) observations of M 87 by the Atacama Large

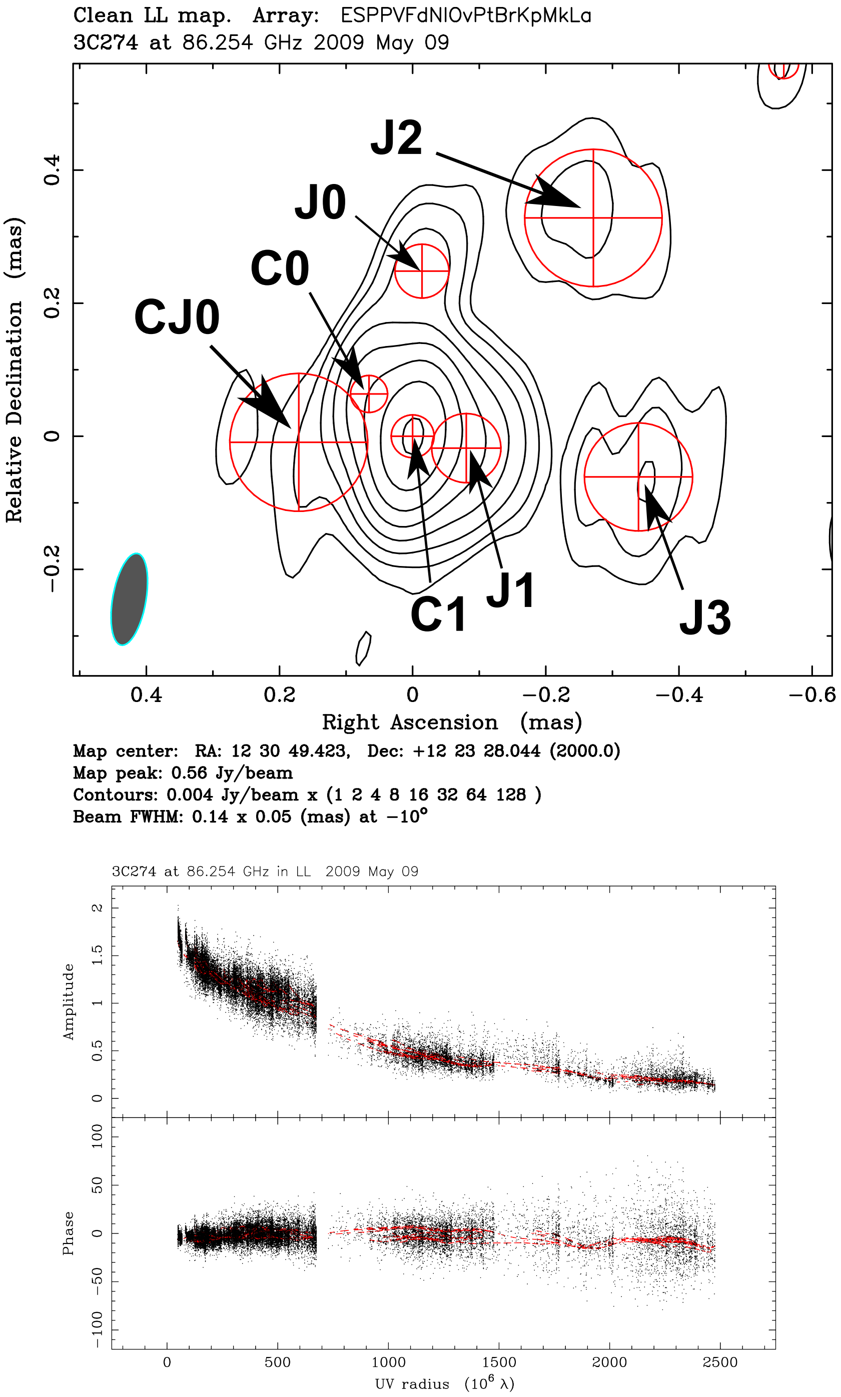

Fig. 3.17 **Top** : GMVA 86 GHz image of the jet of M 87 recovered by the model-fitting. The red ⊕ symbols represent the circular Gaussian models. Their diameter is the full-width half maximum size. The arrows and labels mark the component identification (see text). The post-fit image rms level is ∼ 1.4 mJy/beam. The brightest component (C1) is taken as the center of the image. The size of the restoring beam in this figure is half of the original beam only in the north-south direction. **Bottom** : The same data in the visibility domain. The black dots and red lines represent the observed data and the model, respectively.

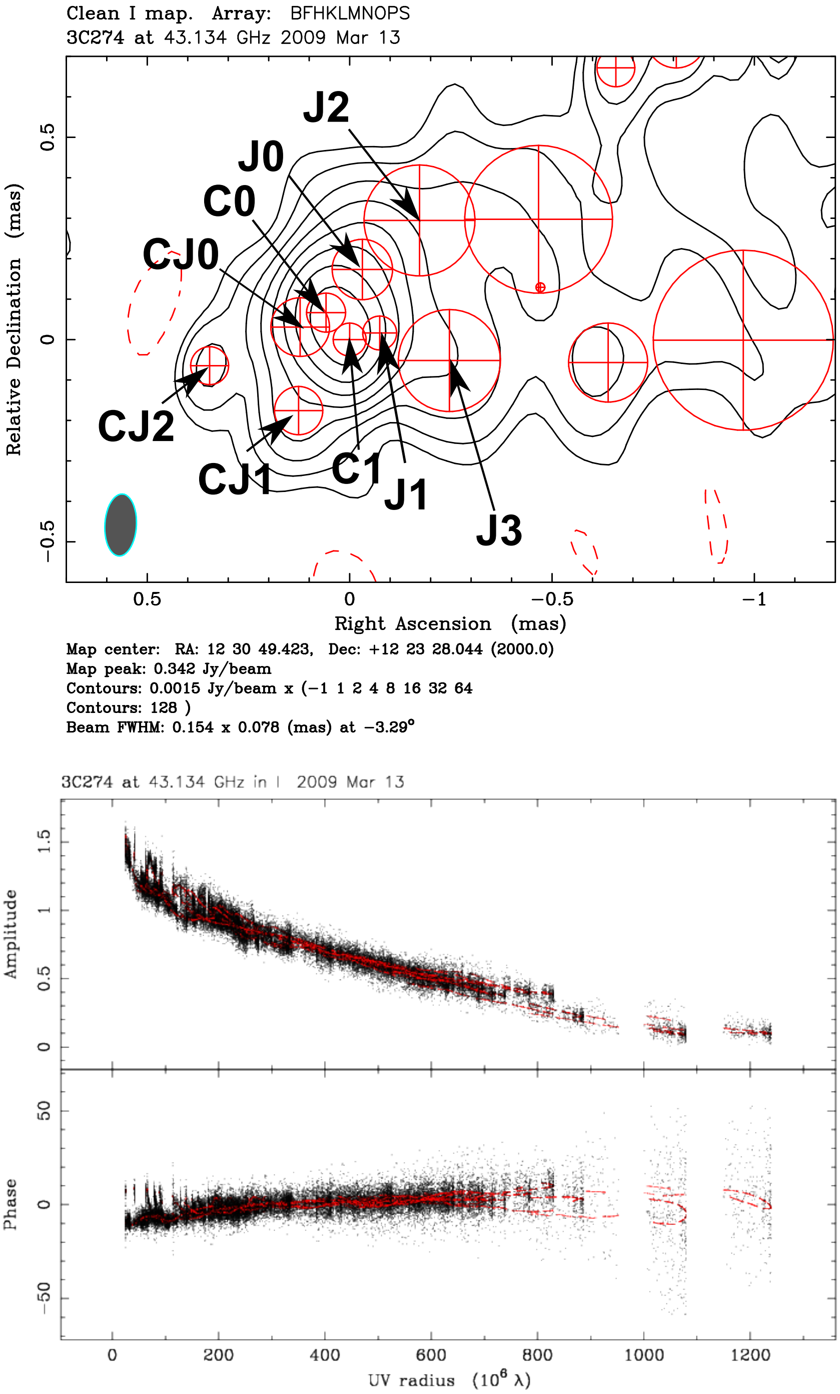

Fig. 3.18 The same as Fig. 3.17 but for the VLBA 43 GHz data. The post-fit rms level is ∼ 1.0 mJy/beam. The size of the restoring beam in this figure is half of that in Fig. 3.16.

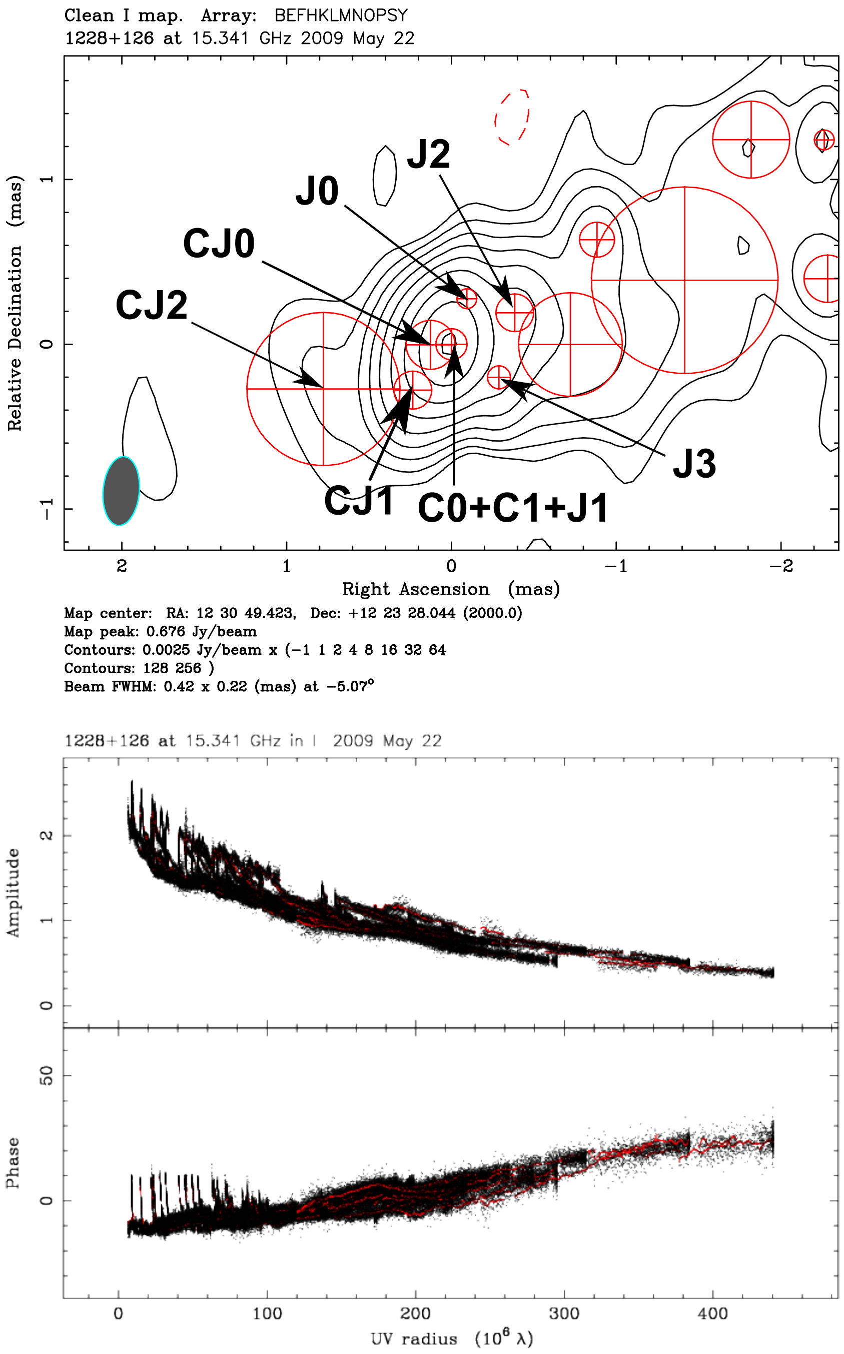

Fig. 3.19 The same as Fig. 3.17 but for the VLBA 15 GHz data. The post-fit rms level is ~ 0.6 mJy/beam. The size of the restoring beam in this figure is half of that in Fig. 3.16.

Table 3.4 M87 jet component parameters obtained by the multi-Gaussian model-fitting described in the text. At each frequency, the observing day of the year is 72 (43 GHz), 129.5 (86 GHz), and 142 (15 GHz) for 2009, respectively. The columns show (1) the region where the component is located, (2) the component identification, (3) the observing frequency, (4) the flux density, (5) the radial distance of a component from the reference component C0, (6) the position angle of the component with respect to north (increasing in clockwise), and (7) the FWHM size. The em-dashes ("–") denote that the values are not available.

Region (1)	ID (2)	Freq (3) (GHz)	Flux (4) (mJy)	r (5) (μas)	θ (6) (deg)	FWHM size (7) (μas)
Core	C0	43	373 ± 27	89 ± 3	41 ± 2	96 ± 5
		86	148 ± 20	91 ± 3	46 ± 2	< 56
		15	–	–	–	–
	C1	43	364 ± 27	0	0	81 ± 4
		86	961 ± 52	0	0	64 ± 3
		15	–	–	–	–
	C0+C1+J1	15[a]	800 ± 31	0	0	189 ± 10
Jet	J0	43	117 ± 15	176 ± 4	−(10 ± 1)	150 ± 7
		86	55 ± 13	249 ± 15	−(3 ± 3)	< 81
		15	56 ± 8	292 ± 6	−(19 ± 1)	< 120
	J1	43	70 ± 12	76 ± 6	−(78 ± 5)	84 ± 13
		86	210 ± 24	82 ± 3	−(102 ± 2)	< 104
		15	–	–	–	–
	J2	43	60 ± 11	341 ± 12	−(30 ± 2)	274 ± 24
		86	88 ± 16	426 ± 8	−(40 ± 1)	206 ± 17
		15	146 ± 13	430 ± 6	−(64 ± 1)	228 ± 11
	J3	43	73 ± 12	252 ± 9	−(102 ± 2)	252 ± 18
		86	71 ± 14	344 ± 10	−(100 ± 2)	< 162
		15	87 ± 10	351 ± 3	−(125 ± 1)	139 ± 7
Counter-jet	CJ0	43	58 ± 11	126 ± 8	76 ± 4	145 ± 17
		86	54 ± 12	171 ± 16	93 ± 5	207 ± 32
		15	279 ± 18	126 ± 7	92 ± 3	297 ± 15
	CJ1	43	40 ± 9	216 ± 15	144 ± 4	119 ± 30
		86	–	–	–	–
		15	116 ± 12	364 ± 6	140 ± 1	230 ± 11
	CJ2	43	15 ± 6	352 ± 65	101 ± 10	< 94
		86	–	–	–	–
		15	47 ± 8	823 ± 42	109 ± 3	929 ± 84

Note : (**a**) Taken as the reference position (i.e., the phase center) at 15 GHz.

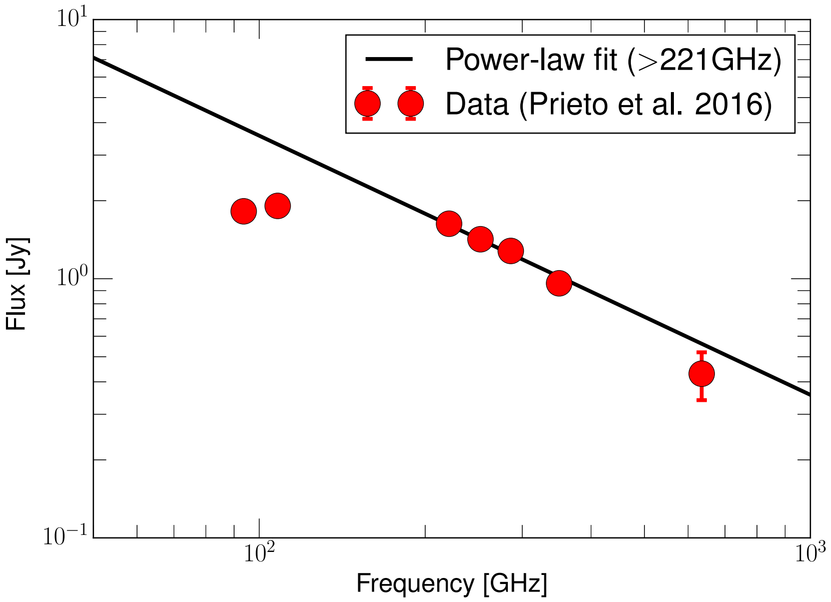

Fig. 3.20 Arc-second scale flux of the radio core of M 87 between 93.7 GHz and 635 GHz measured by ALMA on 3 Jun 2012. The slope of the power-law model, $-(1.1 \pm 0.1)$, was derived excluding the 93.7 and 108 GHz data points which suggest a flat spectrum. The flux density measurements have been taken from Prieto et al. (2016).

Millimeter/submillimeter Array (ALMA) show that the unresolved core of the jet on arc-second scales has a steep spectrum at $\gtrsim 221$ GHz (see Prieto et al. 2016 and Fig. 3.20). By fitting a power-law model to the data, we find that the core spectrum can be described with $\alpha \sim -(1.1 \pm 0.1)$ at 221–635 GHz. On VLBI scales, the spectrum will be less steep (i.e., $\alpha \gtrsim -1$) because the VLBI core is separated from the extended and optically thin jet emission. We also note that our model-fit parameters did not include systematic flux uncertainties for the 43 GHz and 86 GHz data. Therefore, we adopt 10% and 15% of the measured flux densities as uncertainties at each frequency, respectively. The core flux density was also obtained from different observing epochs (separated by maximally ~ 60 days). Previous VLBI observations of M 87 show that the VLBI core flux could be time-variable by a factor of 2 during the phase of a significant radio flare (Hada et al., 2014; Walker et al., 2018). We discuss the potential impact of such a flux density variability later.

We display the synchrotron spectrum of the core in Fig. 3.21 and the model parameters in Table 3.5. We find that typical values of $\nu_{\rm m}$ and $S_{\rm m}$ are in the range of $\sim 110-141$ GHz and $\sim 1.0-1.5$ Jy with the statistical uncertainties of $\lesssim 12$ GHz and $\lesssim 0.2$ Jy, respectively. By performing an inverse-variance weighted average of the values, we obtain the mean values of $\nu_{\rm m} = 128$ GHz and $S_{\rm m} = 1.06$ Jy. We note that the exact value of the optically thin spectral index is not accurately determined. Thus, we take half of the differences between the maximum

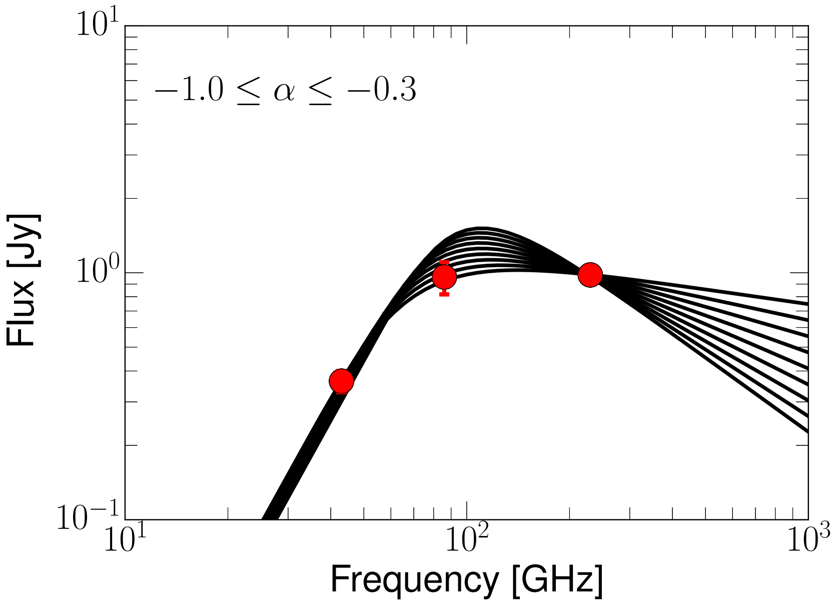

Fig. 3.21 Radio spectrum of the VLBI core of M 87 between 43 GHz and 230 GHz in Mar-May 2009. The red dots show the flux density measurements described in the text and the black solid lines are the synchrotron spectrum models obtained for $-1.0 \leq \alpha \leq -0.3$.

and minimum of $\nu_{\rm m}$ and $S_{\rm m}$ as the characteristic uncertainties in these estimations. This results in $\nu_{\rm m} = 128 \pm 16$ GHz and $S_{\rm m} = 1.06 \pm 0.24$ Jy.

Using these parameters, we can estimate the synchrotron self-absorption (SSA) magnetic field strength $B_{\rm SSA}$ by (Marscher, 1983; Hodgson et al., 2017)

$$B_{\rm SSA} = 10^{-5} b(\alpha) \frac{\theta_{\rm m}^4 \nu_{\rm m}^5 \delta^{2-\alpha}}{S_{\rm m}^2 (1+z)} \quad \text{Gauss} \tag{3.11}$$

where $b(\alpha)$ is a function of the optically thin spectral index whose specific values are tabulated in Marscher (1983), $\theta_{\rm m}$ is the angular size of the emission region in mas which can be taken as 1.8×FWHM of the Gaussian [7], δ is the Doppler factor associated with the underlying flow, z is the redshift of the source ($z = 0.00436$; Smith et al. 2000), and $S_{\rm m}$ and $\nu_{\rm m}$ are in Jy and GHz, respectively.

We take $b(\alpha) = 0.5$ based on the range of α used in our model fitting. We take the FWHM size of the C1 component to obtain $\theta_{\rm m}$. Equation 4.12 depends largely on the exact value of $\theta_{\rm m}$ and the size of the C1 component appears slightly different at 43, 86, and 230 GHz ($\theta_{\rm m} \sim 40-81\,\mu$as if the compact component observed by the EHT corresponds to C1). The turn-over frequency of $\nu_{\rm m} = 128$ GHz is closer to 86 GHz than 230 GHz. Therefore, we take

---

[7] The factor 1.8 was introduced by Marscher (1983) and accounts for the conversion of the geometry between a 2D Gaussian and a sphere projected to the 2D plane.

Table 3.5 Parameters of the synchrotron spectrum models. Each column shows (1) the optically thin spectral index, (2) the turn-over frequency (in GHz), (3) the turn-over flux density (in Jy), and (4) the synchrotron opacity at the turn-over frequency.

α (1)	$\nu_{\rm m}$ (2) (GHz)	$S_{\rm m}$ (3) (Jy)	$\tau_{\rm m}$ (4)
-1.0	109.80 ± 11.59	1.51 ± 0.19	0.66
-0.9	108.85 ± 10.52	1.45 ± 0.16	0.60
-0.8	108.47 ± 9.24	1.39 ± 0.13	0.54
-0.7	108.85 ± 7.82	1.32 ± 0.10	0.48
-0.6	110.22 ± 6.30	1.25 ± 0.07	0.42
-0.5	112.94 ± 4.70	1.19 ± 0.05	0.36
-0.4	117.65 ± 2.98	1.13 ± 0.03	0.29
-0.3	125.72 ± 1.01	1.07 ± 0.01	0.22

$\theta_{\rm m} = 1.8 \times 64\,\mu$as. The apparent motions in the jet are slow near the C1 component (see the next subsection) and the effect of the Dopper boosting is marginal. Then, we obtain $B_{\rm SSA} \sim (27 \pm 21)$ Gauss. This value appears an order of magnitude smaller than what we found from the brightness temperature analysis (§3.2). However, we recall that the VLBI core flux of M 87 was higher by a factor 2 in May 2009 compared to the flux level in the other epochs. The GMVA observations in May 2009 was later than the VLBA 43 GHz observations by ~ 60 days. If the high flux level at 86 GHz is associated with the intrinsic brightening of the core in the later period, we can presume that the flux of the C1 component was $\sim 960/2 \sim 480$ mJy at 86 GHz in Mar-Apr 2009 when the source was observed by the VLBA at 43 GHz and the EHT at 230 GHz. If this is the case, the core spectrum will be substantially inverted between 86 and 230 GHz and the turn-over frequency is most likely at least 230 GHz. By adopting $\nu_{\rm m} \gtrsim 230$ GHz, $\theta_{\rm m} \sim 1.8 \times 40\,\mu$as, and adopting the same parameters as before, we find $B_{\rm SSA} \gtrsim 77$ Gauss. This value is perhaps closer to the true magnetic field strength in the base of the jet in M 87.

Inner jet kinematics

As we noted before, there are systematic offsets in the positions of the jet components with respect to the peak of the total intensities (up to $\sim 100\,\mu$as and larger core separations in later epochs). This may be related to the slow proper motion in the inner jet. Accordingly, we attempt to calculate the speed of the inner jet using the positions of the jet and counter-jet components in the three different observing epochs. We plot the core separation versus time and the corresponding jet kinematics in Fig. 3.22. There is a systematic trend of the core separation being larger in later observing epochs. We note that the core-shift between 15 and 86 GHz due to the opacity effect could be large ($\sim 90\,\mu$as; Hada et al. 2011) and may be an explanation for the large offsets. If the core-shift is the main reason and there is no proper motion in the jet, however, we expect to find the minimum separations between the core and the jet components at 15 GHz. This is the opposite of our finding (i.e., larger separations at 15 GHz). The core-shift is also expected to be much smaller between 43 and 86 GHz ($\sim 20\,\mu$as; Hada et al. 2011) and cannot describe the much larger positional offsets of $\sim 100\,\mu$as of the jet components at 43 and 86 GHz (see Fig. 3.22). Therefore, we consider that the motions in the jet are real.

For each component, the speed is estimated by the least-square fitting of the core separation versus time when all the three epochs are available. If only two of the epochs are available, we simply divide the distance travelled by the component by their time offset. In such case, the uncertainties of the apparent speeds are obtained by the standard error propagation. The mean position of individual component is calculated by averaging the core separation values in different epochs. Then, we assign the difference between the maximum and the minimum core separations as the uncertainty of the mean core separation value. The kinematics information of each component is summarized in Table 3.6. We also plot the apparent jet speed versus the core separation and the bulk Lorentz factor Γ obtained with the viewing angle of 18°.

We find that the jet components at $\lesssim 600\,\mu$as are slow (e.g., $\beta_{\rm app} \sim 0.1-0.2$ at $200-400\,\mu$as). But larger speeds are obtained at larger core separations (e.g., $\beta_{\rm app} \sim 0.6$ for the outermost counter-jet component at $\sim 600\,\mu$as). This speed is consistent with $\beta_{\rm app} \sim 0.5$ obtained by the VLBA 43 GHz monitoring observations of Mertens et al. (2016) and Walker et al. (2018). Within $100\,\mu$as from the reference position, the proper motion speed is essentially 0 within observational uncertainty. We compute the Pearson cross-correlation coefficient between $\langle r \rangle$ and $\beta_{\rm app}$ including all the values in Table 3.6, finding a strong correlation with the correlation coefficient $\rho = 0.89$ with 99.7% significance. Excluding the less reliable component CJ2 which is identified only in two epochs, we still find a strong correlation with $\rho = 0.80$ but with a lower 97% significance. This correlation could be understood as the acceleration of the inner M 87 jet. The bulk Lorentz factor is overall in the range of $\Gamma \lesssim 1.1$ at $\langle r \rangle \lesssim 400\,\mu$as. This is consistent with our results obtained by the jet to counter-jet brightness ratio analysis at $0.2-0.5$ mas core separation (§3.2; see Fig. 3.14). Therefore, our kinematics analysis supports the picture of the slow and mildly accelerating inner jet of M 87.

3.3.2 Frequency dependence of the brightness temperature in the M 87 core

Recent studies of the brightness temperature as a function of frequency relation suggest that the VLBI cores of AGNs may have systematically lower temperatures at 86 GHz than at lower

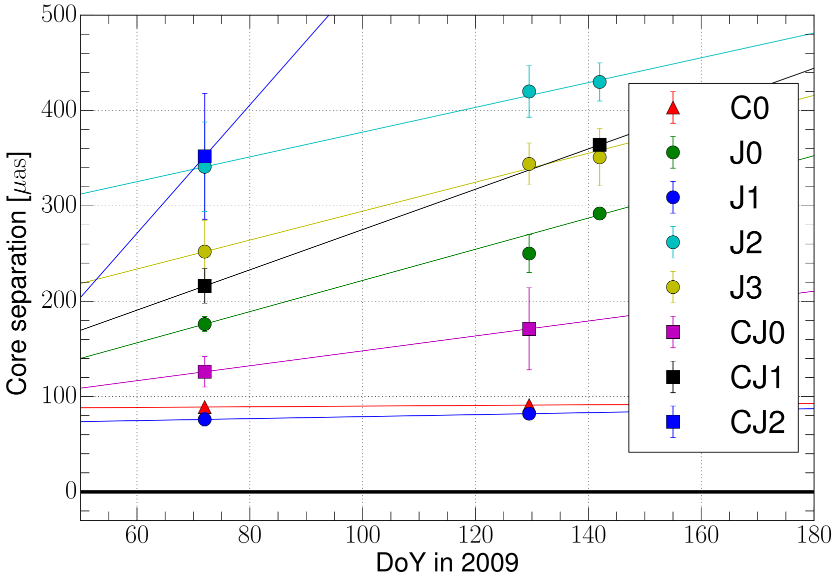

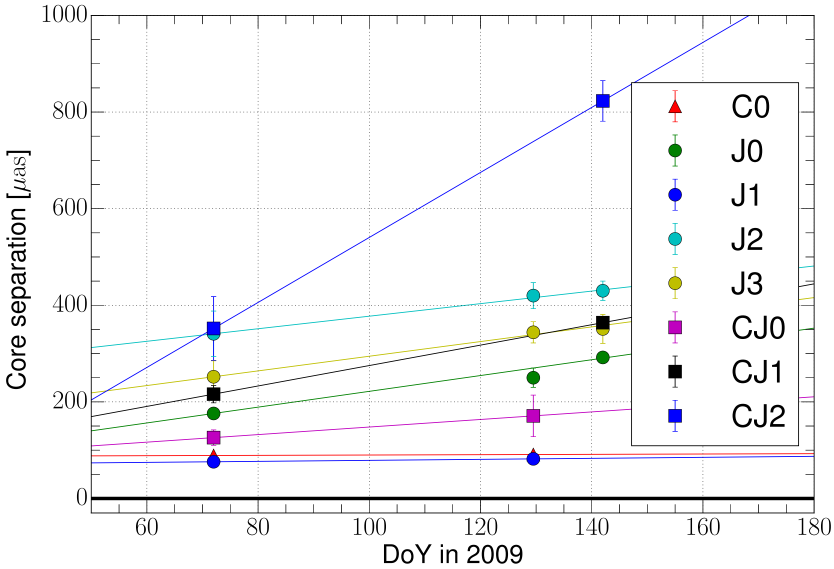

Fig. 3.22 **Top** : Plot of core separation versus time. The vertical axis is the core separation of all the components in μas and the horizontal axis is the Day of Year in 2009. Lines with different colors mark the motion of each VLBI component obtained by the linear regression analysis. **Bottom** : The same plot but including the CJ2 component.

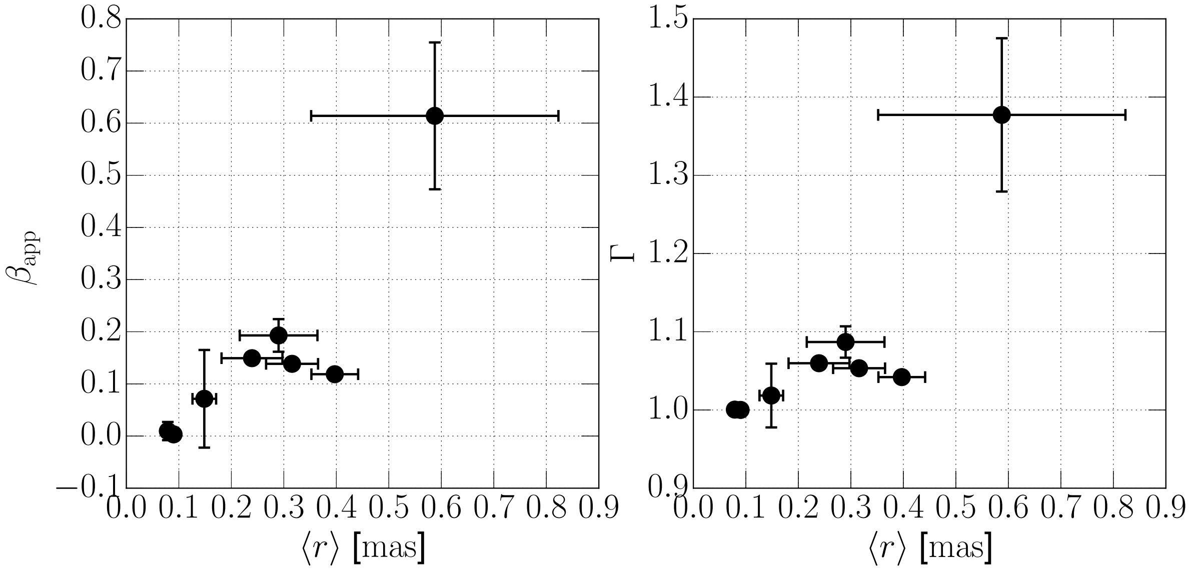

Fig. 3.23 Apparent inner M 87 jet velocity (left) and the bulk Lorentz factor (right) versus the core separation. The jet viewing angle was set to 18° for the right panel. We note that the outermost component with the largest apparent speed is associated with CJ2, whose identification could be potentially less reliable than that of the other components.

Table 3.6 A summary of the jet component kinematics. The columns show (1) the component ID, (2) the mean core separation in μas, (3) the apparent jet speed in μas/yr, and (4) the apparent jet speed in units of c (using the jet speed conversion factor of $1c \approx 4$ mas/yr for M 87).

ID (1)	$\langle r \rangle$ (2)	μ (3)	$\beta_{\rm app}$ (4)
C0	90 ± 1	13 ± 38	0.00 ± 0.01
J0	239 ± 58	597 ± 22	0.15 ± 0.01
J1	79 ± 3	38 ± 70	0.01 ± 0.02
J2	397 ± 44	474 ± 12	0.12 ± 0.01
J3	316 ± 50	554 ± 24	0.14 ± 0.01
CJ0	148 ± 22	286 ± 375	0.07 ± 0.09
CJ1	290 ± 74	772 ± 125	0.19 ± 0.03
CJ2	588 ± 236	2456 ± 563	0.61 ± 0.14

frequencies (Lee et al., 2016; Nair et al., 2018). This is generally interpreted as a signature of the acceleration of the jet flow with its increasing distance from the central engine at lower observing frequencies, based on the fact that the absolute position of the radio core is more distant from the central engine due to the jet opacity effect (i.e., core-shift; Marcaide & Shapiro 1984; Lobanov 1998). We apply the similar analysis to the jet of M 87 in more detail.

Data and Methodology

We compiled a set of the M 87 VLBI core flux densities and sizes measured at 1.6, 2.3, 5.0, 8.6, 15.4, 43, 86, and 230 GHz based on available literature. If no information was available from literature, we reduced and analyzed archival VLBI data by ourselves. Details of the data and the measurements at each frequency are described in the following.

At 1.6 GHz, we made use of archival European VLBI Network (EVN) data sets which were taken by Asada et al. (2014). The data sets were retrieved from the EVN data archive [8]. At 5.0 GHz, we took two archival EVN data sets, which were taken as a part of the work of Giroletti et al. (2012). The visibility data were retrieved from the same EVN data archive. At 2.3 GHz and 8.6 GHz, the VLBI core properties were measured by Pushkarev & Kovalev (2012) based on a single-epoch global VLBI observation. For these measurements, we assume 10% of errors for both the flux densities and the component sizes. At 15 GHz, Kovalev et al. (2005) provide the Gaussian model-fit parameters based on a single epoch VLBA 15 GHz observation of the source made in Feb 2003. Following Kovalev et al. (2005) and Lister et al. (2016), we assume 5% and 10% of the flux and the size errors, respectively. Another VLBA 15 GHz data set from May 2009 (VLBA code BK 145) was retrieved from the MOJAVE database [9] in order to examine a characteristic time-variability of the brightness temperature at this frequency. At 43 GHz, we retrieved three VLBA 43 GHz data sets which were obtained as a part of the long-term monitoring program of Walker et al. (2018) from the NRAO data archive [10]. At 86 GHz, we adopted the brightness temperature values obtained by our GMVA observations (§3.2). At 230 GHz, the model-fit parameters from a single-Gaussian fitting are available from the early EHT observations made in 2009 and 2012 (Doeleman et al., 2012; Akiyama et al., 2015).

When the archival interferometric visibility data are available, we tried to fit the data with an elliptical Gaussian for the core and circular Gaussians for the other jet features. We changed the elliptical model to a circular one in case the elliptical Gaussian could not represent the visibility data properly or the minor axis of the ellipse was uncomfortably small, i.e., smaller than 1/5 of the observing beam. If the circular Gaussian for the core was smaller than the 1/5 beam size limit, we forced the FWHM size to be 1/5 of the observing beam and ran the model-fitting to estimate only the flux. This provided us a lower limit for the brightness temperature. Uncertainties of the model-fit parameters were then estimated following Schinzel et al. (2012). Finally, the apparent brightness temperature $T_{\rm B,app}$ was calculated by using Eq. 3.1 and the standard error propagation was used to estimate the uncertainties of the $T_{\rm B,app}$ values.

---

[8] http://archive.jive.nl/scripts/avo/fitsfinder.php

[9] https://www.physics.purdue.edu/MOJAVE/

[10] https://archive.nrao.edu/archive/advquery.jsp

Results

The properties of the VLBI core obtained by our independent analysis and from the literature are summarized in Table 3.7 The apparent brightness temperature values are plotted against the observing frequency ν in Fig. 3.24. There is a clear anti-correlation between the frequency and the brightness temperature, i.e., the lower brightness temperature values at higher frequencies. Also, the brightness temperature appears to be more time variable at lower frequencies. We calculate the Pearson correlation coefficient ρ using values of $\log T_{\rm B,app}$ and $\log \nu$. We find the coefficient $\rho = -0.82$ at high significance (> 99.99%). We consider that the correlation is strong against the time variability because our $T_{\rm B,app}$ values were obtained from different observing epochs for all frequencies. The strong correlation allows to model the relationship between ν and $T_{\rm B,app}$ by using the following power law:

$$\log T_{\rm B,app} = a \times \log \nu + b \quad . \tag{3.12}$$

We find that the power-law can describe the data with $a = -(0.46 \pm 0.06)$ and $b = 1.2 \pm 0.1$. The model also satisfies the lower limits at 1.6 GHz.

Discussions

We recall that the VLBI core of M 87 has large synchrotron opacity at least at $\lesssim 86$ GHz (see, e.g., §3.2) and is apparently located further downstream of the flow at lower frequencies (Hada et al., 2011). These authors estimate the absolute position of the radio core from the central engine, $z_{\rm core}(\nu)$, to be

$$z_{\rm core}(\nu) = A(\nu/{\rm GHz})^{-B} + C \tag{3.13}$$

where $A = 1.40 \pm 0.16$ mas, $B = 0.94 \pm 0.09$, and $C = -(0.041 \pm 0.012)$ mas at observing frequencies $\nu \lesssim 43$ GHz. This allows us to associate the observed brightness temperature values with those of the underlying flow at certain characteristic distances from the central engine. In this context, we can interpret the strong correlation between $T_{\rm B,app}$ and ν as larger brightness temperature at further downstream of the jet of M 87. We note, however, that Hada et al. (2011) obtained this relationship based on their astrometric VLBA observations up to 43 GHz. Therefore, we use the above relationship as a guidance to estimate the core position at sufficiently low frequencies. For instance, we estimate that the core is located at $z_{\rm core} \sim 0.55 \pm 0.06$ mas westward of the central engine at 1.6 GHz (or equivalently at a deprojected distance of $(247 \pm 29)R_s$ for a viewing angle $\theta = 18^\circ$).

The brightness temperature measured at 230 GHz is almost unaffected by the Doppler boosting if the core is sufficiently close to the central engine where the sheath of the jet is very slow. Under this assumption, the Doppler factor of the inner jet is directly obtained by the brightness temperature ratio between any frequency and 230 GHz. The brightness temperature ratio between 1.6 GHz and 230 GHz is $\sim (230/1.6)^{-(0.46\pm0.06)} \sim 9.7 \pm 2.9$ based on our power-law model. Accordingly, a Doppler factor of $\delta = 9.7 \pm 2.9$ is expected at $z_{\rm core} \sim 0.55 \pm 0.06$ mas. For the jet viewing angle of $\theta = 18^\circ$, however, we find that the Doppler factor is always smaller than ~ 3.2 for any bulk Lorentz factor (see Fig. 3.25). For larger viewing angles, the maximum Doppler factor is even smaller. In order to explain $\delta \sim 9.7$, the viewing angle has to be quite small (e.g., $\lesssim 10^\circ$). The bulk Lorentz factor Γ also has to be large (e.g., $\Gamma \gtrsim 3$ at $z_{\rm core} \sim 0.5$ mas). Such a small viewing angle is however very unlikely for M 87 (see Walker et al. 2018 and references therein). Also, the bulk Lorentz factor of $\gtrsim 3$ is achieved only when the jet is sufficiently accelerated at much longer distances from the central engine (e.g., one arc-second or $\sim 10^5 R_s$ deprojected distances; see Mertens et al. 2016).

Thus, the Doppler boosting scenario could not explain the large brightness temperature at low frequencies. In this regard, it is important to recall that the brightness temperature represents the microscopic energy of the particles emitting the synchrotron radiation [11]. Thus, the higher brightness temperature at further downstream of the jet may be directly understood as intrinsic enhancement of the microscopic particle energies due to in-situ particle accelerations.

3.4 KVN multi-frequency VLBI monitoring of M 87

M 87 is also known to be variable not only in the radio frequencies but also in the GeV and TeV energy bands (e.g., Acciari et al. 2010; Abramowski et al. 2012; Hada et al. 2014; Avachat et al. 2016). On weekly timescales, the flux density variabilities of the radio core and γ-ray are occasionally correlated, suggesting that the compact inner radio jet of M 87 contributes to the production of the high energy emission in this source (e.g., Acciari et al. 2010; Hada et al. 2014). For blazars which have quite small viewing angles, correlated multi-wavelength flux density

---

[11] Strictly speaking, this is true only when the core is sufficiently optically thick. As we discussed elsewhere, however, there are several evidences suggesting that the core is optically thick at least at $\lesssim$ 86 GHz.

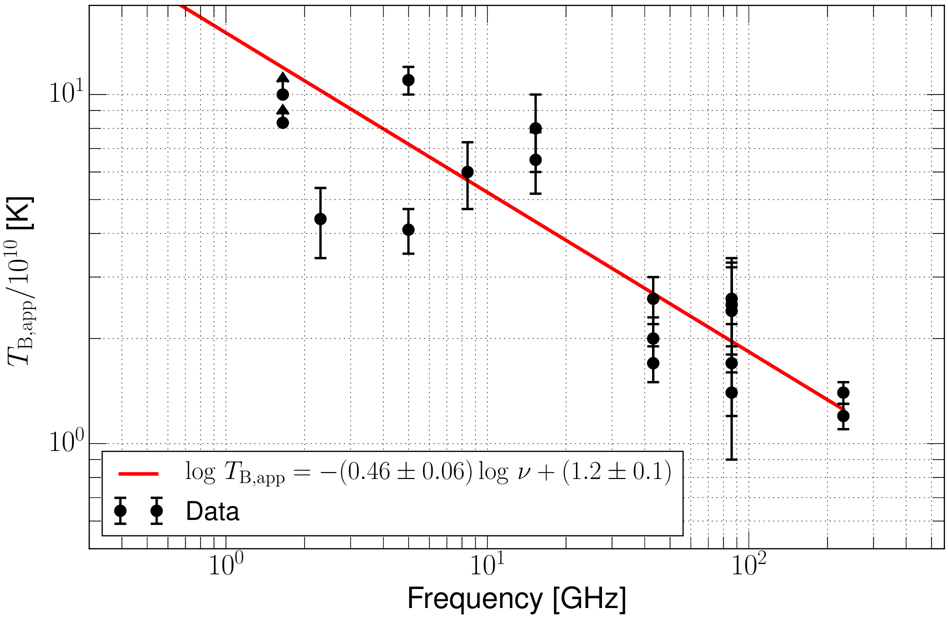

Fig. 3.24 Brightness temperature of the core of M 87 at different frequencies. The red solid line shows a power-law fit to the data (black dots). The upper arrows indicate lower limits of the brightness temperature.

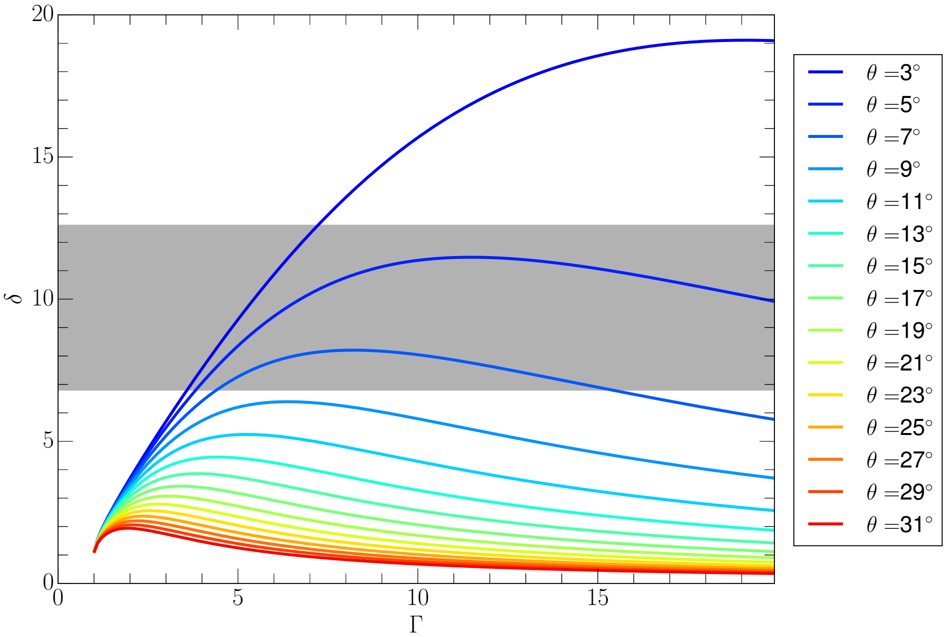

Fig. 3.25 Doppler factor δ versus bulk Lorentz factor Γ required to explain the larger brightness temperature at lower frequencies for different viewing angles in the jet of M 87. The Doppler factor required to explain the brightness temperature ratio between 1.6 and 230 GHz is shown as the gray shaded area.

Table 3.7 Gaussian modelfit properties of the VLBI core of M 87 at different frequencies. We refer to Table 3.2 for the GMVA 86 GHz model parameters. From the left, each column shows (1) the central observing frequency, (2) the observing epoch (in year/month/day) and the project code (for archival data), (3) the interferometric beam size (obtained for the uniform weighting), (4) the core flux density, (5) the core FWHM size (or the FWHM along the major axis for an elliptical Gaussian), (6) the ratio between the minor and the major axis of the elliptical Gaussian, (7) the position angle of the major axis, and (8) the apparent brightness temperature.

ν [GHz]	Epoch, Code [YYYY/MM/DD]	Beam (mas×mas, deg)	S_ν [Jy]	$\psi_{\rm maj}$ [mas]	Ratio [$\psi_{\rm min}/\psi_{\rm maj}$]	PA [degree]	$T_{\rm B,app}$ [10^{10} K]
1.65^a	2008/03/02, EA 036A	12.8×16.8, 81.3	1.94 ± 0.20	< 2.92	1.0	0.0	> 10
	2009/03/07, EA 039	12.0×17.0, 76.4	1.50 ± 0.20	< 2.84	1.0	0.0	> 8.3
2.30^b	2002/03/06	2.37×6.62, −8.0	1.42 ± 0.14	2.74 ± 0.27	0.46	−71	4.4 ± 1.0
4.99^c	2009/06/13, EG 040D	0.97×3.12, −33.6	1.30 ± 0.16	1.25 ± 0.05	0.60	−57	4.1 ± 0.6
	2012/09/12, EG 063B	0.81×1.69, 88.2	1.64 ± 0.13	1.32 ± 0.03	0.43	−73	11 ± 1
8.60^b	2002/03/06	0.63×0.90, 1.83	1.30 ± 0.13	0.60 ± 0.06	1.0	0.0	6.0 ± 1.3
15.3	2003/02/05, BL 111^d	0.48×1.00, −8.8	1.39 ± 0.07	0.41 ± 0.04	0.66	N/A^j	6.5 ± 1.3
	2009/05/22, BK 145^e	0.44×0.84, −5.1	1.16 ± 0.06	0.32 ± 0.03	0.74	−37.4	8.0 ± 2.0
43.1^f	2009/03/13, BW 092^h	0.16×0.31, −3.4	0.89 ± 0.06	0.15 ± 0.01	0.77	42.4	2.6 ± 0.4
	2013/01/12, BW 093A	0.15×0.31, −3.9	0.84 ± 0.04	0.18 ± 0.01	0.60	−37.2	1.7 ± 0.2
	2013/06/03, BW 106	0.16×0.30, −6.8	0.60 ± 0.03	0.14 ± 0.01	0.73	48.2	2.0 ± 0.3
230^g	2009/04/5-7	0.06×0.06, 0.0^i	0.98 ± 0.04	0.040 ± 0.002	1.0	0.0	1.2 ± 0.1
	2012/03/21	0.06×0.06, 0.0^i	0.98 ± 0.05	0.043 ± 0.002	1.0	0.0	1.4 ± 0.1

Notes. The corresponding references are : **(a)** Asada et al. (2014), **(b)** Pushkarev & Kovalev (2012), **(c)** Giroletti et al. (2012), **(d)** Kovalev et al. (2005), **(e)** Kovalev et al. (2007), **(f)** Walker et al. (2018), **(g)** Doeleman et al. (2012); Akiyama et al. (2015). **(e) & (h)** : This data set was also fitted by circular Gaussians in order to cross-identify the VLBI components in the quasi-simultaneous GMVA 86 GHz image (the parameters are available in Table 3.4). The brightness temperatures estimated by the different methods agree well within observational uncertainties. **(i)** : The original publications do not provide an estimate of the synthetic beam size. In order to provide a characteristic angular resolution of the instrument, here we define a circular beam by the inverse of the maximum baseline lengths of the visibility data. **(j)** : The authors do not report the position angle of the elliptical Gaussian.

variabilities are frequently observed. Such behavior is well explained by (i) the extreme Doppler beaming of the emission from a superluminal jet component which is moving close to the line of sight or (ii) the inverse-Compton scattering of the internal (or background) radiation from the jet (or accretion disk, BLR, and NLR) (see Boccardi et al. 2017 and reference therein). For radio galaxies with much larger viewing angles such as M 87, however, the Doppler boosting is much weaker. The weak boosting makes it difficult to understand the exact origin of their radio-γ correlation. The exact origin of the γ-ray ray in M 87 is more ambiguous due to the presence of the jet component HST-1 which is located far from the core (~ 1000 mas) but exhibits strong flaring activities across different observing wavelengths (e.g., Cheung et al. 2007; see the discussions in Abramowski et al. 2012 for an overview for M 87). In this context, long-term radio flux density monitoring of the nuclear region of M 87 at high cadence (e.g., bi-weekly) provides important observational constraints to study the spatial origin and physical nature of the radio and γ-ray variabilities.

Another important aspect of monitoring the VLBI core flux density, especially at multiple frequencies, is that it allows us to study the detailed shape of the synchrotron spectrum and its time evolution without ambiguity. We recall that the electron energy distribution and the magnetic field strength near the central engine are critical elements in various AGN jet launching models (e.g., Blandford & Znajek 1977; Blandford & Payne 1982). Theoretical studies show that a strong magnetic field particularly helps effective jet launching (see Yuan & Narayan 2014 and references therein for a review). One observable signature of the jet launching models with such strong magnetic fields is that the resulting synchrotron radiation will have a significantly inverted or at least flat spectrum up to the observing frequencies of $\gtrsim 100$ GHz (e.g., Broderick & Loeb 2009; Kino et al. 2015). Our analyses of the core brightness temperature at 86 GHz and quasi-simultaneous synchrotron spectrum analysis at 43, 86, and 230 GHz support such scenarios (§3.2 and 3.3). Nevertheless, those analyses did not fully address the fast (i.e., weekly-scale) time variability issue in great detail. In this regard, a fully-simultaneous multi-frequency VLBI core flux density monitoring is necessary, especially at short millimeter wavelengths.

In this section, we present fully-simultaneous VLBI flux density monitoring of M 87 performed at 22, 43, 86 GHz and up to 129 GHz by the Korean VLBI Network over the past four years (2013-2016). Using the data, we especially investigate (i) the long-term and short-term variability properties of the VLBI core light curves and (ii) the synchrotron spectrum of the nuclear region.

3.4.1 Observations and data processing

M 87 was observed by the KVN between Dec. 2012 and Dec. 2016 (in total 31 epochs) as one of the samples included in the interferometric monitoring of gamma-ray bright AGNs program (iMOGABA; Lee et al. 2016). The observations were performed at four different observing frequencies ν simultaneously using the multi-frequency KVN receiver system (Han et al., 2008); 21.700-21.764 GHz (K band), 43.400-43.464 GHz (Q band), 86.800-86.864 GHz (W band), and 129.300-129.364 GHz (D band). Only left-circular polarization was observed with the electronic bandwidth of 64 MHz per each frequency band. The data calibration involved standard VLBI calibration procedures provided by the AIPS software and the frequency phase-transfer as well. Especially, the latter successfully removed fast phase fluctuations induced by the atmosphere at short millimeter wavelengths. Details of the data acquisition, correlation, post-processing, calibration, and especially the phase transfer technique are provided in the literature (see, e.g., Lee et al. 2015, 2016; Algaba et al. 2015; Hodgson et al. 2016). Fringes were successfully detected at the high frequencies (i.e., W and D bands) without ambiguity thanks to the frequency phase transfer. After the a-priori calibration, we averaged the visibility data in both frequency and time. The channel averaging was made for each frequency band separately and the time averaging was made for 30 sec for K and Q bands and 10 sec for W and D bands, respectively. Before the imaging, a certain portion of data suffering from apparent station issues or poor weather conditions were flagged.

The DIFMAP package was used for the initial source imaging. We ran CLEAN and phase-only self-calibration iteratively to calibrate the residual phase drifts. No amplitude self-calibration was made because KVN consists of only three identical KVN stations and there is no closure amplitude relationship. We found signatures of extended and asymmetric jet-like structures at 22 GHz and 43 GHz by excess of flux densities located along the known M 87 jet direction and also by non-zero closure phases. At 86 GHz and 129 GHz, however, the data did not show a clear signature of the extended jet. After the phase self-calibration, we fitted a circular Gaussian model to each visibility data set and obtained the core flux density S_{tot} (in Jy), the FWHM size of the core d (in mas), and the peak flux density (in Jy/beam). The uncertainties of these parameters were estimated following Lee et al. (2016), in which the authors estimated the errors based on the finite signal-to-noise that varies from session to session. At 129 GHz, we adopted a rather large 30% of the flux density value as the uncertainty. This number is obtained based on the scatter of the erroneous residual phases which result from the relatively low SNR at D-band. A possible amplitude loss at the D-band due to the decoherence was also investigated by averaging the data in time from 2 sec to 60 sec and measuring the peak intensity value in the CLEAN image. At the D band, we found that the 10 sec averaging could cause less than 10% of amplitude loss in all epochs. The decoherence loss is most likely smaller at the lower frequencies. The 10% loss is also small compared to the 30% flux uncertainty at the D-band. Therefore, we ignore the decoherence in the following discussions.

3.4.2 Results and analysis

A summary of the observations and the results of the core flux density measurements are shown in Table A.1 of Appendix A. We find that 43%, 65%, 76%, and 38% of all the model-fit components are spatially resolved at the K, Q, W, and D-band, respectively. The mean values of the FWHM sizes of the resolved components are 0.8 ± 0.3, 0.55 ± 0.11, 0.42 ± 0.13, and 0.23 ± 0.09 mas at the K, Q, W, and D-band, respectively. The errors in the sizes were obtained by the standard deviation of each distributions. We recall that the jet of M 87 is resolved into the compact core and the edge-brightened jet on spatial scales even smaller than 0.2 mas (see §3.2). Therefore, the KVN core flux density and size measurements represent the properties of the partially resolved mas-scale core-jet structure on $\lesssim 0.8$ mas (the 22 GHz core size). This angular scale is equivalent to $\lesssim 100R_\mathrm{s}$ projected linear distance.

Figure 3.26 shows the core flux light curves at the four frequency bands. We find that the core flux does not strongly vary beyond $\sim 1\sigma$ error during the four years. We also calculate time-averaged core flux densities by including both resolved and unresolved components. The average flux densities are 1.90 ± 0.15, 1.44 ± 0.19, 1.22 ± 0.14, and 0.88 ± 0.11 Jy at the K, Q, W, and D band, respectively. These values appear to be broadly consistent with previously published core flux densities on similar spatial scales. For instance, Acciari et al. (2010) report ~ 1.2 Jy of the core flux density within 1.2 mas from the intensity peak based on the VLBA 43 GHz observations of the jet of M 87 during its quiescent period. This is comparable to our Q-band flux, which is ~ 1.4 Jy. We also test significance of the variability by computing the reduced chi-square χ^2_red for all the light curves. The χ^2_red values are ~ 0.5, ~ 1, ~ 0.4, and ~ 0.2 at the K, Q, W, and D-band, respectively. This suggests no significant flux density variabilities. Nevertheless, we also note that there is an exceptional flux enhancement in early 2016 when the core flux increased from ~ 1.5 Jy to ~ 2.0 Jy at 43 GHz. The flux enhancement is also clear in the visibility domain (see Fig. 3.27). At 43 GHz, a $\sim$500 mJy visibility amplitude enhancement is significant against 1σ visibility amplitude error of ~ 50 mJy. Comparable visibility amplitudes in the two adjacent epochs (2015-12-28 and 2016-01-13) also suggest that such a flux enhancement is unlikely due to calibration errors. Similar core brightening is seen at 22 GHz and 86 GHz as well, although the trend is less clear at 129 GHz because of the small number of reliable flux measurements.

We also calculate the spectral index of the core in each epoch by fitting a power-law model to the data ($S \propto \nu^{+\alpha}$). The spectral index light curve is shown in Fig. 3.28. The spectral index shows some oscillations with a ~ 1 yr timescale period and another trend of spectral steepening over longer period. Nevertheless, the time-averaged mean value of the spectral index is $\langle\alpha\rangle = -(0.37 \pm 0.10)$ (i.e., mildly steep core spectrum) and most of individual spectral index values are consistent with $\langle\alpha\rangle$ within their uncertainties. We note that this spectrum is different

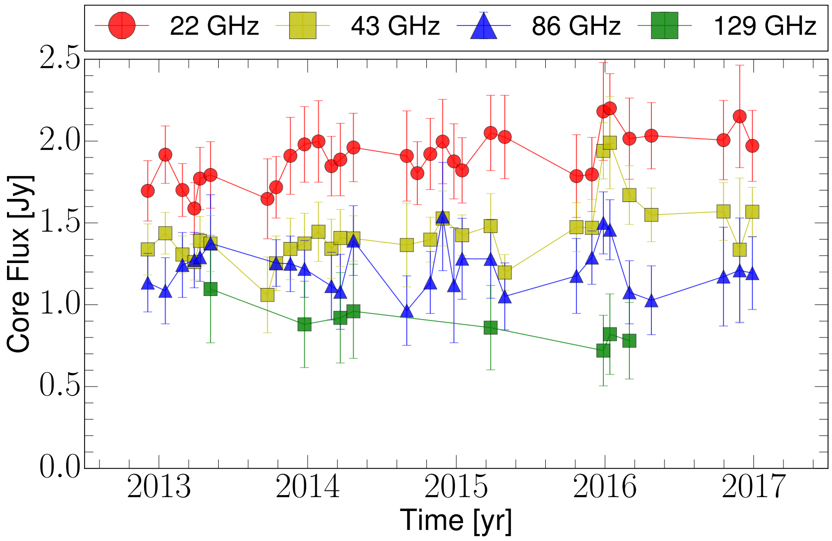

Fig. 3.26 Multi-frequency core flux density light curves obtained by the KVN observations described in the text.

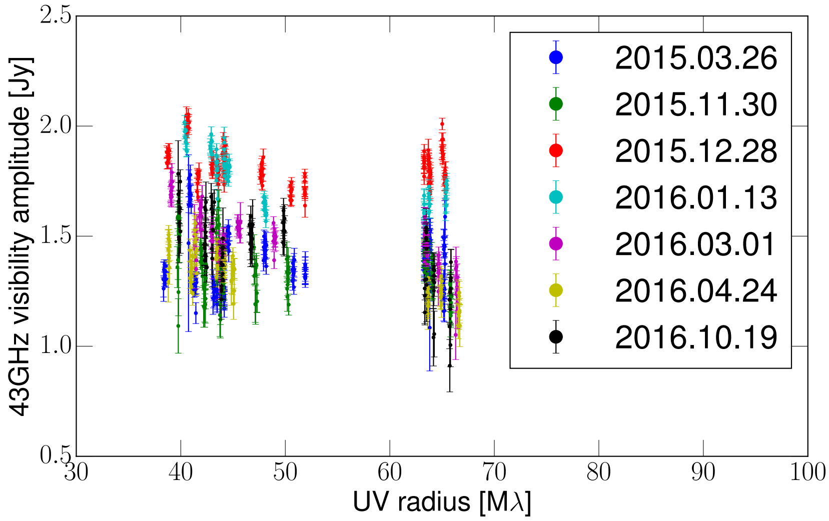

Fig. 3.27 KVN visibility amplitudes of M 87 versus the (u, v) distance at 43 GHz. The legend indicates the observing epochs in the year-month-day format. Note the clear high flux level during 2015-12-28 and 2016-01-13.

from what we found from our earlier analysis of the quasi-simultaneous VLBI observations of M 87. The main reason could be significantly larger beam sizes of KVN. This issue is examined in more detail as follows.

We note that the KVN is known to have limited (u, v) coverage and this could have a significant effect on the core spectral index measurement (see, e.g., Lee et al. 2014, 2016). For instance, the array sensitivity will be different to the extended emission at different observing

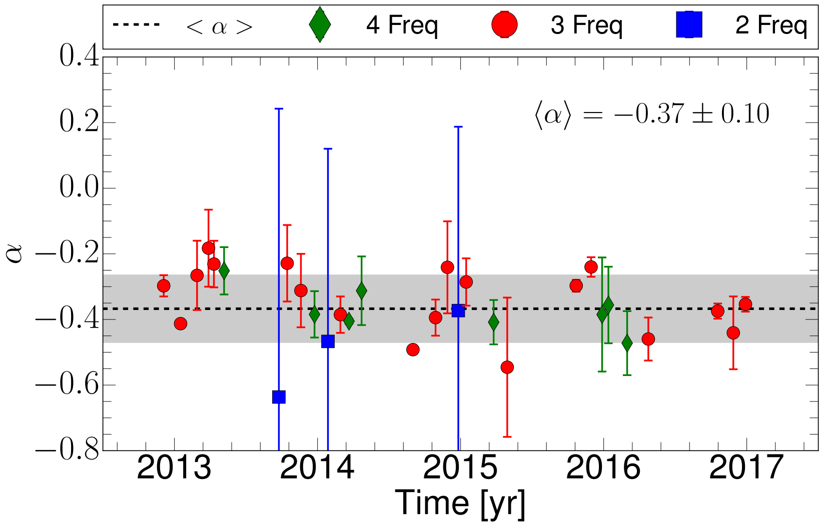

Fig. 3.28 Spectral index light curve of the core of M 87 ($S \propto \nu^{+\alpha}$) between any KVN observing frequenciesKVN observing frequencies. Different symbols in each epoch denote the different number of frequencies available for the power-law fit. The broken line and the shaded region denote the mean and standard deviation of α, respectively.

frequencies purely due to the frequency-dependent (u,v) coverage. We have performed a dedicated imaging simulation in order to investigate this effect and the details of the methods and the results are available in the published literature (see Appendix A of Kim et al. 2018a). We find that an artificial spectral steepening of $\Delta\alpha \sim -(0.23 \pm 0.02)$ is easily possible for the M 87-like jet structure only due to the (u,v)-coverage effect. This corresponds to $\sim 31-36\%$ of flux density decrease from 22 to 129 GHz, suggesting that the spectral index of the core of M 87 is most likely close to zero up to 129 GHz.

We have verified this conclusion by comparing non-simultaneous M 87 core flux measurements available from earlier publications. In this comparison, we assume that the flux density time-variability is negligible, as the KVN data suggest. We pay extra attention to the different angular resolutions of the instruments and the sizes of the core in order to compare the flux densities on a comparable angular scale. First, Pushkarev & Kovalev (2012) obtained the core flux and FWHM size of ∼ 1.3 Jy and ∼ 2.6 mas at 8.6 GHz, respectively. At 2.6 GHz, the authors also obtained a flux density ∼ 1.4 Jy and the size of ∼ 2.6 mas along the major axis of an elliptical Gaussian. Second, the MOJAVE program (Lister et al., 2016) report the core flux of 0.99 ± 0.22 Jy and the size of 0.26 ± 0.44 mas based on 34 epochs of VLBA 15 GHz observations. Third, we take the EHT 230 GHz observations performed in 2009 (Doeleman et al., 2012) and 2012 (Akiyama et al., 2015). The observations report a flux density of ∼ 1 Jy and a size of ∼ 40 μas for an ultra-compact plasma. We note that the 2.6 GHz core size is too large compared to the model-fit size we are discussing here. Therefore, we take the 2.6 GHz

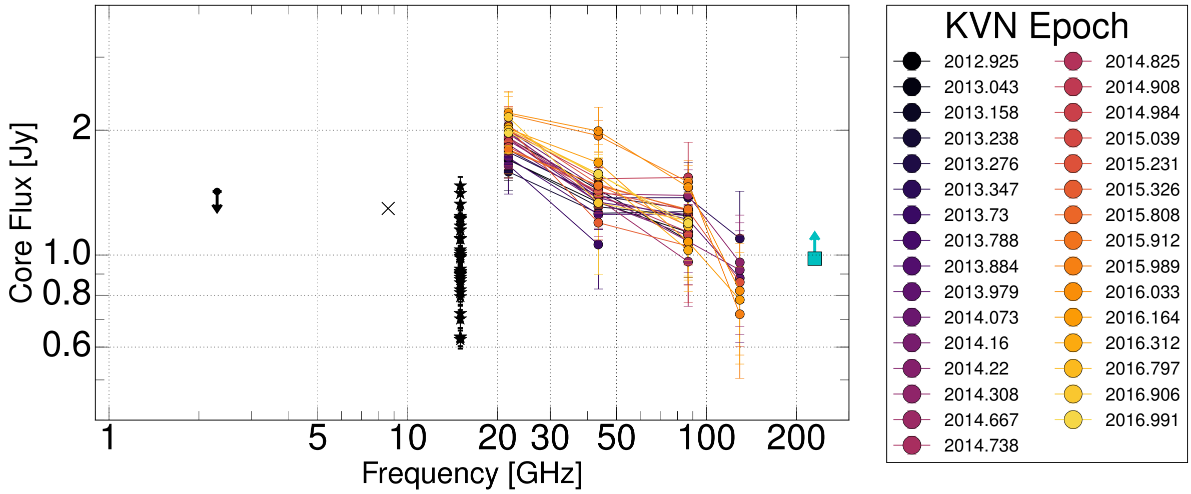

Fig. 3.29 Radio spectrum of the M 87 core region in log-log scale. Different KVN observing epochs are shown with different colors in the legend box. The arrows at 2.6 GHz and 230 GHz indicate upper and lower limits, respectively. The cross and star symbols indicate the core flux density measurements at 8.6 GHz and 15 GHz, respectively. The fully-simultaneous KVN observations are shown by the solid lines. References of the multi-frequency flux information other than the KVN results are (in order of increasing radio frequency): Pushkarev & Kovalev (2012); Lister et al. (2016); Doeleman et al. (2012); Akiyama et al. (2015).

flux as an upper limit with regard to the KVN results. For similar reasons, we regard the EHT flux as lower limits at 230 GHz in our comparison.

Figure 3.29 shows the global radio spectrum of the core region based on the multi-frequency core flux obtained on similar angular scales. There is no clear signature of steep or inverted spectra. In particular, we note that the long-term 15 GHz core flux (FWHM $\sim$ 0.26 mas) is also quite comparable to our results from the four-years of the KVN observations at 86 GHz and 129 GHz (FWHM $\sim$0.42 mas and $\sim$ 0.23 mas, respectively). By calculating the non-simultaneous but resolution-matched spectral index, we find $\alpha_{15-129\,\mathrm{GHz}} \sim -(0.03 \pm 0.23)$. This spectrum agrees well with the lower limit provided by the EHT observations. We note that the KVN 22 GHz core flux density appears slightly high because of more contribution of the extended jet emission. But previous studies show that the core already has a substantially flat spectrum on $\sim$ 1 mas scale (see Fig. 4 of Hada et al. 2012). Therefore, we conclude that the M 87 core on a submilliarcsecond scale has a substantially flat spectrum at least up to 129 GHz and possibly up to 230 GHz.

3.4.3 Discussion

Flux density variability

As for the light curves, the lack of significant core flux density variability during 2013-2016 is interesting, but may not be surprising. Independent groups of researchers have monitored M 87 at the TeV regime ($\gtrsim$100 GeV photon energy) during the same period. Their preliminary reports suggest no statistically significant variabilities in the daily and monthly light curves between 2012-2015 (Sitarek & the MAGIC Collaboration, 2017; Avila et al., 2017). However, Abramowski et al. (2012) report that, in early 2010, a strong TeV flare occurred in M 87 but no significant radio brightening occurred in the core. Therefore, the lack of the radio variability does not necessarily imply that the source was in a quiescent state over the entire period.

On the other hand, Walker et al. (2018) report that the VLBA observed the jet of M 87 at 43 GHz in early 2016 in response to new significant TeV flares. The authors report that no significant jet brightening was detected by the triggered VLBA observations. The earliest VLBA observation of M 87 made by Walker et al. (2018) is 2016 Mar 14 for the 2016 epoch. It is intriguing that our observations show the core brightening in slightly earlier epochs than Mar 2016 (2015 Dec 28 and 2016 Jan 13; the corresponding MJD 57384 and 57401, respectively). In this context, the exceptional flare captured during the KVN monitoring period may suggest a connection between the radio and the TeV, similar to the previous events which accompanied the significant VLBI core brightening by a few 100 mJy over the timescale of a few weeks in the radio band (Acciari et al., 2010; Hada et al., 2014). In the light of this, the Fermi space satellite data of M 87 (100 MeV–100 GeV photon energies) are being analyzed at the time of concluding this thesis in order to see if there exists a significant correlation between our radio and the space satellite γ-ray light curves.

Implication of the core spectrum

The featureless flat spectra of compact radio sources have been interpreted as a clear signature of inhomogeneous plasma consisting of multiple components with different internal energies (i.e., “cosmic conspiracy”; Cotton et al. 1980). We note that the KVN data alone do not allow an accurate spectral decomposition because they lack the required spatial resolution. In spite of this limitation, we can infer that the core region consists of different plasma components with high ($\gtrsim$100 GHz) and low (e.g., $\lesssim$ 100 GHz) synchrotron peak frequencies. The former would correspond to the large internal energy of the plasma. We also note that the core of M 87 radiates the synchrotron emission quite close to the central engine at short millimeter wavelengths (e.g., Hada et al. 2011). Therefore, our results may support the widely investigated AGN jet launching models with strong magnetic fields in the central engine (e.g., Broderick &

Loeb 2009; Kino et al. 2015). This is also consistent with our conclusions in §3.2 and §3.3. The source spectrum in the intermediate frequency range ($15-86$ GHz) is also interesting because this is associated with a moderate peak frequency value. This feature may not be associated with the optically thin jet whose spectrum is already steep at centimeter wavelengths (e.g., Hovatta et al. 2014). Theoretical studies suggest that the entire base of the jet of M 87, whose size is $\sim 40\,\mu$as (Doeleman et al., 2012), could not have a too strong magnetic field. For instance, Kino et al. (2015) show that, if the magnetic field is as strong as ~ 300 G, the pure electromagnetic jet power will exceed the observed total jet power of M 87. Based on this, the authors suggest that the jet base may consist of both strong and weakly magnetized plasma. In this context, the latter may contribute to the flat spectrum in the intermediate frequency ($15-86$ GHz).

3.5 Summary of the multi-frequency VLBI observations

We summarize the main conclusions based on the multi-frequency VLBI observations of M 87 as follows.

- We measured the synchrotron spectrum of the VLBI core region by combining quasi-simultaneous VLBI observations performed at 15 GHz (May 2009), 43 GHz (Mar 2009), 86 GHz (May 2009), and 230 GHz (Apr 2009). Our analysis suggests a value for the synchrotron turn-over frequency of $\sim 110-130$ GHz and the turn-over flux density of $\sim 1.1-1.5$ Jy for the optically thin spectral index of $\alpha \sim -(0.3-1.0)$ ($S \propto \nu^{+\alpha}$). The exact value of the synchrotron self-absorption magnetic field strength however remains ambiguous due to the uncertainties in the core sizes and the time-variability of the core flux in this epoch.

- The same data sets were analyzed to study apparent motions in the inner jet of M 87 within 0.5 mas from the VLBI core. Taking the advantage of the high-resolution jet structure information provided by the GMVA 86 GHz image, we were able to cross-identify several jet as well as counter-jet components and detect their systematic outward motions (but with less significance for the counter-jet). Overall, the components move at slow speed ($\beta_{\rm app} \lesssim 0.2$). But there is a strong correlation between the distances from the core and the apparent speeds, suggesting mild jet acceleration.

- The apparent brightness temperature of the core is generally low at high frequencies (e.g., $\lesssim 3\times10^{10}$ K at $\gtrsim 43$ GHz), but significantly larger values are found at lower frequencies (e.g., a lower limit of $\sim 10^{11}$ K at 1.6 GHz). In order to understand this behaviour, we applied a physical model in which the apparent brightness temperatures at lower frequencies are more Doppler-boosted due to the faster accelerating flow. We find that the required large Doppler factor can be hardly achieved in the inner jet of M 87. The more plausible scenario is an intrinsically larger brightness temperature due to the increasing internal energies of the jet particles at larger distances from the central engine.

- The multi-frequency flux density and spectral index light curves of the core of M 87 were obtained based on the multi-year VLBI flux monitoring with the KVN. The core does not show a significant flux variability at $22-129$ GHz during 2013–2016 except a significant core brightening in late 2015 and early 2016 which may be associated with a near-in-time TeV flare reported in literature (Walker et al., 2018). The spectral index of the core is also stationary in time, but weak level of variabilities are seen. The time-averaged core spectrum suggests a persistently flat spectrum up to at least 129 GHz, which is an indication of a large magnetic field strength in the base of the jet.

Chapter 4

Millimeter VLBI polarimetry of 3C 84

Parts of this chapter have been published in the following journal article; Kim et al. 2019.
Credit: Kim et al., A&A, 622, 196, 2019, reproduced with permission © ESO.

4.1 Introduction

Magnetic fields in the vicinity of central black holes (BHs) play a central role in the launching, acceleration, and collimation of relativistic jets in active galactic nuclei (AGN). Radio polarimetry at high angular resolution (i.e., VLBI polarimetry) allows to study the strength and topology of the magnetic fields near the central engine. Based on the theory of synchrotron radiation, the radio emission from AGN jets can be linearly polarized up to $\sim 70\%$ if the observed region is optically thin and contains spatially ordered magnetic fields (e.g., Pacholczyk 1970; Rybicki & Lightman 1979). In contrast, previous polarimetric VLBI observations of AGN show that the degree of linear polarization is typically much lower in the VLBI core regions ($m_L \lesssim 5\%$; Lister & Homan 2005; Jorstad et al. 2007). It is well known that the intrinsic or observed degrees of the linear polarizations could be low for several reasons; (i) a high opacity in the core region and synchrotron self-absorption, (ii) a large Faraday depth and Faraday depolarization, (iii) spatially disordered magnetic fields within the observing beam (e.g., due to turbulence in plasma; see Marscher 2014), and/or (iv) depolarization due to large rotation of the polarization angle rotation within the observing band (i.e., bandwidth depolarization; see Gabuzda 2015 for a review). In this regard, observations at millimeter wavelengths are advantageous because the synchrotron opacity is reduced and the Faraday depolarization is also weaker than at centimeter wavelengths. Owing to the smaller beam size in a VLBI array operating at millimeter wavelengths, the beam depolarization will be reduced in comparison to connected interferometers or single-dish telescope observations. This makes millimeter VLBI

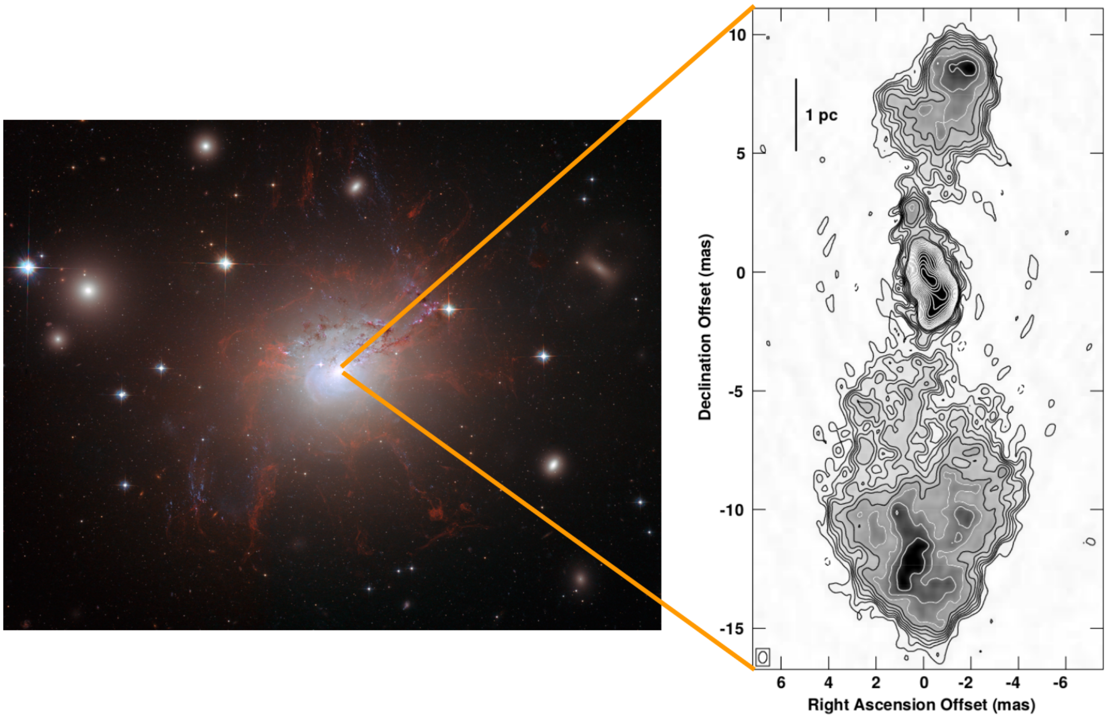

Fig. 4.1 **Left** : Hubble Space Telescope image of the host galaxy NGC 1275. Credit : NASA, ESA, and the Hubble Heritage (STScI/AURA)-ESA/Hubble Collaboration. **Right** : Deep VLBI image of the parsec-scale jet of 3C 84 at 22 GHz. The figure has been taken from Walker & Anantharamaiah (2003).

polarimetry as a suitable technique to study the polarization properties of the compact core regions in the jets of AGNs.

The radio galaxy 3C 84 (Perseus A, NGC 1275; see Fig. 4.1) has been an intriguing source in terms of its polarization properties. Previous observations in the centimeter bands suggest that the linear polarization in the core region of this source is extremely weak ($< 0.1\%$ at observing wavelengths $\lambda > 2$ cm; Taylor et al. 2006). This is an unusually low level of polarization compared to those of other sources observed at the same wavelengths (Lister & Homan, 2005), suggesting that the extremely low polarization may be associated with the intrinsic properties of 3C 84. 3C 84 is a nearby source at the redshift $z = 0.0176$ and the corresponding luminosity distance is $d_L = 75$ Mpc (Strauss et al., 1992) [1] For 3C 84, the mass of the central BH is massive ($M_{\rm BH} \sim 9 \times 10^8 M_\odot$; Scharwächter et al. 2013). The combination of the proximity and the large black hole mass thus (i) allows to reach a linear scale of ~ 0.0125 pc or $\sim 200 R_{\rm s}$ with a 50μas scale beam provided by global millimeter VLBI observations at 86 GHz and (ii) provides a good opportunity to study the polarization properties in the core region.

---

[1] Here, we assume a ΛCDM cosmology with $H_0 = 71$ km/s/Mpc, $\Omega_\Lambda = 0.73$, and $\Omega_M = 0.27$.

At short millimeter wavelengths (e.g., $\lambda \lesssim 2\,\mathrm{mm}$), Plambeck et al. (2014) observed 3C 84 using the Combined Array for Research in Millimeter Astronomy (CARMA) at 230 GHz with the Submillimeter Array (SMA) at 345 GHz, which provide arc-second scale angular resolutions at those frequencies. They reported a linear polarization degree of $m_L \gtrsim 1\%$ on arc-second angular scales. The authors also found an unusually high rotation measure RM $\sim 9\times10^5\,\mathrm{rad/m^2}$. The IRAM 30 m Telescope observed the source at 86 GHz and 230 GHz regularly and the results show comparably large but slightly smaller RM of $\sim 7\times10^4\,\mathrm{rad/m^2}$ (Agudo et al., 2014, 2018b). The CARMA and IRAM 30 m Telescope observations both show that the degree of linear polarization and the polarization angle are variable on monthly timescales. The variability timescale suggests that the origin of the linear polarization is compact (the apparent size $\lesssim 1c\times 1$ month~ 0.025 pc or ~ 0.1 mas). As mentioned above, the core of the milli-arcsecond scale jet is only weakly polarized at centimeter wavelengths (upper limit of $\sim 0.1\%$ at $\lesssim 15$ GHz with a marginal detection of $m_L \sim 0.2\%$ at 22 GHz; Taylor et al. 2006). Based on this, Taylor et al. (2006) suggested that a strong Faraday depolarization with RM$\gtrsim 10^4\,\mathrm{rad/m^2}$ could explain the non-detection of the linear polarization at the long wavelengths. In this context, the high RM obtained by Plambeck et al. (2014) and Agudo et al. (2018b) may provide a physically consistent scenario. However, the limited angular resolution of the single-dish and connected interferometer observations did not yet allow to pinpoint the exact location of the origin of the linear polarization on sub milli-arcsecond scale. In this regard, the Global Millimeter VLBI Array (GMVA) enables a sensitive polarization imaging of the source at 86 GHz and overcomes the aforementioned limitations. The observing frequency of 86 GHz also nicely bridges the gap between $\lesssim 22$ GHz and $\gtrsim 230$ GHz, which is important to better understand the results from previous observations (e.g., Aller et al. 2003; Agudo et al. 2010; Trippe et al. 2012; Plambeck et al. 2014; Nagai et al. 2017; Agudo et al. 2018b) and develop a coherent, self-consistent physical scenario.

Motivated by this, we study the multi-frequency polarization properties of the inner jet of 3C 84 at millimeter wavelengths. We make use of data sets from GMVA observations at 86 GHz and other quasi-simultaneous Very Long Baseline Array (VLBA) observations at 43 GHz and 15 GHz. In §2, we describe the details of the VLBI observations, the data reduction, and the parameter measurements. Our major findings are presented in §3 and the physical implications of the results are discussed in §4. We then provide a summary of our main conclusions in §5.

4.2 Observations and data reduction

4.2.1 GMVA 86 GHz data

We observed 3C 84 in May 2015 using the GMVA with dual circular polarization feeds (LCP and RCP) at 86 GHz. The source was observed as a part of the γ-ray emitting AGN samples regularly monitored by semiannual GMVA observations, which complement the VLBA-BU-BLAZAR monitoring program (Jorstad et al. 2017; for the GMVA see, e.g., Rani et al. 2015; Hodgson et al. 2017; Casadio et al. 2017). In total, 11 antennas observed 3C 84 in this epoch (8 VLBA and 3 European antennas). The following radio telescopes participated (abbreviations in parentheses): Brewster (BR), Effelsberg (EB), Fort Davis (FD), the Green Bank Telescope (GB), Kitt Peak (LP), Los Alamos (LA), Mauna Kea (MK), North Liberty (NL), Onsala (ON), Owens Valley (OV), and Pie Town (PT). 3C 84 was observed for 8 hrs with each VLBI scan lasting ~ 7 min (duty cycle ~ 0.5). The data from each station were recorded at a bitrate of 2 Gbps with 2 bit digitization. In each polarization, the data were channelized in 8 IFs (thus 256 MHz wide bandwidth per polarization and 32 MHz per IF per polarization). After observations, the data were correlated by the DiFX VLBI correlator of the Max-Planck-Institut für Radioastronomie in Bonn, Germany (Deller et al., 2011). We summarize the relevant details of the GMVA observations in Table 4.1.

Total intensity calibration and imaging

The correlated data were post-processed using the standard VLBI data calibration procedures available in the Astronomical Image Processing System (AIPS) (Greisen 1990; see also Martí-Vidal et al. 2012 for the overall GMVA data analysis scheme). For the phase calibration, we first removed the large sub-band delays and phase jumps across the IFs by choosing high signal-to-noise (S/N) scans using the AIPS task FRING (i.e., manual phase-calibration). After aligning the phases across the IFs for all stations, we solved the time-dependent phase variations by the global-fringe fitting using AIPS FRING. Details of the fringe-fitting parameters are as follows. We adopted a S/N threshold of 5 for the fringe detection. Since the phases were already aligned across the frequencies, we used frequency-averaged power spectra to determine a set of multi-band delays, fringe rates, and phases for all IFs. This improved the S/N of the fringe detections (i.e., `aparm(5)=1` in FRING). We adopted a rather long solution interval of 4 minutes in order to detect as many fringes as possible, especially for long baselines (see§4.2 of Martí-Vidal et al. 2012 and references therein for detailed discussions about the optimal fringe fitting procedure of the GMVA data). The solution interval was then moved forward in time in every minute step[2]. This setup allowed robust fringe detections up to a (u,v)-spacing of $\sim 3G\lambda$. After the phase calibration, the a-priori visibility amplitude calibration was performed using the AIPS task APCAL. We used the system temperature, the antenna gain, and the elevation dependent gain curves provided by the observatories. The opacity correction was made for all antennas except Onsala which already included the opacity effect in the system temperature. The cross-hand delays were solved using the cross-hand (i.e., RL or LR) power spectra of high S/N scans using the AIPS task RLDLY. After RLDLY, the data were averaged in frequency and exported outside AIPS for the imaging analysis.

We note that the fringe fitting of millimeter VLBI data is generally a quite complex procedure. The short solution interval leads to low S/N and more non-detections while the long solution interval does not sufficiently take into account the rapid phase fluctuations introduced by the atmosphere (thus leading to non-negligible decoherence and amplitude losses; see the discussions in Martí-Vidal et al. 2012). We examined the decoherence issue by calibrating the data in an independent way once again with a much shorter fringe-fitting solution interval. For the purpose, we set the fringe solution interval to be only 10 seconds and maintained the same S/N threshold (5). We also used a quite narrow fringe search window for the delays and fringe rates (± 10 ns and ± 25 mHz, respectively). This kind of approach generally helps to avoid fake fringe detections due to noise in the delay-rate space (e.g., Martí-Vidal et al. 2012). By comparing the two different calibrations, we confirmed that the decoherence amplitude loss was less than 10% in this epoch for a 10 sec time averaging. On the other hand, we found that $\sim 31\%$ of the data were lost with the short solution interval compared to the calibration which used the longer integration time. The data loss was more serious at longer baselines (e.g., $\sim 48\%$ of the data were lost for baselines involving MK). Although a certain level of data loss helps to remove noisy or unreliable measurements associated with various systematics, a data loss of more than 30% appears to be unacceptable for the imaging. Therefore, we adopted the longer solution interval for further imaging and analysis.

After the a-priori calibrations, the reduced visibility data were loaded into the Difmap package (Shepherd et al., 1994). The frequency-averaged visibilities were further time-averaged over 10 seconds. We also flagged outlying visibilities which were caused by significant antenna pointing and/or focus errors and other systematic issues. Then, we imaged the source structure in Stokes I using CLEAN and self-calibration algorithms implemented in Difmap iteratively. We paid extra attention to reproduce the visibility amplitudes at short (u,v) distances. After the final round of CLEAN and self-calibration, the achieved total flux density was comparable to the a-priori calibrated amplitudes of several inner baselines, e.g., LA-PT, LA-FD, and EB-ON.

---

[2] Specifically, we adopted `solint=4` and `solsub=4` in the AIPS task FRING which resulted in the AIPS timeranges of `0/00:00:00-0/00:04:00`, `0/00:01:00-0/00:05:00`, `0/00:02:00-0/00:06:00`, and so on.

Table 4.1 Summary of the polarimetric VLBI observations of 3C 84 in May 2015.

Stations (1)	Epoch (2) [yy/mm/dd]	$\nu_{\rm obs}$ (3) [GHz]	Beam (4) [mas, deg]	$I_{\rm peak}$ (5) [Jy/bm]	$S_{\rm tot}$ (6) [Jy]	$\sigma_{\rm I}$ (7) [mJy/bm]	$PI_{\rm peak}$ (8) [mJy/bm]	$P_{\rm tot}$ (9) [mJy]	$\sigma_{\rm P}$ (10) [mJy/bm]
VLBA(8) +GBT+EB+ON	2015/05/16	86.252	$0.048\times 0.14\ (-16)$	1.82	12.0	0.53	27.7	42.0	2.75
VLBA(10)	2015/05/11	43.115	$0.15\times 0.30\ (1.0)$	3.82	17.0	1.24	12.3	16.8	0.96
VLBA(10)	2015/05/18	15.352	$0.42\times 0.63\ (-8.7)$	4.00	28.8	1.30	<2.20	–	0.44

(1) Antennas participating in each epoch. Numbers in the bracket indicates the number of the VLBA antennas participated. (2) The observing epoch in year/month/day format. (3) Center frequency. (4) The restoring beam for the uniform weighting. Minor axis × major axis in mas (the position angle in degrees measured counterclockwise from North). (5) Total intensity peak. (6) Total flux density integrated over the entire VLBI image. (7) Total intensity rms level. (8) Linear polarization intensity peak (upper limit for 5σ significance). (9) Integrated linearly polarized flux density of the core region obtained by the quadratic sum of the integrated Stokes Q and U flux densities in the region where significant linear polarization intensities are found ("–" means no significant linear polarization in the region displayed in Fig. 4.3 and 4.4). (10) The polarization intensity noise level.

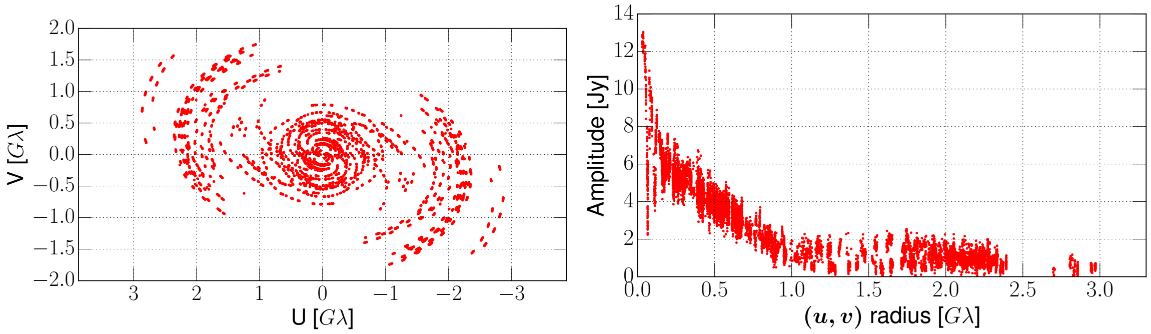

Fig. 4.2 Stokes I visibilities of the GMVA 86 GHz data. **Left** : (u,v)-coverage after the a-priori calibration and additional flagging for the imaging. **Right** : Radial distribution of the visibility amplitudes after the last round of the CLEAN and self-calibration. The visibility data were binned in 30 sec for clarity.

We also examined the accuracy of the absolute flux level of the source by making use of other calibrators (e.g., 3C 454.3, BL Lac, CTA 102, and OJ 287) following Koyama et al. (2016) and corrected for residual calibration effects. After all, we achieved $\sim$ 12 Jy of the total Stokes I flux density and estimate that this flux could be uncertain by $\sim$ 30% (see Kim et al. 2019 for more details). The resulting (u, v) coverage and the radial distribution of the visibility amplitude are shown in Fig. 4.2.

Polarization calibration

In order to correct for the instrumental polarization of each antenna, the so-called antenna D-terms have to be determined. This is done using a source model, which is decomposed into a finite number of polarized sub-regions. After the total intensity imaging, we performed additional calibrations for the linear polarization imaging as follows. First, we removed the residual gain amplitude differences between the RCP and LCP using the AIPS task CALIB. Then, the antenna polarization leakages were estimated and solved using the AIPS task LPCAL (Leppanen et al., 1995). The LPCAL procedure requires a specific input visibility data set and the corresponding source model (either CLEAN components or an image). 3C 84 is generally known as a good polarization calibrator for its low degree of polarization (e.g., Taylor et al. 2006). Also, the jet of 3C 84 appears to be more core-dominated at shorter mm-wavelengths (see, e.g., Jorstad et al. 2017). In addition, our GMVA data set of 3C 84 also covers a wide range of parallactic angles thanks to the high declination of the source. Therefore, we attempted to estimate the polarization leakages using 3C 84 itself by dividing the CLEAN model into several discrete regions. For all stations, the resulting D-term solutions were consistent across the 8 IFs. In order to check the correctness of the D-terms determined by 3C 84, we also estimated the polarization leakages using the other calibrators which were observed in the same GMVA session. Among them, we particularly selected 3C 454.3, BL Lac, CTA 102, and OJ 287, which are often used as VLBI polarization calibrators because of their large flux density and compactness. We found that the D-terms are consistent (within a few percent for the D-term amplitudes). We also made linear polarization images of 3C 84 applying the D-term solutions obtained from the other sources. The polarization morphology was overall consistent, but with the exception for D-terms derived from 3C 454.3, which is not point-like enough (see Casadio et al. 2017 and Appendix B). Our previous GMVA polarization imaging experiments show that the most accurate D-terms and best polarization image is obtained by averaging the D-term solutions obtained from different sources (Casadio et al., 2017). Therefore, all the D-terms were vector-averaged (i.e., for the real and the imaginary parts separately) and applied to the data of 3C 84 in order to obtain a final polarization image for further data analysis. The average D-terms are shown in Table 4.2. The errors were obtained by propagating the standard deviations of the real and imaginary parts of the complex D-terms. For reference, we provide the GMVA polarization images and the visibilities of the other sources observed in this epoch in Appendix B. The 86 GHz polarization morphologies of the other sources are overall consistent with their close-in-time VLBA 43 GHz polarization images available from the VLBA-BU-BLAZAR project database[3], providing further confidence on our polarization calibration.

We estimated the impact of the residual polarization leakages in the linear polarization image. Following Roberts et al. (1994), the excess of the noise level in the polarization image due to the D-term errors, $\sigma_{\rm D}$, is given by

$$\sigma_{\rm Dterm} = \frac{\Delta m}{\sqrt{N_{\rm ant} \times N_{\rm IF} \times N_{\rm scan}}} \sqrt{I^2 + (0.3 \times I_{\rm peak})^2} \tag{4.1}$$

where Δm is the uncertainty of the D-term amplitudes, $N_{\rm ant}$ is the number of the observing antennas, $N_{\rm IF}$ is the number of the IFs, $N_{\rm scan}$ is the total number of independent scans (e.g., with different parallactic angles), I is the pixel values of the Stokes I image, $I_{\rm peak}$ is the peak of the Stokes I image, and the factor 0.3 in front of $I_{\rm peak}$ accounts for the scatter of the noise across the entire polarization image (see also Hovatta et al. 2012). Based on the standard deviation of the D-term amplitudes, we assumed $\Delta m = 0.03$ (Table 4.2). The other parameters are deterministic. We took $N_{\rm ant} = 11$ and $N_{\rm IF} = 8$ from the data. For $N_{\rm scan}$, the total number of fully independent scans is $N_{\rm scan} = 8$. Accordingly, we found $\sigma_{\rm D}$ to be of order of $\sim 10^{-3} I_{\rm peak}$ (or equivalently $\sigma_{\rm D}/I_{\rm peak} \sim 0.1\%$ of systematical error in the degree of linear polarization). We find that the rms noise of the linear polarization image is higher than the total intensity by $\sim$ 2 mJy/beam (see

---

[3] https://www.bu.edu/blazars/VLBAproject.html

Table 4.2 Summary of the antenna D-terms at 86 GHz. The Green Bank Telescope was used as the reference antenna. The columns show (1) the station code, (2,3) the amplitude (m) and phase (χ) of the D-terms for the RCP, and (4,5) the same for the LCP.

Station	RCP		LCP	
	m [%]	χ [deg]	m [%]	χ [deg]
(1)	(2)	(3)	(4)	(5)
BR	5.8 ± 2.7	$-(106 \pm 16)$	7.2 ± 2.7	$-(48 \pm 20)$
EB	4.5 ± 2.1	56 ± 24	2.3 ± 2.5^a	98 ± 40^a
FD	7.9 ± 2.9	23 ± 13	7.0 ± 3.6	$-(141 \pm 25)$
GB	1.7 ± 2.4^a	$-(162 \pm 46)^a$	2.6 ± 1.3	$-(66 \pm 44)^a$
KP	3.1 ± 2.8	178 ± 30	3.8 ± 1.7	88 ± 14
LA	10.7 ± 1.6	139 ± 9	10.1 ± 2.1	32 ± 13
MK	3.9 ± 3.1	11 ± 25	4.3 ± 1.9	$-(90 \pm 23)$
NL	4.8 ± 1.6	$-(167 \pm 21)$	3.7 ± 1.3	70 ± 13
ON	5.9 ± 1.9	$-(178 \pm 27)$	4.8 ± 2.4	$-(4 \pm 36)$
OV	3.6 ± 2.4	$-(48 \pm 38)$	5.4 ± 1.7	$-(127 \pm 21)$
PT	8.2 ± 5.6	7 ± 8	9.6 ± 3.4	$-(134 \pm 21)$

Notes. a : Small D-term amplitudes induce large uncertainties in the D-term phases.

Table 4.1). This number seems to be in agreement with the value of $\sigma_{\rm Dterm} \sim 1.8$ mJy/beam for $I_{\rm peak} \sim 1.8$ Jy/beam.

The absolute electric vector position angle (EVPA χ) of 3C 84 was corrected as follows. The POLAMI (Polarimetric Monitoring of AGN at Millieter Wavelength) program[4](Agudo et al., 2018a; Thum et al., 2018; Agudo et al., 2018b), which uses the XPOL polarimeter installed on the IRAM 30 m Telescope (Thum et al., 2008), provided independently measured absolute EVPAs of several AGN sources from their observations on 2015 May 11 and 25 (i.e., five and nine days offsets from the GMVA observations, respectively). We found several overlapping sources between POLAMI and our GMVA observations. Then, we made polarization images of the corresponding AGN calibrators – 3C 454.3, BL Lac, and OJ 287 – by using the same D-term solutions which were applied to 3C 84. The spatially integrated EVPAs of the VLBI images were compared with the POLAMI results and we obtained a consistent EVPA correction value. After calibrating the absolute EVPA, we estimate possible errors in the polarization angle at 86 GHz as follows.

1. The three AGN calibrators showed consistent VLBI angle correction within $\lesssim 10^\circ$ of uncertainty. Thus, we adopt 10° as the uncertainty in the absolute EVPA correction.

---

[4] http://polami.iaa.es

2. The polarization angle of the source is correlated with the D-term phases (see Eq. 3 and 13 of Leppanen et al. 1995). The uncertainty of the former is expected to be half of the latter. Based on the mean value of the D-term phase errors, $\sim 24^\circ$ (Table 4.2), we expect that the EVPA of 3C 84 could be uncertain by $\sim 24/2 = 12^\circ$.

3. Because of the thermal noises, the EVPA could be also uncertain by $1/(2 \times \mathrm{S/N})$ radian (Roberts et al., 1994). For a signal-to-noise of ~ 10 in the polarization image, the corresponding angle uncertainty is $\sim 2.8^\circ$.

Assuming that these three uncertainties are independent of each other, we can add the errors in quadrature. Accordingly, we estimate the overall uncertainty in the polarization angle to be $\sim 16^\circ$ in the GMVA polarization image of 3C 84. We note that the signal-to-noise varies from pixel to pixel, and the third error term could increase up to $\sim 6^\circ$ for a marginal S/N of 5. But the overall uncertainty of the EVPA is nearly the same (i.e., $\sim 17^\circ$).

4.2.2 Contemporaneous 43 GHz and 15 GHz VLBA data

We also took archival polarimetric VLBA data of 3C 84 obtained at different observing frequencies. The MOJAVE program[5](Lister et al., 2009) and the VLBA-BU-BLAZAR project(Jorstad & Marscher, 2016) provide fully calibrated VLBA data of large number of AGNs (including 3C 84) at 15 GHz and 43 GHz, respectively. In order to minimize the time-variability effect in the later analysis, we searched the VLBA 15 GHz and 43 GHz databases in order to find observations which were closest in time to our GMVA observations. We found archival observations which were performed within $\lesssim 5$ days from the GMVA run. We note that the jet of 3C 84 is slow near the core ($\sim 0.1c \sim 0.1$ mas/yr$\sim 2\,\mu$as/week; Walker et al. 1994; Suzuki et al. 2012). If the time scale of the variability in the core is associated with such a jet speed, we consider that a $\lesssim$1 week time difference should be sufficiently small.

The archival observations were made with the same total bandwidth of 256 MHz per polarization using the dual circular polarization setup (i.e., RCP and LCP feeds). We made the Stokes I, Q, and U maps at the two frequencies using the Difmap package in a similar way as the GMVA images were created. We found that the noise level of the polarization image was slightly lower than the total intensity at both 15 GHz and 43 GHz. This indicates that the effects of the D-term errors are sufficiently small at these frequencies. We assume that the absolute EVPA measurement errors of these data sets are 5° and 10° at 15 GHz and 43 GHz based on Lister & Homan (2005) and Jorstad et al. (2005), respectively. The overall EVPA uncertainty was then obtained in the same way as described in §4.2.1. We summarize more details of the two data sets in Table 4.1.

---

[5] https://www.physics.purdue.edu/MOJAVE/

The VLBA 43 GHz data provided by the VLBA-BU-Blazar program contain four separated IFs with different central frequencies (43.0075, 43.0875, 43.1515, and 43.2155 GHz). The polarization calibration has been performed separately for the individual IFs (i.e., for their different D-terms and absolute EVPA corrections; see §3.1 of Jorstad et al. 2005). This allows to measure the polarization properties within the 43 GHz band. Therefore, we also made four polarization images for the four separate IFs.

4.2.3 Other VLBA 43 GHz data

Thanks to the good time coverage of the observations performed by the VLBA-BU-BLAZAR program, more VLBA 43 GHz data of 3C 84 were available during 2015 (eight epochs; Feb, Apr, May, Jun, Jul, Aug, Sep, and Dec). We have made polarization images from these data as well in order to study the time variation of the linear polarization. During the polarization imaging, additional data flagging and editing have been made if some antennas or baselines showed larger systematic errors. The BU database shows that a weak polarization feature exists near the core of the jet in all epochs during 2015. We were able to produce similar images from the same visibility data sets. But the polarization imaging appears to be less robust in some epochs (Feb, Jun, Aug, and Dec). These epochs were excluded in the further analysis. After all, reliable polarization features have been detected with high significance in four out of the eight epochs (Apr, May, Jul, and Sep). In addition to the linear polarization, we also measured the unpolarized flux density of the core in all the eight epochs by the Gaussian model-fitting analysis (see §4.2.5). Details of these data are summarized in Appendix C.

4.2.4 Contemporaneous ALMA data

Finally, we made use of publicly available quasi-simultaneous linear polarization measurements of 3C 84 made in May 2015 at shorter millimeter wavelengths, which are available from the Atacama Large Millimeter/submillimeter Array (ALMA) Calibrator Source Catalogue [6]. The ALMA observations were made at 97.5, 233.0, and 343.5 GHz and the source was unresolved up to the (u,v) distances of 537.5 $k\lambda$ at all frequencies. Based on this information, we constrain the size of the source to be $< 1/(537.5\times10^3)$ rad$\approx$ 0.38 arc second. We provide a summary of the ALMA total and polarized flux measurements in Table 4.3.

---

[6] https://almascience.eso.org/alma-data/calibrator-catalogue

Table 4.3 Summary of the ALMA archival data. The columns show (1) the observing epoch, (2) the central frequency, (3) the total flux density, (4) the degree of the linear polarization, and (5) the EVPA.

Epoch (1) [yyyy/mm/dd]	$\nu_{\rm obs}$ (2) [GHz]	$S_{\rm tot}$ (3) [Jy]	m_L (4) [%]	EVPA (5) [deg]
2015/05/31	97.5	17.14 ± 0.57	0.6 ± 0.3	82 ± 20
	233.0	9.82 ± 0.33	1.0 ± 0.3	$-(29 \pm 12)$
	343.5	6.85 ± 0.23	0.3 ± 0.3	18 ± 43

4.2.5 Model-fitting, polarization measurements, and their uncertainties

In order to parameterize the properties of the VLBI core region in Stokes I, we used the MODELFIT procedure of the Difmap package. At each frequency, the visibilities of the VLBI data were fitted by circular Gaussians. This provided us the flux density and the FWHM size of the core. We estimated the uncertainties of the parameters following Schinzel et al. (2012). For the absolute flux density at 86 GHz, we conservatively assume a flux density error of 30% due to the absolute flux density calibration (see Kim et al. 2019 for more details).

The polarized components were identified by significant local maxima of the linearly polarized intensities in the image plane. We clipped out pixels whose linearly polarized intensity values PI were smaller than $5\sigma_{\rm P}$ [7]. Similarly, pixels whose total intensities were smaller than $3\sigma_{\rm I}$ were clipped as well. Then, we estimated the polarization parameters by integrating the Stokes I, Q, and U pixel values and computing their quadratic sums or ratios. Specifically, the parameters were calculated as following:

$$Q_{\rm tot} = \Sigma Q_{i,j} \times A_{\rm pixel}/A_{\rm beam} \quad \text{(in Jy)} \tag{4.2}$$

$$U_{\rm tot} = \Sigma U_{i,j} \times A_{\rm pixel}/A_{\rm beam} \quad \text{(in Jy)} \tag{4.3}$$

$$S = \Sigma I_{i,j} \times A_{\rm pixel}/A_{\rm beam} \quad \text{(in Jy)} \tag{4.4}$$

$$P = \sqrt{Q_{\rm tot}^2 + U_{\rm tot}^2} \quad \text{(in Jy)} \tag{4.5}$$

$$m_L = P/S \times 100 \quad \text{(in percent)} \tag{4.6}$$

$$\chi = 0.5\arctan(U_{\rm tot}/Q_{\rm tot}) \quad \text{(in radian)} \tag{4.7}$$

---

[7] We note that measurements of the linearly polarized flux density is subject to the Rice bias. However, the effect of the de-biasing becomes marginal at S/N ratio of $\gtrsim 5$ (see, e.g., Wardle & Kronberg 1974). Therefore, we do not correct for it in the integration.

where Q_{tot}, U_{tot}, and S are the integrated flux densities of Stokes Q, U, and I obtained by integrating the their pixel values $Q_{i,j}$, $U_{i,j}$, and $I_{i,j}$ at each pixel (i,j), A_{pixel} and A_{beam} are respectively the areas of each pixel and the beam[8], P is the linearly polarized flux density, m_L is the degree of linear polarization, and χ is the EVPA. We assumed that the polarization flux density P was uncertain by $\sim 30\%$ at all frequencies given their low brightness. As for the unpolarized flux density S, we assumed 10% errors at 15 GHz and 43 GHz based on literature (Lister & Homan, 2005; Jorstad et al., 2005), but 30% at 86 GHz for the reasons mentioned above. The uncertainty of the linear polarization degree m_L was then obtained by the standard error propagation of P and S. Finally, the EVPA error of each component was obtained as described in §4.2.1.

4.3 Results

4.3.1 Total intensity structure and the core flux density

In Fig. 4.3 we show the polarimetric VLBI images of 3C 84 at 15 and 43 GHz in May 2015. The GMVA images, restored with different beam sizes, are shown in Fig. 4.4. In particular, the GMVA images show the detailed source structure of the edge-brightened jet at a remarkable dynamic range of ~ 3400, this is the highest to date at this frequency.

At the observing frequencies of $\gtrsim 43$ GHz, the inner jet of 3C 84 is highly edge-brightened. The edge-brightening is visible down to the core distance $z \sim 0.4$ mas at 43 and 86 GHz (see Fig. 4.5). At 86 GHz, the edge-brightening is visible down to $z \sim 0.2$ mas. At $z \lesssim 0.2$ mas, the sub-nuclear structure of the core is highly resolved in the E-W direction, featuring a complicated morphology. The morphology of the extended jet (z$\sim 0.5-4$ mas) is similar at 43 and 86 GHz when the GMVA image is restored with a slightly larger beam (c.f., Fig. 4.3 and 4.4). However, the emission is overall fainter at 86 GHz. Also, there is a bright and compact “hotspot” within the lobe-like jet structure at $z \gtrsim 2$ mas and the “hotspot” is closer to the eastern edge of the limb-brightened jet.

We show the flux densities and the FWHM sizes of the core obtained by the model-fitting analysis in Table 4.4. The FWHM size of the core is the largest at 15 GHz and is comparable at 43 and 86 GHz ($\sim$0.14 mas). However, the visibility amplitude distribution of the GMVA data at long (u,v) distances (e.g., $1.0-2.5\,G\lambda$) clearly shows presence of a smaller fine-scale structure (see Fig. 4.2). Interestingly, the flux density of the core is strongly inverted between 15 and 43 GHz. The spectrum is still slightly inverted (or at least flat) between 43 and 86 GHz

---

[8] The area of the elliptical Gaussian beam is obtained by $A_{\mathrm{Beam}} = \pi\psi_{\mathrm{maj}}\psi_{\mathrm{min}}/4\ln 2$ where $\psi_{\mathrm{maj,min}}$ are the FWHM of the elliptical Gaussian along the major and minor axis, respectively.

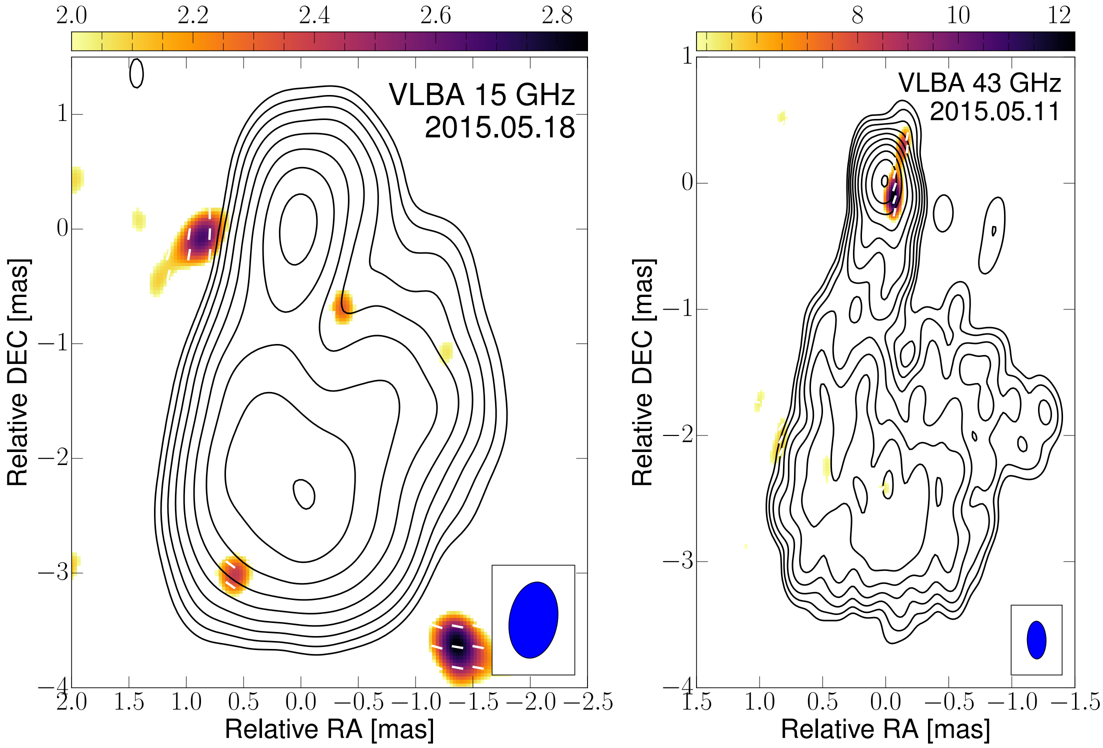

Fig. 4.3 Polarimetric VLBI images of 3C 84 at 15 GHz and 43 GHz. In both panels, the contours show the total intensity and increase by a factor of 2 from the lowest level. The color scale represents the polarized intensity (in mJy/beam). The white bars in the images display the apparent EVPA. The blue ellipses in the bottom right corners show the restoring beams. **Left** : VLBA 15 GHz image. The contours start at 30 mJy/beam. The color scale starts at 2.0 mJy/beam. **Right** : VLBA 43 GHz image. The contours start at 7 mJy/beam. The color scale starts at 4.8 mJy/beam.

Table 4.4 VLBI model-fit core properties of 3C 84 in May 2015. The columns show (1) the central observing frequency and (2,3) the total flux density and the FWHM size of the Gaussian model.

ν_{obs} (1) [GHz]	S_{mod} (2) [Jy]	FWHM (3) [mas]
86	5.6 ± 1.7	0.13 ± 0.04
43	4.8 ± 0.7	0.14 ± 0.01
15	2.6 ± 0.4	0.27 ± 0.02

(see Fig. 4.6). We model the inverted synchrotron spectrum between 15 and 86 GHz using a single power law $S \propto \nu^{+\alpha}$ where S is the flux density, ν is the observing frequency, and α

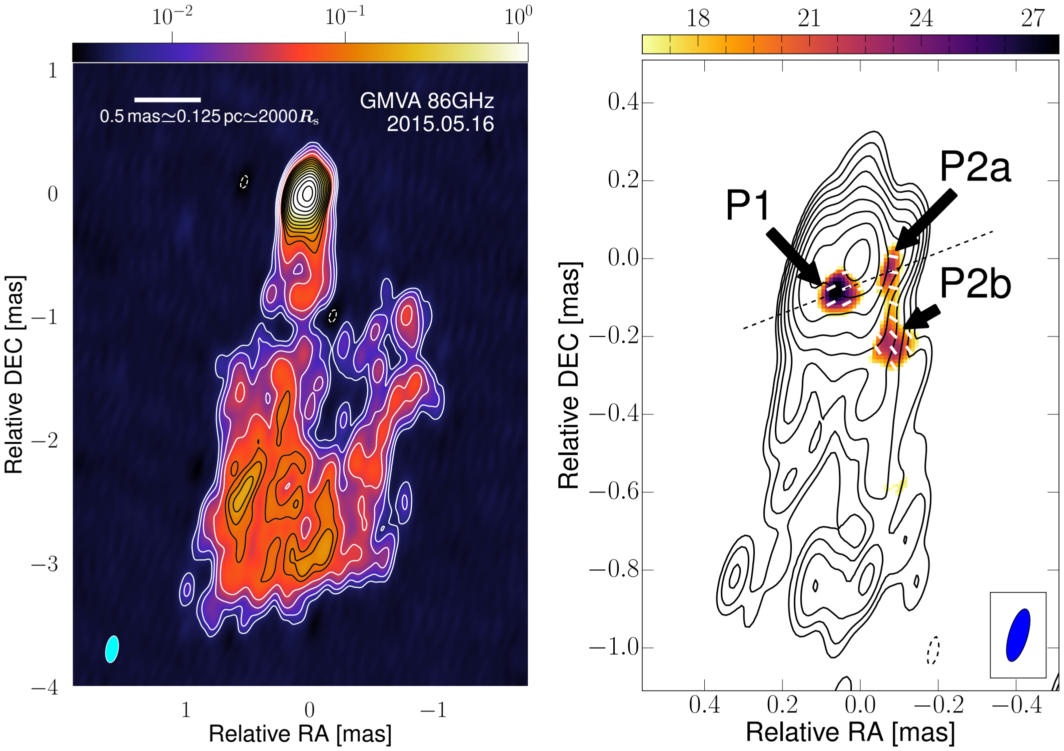

Fig. 4.4 GMVA 86 GHz images of 3C 84. In both panels, the contours show the total intensity and increase by a factor of 2 from the lowest level (5 mJy/beam). A negative contour of −5 mJy/beam is also shown with dashed lines. **Left** : The Stokes I image restored with an elliptical beam of 0.22×0.10 mas and a position angle of $-10°$. This beam is slightly larger than the full resolution offered by the GMVA data. The peak intensity of this image is 3.04 Jy/beam. The cyan ellipse in the left bottom corner illustrates the elliptical beam. The color scale represents the Stokes I pixel values in Jy/beam. The white bar and the text in the upper left corner denote the projected spatial scale in the image. **Right** : The inner jet structure obtained with the full angular resolution of the GMVA data. The color scale represents the linear polarization intensity and starts from 16.5 mJy/beam. The dashed line denotes the transverse cut corresponding to Fig. 4.14. See the text for details.

is the spectral index (optically thin if $\alpha < 0$). We find $\alpha = -(0.51 \pm 0.10)$, which indicates strong self-absorption in the core at least up to 86 GHz.

The time variation of the core flux density at 43 GHz is shown in Fig. 4.7. We also provide the corresponding peak intensity in the same figure. The flux density clearly increases from ~ 4 Jy in the earliest epoch (Feb 2015) to ~ 6 Jy around Jun and Jul 2015, and then decreases afterwards. This may be a part of the known complex flux density variation of the source, which is also seen on longer timescales (e.g., Hodgson et al. 2018).

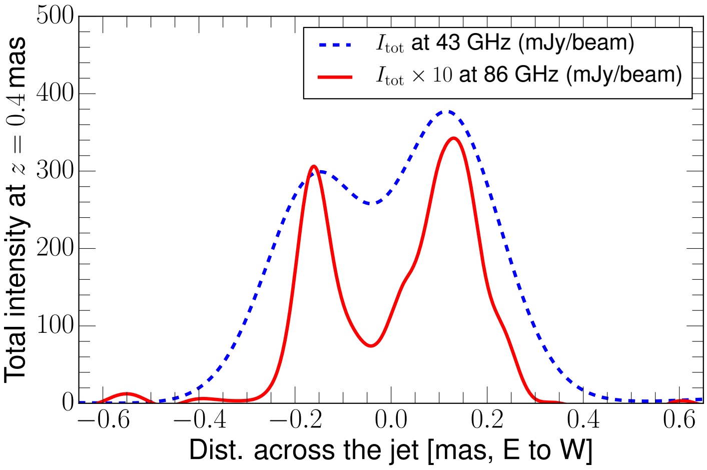

Fig. 4.5 Transverse jet intensity profiles at 43 GHz (blue dashed line) and 86 GHz (red solid line) from a slice through the jet at 0.4 mas core separation (increasing towards west).

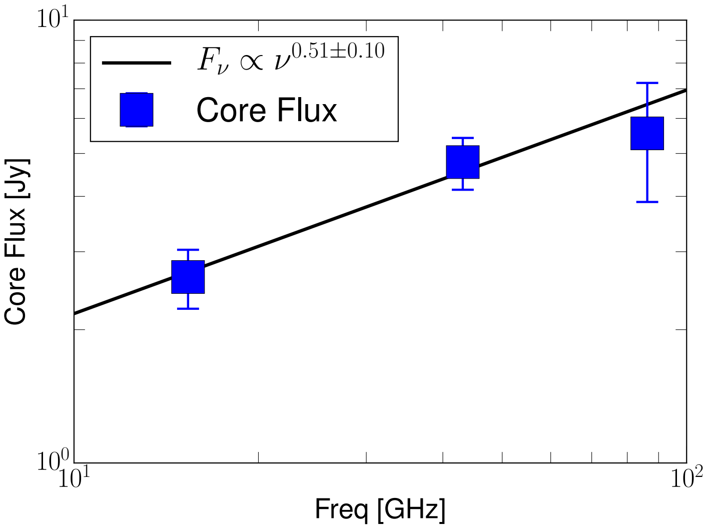

Fig. 4.6 Total intensity spectrum of the VLBI core region between 15 GHz and 86 GHz.

4.3.2 Linear polarization in the core region

Figure 4.8 shows the linear polarization structure in the core region at 43 and 86 GHz in more detail, using the same VLBA 43 GHz restoring beam. The linear polarizations in the core region are significant at both frequencies ($PI_{\rm peak}/\sigma_{\rm P}$ ∼13 and 10 at 86 and 43 GHz, respectively). On the other hand, we could not detect any significant polarization at 15 GHz. Based on the polarization noise level at 15 GHz, a $5\sigma_{\rm P}$ upper limit of the fractional linear polarization m_L is $\sim 0.1\%$. This is consistent with the previous polarization imaging of the source (Taylor et al., 2006).

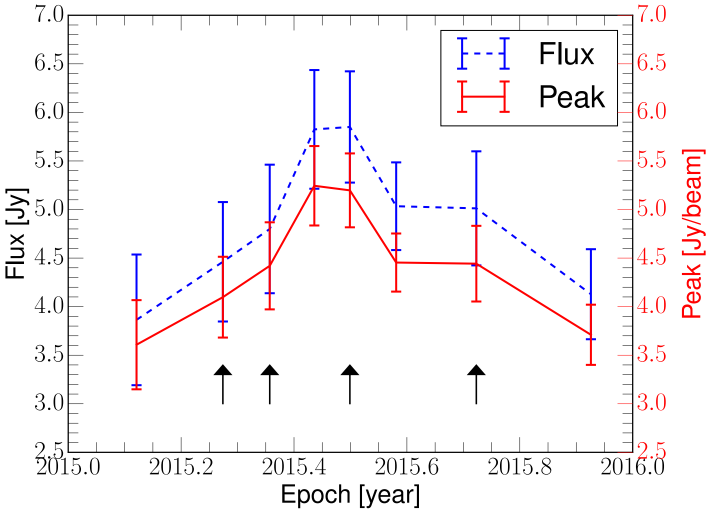

Fig. 4.7 VLBA 43 GHz core flux density and the peak values during 2015. Arrows indicate epochs when reliable polarization has been detected.

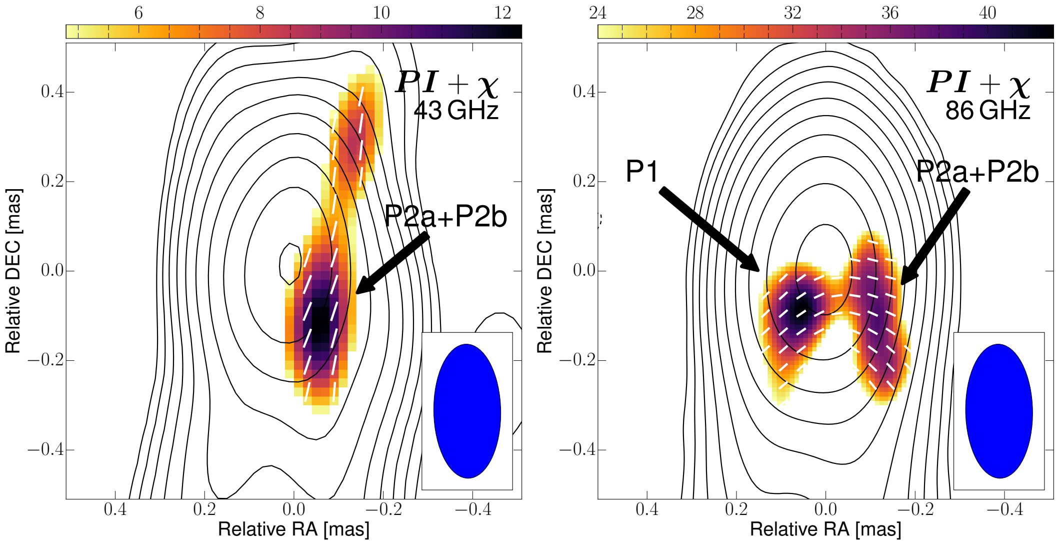

Fig. 4.8 Comparison of the total intensity, the polarized intensity (*PI*), and the polarization angle (χ) in the nuclear region at 43 and 86 GHz. The maps are restored with the same VLBA 43 GHz CLEAN beam and displayed over the same RA and DEC ranges (±0.5 mas). The arrows show the polarized component identifications. **Left** : The same as the central panel of Fig. 4.3 (43 GHz) but zoomed in the core. **Right** : GMVA 86 GHz total and linear polarization image restored with the VLBA 43 GHz beam. The contours start at 6 mJy/beam and increase by a factor of 2 from the lowest level. The color scale starts from 24 mJy/beam.

At 86 GHz, we find two major polarized components, P1 and P2, which are located eastward and westward of the peak of the total intensity, respectively (see Fig. 4.8). The P2 component – the westward feature at 86 GHz – is found in the 43 GHz image as well. In contrast, the P1 component – the eastward feature – has no clear counter-part in the 43 GHz image. The linearly polarized components are slightly offset from the peak of the total intensity at both frequencies and lie closer to the approaching jet. At 43 GHz, we find another polarized feature to the north of the core at a separation of ~ 0.3 mas (∼8 mJy/beam; see Fig. 4.8). We searched the VLBA-BU-BLAZAR database in order to see if the polarization north of the core is persistent and visible in many epochs. Near the core, polarization features are found in a number of epochs. However, we did not find a strong evidence for the persistent polarization in the north of the core. Except this feature, additional VLBA 43 GHz images in the other epochs show similar level of linear polarization (Fig. 4.9). But the peak of the linear polarization apparently moves by ~ 0.2 mas, especially in the E-W direction with respect to the peak of the total intensity. The typical size of the VLBA 43 GHz beam is ~ 0.15 mas in the same direction and we consider that the position shifts by ~ 0.2 mas are real and significant against the positional errors.

At 86 GHz, the degrees of linear polarization m_L are $\sim 3-7\%$ in the full-resolution GMVA polarization image (i.e., P1 and P2). The m_L values are decreased when the VLBA 43 GHz restoring beam is used ($m_L \sim 1-2\%$). At 43 GHz, the P2 component has lower fractional linear polarization of $\sim 0.5-0.6\%$. Similar m_L values are found in the other VLBA 43 GHz images from different observing epochs. Using the polarization image noise level at 43 GHz, we estimate a $5\sigma_{\rm P}$ upper limit of m_L for P1 is $\sim 0.2\%$ at 43 GHz. We provide in Table 4.54.5 a summary of the multi-frequency polarization properties in May 2015. The polarization properties of the core region from the other VLBA 43 GHz observations are listed in Appendix C.

4.3.3 Rotation measure between 43 GHz and 343.5 GHz in May 2015

Using the available multi-frequency EVPA measurements in May 2015, we compute the rotation measure (RM) associated with the gradient of the EVPA versus the squared wavelength. The intrinsic EVPA, $\chi_{\rm int}$, of a linearly polarized wave passing through magnetized plasma is rotated due to the interaction between the wave and the magnetic field. The resulting EVPA, $\chi(\lambda)$, observed at a wavelength λ is

$$\chi(\lambda) = \chi_{\rm int} + {\rm RM} \times \lambda^2 \tag{4.8}$$

where RM is the rotation measure obtained after solving the $n\pi$ angle ambiguity in the observed EVPAs. We solve the $n\pi$ accurately by combining the VLBI and ALMA polarization measurements. For this, we compute the spatially integrated EVPAs of the VLBI core region at 43 and 86 GHz and assume that most of the polarized fluxes observed at 97.5, 233.0, and 343.5 GHz by ALMA are produced by the same region. At 43 GHz, the spatially integrated

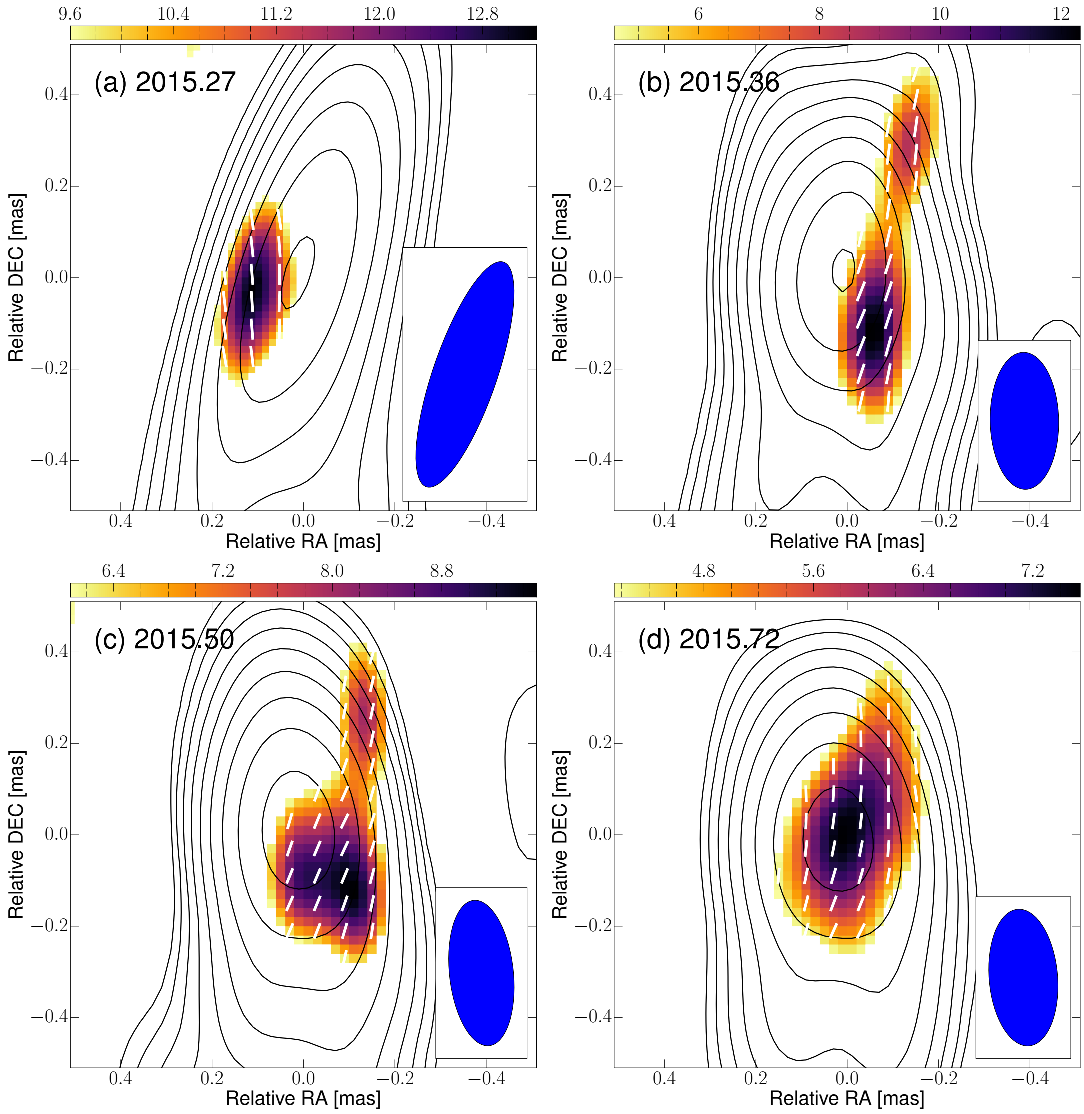

Fig. 4.9 VLBA 43 GHz polarization images of 3C 84 zoomed into the core. Labels in the upper left of each panel denotes the observing epoch. The contours show the total intensity and start from 25, 7, 10, and 20 mJy/beam and increase by factor of 2 for the panels (a), (b), (c), and (d), respectively. The color bar indicates the linear polarization intensity in mJy/beam. Only pixels whose linear polarization intensities are above 5σ level are displayed.

EVPAs are nearly identical as those reported in Table 4.5. At 86 GHz, we derive a spatially integrated core EVPA of $\chi = 86^\circ \pm 16^\circ$.

We then resolve the $n\pi$ ambiguity as follows (see also Hovatta et al. 2012). We consider a large range of possible $n\pi$ rotations and try to find a best λ^2 fit to the data which provides the smallest chi-square value. Specifically, we rotate the EVPAs at 86.0, 97.5, 233.0, and 343.5 GHz by $(n_1, n_2, n_3, n_4) \times \pi$ radian where $n_i \in (-30, -29, ..., 29, 30)$ and $i \in (1, 2, 3, 4)$.

Table 4.5 Properties of the polarized components in May 2015. The columns show (1) the central frequency, (2) the component identification, (3) the Stokes I flux density, (4) the degree of linear polarization, and (5) the EVPA. The Stokes I flux densities are consistent at the four separate frequencies within the 43 GHz band and we omit the numbers for the rest three frequencies.

$\nu_{\rm obs}$ (1) [GHz]	ID (2)	S_ν (3) [Jy]	m_ν (4) [%]	χ_ν (5) [deg]
86.252	P1	1.3 ± 0.4	3.0 ± 1.3	$-(53 \pm 16)$
	P1[a]	1.8 ± 0.5	1.3 ± 0.6	$-(46 \pm 16)$
	P2a	0.31 ± 0.09	7.0 ± 3.0	89 ± 16
	P2b	0.09 ± 0.03	30 ± 13[b]	51 ± 16
	P2a+P2b[a]	0.9 ± 0.3	2.5 ± 1.0	72 ± 16
43.0075	P2a+P2b	2.0 ± 0.2	0.44 ± 0.14	$-(9 \pm 10)$
43.0875			0.49 ± 0.16	$-(20 \pm 10)$
43.1515			0.53 ± 0.17	$-(24 \pm 10)$
43.2155			0.43 ± 0.13	$-(15 \pm 10)$
15.352		N/A	< 0.1[c]	N/A

Notes. a : Obtained from the image in panel (B) of Fig. 4.8. **b** : The component is associated with the outer edge of the jet and could have higher systematic uncertainties than our estimation. **c** : A 5σ upper limit from the non-detection.

We then calculate the chi-square value for a set of n_i by fitting the λ^2 model. We note that $n = 30$ corresponds to a very large RM of $\sim 10^8\,{\rm rad/m^2}$ for our frequency range. Similarly, a single 1π rotation of the EVPA within the 43 GHz band corresponds to a comparable RM. Previous observations do not provide any hint of such a large RM in this source (see Plambeck et al. 2014). Therefore, our calculations exclude RM as large as $\gtrsim 10^8\,{\rm rad/m^2}$ and we also do not apply the $n\pi$ rotation within the 43 GHz band. As for the significance, we have $8 - 2 = 6$ degrees of freedom and any λ^2 model with chi-squares smaller than 12.59 can be considered as significant at 95% confidence.

Our procedure provides a best λ^2 model with $n_1 = -3$, $n_2 = -3$, $n_3 = -3$, and $n_4 = -3$[9]. The corresponding chi-square and reduced chi-square values are 3.51 and 0.59, respectively. The best λ^2 model and the $n\pi$-corrected EVPAs are shown in Fig. 4.10. From this correction, we obtain RM$= (2.04 \pm 0.03) \times 10^5\,{\rm rad/m^2}$ and $\chi_{\rm int} = -(584 \pm 7)^\circ$, or equivalently $\chi_{\rm int} = -(44 \pm 7)^\circ$. This RM is large compared to the values found in other AGNs in general (e.g., Jorstad et al. 2005) and is comparable to RM$\sim 9 \times 10^5\,{\rm rad/m^2}$ found by Plambeck et al. (2014).

---

[9] This is equivalent to rotating only the 43 GHz EVPA by $+3\pi$ radian.

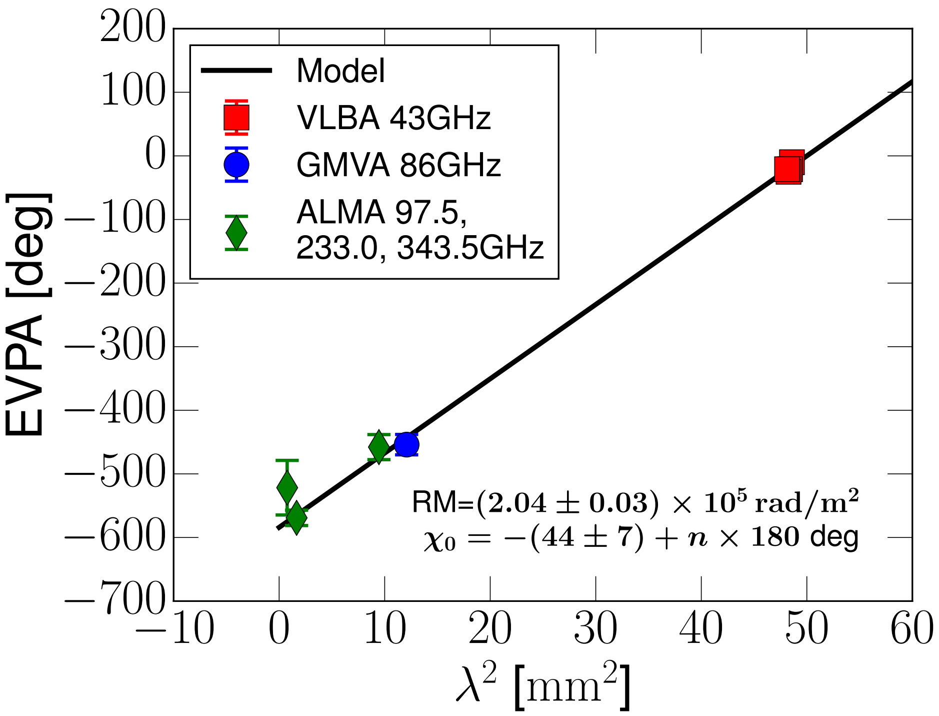

Fig. 4.10 Spatially integrated EVPA (error bars) versus the squared wavelength λ^2 and the best λ^2 fit (solid line) in May 2015.

We also produce a two-dimensional distribution of the RM values in the image plane by aligning the 43 and 86 GHz EVPA images for an illustration. We align the peaks of the total intensity at 43 and 86 GHz assuming that the spatial offset of the two images – e.g., due to the opacity effect (i.e., the core-shift; Lobanov 1998) – is smaller than 15μas, which corresponds to $\sim 30\%$ of the minor axis of the observing beam at 86 GHz. We applied the $n_1 = -3$ correction to the GMVA image. We also blanked pixels whose linearly polarized intensities are below $5\sigma_P$ level either in the VLBA 43 GHz or GMVA 86 GHz images. The resulting 43-86 GHz RM image is shown in Fig. 4.11. We find typical RM values of $\sim 3 \times 10^5\,\mathrm{rad/m^2}$ in the image plane, which is comparable to the value found by the spatially integrated EVPAs.

4.3.4 Rotation measure within the 43 GHz band

We also measure the RM within the 43 GHz band using the EVPAs at the four IFs. Before applying the RM fitting procedure, we checked the significance of the EVPA rotation in 3C 84 by analyzing two additional comparison sources 0235+164 and 3C 279. These sources were observed together with 3C 84 by the VLBA-BU-BLAZAR program in the same epochs. Their polarization calibrations were also completely identical to 3C 84. If the EVPA variation within

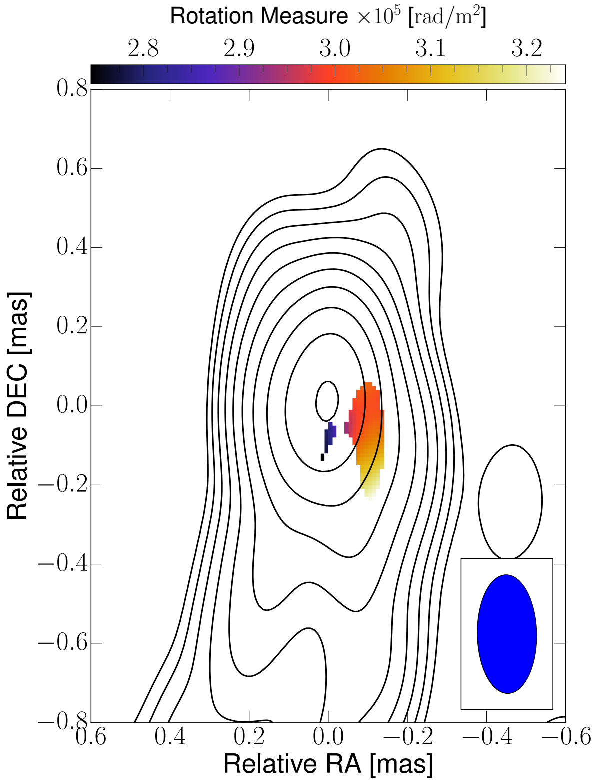

Fig. 4.11 43-86 GHz RM distributions obtained as described in the text. The image is displayed with the same contours as in the left panel of Fig. 4.3. The blue ellipse shows the VLBA 43 GHz restoring beam. The color bar indicates the RM values (in units of $10^5 \mathrm{rad/m^2}$).

the 43 GHz band is dominated by systematic calibration errors, the variations will be the same in 0235+164, 3C 279, and the target source 3C 84. If there is an intriscally large RM in 3C 84, however, the angle change of 3C 84 within the 43 GHz band should be larger than – and uncorrelated with – the variations in 0235+164 and 3C 279.

For the purpose, the EVPAs of the core region of the two sources were measured in the same way as 3C 84. In Fig. 4.12 we show deviations of the EVPAs at each IFs, χ, from the mean EVPAs, $\langle\chi\rangle$, for 0235+164 and 3C 279. The EVPA variation within the 43 GHz band is only $\lesssim 6^\circ$ for 3C 279 in all the four epochs ($\lesssim 8^\circ$ for 0235+164). This appears to be insignificant compared to the 10° EVPA error budget that we assumed for the 43 GHz EVPAs. Also, the $\chi - \langle\chi\rangle$ values of the two sources show strong correlations (see Fig. 4.12), probably indicating that the $6^\circ - 8^\circ$ EVPA variation within the 43 GHz band is the effect of the residual calibration errors. For any $6^\circ - 8^\circ$ EVPA offset within the 43 GHz band, therefore, we consider that any in-band RM values smaller than $(2-3) \times 10^5\,\mathrm{rad/m^2}$ is not significant against the calibration errors.

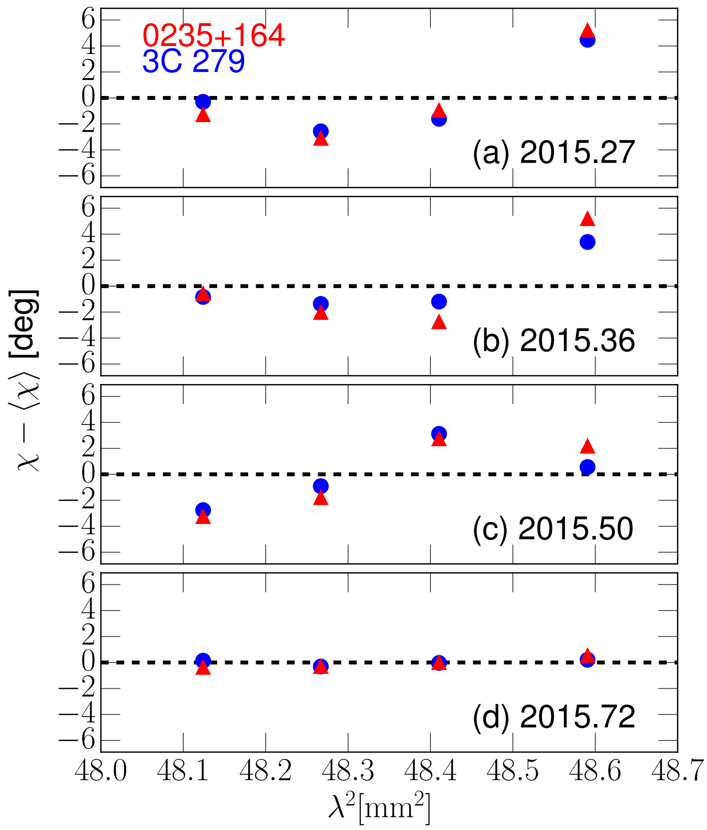

Fig. 4.12 Variation of the measured EVPA in 4 sub-bands of the VLBA 43 GHz observing band at different observing epochs. Red triangles and blue circles are for 0235+164 and 3C 279, respectively. Error bars are omitted for clarity. Note the strong correlation between the two very different sources.

Table 4.6 RM within the VLBA 43 GHz band. From left to right, columns denote the observing epoch, the RM, and the EVPA interpolated to the central frequency of the 43 GHz band (43.1155 GHz).

Epoch [yyyy/mm/dd]	RM [$\times 10^5$ rad/m^2]	χ [deg]
2015/04/12	$-(6.2 \pm 2.6)$	11 ± 5
2015/05/11	2.7 ± 3.5	$-(14 \pm 5)$
2015/07/02	6.8 ± 3.3	$-(11 \pm 5)$
2015/09/22	5.2 ± 4.2	$-(8 \pm 5)$

We performed the same analysis to 3C 84 and show the EVPAs within the 43 GHz band in Fig. 4.13. The EVPAs of 3C 84 vary by a large amount within the 43 GHz band ($\sim 15^\circ - 21^\circ$). Such a large EVPA variation cannot be explained by the systematic EVPA errors due to the residuals of the calibration ($\lesssim 8^\circ$). The EVPA variation in 3C 84 is also not correlated with

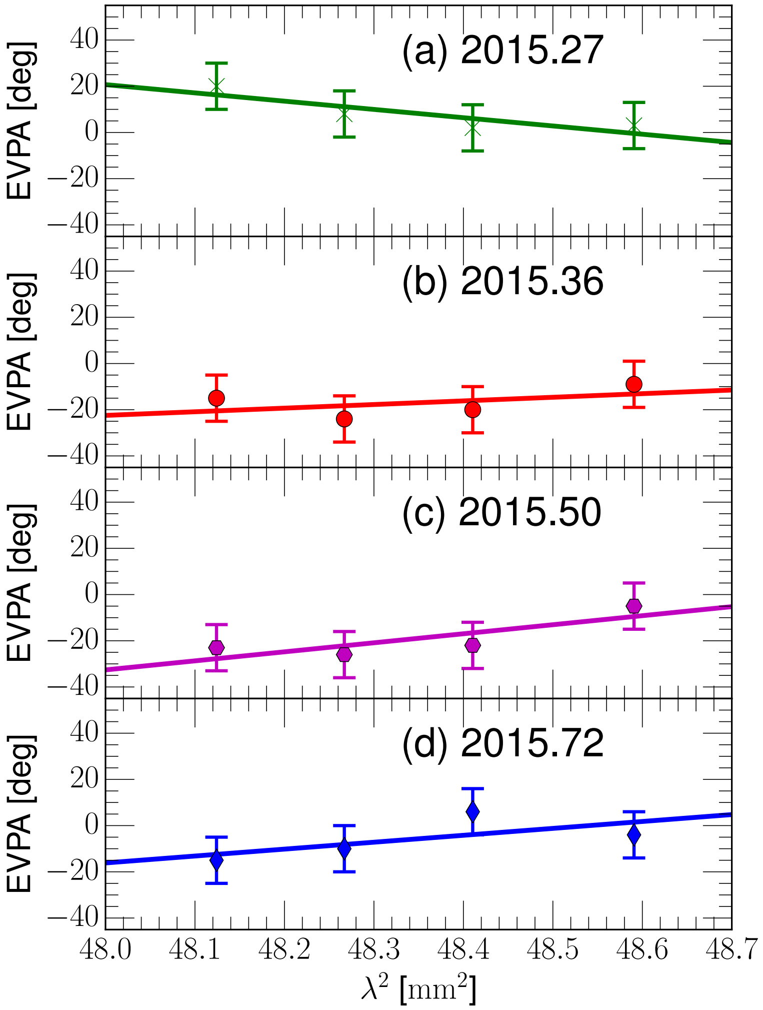

Fig. 4.13 EVPAs of 3C 84 versus the squared wavelength λ^2 within the VLBA 43 GHz band (error bars) and the best-fit Faraday rotation model (solid line).

those of 0235+164 and 3C 279. This justifies to compute the rotation measure of 3C 84 within the 43 GHz band. The RM values obtained with the best λ^2 models are listed in Table 4.6. Our calculations result in large, significant RM values of $|\mathrm{RM}| \gtrsim 5 \times 10^5\,\mathrm{rad/m^2}$ in three out of the four epochs. Such large RM values are most likely intrinsic to the source. We also note the sign of the RM is negative in Apr 2015. The negative sign appears to be significant against the calibration errors because the strongly correlated EVPAs of the comparison sources show increasing EVPA with increasing λ^2 (i.e., positive RM). If our measurement in this epoch is dominated by the systematic errors, we expect to find a positive RM for 3C 84 as well. This is however not the case.

4.4 Discussions

4.4.1 Polarization structure

The VLBA 43 GHz and GMVA 86 GHz polarization images (Fig. 4.4 and 4.8) reveal significant linear polarization features in the VLBI core region. The core size can be approximated by a Gaussian whose FWHM is ~ 0.13 mas, which is equivalent to ~ 0.033 pc or $650R_s$. The linear polarization variability on monthly timescales provides a tight upper limit on the spatial scale of such features ($1c \times 1$ month ~ 0.025 pc $\sim 490R_s$ Plambeck et al. 2014; Agudo et al. 2018b). We also note that the spectrum of the linearly polarized flux density between 97.5 and 233.0 GHz measured by ALMA is nearly flat (the flux densities ~ 100 mJy at both frequencies; see Table 4.3). This suggests that the polarized emission originates from from a region which is still synchrotron self-absorbed (opacity close to unity). Therefore, it is likely that the polarized emission from the VLBI region accounts for a significant fraction of the polarized flux densities measured by previous lower angular resolution observations at millimeter wavelengths.

Another interesting feature is the polarization morphology at 86 GHz. The polarized features P1 and P2, which may be associated with the underlying edge-brightened jet, show significantly different degrees of linear polarization. In order to illustrate the polarization asymmetry, we show in Fig. 4.14 the intensity profiles of the 86 GHz core region (i.e., pixel values) following an east-west cut along a position angle PA$= -69^\circ$, as displayed in Fig. 4.4. The shaded area in the figure represents 30% uncertainties of the pixel values at 86 GHz. The 43 GHz polarization images (Fig. 4.9) also show that the peak of the polarization is displaced by ~ 0.2 mas east and west to the total intensity peak, depending on the observing epoch. This implies that the direction of the transverse polarization asymmetry changes with time on at least monthly timescales.

High resolution polarimetric observations of other jets in AGNs also show such a transverse polarization asymmetry (e.g., Gómez et al. 2008; O'Sullivan & Gabuzda 2009; Clausen-Brown et al. 2011; Gómez et al. 2016). This could be due to the geometry of the jet and/or the structure of the magnetic field (e.g., the jet viewing angle, the opening angle, and the magnetic pitch angle; Lyutikov et al. 2005; Clausen-Brown et al. 2011; Porth et al. 2011). But we note that the spatially integrated EVPA after the Faraday rotation correction is $\chi_{\rm int} = -(44 \pm 7)^\circ$ (or $136^\circ \pm 7^\circ$) in the May 2015 epoch. The intrinsic EVPA of the jet is expected to be parallel or perpendicular to the inner jet direction, if the magnetic field is purely toroidal or axial (Lyutikov et al., 2005). However, the intrinsic EVPA is neither parallel nor perpendicular to the inner jet whose position angle is approximately 170° (see Fig. 4.3). The magnetic field orientation therefore appears to be oblique to the jet. Also, the highly time-variable polarization structure in the core region at 43 GHz, which accompanied a contemporaneous radio outburst,

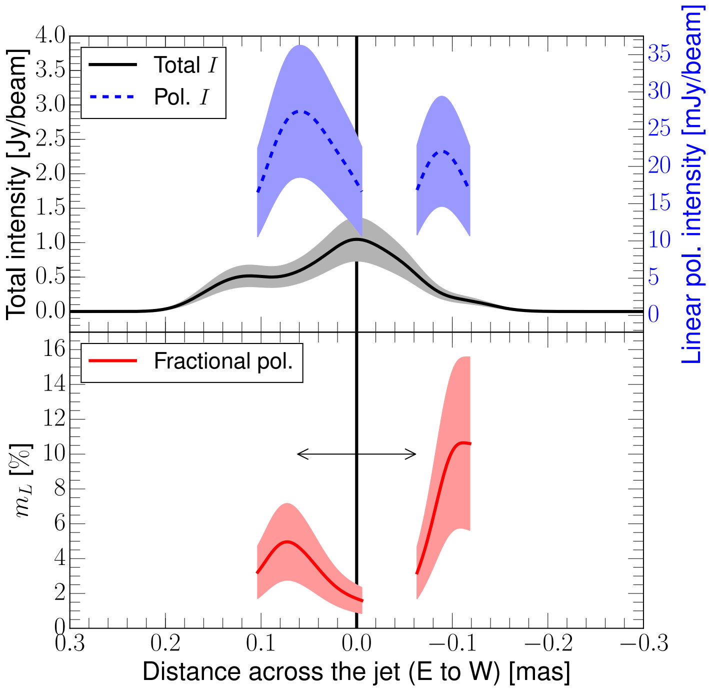

Fig. 4.14 (**Top**) total intensity, linear polarization intensity and (**bottom**) degree of linear polarization at 86 GHz obtained by the slice transverse to the core and calculated by the pixel values in the image plane (negative core separation towards west; see Fig. 4.8). The solid black line indicates position of the total intensity peak and the arrow in the lower panel denotes the FWHM size of the core at 86 GHz. Only linear polarization higher than 6σ level is shown.

makes it difficult to understand the polarization asymmetry with a unique explanation. Similar inhomogeneous, asymmetric polarization structure could be produced when the plasma in the flow is dominated by turbulence associated with a newly emerging VLBI component from the core region (e.g., Marscher 2014).

4.4.2 Polarization spectrum and the origin of the large EVPA rotation

The fractional polarization of the VLBI core sharply increases with decreasing observing wavelengths (§4.3.2). Motivated by this, we compile the m_L values obtained by other VLBI, single-dish, and connected interferometer observations at different wavelengths. The resulting linear polarization spectrum is shown in Fig. 4.15. We find sharply increasing fractional linear polarization at higher observing frequencies. The trend can be well approximated by a power-law $m_L \propto \nu^{0.77\pm0.18}$ if both VLBI and non-VLBI measurements are included in the fitting. The VLBI core may have a steeper power-law index. At the shortest millimeter wavelengths (e.g., $\nu \gtrsim 200$ GHz), however, the fractional polarization is significantly time-variable.

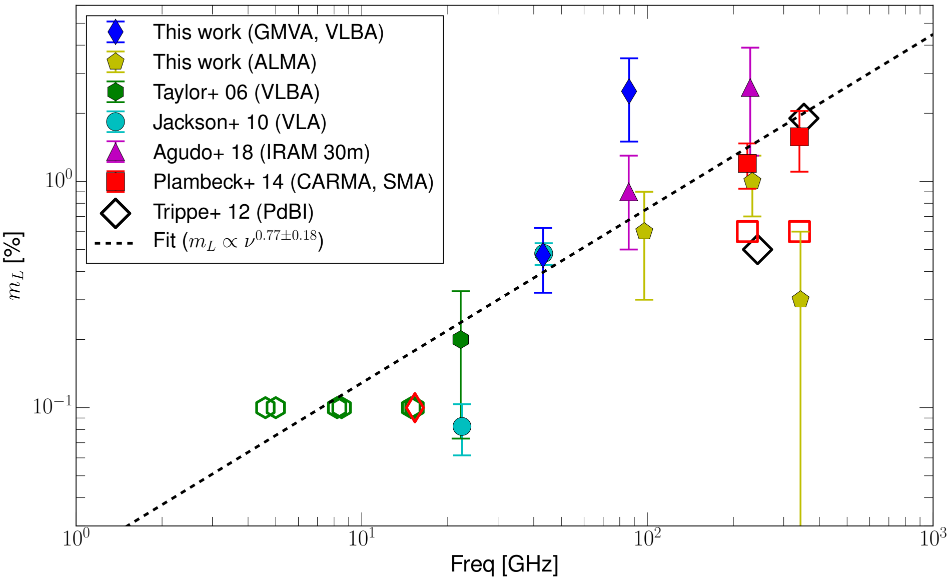

Fig. 4.15 Degrees of linear polarization of 3C 84 from this work and previous VLBA observations (Taylor et al., 2006) and spatially integrated single-dish or connected-interferometer observations from the literature (Jackson et al., 2010; Trippe et al., 2012; Plambeck et al., 2014; Agudo et al., 2018b). All the VLBI polarization measurements were made from the pixel values near the peak of the Stokes *I* in the VLBI core region. Filled and open symbols of the same marker indicate measured values and upper limits, respectively. Citations and corresponding instruments are shown in the legend. We note that at 230 GHz only upper limits were observed before May 2011 (Trippe et al., 2012; Plambeck et al., 2014). After October 2011, Plambeck et al. (2014) report a significantly higher linear polarization degree.

The increase of the fractional linear polarization m_L towards higher frequencies can be caused by several effects. If the core represents a surface of the jet where the synchrotron opacity is close to unity at each observing frequency (e.g., Lobanov 1998), the synchrotron emission at higher frequencies originate from closer to the central engine where the jet opacity is higher. Therefore, the emission at the higher frequencies originates from the inner jet regions, which are closer to the central engine. Based on this argument and the fact that most of the jets show steep spectral indices between 86 and 230 GHz, Agudo et al. (2010, 2014) compared the linear polarization degrees measured for a number of AGN sources at 230 GHz and 86 GHz by the IRAM 30 m Telescope and found significantly higher m_L at the higher frequency (a factor $\sim 1.6-2.6$ larger). Similar results were obtained by longer polarization monitoring observations (Agudo et al., 2018b). The authors concluded that magnetic fields are more ordered in the upstream of the jet. In 3C 84, however, the synchrotron opacity is high and the observed linear polarization can be increased with decreasing opacity at higher frequencies because of the self-absorption effect (e.g., Pacholczyk 1970; Jones & O'Dell 1977).

However, the RM in 3C 84 is very large (RM$\sim 10^{(5-6)}$ rad/m^2; §4.3.3 and 4.3.4). For such a large RM, the Faraday depolarization is expected to be strong even at millimeter wavelengths (see §4.4.3) could be an explanation for the increasing fractional linear polarization at higher frequencies (Fig. 4.15). We note that the opacity effect can cause a large EVPA rotation near the synchrotron turn-over frequency and the EVPA rotation may not be associated with the Faraday rotation. On the other hand, we note that the fractional bandwidth of the VLBA 43 GHz data is only 256 MHz/43 GHz$\sim 6\times10^{-3}$. For such a small fractional bandwidth, the EVPA variation within the VLBA 43 GHz band may not be solely explained by the opacity effect (e.g., Jones & O'Dell 1977). Therefore, the EVPA change is likely associated with the Faraday rotation.

The impact of Faraday rotation is also suggested by the relatively strong circular polarization in 3C 84. At 15 and 22 GHz, Homan & Wardle (2004) found a large degree of circular polarization $m_C \sim 1-3\%$ in the inner jet of 3C 84. Single-dish observations at $5-8$ GHz to $86-230$ GHz also reveal a few $\times 0.1\%$ of circular polarization (Aller et al., 2003; Agudo et al., 2010; Thum et al., 2018; Myserlis et al., 2018). Therefore, Homan & Wardle (2004) and Thum et al. (2018) suggest that the circular polarization in 3C 84 is generated by Faraday conversion, which converts the linear to the circular polarization accompanied by Faraday rotation (e.g., Jones & O'Dell 1977; Wardle & Homan 2003; MacDonald & Marscher 2018). The circular polarization can be alternatively generated without Faraday rotation by purely random magnetic fields in the plasma in and around the jet (e.g., Wardle & Homan 2003), accompanying frequent sign changes in the circular polarization. However, stable sign of the circular polarization of 3C 84 over several years (e.g., Myserlis et al. 2018) seems to support the connection between Faraday rotation and conversion.

4.4.3 Faraday depolarization models

As discussed in §4.4.2, we consider that the large EVPA rotation in 3C 84 is due to Faraday rotation. Therefore, we test a variety of Faraday depolarization models to investigate the impact of the Faraday depolarization and to better understand the nature of the Faraday screen. We note that Faraday rotation is perhaps not the only explanation to understand the complicated polarization properties of the source, but it offers a physical meaningful possibility to understand the polarization properties of the source.

In the context of the canonical AGN models, an external Faraday screen can be located in various places. The parsec-scale accretion disk of 3C 84, which blocks the counter-jet emission by free-free absorption of a surrounding ionized plasma (Walker et al., 2000), may be able to block inner portion of the approaching jet. Further inward, the accretion flow of 3C 84 (e.g., a radiatively inefficient accretion flow; RIAF) may act as a foreground Faraday screen (Plambeck et al., 2014). Taylor et al. (2006) also suggest that the interstellar and intergalactic medium in and around the host galaxy of 3C 84 (NGC 1275) also affects the observed linear polarization of 3C 84.

Accordingly, we model the Faraday depolarization in 3C 84 with three simple analytical models (see §4.4.3 and 4.4.3 for their corresponding physical implications):

1. A foreground screen with *disordered* magnetic field geometry and *random* RM fluctuations.
2. A foreground screen with *ordered* magnetic field geometry and a *smooth* RM gradient across the observing beam.
3. An internal Faraday depolarization *within the homogeneous jet* with *uniform* magnetic field geometry.

Following Burn (1966), we write the observed fractional linear polarization $m_{\rm obs}$ for each case by

$$\text{Case I}: \quad m_{obs} = m_0 \exp(-2\sigma^2\lambda^4) \tag{4.9}$$

$$\text{Case II}: \quad m_{obs} = m_0 \left| \frac{\sin(\Delta\mathrm{RM}\lambda^2)}{\Delta\mathrm{RM}\lambda^2} \right| \tag{4.10}$$

$$\text{Case III}: \quad m_{obs} = m_0 \left| \frac{\sin(2\mathrm{RM}\lambda^2)}{2\mathrm{RM}\lambda^2} \right| \tag{4.11}$$

where m_0 is the intrinsic degree of linear polarization, λ is the observing wavelength, σ is the standard deviation of the dispersion of the RM of the external screen, ΔRM is the RM gradient across the observing beam, and RM is the observed rotation measure. For each case, we compute $m_{\rm obs}$ as function of λ as follows. For Case I, we further assume that $\sigma = \varepsilon \times \mathrm{RM}$ where ε is a scaling factor defining the level of the inhomogeneity of the RM in the external screen. For the purpose, we assume a rather inhomogeneous medium with $\varepsilon = 1$. For Case II, we similarly assume that ΔRM is comparable to the observed RM. We note that the sine terms in Eq. 4.10 and 4.11 make a direct comparison of the expected linear polarization and the sparsely sampled $m_{\rm obs}$ difficult. Therefore, we take only the conservative upper limits of $m_{\rm obs} \leq m_0/\Delta\mathrm{RM}\lambda^2$ and $m_{\rm obs} \leq m_0/2\mathrm{RM}\lambda^2$ for Case II and III, respectively. We then choose $m_0 = 10\%$ because this value is the theoretical upper limit for an optically thick region (e.g., Pacholczyk 1970). We note that the actual value of m_0 could be slightly lower if the magnetic field geometry in the jet is less uniform. For the RM values, we take RM$\sim 9 \times 10^5\,\mathrm{rad/m^2}$. Such a high value is necessary in order to account for our results (Table 4.6) and the previously found largest RM values (Plambeck et al., 2014). Based on these assumptions and parameters,

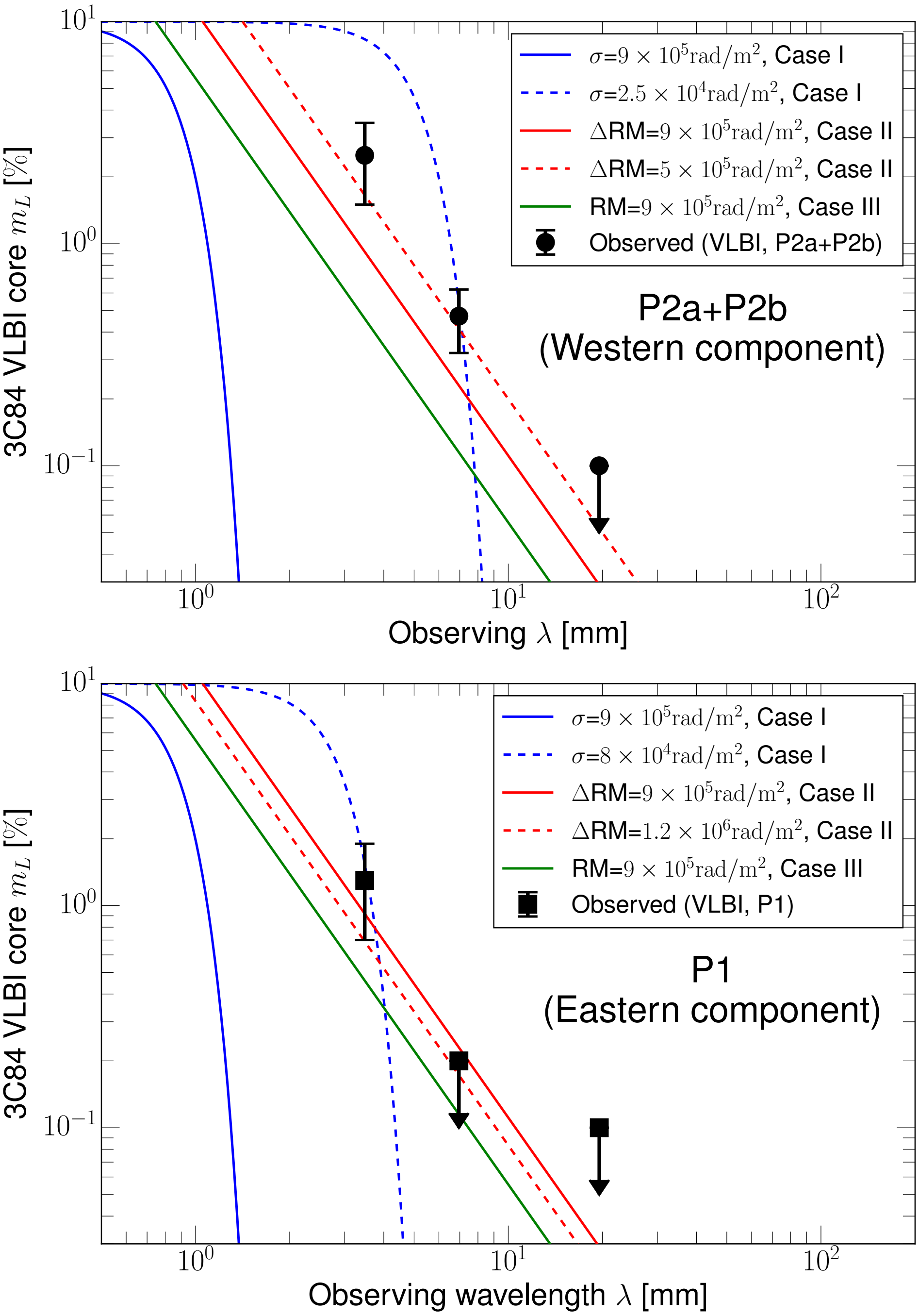

Fig. 4.16 Upper limits for m_L for external (Case I and II) and internal (Case III) Faraday depolarization and the VLBI polarization from observations. Arrows indicate upper limits. The top and bottom panels are for the P2 and P1 components, respectively. See text for details.

we compare the $m_{\rm obs}$ curves obtained by Eq. 4.9, 4.10, and 4.11 with the observed m_L values of the P2 and P1 components. In order to avoid the time-variability issue, we choose the m_L values obtained from the quasi-simultaneous observations in May 2015. In order to avoid further confusions due to the different angular resolutions at 43 and 86 GHz, we take the m_L measured with the same VLBA 43 GHz beam as reported in Table 4.5. In particular, the P1 component is not detected at 43 GHz and we use an upper limit of $m_L = 0.2\%$ at 43 GHz (§4.3.2). At 15 GHz, we similarly take an upper limit of $m_L = 0.1\%$ for both P2 and P1.

We show the upper limits obtained from the depolarization models and the observational results in Fig. 4.16. In Case I (blue lines), the large RM dispersion $\sigma \sim 9 \times 10^5\,\mathrm{rad/m^2}$ with $\varepsilon = 1$ gives very tight upper limits for m_{obs} and cannot reproduce the observed fractional polarization between 15 and 86 GHz. Instead, a much smaller $\sigma \sim 2.5 \times 10^4\,\mathrm{rad/m^2}$ is necessary for P2 (broken blue line) as well as for P1 ($\sigma \sim 8 \times 10^4\,\mathrm{rad/m^2}$). Such small σ values suggest small ε values, which indicate highly homogeneous foreground screens ($\varepsilon = \sigma/\mathrm{RM}$ ~0.03 and 0.09 for P2 and P1, respectively). On the other hand, the second scenario (Case II, blue lines) leads to much smaller Faraday depolarization and better explains the observations. We find that $\Delta\mathrm{RM} \sim 5 \times 10^5\,\mathrm{rad/m^2}$ and $\sim 1.2 \times 10^6\,\mathrm{rad/m^2}$ could reproduce the polarization spectrum of P2 and P1, respectively. Finally, the Case III leads to to a rather strong depolarization and appears to be in conflict with the observational results. We investigate the physical implications of these models in the following.

Case I : Accretion flow as the foreground screen

In the vicinity of the central engine, the accretion flow (e.g., RIAF) in front of the inner jet of 3C 84 can act as an external screen, which corresponds to the inhomogeneous foreground medium in Case I. In a RIAF-type flow, magnetohydrodynamic (MHD) turbulences can be easily induced by the magnetorotational instabilities (Balbus & Hawley, 1991, 1998). One of good examples is the massive BH Sagittarius A* in the galactic center. For instance, Johnson et al. (2015) detected linear polarization of the radio source on small spatial scales of $\lesssim 10R_s$ scale and claimed a short coherence length of the magnetic field ($\sim 6R_s$). Our line of sight could intersect with such a flow due to the large viewing angle $\theta \sim (30-60)^\circ$ of the jet of 3C 84 (Walker et al., 1994; Fujita & Nagai, 2017). If this is the case, however, we do not expect to find linearly polarized emission from the source at 43 and 86 GHz with $m_L \sim (0.1-1.0)\%$ (Fig. 4.16), which is incompatible with our observations. Our analytical model with the $\varepsilon = \sigma/\mathrm{RM}$ parameter certainly simplifies many details of the disk-jet system, but detailed numerical simulations of polarized radiative transfer suggest that the depolarization by the disk can be generally very strong (e.g., Mościbrodzka et al. 2017). In this context, the accretion flow may not be able to explain the Faraday rotation and Faraday depolarization.

Another problem of explaining the large RM in 3C 84 by the accretion flow was shown by Plambeck et al. (2014). The authors adopted a semi-analytic model of the spherical mass accretion onto the central BH assuming a well ordered and radial magnetic field configuration.

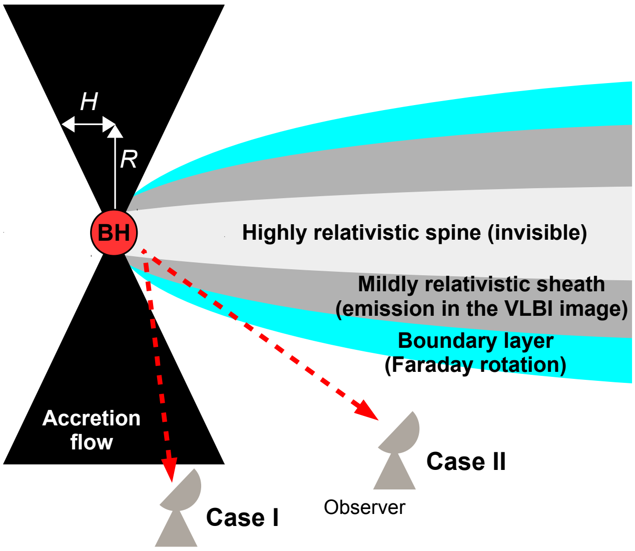
H
R
BH
Highly relativistic spine (invisible)
Mildly relativistic sheath
(emission in the VLBI image)
Boundary layer
(Faraday rotation)
Accretion
flow
Case II
Observer
Case I

Fig. 4.17 Illustration of the geometry discussed throughout Sect. 4.3.3 and 4.4.3. We note that the figure is not drawn to scale.

The authors attempted to relate the observed rotation measure to the expected mass accretion rate, because a higher accretion rate with more matter will induce larger Faraday rotation. They found that the observed rotation measure of $\sim 9 \times 10^5\,\mathrm{rad/m^2}$ is too small to account for the expected mass accretion in this source. This led Plambeck et al. (2014) to the following conclusions: (i) the true magnetic field strength in the accretion flow is much weaker than the equipartition field strength, (ii) the magnetic field topology is more disordered and complex rather than purely radial, and/or (iii) the accretion disk is highly disk-like and the line-of-sight towards the inner jet does not intersect with the accretion flow. The thin-disk like geometry of the accretion flow is probably the most suitable explanation among these possibilities, because it could explain our results without fine-tuning the other physical properties of the accretion flow.

In a simplistic scenario in which a line of sight does not intersect with a relatively thin accretion disk, we can estimate the ratio of the disk height H and the disk radius R, H/R, using a simplified inner jet-disk geometry (Fig. 4.17). The line of sight will not intersect with the accretion disk if $\theta + \tan^{-1}(H/R) \lesssim 90^\circ$ or $H/R \lesssim \tan(90 - \theta)$ where θ is the jet viewing angle. If we adopt $\theta \sim 30^\circ$ (60°) (Walker et al., 1994; Fujita & Nagai, 2017), the resulting height to radius ratio is $H/R \lesssim 1.7$ $(\lesssim 0.6)$. Numerical simulations suggest that even smaller ratio is perhaps possible when strong poloidal magnetic field threads the accretion disk and compresses it vertically against the magnetorotational instability (e.g., McKinney et al. 2012).

Case II : Faraday rotation and depolarization due to the transverse structure of the jet

The upper limits on m_{obs} obtained for Case II, which involves ordered magnetic field and smooth RM gradient, showed a better agreement with the observational results. In this regard, we note that the boundary layer of the jet, which contains mildly-relativistic or thermal particles, could contribute to the observed Faraday rotation as well. The inner jet of 3C 84 presumably originates from the central rotating BH and/or the inner accretion disk (Blandford & Znajek, 1977; Blandford & Payne, 1982). Stronger and more ordered magnetic fields are expected in the inner jets of AGNs with highly magnetic energy dominated jet launching regions (e.g., Zamaninasab et al. 2014; Martí-Vidal et al. 2015). The rotation of the central engine (BH and/or accretion disk) twists the magnetic field and leads to a large scale helical structure, which can collimate the plasma outflow. (see, e.g., Tchekhovskoy 2015). Such magnetic field configurations are also used to explain the transverse RM gradients in parsec-scale jets (e.g., Zavala & Taylor 2005; Hovatta et al. 2012; Gabuzda et al. 2017). The boundary layer of such an outflow may provide the necessary Faraday screen for Case II.

Specifically, the inner jet of 3C 84 shows a clear edge-brightening (e.g., see Fig. 4.5 and Giovannini et al. 2018) and therefore provides evidence for non-uniform transverse structure. The origin of the edge-brightening is most likely complicated, involving various physical conditions and processes in the jet, the layer between the jet and ambient medium, and the central engine (e.g., Laing 1980; Komissarov 1990; Wardle et al. 1994; Contopoulos et al. 2009). Their effects are most likely important in the observed polarization properties (Sokoloff et al., 1998; Perlman et al., 1999; Pushkarev et al., 2005; Porth et al., 2011; MacDonald et al., 2015; Pasetto et al., 2018). We also note the reversal of the sign of the RM in time (Fig. 4.13 and Table 4.6). This can be explained only by the reversal of the magnetic field direction with respect to the line of sight and suggests the jet origin of the Faraday rotation (e.g., Hovatta et al. 2012; Lico et al. 2017). Mildly relativistic particles in the boundary layer of the jet, which may be intermixed with the thermal particles, could explain the simultaneous and co-spatial Faraday conversion and large Faraday rotation.

The basic geometry of Case II discussed in this section is displayed in Fig. 4.17.

4.4.4 Estimation of the jet magnetic field strength and electron density

If the large RM of $\sim 9\times10^{5}\,\mathrm{rad/m^{2}}$ is generated by the sheath of the jet, we can estimate the magnetic field strength and electron density in the jet based on several assumptions. First, the magnetic field strength in the jet can be independently estimated using synchrotron self-absorption (SSA) theory. Following Marscher (1983), the SSA magnetic field strength B_{SSA} in the core region is given by

$$B_{SSA} = 10^{-5} b(\alpha) \frac{\theta_m^4 \nu_m^5 \delta}{S_m^2 (1+z)} \quad \text{Gauss} \tag{4.12}$$

where α is the spectral index of the optically thin emission beyond the turn-over frequency, $b(\alpha)$ is a constant of the spectral index tabulated in Marscher (1983), S_m is the flux density (in Jy) at the turn-over frequency ν_m (in GHz), θ_m is the angular size of the source (in mas) at ν_m, $\delta = 1/\Gamma(1-\beta\cos\theta)$ is the Doppler factor, Γ is the bulk Lorentz factor, $\beta = \beta_{\rm app}/(\sin\theta + \beta_{\rm app}\cos\theta)$ is the intrinsic jet velocity (in units of the speed of light c), $\beta_{\rm app}$ is the apparent jet velocity (in units of c), and θ is the jet viewing angle. Before computing Eq. 4.12, we note that the exact value of the turn-over frequency is not constrained by our data alone, although the flat spectrum is seen at least up to 86 GHz and suggests a turn-over at $\nu_m \gtrsim 86$ GHz. Also, Korean VLBI Network monitoring observations of the inner jet of 3C 84 at 86 and 129 GHz reveal a steep spectrum (Hodgson et al., 2018). Therefore, we attempt to estimate a rough value of $B_{\rm SSA}$ assuming $\nu_m = 86$ GHz.

Bearing this in mind, we plug in the following parameters in Eq. 4.12. We assume $\alpha = -0.75$ beyond the turn-over frequency. The corresponding value of $b(\alpha)$ is 0.75. Since we set $\nu_m = 86$ GHz, we take $S_m = (5.6 \pm 1.7)$ Jy and $\theta_m = 1.8 \times (0.14 \pm 0.01)$ mas[10] based on the Gaussian model-fit properties of the core at 86 GHz. We then find $B_{\rm SSA} \sim (21 \pm 14) \times \delta$ G. The inner jet of 3C 84 near its VLBI core is slow ($\beta_{\rm app} \sim 0.1$; Walker et al. 1994; Suzuki et al. 2012; Jorstad et al. 2017) and the jet viewing angle is also relatively large ($\theta \sim 30^\circ - 60^\circ$; Walker et al. 1994; Fujita & Nagai 2017). For such parameters, we find a small Doppler factor of $\delta \sim 1.1$. Accordingly, the resulting magnetic field strength is $B_{\rm SSA} \sim (21 \pm 14)$ G. It is also interesting to note that some studies suggest much larger Doppler factors of $\delta \sim 2-4$ (Abdo et al., 2009; Aleksić et al., 2014). If this is the case, the magnetic field strength will be also higher by a factor of $2-4$.

The rotation measure can be expressed using the magnetic field and the electron density in the Faraday screen by

$$\frac{\rm RM}{\rm rad/m^2} = 8.1 \times 10^5 \int_{\rm source}^{\rm telescope} \left(\frac{n_e}{\rm cm^{-3}}\right) \left(\frac{B_{||}}{\rm G}\right) \left(\frac{dl}{\rm pc}\right) \tag{4.13}$$

where n_e is the number density of the thermal electrons between the source of the synchrotron radiation and the telescope, $B_{||}$ is the line-of-sight component of the magnetic field, and dl is the path length through the plasma from the source toward the observer. We assume that (i) the jet is uniform and (ii) the $B_{\rm SSA}$ is an average magnetic field strength. For the path length, we further assume (iii) a spherical geometry and convert the VLBI core size θ_m into the linear size of the emission region. Then we can rewrite Eq. 4.13 to estimate the average electron number density as

---

[10] The factor 1.8 accounts for the geometric conversion of a sphere into a 2D Gaussian by the sky projection.

$$\frac{n_e}{\mathrm{cm}^{-3}} \sim 1.2\times10^{-6}\left(\frac{\mathrm{RM}}{\mathrm{rad/m^2}}\right)\left(\frac{B_{SSA}}{\mathrm{G}}\right)^{-1}\left(\frac{\theta_m}{\mathrm{pc}}\right)^{-1} \quad . \tag{4.14}$$

For a RM $\sim 9\times10^5\,\mathrm{rad/m^2}$ and a Doppler factor $\delta \sim 1.1$, we find $n_e = (0.8\pm0.5)\,\mathrm{cm}^{-3}$. The number density will be lower by a factor of $2-4$ if the Doppler factor of the jet of 3C 84 is larger ($\delta \sim 2-4$). This n_e can be compared with the particle density of the ambient medium. Fujita & Nagai (2017) suggest $n_e \sim 8\,\mathrm{cm}^{-3}$ for the ambient medium on sub-parsec scales in 3C 84. Our estimated electron density of the jet is an order of magnitude lower than this, and appears to be plausible to collimate the inner jet of 3C 84 (e.g., Nagai et al. 2014).

4.5 Summary of conclusions

In this chapter, we presented results from the millimeter polarimetric VLBI observations of the radio galaxy 3C 84 and analysis of the spectral and polarimetric structure of the core region at multiple frequencies. We summarize our results and main conclusions as follows:

- We found linearly polarized emission of 3C 84 in the compact VLBI core region at 86 GHz. The VLBI core is compact (the FWHM size ~ 0.13 mas or equivalently 0.033 pc$\sim 650R_s$) and is linearly polarized by $\sim 2.5\%$ at 86 GHz. The transverse profile of the fractional linear polarization m_L is asymmetric with respect to the peak of the total intensity. The polarization morphology is variable in time during 2015. During the same period, we also found a small radio outburst in the VLBI core. The transverse polarization asymmetry and the time variability may be associated with the ejection of a new VLBI component from the core region or turbulence in the flow.

- The synchrotron spectrum of the VLBI core is inverted up to 86 GHz, and the degree of linear polarization increases with frequency following a power-law $m_L \propto \nu^{0.77}$. This can be explained either by the synchrotron opacity or by Faraday rotation.

- Using the quasi-simultaneous observations in May 2015, we find a large RM in the core region of RM$\sim 2\times10^5\,\mathrm{rad/m^2}$ between 43-343.5 GHz. This is comparable to the previously reported RM of Plambeck et al. (2014) which was obtained using the CARMA and SMA. Additional VLBA 43 GHz polarization images reveal a comparable RM of the VLBI core in the other epochs in 2015. But we also found a sign flip of the RM between Apr and Jun 2015. The EVPA also varies significantly within the relatively narrow VLBA

43 GHz observing band. We conclude that the EVPA change is due to Faraday rotation rather than due to a changing opacity.

- We explored different types of Faraday screens in order to explain the inverted polarization spectrum caused by Faraday depolarization. The relatively high polarization at 43 and 86 GHz suggests an external screen with a fairly small RM dispersion or highly uniform RM distribution with a smooth RM gradient. We find that a turbulent, RIAF type accretion flow will provide a too strong depolarization and is not suitable to explain the observed spectrum of the linear polarization. In order to exclude strong depolarization from the accretion flow by the geometry, the accretion flow has to be highly disk-like ($H/R \lesssim 1.7$ for $\theta = 30^\circ$). Alternatively, the boundary shear layer of a stratified jet with ordered magnetic fields – containing both mildly relativistic and thermal particles – could provide the weaker depolarization and perhaps explains the RM sign flip.

- Based on synchrotron self-absorption and adopting a small Doppler factor $\delta \sim 1.1$ near the VLBI core, we obtain the SSA magnetic field strength of $B_{\rm SSA} = (21 \pm 14)$ G. Assuming a uniform jet and combine the RM and the $B_{\rm SSA}$, finding the average electron density in the jet $n_e = (0.8 \pm 0.5)\,{\rm cm}^{-3}$. The magnetic field strength and the electron density will be respectively higher and lower by a factor of $2-4$ if the Doppler is as large as $\delta \sim 2-4$. In both cases, the jet has at least an order of magnitude lower electron number density than the ambient medium around the inner sub-parsec scale jet. Thus the jet appears to be light and not heavy.

Chapter 5

Summary

Since the early discovery of relativistic jets in AGNs, physical mechanisms responsible for the launching, acceleration, and collimation of these flows have been actively investigated. During the last decades, substantial progress has been made in both theory and observations, providing deeper insights about the underlying physics of the outflow structure and propagation (on spatial scales of $\sim 10^2 - 10^6$ gravitational radii). Recent improvements in the computing power allow for numerical studies, yielding valuable information on parameters such as the mass accretion, jet formation, initial jet acceleration, and detailed transverse structure of the outflows on scales of sub-parsecs and even smaller. Nowadays, a number of numerical simulations can routinely reproduce relativistic jets from the central rotating BH and accretion disk. In spite of such a progress, however, there has been no strong consensus about which model best represents the detailed physics of the central engine. This is mainly because the jet formation process occurs on very tiny spatial scales (a few to tens of Schwarzschild radii R_s) and the different physical models are not clearly distinguished by observations with much poorer spatial resolutions (e.g., $\gtrsim 10^3 R_s$).

This thesis describes our attempts of studying the innermost jets of the nearby radio galaxies by high-spatial-resolution, millimeter-VLBI observations and providing better constraints on the theoretical models. In this chapter, we provide conclusions and a final summary of the work as follows.

Main conclusions on M 87

Chapter 3 of this thesis was focused on the first target of our study, the archetypical giant radio galaxy M 87. M 87 is one of the nearest AGNs with a prominent relativistic jet. Because of its relative proximity ($\sim 16\,$Mpc) and the super massive central BH ($\sim 6 \times 10^9 M_\odot$), global millimeter VLBI observations at 86 GHz with a 50μas angular resolution can resolve the outflow structure at a spatial resolution of only 0.004 pc or $7R_s$ (or equivalently $\sim$ 10 light-days). By taking this advantage, we probed the base region of the jet in M 87 on the projected linear scales of $\sim 7-100R_s$ from the central engine using the GMVA. In order to study the dynamical, spectral, and time variability properties of the jet in M 87, our studies also combined data/results from contemporaneous or other VLBI observations of M 87 at different observing frequencies between 1.6 GHz and 230 GHz.

The GMVA images obtained during 2004-2015 reveal the fine-scale structure of the outflow at the highest resolution and sensitivity to date. Over a decade, the jet of M 87 shows a consistent morphology such as a bright and compact core, edge-brightened jet, weak counter-jet feature, and a faint lane of emission between the edges of the jet.

The FWHM size of the VLBI core obtained by the Gaussian model-fitting of the GMVA data is only $\sim 11R_s$ at 86 GHz. The GMVA and KVN observations show that the core properties do not vary significantly over monthly and yearly timescales at $\gtrsim$ 86 GHz, but (rarely) the flux density does vary significantly in exceptional epochs. One of the most interesting characteristics of the VLBI core is that the apparent brightness temperature of the core region is only $\sim (1-3)\times 10^{10}$ K, which is an order of magnitude lower than the equipartition brightness temperature of the core of M 87 ($\sim 2\times 10^{11}$ K). This indicates the core is more magnetic energy dominated. Our analysis suggests that the magnetic field strength in the compact VLBI core region is $\sim 61-210$ G for an equipartition magnetic field strength of order of ~ 1 G. We also find from the (i) quasi-simultaneous VLBA, GMVA, and EHT observations between 43–230 GHz and (ii) fully simultaneously measured spectrum of the VLBI core by KVN monitoring observations between 2012-2016 that the synchrotron turn-over frequency of the core of M 87 is persistently very high ($\gtrsim$ 100 GHz). **All of them point toward the magnetic energy dominated jet launching region** (e.g., Meier 2012).

Assuming a self-similar and axisymmetric expansion of the edge-brightened jet at the projected distances $\lesssim 100R_s$, we estimate the diameter of the jet launching region is $\sim (4.0-5.5)R_s$. Our result is consistent with the results of previous (pre-ALMA) EHT observations at 230 GHz (Doeleman et al., 2012; Akiyama et al., 2015). The ergosphere diameter of the rotating central BH is expected to be only $(1-2)R_s$ and could not explain the large size. Instead, the wide diameter may indicate the inner accretion disk of the rotating BH as the origin of the edges of the jet. We also made use of the jet-to-counter jet brightness ratio in order to constrain the speed of the innermost jet. For the reasonable range of the jet viewing angle, the apparent speed of the jet $\beta_{\rm app}$ should be low: $\beta_{\rm app}\sim(0.1-1.0)$ within the projected distances of $\sim 100R_s$ (corresponding bulk Lorentz factor $\Gamma\lesssim 1.15$ with the jet viewing angle of $\theta=18^\circ$). No structural variation was seen in the inner jet of M 87 over two days timescale and suggests $\beta_{\rm app}\lesssim 1.0$. Additionally, the increasing jet-to-counter jet ratio at larger core separation suggests a mild jet acceleration. These findings were confirmed by the detection of apparent motions and mild acceleration of several inner jet components within the innermost ~ 0.5 mas in May 2009 ($\beta_{\rm app} \lesssim 0.2$). **The rather wide base of the sheath, its slow motion speed in the inner region, and the mild acceleration suggest that the bright edges of the jet originates from the inner accretion disk, which is then mildly accelerated by, e.g., magnetohydrodynamic processes**. However, this conclusion does not exclude the presence of a narrower "spine", which may originate from the central BH and propagate at higher speeds.

We studied the accelerating jet model furthermore by using the VLBI core brightness temperature measured in between 1.6 GHz and 230 GHz under the assumption that the core brightness temperature is Doppler-boosted by the bulk motions of the underlying flow at lower frequencies while the intrinsic brightness temperature remains unchanged. The brightness temperature $T_{\rm B}$ is found to be significantly higher at lower observing frequencies, following a power-law $T_{\rm B} \propto \nu^{-0.46}$. The required Doppler factor is also large (e.g., $\delta \sim 10$ at ~ 0.5 mas from the central engine). On the other hand, it is very difficult to achieve such a large Doppler factor by the combination of the known jet speeds and the viewing angle of M 87. Therefore, we conclude that **microscopic particle acceleration process takes place in the innermost jet of M 87 already within ~ 0.5 mas from the core (projected distances of ~ 0.04 pc or $70R_s$). This process significantly increases the intrinsic brightness temperature at the downstream of the jet**.

Finally, we investigated the spine-sheath scenario in the jet of M 87 only assuming a traverse velocity gradient perpendicular to the jet. We particularly analyzed the brightness ratio between the central hump of faint emission and the bright edges in the time-averaged (i.e., stacked) GMVA image. The edge of the jet was about two times brighter than the faint central hump, which might be the spine. We find that the spine has to move at very high speeds in order to explain this brightness ratio ($\Gamma \sim 13-17$ for $\theta = 18^{\circ}$). Such a speed is found in the component HST-1, which also moves at a comparable superluminal speed (e.g., Biretta et al. 1999). However, some studies report that the central ridge of the jet is comparably bright or more brighter than the edges, especially at lower observing frequencies and larger distances from the VLBI core (e.g., Asada et al. 2016). This cannot be explained by the pure transverse velocity stratification scenario. Therefore, we conclude that **the physical mechanism producing the observed transverse intensity profile is most likely not a single one; it may results from the combination of the transverse velocity gradient and other effects such as the plasma composition or the magnetic field strength, which can lead to different intrinsic synchrotron emissivities in the sheath and spine**. Alternatively, the central ridge found in our observations may correspond not to the true spine along the central axis of the jet, but instead the ridge may represent an emission of a filamentary structure on the outer layer of the jet.

Main conclusions on 3C 84

In Chapter 4 we presented our study of another nearby radio galaxy 3C 84, focusing on the spectral and polarization properties of the VLBI core region. The source is located at a luminosity distance of ~ 75 Mpc and has a massive central BH $M_{\rm BH} \sim 9 \times 10^8 M_\odot$. This allows a global millimeter VLBI observation with the 50μas beam to resolve the inner jet structure at a spatial resolution of 0.0125 pc or $250R_s$. The source is also located in the center of the Perseus cluster. Therefore, the central radio source 3C 84 has implications for the large-scale structure and physical properties of the cluster (e.g., Fabian 2012). 3C 84 is well known as one of the most weakly polarized radio galaxies and for its high RM of $\sim 10^6\,\mathrm{rad/m^2}$. The weak linear polarization is usually more common in radio galaxies (e.g., Lister & Homan 2005) and the prominent inner jet of 3C 84 is highly edge-brightened (e.g., Nagai et al. 2014; Giovannini et al. 2018). These properties suggest that the jets of 3C 84 and M 87 may show similar observational properties. Therefore, 3C 84 is another ideal target for a high spatial resolution millimeter VLBI observation.

In our work, we used the polarization images of the source obtained by the GMVA at 86 GHz as well as with the VLBA at 43 and 15 GHz. Our study also combined publicly available quasi-simultaneous total and polarized flux densities of 3C 84 obtained by the Atacama Large Millimeter/submillimeter Array (ALMA) based on observations at 97.5, 233.0, and 343.5 GHz. The GMVA image of 3C 84 shows the fine-scale structures of the edge-brightened jet at a remarkable dynamic range of ~ 3400, which is the highest to date at this frequency. The compact VLBI core region at 86 GHz has a FWHM size of ~ 0.13 mas (0.033 pc $\sim 650R_s$), but the visibility amplitude distribution suggests a more complicated substructure elongated in the E-W direction. The main features of the image are consistent with the results of the space VLBI observations of the source at 22 GHz (Giovannini et al., 2018).

We detect significant linear polarization in the VLBI core for the first time at 86 GHz (the fractional linear polarization $m_L \sim 2.5\%$). The fractional linear polarization as well as the unpolarized flux density S_ν of the core both show inverted spectra ($m_L \propto \nu^{0.77}$ and $S_\nu \propto \nu^{0.51}$). The ALMA polarization measurements also reveal a flat spectrum of the polarized flux density between 97.5 and 233.0 GHz. This suggests that **a substantial amount of the linearly polarized emission originates from the compact VLBI core region, especially at millimeter wavelengths.** On the other hand, we also found very large rotation measures in the VLBI core region (|RM| of order of $\sim 10^{(5-6)}\,\mathrm{rad/m^2}$), which is large enough to reduce the degree of linear polarization even at millimeter wavelengths. Thus, **the spectrum of the polarization may be explained by the changing opacity of the plasma at different frequencies or Faraday depolarization effect.** Interestingly, the jet of 3C 84 shows significant variabilities in the polarization structure and RM when the VLBI core underwent a small but significant radio flare during 2015.

We tested several Faraday depolarization models in order to better understand the observed polarization spectrum. Our models assumed (i) a turbulent hot accretion flow in front of the inner jet or (ii) a boundary layer of the jet (i.e., "sheath") with ordered magnetic field geometry as the potential Faraday screen. The turbulent accretion flow model provides too strong depolarization to explain values of m_L of the order of $\sim (0.1-1.0)\%$ at 43 and 86 GHz. Instead, the latter model shows a better agreement with the data. Therefore, we conclude that **the significant Faraday rotation likely originates from the boundary layer of the jet threaded by ordered magnetic fields. A highly disk-like accretion flow will marginally depolarize the observed emission. In this case, the disk height to disk radius ratio needs to be** $H/R < 1.7$ (< 0.6) **for** $\theta = 30^\circ$ (60°).

Finally, we estimated the magnetic field strength and electron density in the jet using synchrotron self-absorption theory and the observed RM. For a small Doppler factor $\delta \sim 1.1$ in the VLBI core region and a synchrotron turn-over frequency of $\nu_m \sim 86\,\mathrm{GHz}$, we obtain the magnetic field strength of $B_{\mathrm{SSA}} = (21 \pm 14)\,\mathrm{G}$ and the average electron number density of $n_e = (0.8 \pm 0.5)\,\mathrm{cm}^{-3}$ in the jet. The electron number density in the ambient medium surrounding the sub-parsec scale jet is $n_e \sim 8\,\mathrm{cm}^{-3}$ (Fujita & Nagai, 2017). Therefore, **the particle density of the jet is lower than the ambient medium by an order of magnitude. Such a density gradient indicates that the jet is light and not heavy in terms of matter density. The density gradient may help the jet collimation as well.**.

Future work

The work presented in the thesis probes certain aspects of the sub-parsec structure of the jets in M 87 and 3C 84. However, many open questions remain to be answered for these objects, especially for M 87. One of crucial studies is to obtain a detailed velocity field of the inner jet within the projected distances of $100R_s$ from the central engine. The velocity field will allow us to test various and specific physical models to understand the very initial jet acceleration mechanism (e.g., Mertens et al. 2016). For this, it is indispensable to monitor the source structure intensively at 86 GHz with high sensitivity and short time cadence. Further VLBI monitoring observations are being performed and analyzed at the moment of concluding this PhD thesis. Previous connected interferometer observations provide a hint of large RM in the nuclear region of M 87 (Kuo et al., 2014). However, detailed properties of the polarization and synchrotron spectrum of M 87 are still not well known on sub-parsec scales. The GMVA observation in 2015 was made with the dual circular polarization feeds and the corresponding analysis is ongoing. Another deep polarization imaging observation of M 87 with a global 43 GHz VLBI array – including the phased Karl G. Jansky Very Large Array and the 100 m Robert C. Byrd Green Bank Telescope – was proposed and also accepted (PI : J.-Y. Kim, year : 2018). Another important coming work is to obtain even a deeper image of the jet of M 87 at 86 GHz, with significantly improved angular resolution in the N-S direction. As of 2018, the ALMA phasing system has been successfully installed (Matthews et al., 2018) and the phased ALMA participates in the GMVA observations regularly since early 2017. Recently performed GMVA observations of M 87 in 2018 with the phased ALMA (PI : R.-S. Lu) will be able to find a number of interesting results beyond our GMVA observations. Finally, future observations of M 87 by the Event Horizon Telescope at 230 GHz (Doeleman et al., 2012) and RadioAstron at 22 GHz (e.g., Gómez et al. 2016) are also expected to make substantial progresses in our understanding of the AGN jet physics. Their angular resolution is expected to be only $\sim 20\,\mu$as and the observations should be able to image the central engine region of M 87 directly at a spatial resolution of only $\sim 3R_s$.

References

Abdo, A. A., Ackermann, M., Ajello, M., et al. 2009, ApJ, 699, 31

Abramowski, A., Acero, F., Aharonian, F., et al. 2012, ApJ, 746, 151

Acciari, V. A., Aliu, E., Arlen, T., et al. 2010, ApJ, 716, 819

Agudo, I., Thum, C., Gómez, J. L., & Wiesemeyer, H. 2014, A&A, 566, A59

Agudo, I., Thum, C., Molina, S. N., et al. 2018a, MNRAS, 474, 1427

Agudo, I., Thum, C., Ramakrishnan, V., et al. 2018b, MNRAS, 473, 1850

Agudo, I., Thum, C., Wiesemeyer, H., & Krichbaum, T. P. 2010, ApJS, 189, 1

Akiyama, K., Asada, K., Fish, V., et al. 2018, Galaxies, 6, 15

Akiyama, K., Lu, R.-S., Fish, V. L., et al. 2015, ApJ, 807, 150

Aleksić, J., Ansoldi, S., Antonelli, L. A., et al. 2014, A&A, 564, A5

Algaba, J.-C., Zhao, G.-Y., Lee, S.-S., et al. 2015, Journal of Korean Astronomical Society, 48, 237

Aller, H. D., Aller, M. F., & Plotkin, R. M. 2003, Ap&SS, 288, 17

Antonucci, R. R. J. & Miller, J. S. 1985, ApJ, 297, 621

Asada, K. & Nakamura, M. 2012, ApJ, 745, L28

Asada, K., Nakamura, M., Doi, A., Nagai, H., & Inoue, M. 2014, ApJ, 781, L2

Asada, K., Nakamura, M., & Pu, H.-Y. 2016, ApJ, 833, 56

Avachat, S. S., Perlman, E. S., Adams, S. C., et al. 2016, ApJ, 832

Avila, D., Alfaro, R., Galván, A., et al. 2017, Proceedings of Science, 301, 607

Baade, W. & Minkowski, R. 1954, ApJ, 119, 206

Bach, U., Kadler, M., Krichbaum, T. P., et al. 2003, in Proceedings of the Second ENIGMA Meeting, 216–223

Baczko, A.-K., Schulz, R., Kadler, M., et al. 2016, A&A, 593, A47

Bae, H.-J. & Woo, J.-H. 2014, ApJ, 795, 30

Baganoff, F. K., Maeda, Y., Morris, M., et al. 2003, ApJ, 591, 891

Balbus, S. A. & Hawley, J. F. 1991, ApJ, 376, 214

Balbus, S. A. & Hawley, J. F. 1998, Reviews of Modern Physics, 70, 1

Baring, M. G. 2012, Particle Acceleration in Turbulent Magnetohydrodynamic Shocks, ed. M. Boettcher, D. E. Harris, & H. Krawczynski, 245–295

Beckmann, V. & Shrader, C. R. 2012, Active Galactic Nuclei (Wiley-VCH)

Begelman, M. C. & Li, Z.-Y. 1994, ApJ, 426, 269

Belloni, T. 2010, The Jet Paradigm (Springer-Verlag)

Bentz, M. C., Walsh, J. L., Barth, A. J., et al. 2009, ApJ, 705, 199

Bird, S., Harris, W. E., Blakeslee, J. P., & Flynn, C. 2010, A&A, 524, A71

Biretta, J. A., Sparks, W. B., & Macchetto, F. 1999, ApJ, 520, 621

Birkinshaw, M. 1991, The stability of jets, ed. P. A. Hughes (Cambridge University Press), 278–341

Blaes, O. 2014, Space Sci. Rev., 183, 21

Blandford, R. D. & Begelman, M. C. 1999, MNRAS, 303, L1

Blandford, R. D. & Königl, A. 1979, ApJ, 232, 34

Blandford, R. D. & Payne, D. G. 1982, MNRAS, 199, 883

Blandford, R. D. & Znajek, R. L. 1977, MNRAS, 179, 433

Boccardi, B., Krichbaum, T. P., Bach, U., Bremer, M., & Zensus, J. A. 2016a, A&A, 588, L9

Boccardi, B., Krichbaum, T. P., Bach, U., et al. 2016b, A&A, 585, A33

Boccardi, B., Krichbaum, T. P., Ros, E., & Zensus, J. A. 2017, A&A Rev., 25, 4

Bondi, H. 1952, MNRAS, 112, 195

Bonnoli, G., Ghisellini, G., Foschini, L., Tavecchio, F., & Ghirlanda, G. 2011, MNRAS, 410, 368

Böttcher, M. 2012, Special Relativity of Jets, 17–38

Brenneman, L. W. & Reynolds, C. S. 2009, ApJ, 702, 1367

Brentjens, M. A. & de Bruyn, A. G. 2005, A&A, 441, 1217

Broderick, A. E. & Loeb, A. 2009, ApJ, 697, 1164

Burbidge, E. M., Burbidge, G. R., & Prendergast, K. H. 1959, ApJ, 130, 26

Burbidge, G. R. 1961, Nature, 190, 1053

Burn, B. J. 1966, MNRAS, 133, 67

Camenzind, M. 1986, A&A, 156, 137

Carilli, C. L., Bartel, N., & Linfield, R. P. 1991, AJ, 102, 1691

Casadio, C., Krichbaum, T., Marscher, A., et al. 2017, Galaxies, 5, 67

Chael, A. A., Johnson, M. D., Bouman, K. L., et al. 2018, ApJ, 857, 23

Chael, A. A., Johnson, M. D., Narayan, R., et al. 2016, ApJ, 829, 11

Cheung, C. C., Harris, D. E., & Stawarz, Ł. 2007, ApJ, 663, L65

Chidiac, C., Rani, B., Krichbaum, T. P., et al. 2016, A&A, 590, A61

Cicone, C., Maiolino, R., Sturm, E., et al. 2014, A&A, 562, A21

Clausen-Brown, E., Lyutikov, M., & Kharb, P. 2011, MNRAS, 415, 2081

Clausen-Brown, E., Savolainen, T., Pushkarev, A. B., Kovalev, Y. Y., & Zensus, J. A. 2013, A&A, 558, A144

Cohen, M. H., Cannon, W., Purcell, G. H., et al. 1971, ApJ, 170, 207

Comastri, A. 2004, in Astrophysics and Space Science Library, Vol. 308, Supermassive Black Holes in the Distant Universe, ed. A. J. Barger (Springer), 245

Contopoulos, I. 2018, MNRAS, 473, L146

Contopoulos, I., Christodoulou, D. M., Kazanas, D., & Gabuzda, D. C. 2009, ApJ, 702, L148

Cornwell, T. & Fomalont, E. B. 1999, in Astronomical Society of the Pacific Conference Series, Vol. 180, Synthesis Imaging in Radio Astronomy II, ed. G. B. Taylor, C. L. Carilli, & R. A. Perley (Astronomical Society of the Pacific), 187

Cotton, W. D. 1995, in Astronomical Society of the Pacific Conference Series, Vol. 82, Very Long Baseline Interferometry and the VLBA, ed. J. A. Zensus, P. J. Diamond, & P. J. Napier (Astronomical Society of the Pacific), 189

Cotton, W. D., Wittels, J. J., Shapiro, I. I., et al. 1980, ApJ, 238, L123

Croton, D. J., Springel, V., White, S. D. M., et al. 2006, MNRAS, 365, 11

Curtis, H. D. 1918, Publications of Lick Observatory, 13, 9

De Villiers, J.-P., Hawley, J. F., Krolik, J. H., & Hirose, S. 2005, ApJ, 620, 878

Deller, A. T., Brisken, W. F., Phillips, C. J., et al. 2011, Publications of the Astronomical Society of the Pacific, 123, 275

Doeleman, S. S., Fish, V. L., Schenck, D. E., et al. 2012, Science, 338, 355

Elitzur, M. 2007, in Astronomical Society of the Pacific Conference Series, Vol. 373, The Central Engine of Active Galactic Nuclei, ed. L. C. Ho & J.-W. Wang (Astronomical Society of the Pacific), 415

Fabian, A. C. 1994, Annual Review of Astronomy and Astrophysics, 32, 277

Fabian, A. C. 2008, Astronomische Nachrichten, 329, 155

Fabian, A. C. 2012, ARA&A, 50, 455

Fanaroff, B. L. & Riley, J. M. 1974, MNRAS, 167, 31P

Fender, R. P., Belloni, T. M., & Gallo, E. 2004, MNRAS, 355, 1105

Fromm, C. M., Ros, E., Perucho, M., et al. 2013, A&A, 557, A105

Fuhrmann, L., Krichbaum, T. P., Witzel, A., et al. 2008, A&A, 490, 1019

Fujita, Y. & Nagai, H. 2017, MNRAS, 465, L94

Gabuzda, D. C. 2015, in Astrophysics and Space Science Library, Vol. 414, The Formation and Disruption of Black Hole Jets, ed. I. Contopoulos, D. Gabuzda, & N. Kylafis (Springer), 117

Gabuzda, D. C., Roche, N., Kirwan, A., et al. 2017, MNRAS, 472, 1792

García-Burillo, S., Combes, F., Ramos Almeida, C., et al. 2016, ApJ, 823, L12

Gebhardt, K., Adams, J., Richstone, D., et al. 2011, ApJ, 729, 119

Ghisellini, G., ed. 2013, Lecture Notes in Physics, Berlin Springer Verlag, Vol. 873, Radiative Processes in High Energy Astrophysics

Ghisellini, G., Tavecchio, F., & Chiaberge, M. 2005, A&A, 432, 401

Ghisellini, G., Tavecchio, F., Maraschi, L., Celotti, A., & Sbarrato, T. 2014, Nature, 515, 376

Giannios, D. & Spruit, H. C. 2006, A&A, 450, 887

Gillessen, S., Eisenhauer, F., Trippe, S., et al. 2009, ApJ, 692, 1075

Gilli, R., Salvati, M., & Hasinger, G. 2001, A&A, 366, 407

Giovannini, G., Savolainen, T., Orienti, M., et al. 2018, Nature Astronomy, 33

Giroletti, M., Hada, K., Giovannini, G., et al. 2012, A&A, 538, L10

Gómez, J. L., Lobanov, A. P., Bruni, G., et al. 2016, ApJ, 817, 96

Gómez, J. L., Marscher, A. P., Jorstad, S. G., Agudo, I., & Roca-Sogorb, M. 2008, ApJ, 681, L69

Gopal-Krishna & Wiita, P. J. 2002, New A Rev., 46, 357

Greisen, E. W. 1990, in Acquisition, Processing and Archiving of Astronomical Images, ed. G. Longo & G. Sedmak, 125–142

Hada, K., Doi, A., Kino, M., et al. 2011, Nature, 477, 185

Hada, K., Giroletti, M., Kino, M., et al. 2014, ApJ, 788, 165

Hada, K., Kino, M., Doi, A., et al. 2016, ApJ, 817, 131

Hada, K., Kino, M., Doi, A., et al. 2013, ApJ, 775, 70

Hada, K., Kino, M., Nagai, H., et al. 2012, ApJ, 760

Hada, K., Park, J. H., Kino, M., et al. 2017, PASJ, 69, 71

Hales, C. A. 2017, AJ, 154, 54

Han, S.-T., Lee, J.-W., Kang, J., et al. 2008, International Journal of Infrared and Millimeter Waves, 29, 69

Hardee, P., Mizuno, Y., & Nishikawa, K.-I. 2007, Ap&SS, 311, 281

Hardee, P. E. 2000, ApJ, 533, 176

Hardee, P. E. & Eilek, J. A. 2011, ApJ, 735, 61

Hawley, J. F. & Krolik, J. H. 2006, ApJ, 641, 103

Heckman, T. M. & Best, P. N. 2014, ARA&A, 52, 589

Ho, L. C. 2008, ARA&A, 46, 475

Hodgson, J. A., Krichbaum, T. P., Marscher, A. P., et al. 2017, A&A, 597, A80

Hodgson, J. A., Lee, S.-S., Zhao, G.-Y., et al. 2016, Journal of Korean Astronomical Society, 49, 137

Hodgson, J. A., Rani, B., Lee, S.-S., et al. 2018, MNRAS, 475, 368

Högbom, J. A. 1974, A&AS, 15, 417

Homan, D. C., Lister, M. L., Kovalev, Y. Y., et al. 2015, ApJ, 798, 134

Homan, D. C., Ojha, R., Wardle, J. F. C., et al. 2002, ApJ, 568, 99

Homan, D. C. & Wardle, J. F. C. 2004, ApJ, 602, L13

Hovatta, T., Aller, M. F., Aller, H. D., et al. 2014, AJ, 147, 143

Hovatta, T., Lister, M. L., Aller, M. F., et al. 2012, AJ, 144, 105

Hoyle, F. & Fowler, W. A. 1963, MNRAS, 125, 169

Hughes, P. A., Aller, H. D., & Aller, M. F. 1985, ApJ, 298, 301

Ichimaru, S. 1977, ApJ, 214, 840

Igumenshchev, I. V., Narayan, R., & Abramowicz, M. A. 2003, ApJ, 592, 1042

Jackson, N., Browne, I. W. A., Battye, R. A., Gabuzda, D., & Taylor, A. C. 2010, MNRAS, 401, 1388

Jansky, K. G. 1933, Nature, 132, 66

Johnson, M. D., Fish, V. L., Doeleman, S. S., et al. 2015, Science, 350, 1242

Jones, T. W. & O'Dell, S. L. 1977, ApJ, 214, 522

Jorstad, S. & Marscher, A. 2016, Galaxies, 4, 47

Jorstad, S. G., Marscher, A. P., Lister, M. L., et al. 2005, AJ, 130, 1418

Jorstad, S. G., Marscher, A. P., Morozova, D. A., et al. 2017, ApJ, 846

Jorstad, S. G., Marscher, A. P., Stevens, J. A., et al. 2007, AJ, 134, 799

Junor, W., Biretta, J. A., & Livio, M. 1999, Nature, 401, 891

Kara, E., Alston, W. N., Fabian, A. C., et al. 2016, MNRAS, 462, 511

Kellermann, K. I., Condon, J. J., Kimball, A. E., Perley, R. A., & Ivezić, Ž. 2016, ApJ, 831, 168

Kellermann, K. I. & Pauliny-Toth, I. I. K. 1969, ApJ, 155, L71

Kellermann, K. I., Sramek, R. A., Schmidt, M., Green, R. F., & Shaffer, D. B. 1994, AJ, 108, 1163

Kim, J.-Y., Krichbaum, T.-P., Lu, R.-S., et al. 2018a, A&A, 616, A188

Kim, J.-Y., Krichbaum, T.-P., Marscher, A., et al. 2019, A&A, 622, A196

Kim, J.-Y., Lee, S.-S., Hodgson, J. A., et al. 2018b, A&A, 610, L5

Kim, J.-Y., Lu, R.-S., Krichbaum, T., et al. 2016, Galaxies, 4, 39

Kino, M., Takahara, F., Hada, K., et al. 2015, ApJ, 803, 30

Komissarov, S. 2012, Central Engines: Acceleration, Collimation and Confinement of Jets, ed. M. Boettcher, D. E. Harris, & H. Krawczynski (Wiley-VCH), 81–114

Komissarov, S. S. 1990, Soviet Astronomy Letters, 16, 284

Komissarov, S. S., Barkov, M. V., Vlahakis, N., & Königl, A. 2007, MNRAS, 380, 51

Komissarov, S. S., Vlahakis, N., & Königl, A. 2010, MNRAS, 407, 17

Komissarov, S. S., Vlahakis, N., Königl, A., & Barkov, M. V. 2009, MNRAS, 394, 1182

Kormendy, J. & Ho, L. C. 2013, ARA&A, 51, 511

Kovalev, Y. Y., Kardashev, N. S., Kellermann, K. I., et al. 2016, ApJ, 820, L9

Kovalev, Y. Y., Kellermann, K. I., Lister, M. L., et al. 2005, AJ, 130, 2473

Kovalev, Y. Y., Lister, M. L., Homan, D. C., & Kellermann, K. I. 2007, ApJ, 668, L27

Koyama, S., Kino, M., Giroletti, M., et al. 2016, A&A, 586, A113

Krichbaum, T. P., Alef, W., Witzel, A., et al. 1998, A&A, 329, 873

Krichbaum, T. P., Graham, D. A., Bremer, M., et al. 2006, in Journal of Physics Conference Series, Vol. 54, 328–334

Krichbaum, T. P., Roy, A., Lu, R.-S., et al. 2014, in Proceedings of the 12th European VLBI Network Symposium and Users Meeting (EVN 2014). 7-10 October 2014. Cagliari, Italy., 13

Kuo, C. Y., Asada, K., Rao, R., et al. 2014, ApJ, 783, L33

Laing, R. A. 1980, MNRAS, 193, 439

Lee, S.-S., Byun, D.-Y., Oh, C. S., et al. 2015, Journal of Korean Astronomical Society, 48, 229

Lee, S.-S., Lobanov, A. P., Krichbaum, T. P., & Zensus, J. A. 2016, ApJ, 826, 135

Lee, S.-S., Petrov, L., Byun, D.-Y., et al. 2014, AJ, 147

Leppanen, K. J., Zensus, J. A., & Diamond, P. J. 1995, AJ, 110, 2479

Lico, R., Gómez, J. L., Asada, K., & Fuentes, A. 2017, MNRAS, 469, 1612

Lisakov, M. M., Kovalev, Y. Y., Savolainen, T., Hovatta, T., & Kutkin, A. M. 2017, MNRAS, 468, 4478

Lister, M. L., Aller, H. D., Aller, M. F., et al. 2009, AJ, 137

Lister, M. L., Aller, M. F., Aller, H. D., et al. 2016, AJ, 152

Lister, M. L. & Homan, D. C. 2005, AJ, 130, 1389

Lobanov, A., Hardee, P., & Eilek, J. 2003, New A Rev., 47, 629

Lobanov, A. P. 1998, A&A, 330, 79

Lobanov, A. P. 2005, ArXiv Astrophysics e-prints [astro-ph/0503225]

Lobanov, A. P. & Zensus, J. A. 2001, Science, 294, 128

Lu, R.-S., Broderick, A. E., Baron, F., et al. 2014, ApJ, 788, 120

Ly, C., Walker, R. C., & Junor, W. 2007, ApJ, 660, 200

Lynden-Bell, D. 1969, Nature, 223, 690

Lynden-Bell, D. 2003, MNRAS, 341, 1360

Lynden-Bell, D. 2015, in Astrophysics and Space Science Library, Vol. 414, The Formation and Disruption of Black Hole Jets, ed. I. Contopoulos, D. Gabuzda, & N. Kylafis (Springer), 1

Lynden-Bell, D. & Rees, M. J. 1971, MNRAS, 152, 461

Lyubarsky, Y. 2009, ApJ, 698, 1570

Lyutikov, M., Pariev, V. I., & Gabuzda, D. C. 2005, MNRAS, 360, 869

MacDonald, N. R. & Marscher, A. P. 2018, ApJ, in press

MacDonald, N. R., Marscher, A. P., Jorstad, S. G., & Joshi, M. 2015, ApJ, 804, 111

Madejski, G. . & Sikora, M. 2016, ARA&A, 54, 725

Malkan, M. A. & Sargent, W. L. W. 1982, ApJ, 254, 22

Marcaide, J. M. & Shapiro, I. I. 1984, ApJ, 276, 56

Marrone, D. P., Moran, J. M., Zhao, J.-H., & Rao, R. 2006, ApJ, 640, 308

Marrone, D. P., Moran, J. M., Zhao, J.-H., & Rao, R. 2007, ApJ, 654, L57

Marscher, A. 2016, Galaxies, 4, 37

Marscher, A. P. 1983, ApJ, 264, 296

Marscher, A. P. 2011, Nature, 477, 164

Marscher, A. P. 2014, ApJ, 780, 87

Marscher, A. P., Jorstad, S. G., Larionov, V. M., et al. 2010, ApJ, 710, L126

Martí-Vidal, I., Krichbaum, T. P., Marscher, A., et al. 2012, A&A, 542, A107

Martí-Vidal, I., Muller, S., Vlemmings, W., Horellou, C., & Aalto, S. 2015, Science, 348, 311

Matthews, L. D., Crew, G. B., Doeleman, S. S., et al. 2018, Publications of the Astronomical Society of the Pacific, 130, 015002

McKinney, J. C. 2006, MNRAS, 368, 1561

McKinney, J. C., Tchekhovskoy, A., & Blandford, R. D. 2012, MNRAS, 423, 3083

Meier, D. L. 2012, Black Hole Astrophysics: The Engine Paradigm (Springer-Verlag Berlin Heidelberg)

Merloni, A., Heinz, S., & di Matteo, T. 2003, MNRAS, 345, 1057

Mertens, F., Lobanov, A. P., Walker, R. C., & Hardee, P. E. 2016, A&A, 595, A54

Misner, C. W., Thorne, K. S., & Wheeler, J. A. 1973, Gravitation (San Francisco: W.H. Freeman and Co.)

Montier, L., Plaszczynski, S., Levrier, F., et al. 2015a, A&A, 574, A135

Montier, L., Plaszczynski, S., Levrier, F., et al. 2015b, A&A, 574, A136

Mościbrodzka, M., Dexter, J., Davelaar, J., & Falcke, H. 2017, MNRAS, 468, 2214

Mościbrodzka, M., Falcke, H., & Shiokawa, H. 2016, A&A, 586, A38

Myserlis, I., Angelakis, E., Kraus, A., et al. 2018, A&A, 609, A68

Nagai, H., Fujita, Y., Nakamura, M., et al. 2017, ApJ, 849, 52

Nagai, H., Haga, T., Giovannini, G., et al. 2014, ApJ, 785, 53

Nair, D. G., Lobanov, A. P., Krichbaum, T. P., et al. 2018, A&A, in press, doi:10.1051/0004-6361/201833122

Narayan, R., Igumenshchev, I. V., & Abramowicz, M. A. 2003, PASJ, 55, L69

Narayan, R. & Yi, I. 1994, ApJ, 428, L13

O'Sullivan, S. P. & Gabuzda, D. C. 2009, MNRAS, 393, 429

Pacholczyk, A. G. 1970, Radio astrophysics. Nonthermal processes in galactic and extragalactic sources (San Francisco: Freeman)

Panaitescu, A. & Kumar, P. 2002, ApJ, 571, 779

Pasetto, A., Carrasco-González, C., O'Sullivan, S., et al. 2018, A&A, 613, A74

Penrose, R. & Floyd, R. M. 1971, Nature Physical Science, 229, 177

Perley, R. A. & Butler, B. J. 2013, The Astrophysical Journal Supplement Series, 204, 19

Perlman, E. S., Biretta, J. A., Zhou, F., Sparks, W. B., & Macchetto, F. D. 1999, AJ, 117, 2185

Perucho, M., Martí-Vidal, I., Lobanov, A. P., & Hardee, P. E. 2012, A&A, 545, A65

Plambeck, R. L., Bower, G. C., Rao, R., et al. 2014, ApJ, 797, 66

Porth, O., Fendt, C., Meliani, Z., & Vaidya, B. 2011, ApJ, 737, 42

Prieto, M. A., Fernández-Ontiveros, J. A., Markoff, S., Espada, D., & González-Martín, O. 2016, MNRAS, 457, 3801

Pu, H.-Y., Wu, K., Younsi, Z., et al. 2017, ApJ, 845, 160

Pushkarev, A. B., Gabuzda, D. C., Vetukhnovskaya, Y. N., & Yakimov, V. E. 2005, MNRAS, 356, 859

Pushkarev, A. B. & Kovalev, Y. Y. 2012, A&A, 544, A34

Pushkarev, A. B., Kovalev, Y. Y., Lister, M. L., & Savolainen, T. 2009, A&A, 507, L33

Pushkarev, A. B., Kovalev, Y. Y., Lister, M. L., & Savolainen, T. 2017, MNRAS, 468, 4992

Rani, B., Krichbaum, T. P., Marscher, A. P., et al. 2015, A&A, 578, A123

Readhead, A. C. S. 1994, ApJ, 426, 51

Rees, M. J. 1966, Nature, 211, 468

Reid, M. J., Biretta, J. A., Junor, W., Muxlow, T. W. B., & Spencer, R. E. 1989, ApJ, 336, 112

Roberts, D. H., Wardle, J. F. C., & Brown, L. F. 1994, ApJ, 427, 718

Rybicki, G. B. & Lightman, A. P. 1979, Radiative processes in astrophysics (Wiley-VCH)

Ryle, M. 1962, Nature, 194, 517

Salpeter, E. E. 1964, ApJ, 140, 796

Sandage, A. 1965, ApJ, 141, 1560

Savolainen, T., Wiik, K., Valtaoja, E., & Tornikoski, M. 2008, in Extragalactic Jets: Theory and Observation from Radio to Gamma Ray, Vol. 386, 451

Sądowski, A., Narayan, R., Penna, R., & Zhu, Y. 2013, MNRAS, 436, 3856

Scharwächter, J., McGregor, P. J., Dopita, M. A., & Beck, T. L. 2013, MNRAS, 429, 2315

Schinzel, F. K., Lobanov, A. P., Taylor, G. B., et al. 2012, A&A, 537, A70

Schmidt, M. 1963, Nature, 197, 1040

Schmitt, H. R., Antonucci, R. R. J., Ulvestad, J. S., et al. 2001, ApJ, 555, 663

Seyfert, C. K. 1943, ApJ, 97, 28

Shakura, N. I. & Sunyaev, R. A. 1973, A&A, 24, 337

Shepherd, M. C., Pearson, T. J., & Taylor, G. B. 1994, in BAAS, Vol. 26, Bulletin of the American Astronomical Society, 987–989

Shields, G. A. 1999, PASP, 111, 661

Simpson, C. 2005, MNRAS, 360, 565

Singal, A. K. 2009, ApJ, 703, L109

Singh, C. B., Mizuno, Y., & de Gouveia Dal Pino, E. M. 2016, ApJ, 824, 48

Sitarek, J. & the MAGIC Collaboration. 2017, Proceedings of Science, 301, 658

Smith, R. J., Lucey, J. R., Hudson, M. J., Schlegel, D. J., & Davies, R. L. 2000, MNRAS, 313, 469

Sokoloff, D. D., Bykov, A. A., Shukurov, A., et al. 1998, MNRAS, 299, 189

Spitzer, Jr., L. & Saslaw, W. C. 1966, ApJ, 143, 400

Spruit, H. C., Foglizzo, T., & Stehle, R. 1997, MNRAS, 288, 333

Stawarz, Ł., Aharonian, F., Kataoka, J., et al. 2006, MNRAS, 370, 981

Strauss, M. A., Huchra, J. P., Davis, M., et al. 1992, ApJS, 83, 29

Suzuki, K., Nagai, H., Kino, M., et al. 2012, ApJ, 746, 140

Taylor, G. B., Carilli, C. L., & Perley, R. A., eds. 1999, Astronomical Society of the Pacific Conference Series, Vol. 180, Synthesis Imaging in Radio Astronomy II (Astronomical Society of the Pacific)

Taylor, G. B., Gugliucci, N. E., Fabian, A. C., et al. 2006, MNRAS, 368, 1500

Tchekhovskoy, A. 2015, in Astrophysics and Space Science Library, Vol. 414, The Formation and Disruption of Black Hole Jets, ed. I. Contopoulos, D. Gabuzda, & N. Kylafis (Springer), 45

Tchekhovskoy, A. & Bromberg, O. 2016, MNRAS, 461, L46

Tchekhovskoy, A., Narayan, R., & McKinney, J. C. 2010, New A, 15, 749

Tchekhovskoy, A., Narayan, R., & McKinney, J. C. 2011, MNRAS, 418, L79

The Astropy Collaboration, Price-Whelan, A. M., Sipőcz, B. M., et al. 2018, ArXiv e-prints [[arXiv]1801.02634]

Thompson, A. R., Moran, J. M., & Swenson, Jr., G. W. 2017, Interferometry and Synthesis in Radio Astronomy, 3rd Edition (Springer)

Thum, C., Agudo, I., Molina, S. N., et al. 2018, MNRAS, 473, 2506

Thum, C., Wiesemeyer, H., Paubert, G., Navarro, S., & Morris, D. 2008, PASP, 120, 777

Tombesi, F., Meléndez, M., Veilleux, S., et al. 2015, Nature, 519, 436

Trippe, S. 2014, Journal of Korean Astronomical Society, 47, 15

Trippe, S., Bremer, M., Krichbaum, T. P., et al. 2012, MNRAS, 425, 1192

Tseng, C.-Y., Asada, K., Nakamura, M., et al. 2016, ApJ, 833, 288

Türler, M., Courvoisier, T. J. L., & Paltani, S. 2000, A&A, 361, 850

Urry, C. M. & Padovani, P. 1995, PASP, 107, 803

Uttley, P., Cackett, E. M., Fabian, A. C., Kara, E., & Wilkins, D. R. 2014, A&A Rev., 22, 72

van Cittert, P. H. 1934, Physica, 1, 201

Vanden Berk, D. E., Richards, G. T., Bauer, A., et al. 2001, AJ, 122, 549

Vernaleo, J. C. & Reynolds, C. S. 2006, ApJ, 645, 83

Vlahakis, N. & Königl, A. 2003, ApJ, 596, 1080

Volonteri, M. 2012, Science, 337, 544

Walker, R. C. & Anantharamaiah, K. R. 2003, AJ, 125, 1756

Walker, R. C., Dhawan, V., Romney, J. D., Kellermann, K. I., & Vermeulen, R. C. 2000, ApJ, 530, 233

Walker, R. C., Hardee, P. E., Davies, F. B., Ly, C., & Junor, W. 2018, ApJ, 855, 128

Walker, R. C., Ly, C., Junor, W., & Hardee, P. J. 2008, Journal of Physics Conference Series, 131, 012053

Walker, R. C., Romney, J. D., & Benson, J. M. 1994, ApJ, 430, L45

Walsh, J. L., Barth, A. J., Ho, L. C., & Sarzi, M. 2013, ApJ, 770, 86

Wardle, J. F. C., Cawthorne, T. V., Roberts, D. H., & Brown, L. F. 1994, ApJ, 437, 122

Wardle, J. F. C. & Homan, D. C. 2003, Ap&SS, 288, 143

Wardle, J. F. C. & Kronberg, P. P. 1974, ApJ, 194, 249

Whitney, A. R. 2000, in International VLBI Service for Geodesy and Astrometry 2000 General Meeting Proceedings, ed. F. Takahashi, 187–205

Whitney, A. R., Shapiro, I. I., Rogers, A. E. E., et al. 1971, Science, 173, 225

Wilson, T. L., Rohlfs, K., & Huttemeister, S. 2012, Tools of Radio Astronomy, 5th edition (Springer-Verlag Berlin Heidelberg)

Woltjer, L. 1959, ApJ, 130, 38

Yuan, F., Bu, D., & Wu, M. 2012a, ApJ, 761, 130

Yuan, F. & Narayan, R. 2014, ARA&A, 52, 529

Yuan, F., Wu, M., & Bu, D. 2012b, ApJ, 761, 129

Zamaninasab, M., Clausen-Brown, E., Savolainen, T., & Tchekhovskoy, A. 2014, Nature, 510, 126

Zavala, R. T. & Taylor, G. B. 2005, ApJ, 626, L73

Zel'dovich, Y. B. & Novikov, I. D. 1964, Soviet Physics Doklady, 9, 246

Zensus, J. A. 1997, ARA&A, 35, 607

Zernike, F. 1938, Physica, 5, 785

Appendix A

Model-fit parameters of the VLBI core of the M 87 jet obtained by KVN observations

Table A.1 KVN observing epochs and M 87 core model-fit parameters. The columns show (1) the mean observing epoch, (2) the corresponding MJD, (3) the central observing frequency, (4) the core flux density, (5) the peak intensity, (6) the core FWHM size, (7) the image rms noise level after subtracting the Gaussian model, (8) and (9) the major and minor axis of the elliptical observing beam, and (10) the beam position angle in degree (zero to North, increase in CCW).

Epoch (yyyy-mm-dd) (1)	MJD (2)	$\nu_{\rm obs}$ (GHz) (3)	S_ν (Jy) (4)	$S_{\rm peak}$ (Jy/beam) (5)	d (mas) (6)	$\sigma_{\rm rms}$ (mJy/beam) (7)	$B_{\rm maj}$ (mas) (8)	$B_{\rm min}$ (mas) (9)	$B_{\rm PA}$ (deg) (10)
2012-12-04	56265	21.7	1.7±0.2	1.7±0.1	< 0.31	10.0	5.70	3.22	−68.0
		43.4	1.3±0.2	1.3±0.1	< 0.17	9.0	2.84	1.61	−66.3
		86.8	1.1±0.2	1.1±0.1	0.18±0.02	13.9	1.39	0.83	−67.0
2013-01-16	56308	21.7	1.9±0.2	1.8±0.1	0.91±0.06	8.0	5.33	3.32	−79.5
		43.4	1.4±0.1	1.3±0.1	0.54±0.04	5.6	2.67	1.66	−81.0
		86.8	1.1±0.2	0.8±0.1	0.53±0.08	17.8	1.49	0.81	−63.4
2013-02-27	56350	21.7	1.7±0.2	1.7±0.1	< 0.27	7.6	5.43	3.36	−84.9
		43.4	1.3±0.1	1.2±0.1	0.56±0.04	4.9	2.76	1.64	−89.1
		86.8	1.2±0.2	1.0±0.1	0.50±0.06	15.2	1.43	0.82	−88.5
2013-03-28	56380	21.7	1.6±0.2	1.6±0.1	0.58±0.04	7.9	5.33	3.26	−78.3
		43.4	1.3±0.1	1.2±0.1	0.38±0.02	4.8	2.66	1.66	−75.9
		86.8	1.3±0.2	1.0±0.1	0.52±0.05	10.9	1.35	0.79	−80.4
2013-04-11	56394	21.7	1.8±0.2	1.8±0.1	0.40±0.03	10.2	5.41	3.24	−75.3
		43.4	1.4±0.2	1.3±0.1	< 0.15	8.1	2.66	1.64	−76.2
		86.8	1.3±0.2	1.1±0.1	0.52±0.05	8.2	2.62	0.97	49.3
2013-05-07	56419	21.7	1.8±0.2	1.8±0.1	0.46±0.04	11.4	5.48	3.28	−72.2
		43.4	1.4±0.2	1.3±0.1	0.50±0.05	10.6	2.63	1.74	−73.4
		86.8	1.4±0.3	0.9±0.2	0.7±0.1	29.0	1.38	0.82	−76.4
		129.3	1.1±0.3	0.9±0.3	0.4±0.1	32.5	0.85	0.64	−72.8
2013-09-24	56559	21.7	1.7±0.2	1.6±0.2	0.71±0.08	17.9	5.39	3.25	−77.9
		43.4	1.1±0.2	1.0±0.2	< 0.31	24.7	2.82	1.52	−78.9
2013-10-15	56581	21.7	1.7±0.2	1.7±0.1	0.74±0.06	10.2	5.34	3.49	−83.3
		43.4	1.3±0.2	1.2±0.1	< 0.19	11.0	2.77	1.63	−70.1
		86.8	1.3±0.1	1.0±0.1	0.57±0.05	7.7	1.49	0.79	−77.4
2013-11-19	56616	21.7	1.9±0.2	1.8±0.2	< 0.35	14.4	5.19	3.37	−85.0

Table A.1 Continued.

Epoch (yyyy-mm-dd) (1)	MJD (2)	ν_{obs} (GHz) (3)	S_ν (Jy) (4)	S_{peak} (Jy/beam) (5)	d (mas) (6)	σ_{rms} (mJy/beam) (7)	B_{maj} (mas) (8)	B_{min} (mas) (9)	B_{PA} (deg) (10)
		43.4	1.3±0.2	1.3±0.1	< 0.20	13.0	2.60	1.65	−83.8
		86.8	1.3±0.2	1.1±0.1	0.38±0.04	11.3	1.31	0.81	−86.3
2013-12-24	56650	21.7	2.0±0.2	2.0±0.2	< 0.32	13.4	5.28	3.19	−89.5
		43.4	1.4±0.2	1.3±0.1	< 0.19	12.3	2.65	1.63	−89.7
		86.8	1.2±0.2	1.0±0.1	0.39±0.04	12.0	1.34	0.77	−89.2
		129.3	0.9±0.3	0.8±0.3	< 0.09	15.4	0.98	0.51	−71.4
2014-01-27	56685	21.7	2.0±0.3	1.9±0.2	0.88±0.08	15.4	5.18	3.35	89.2
		43.4	1.5±0.2	1.4±0.1	0.35±0.03	11.2	2.57	1.76	−84.6
2014-02-28	56716	21.7	1.9±0.2	1.9±0.1	< 0.29	8.9	5.19	3.57	−82.4
		43.4	1.3±0.2	1.3±0.1	0.51±0.05	12.1	2.69	1.9	−83.6
		86.8	1.1±0.2	0.8±0.1	0.66±0.10	57.7	1.46	0.93	73.1
2014-03-22	56738	21.7	1.9±0.2	1.9±0.2	0.66±0.06	12.9	5.3	3.25	−86.5
		43.4	1.4±0.2	1.4±0.1	0.43±0.04	10.7	2.63	1.65	−85.9
		86.8	1.1±0.2	1.0±0.2	0.22±0.03	23.7	1.36	0.8	−84.4
		129.3	0.9±0.3	0.9±0.3	< 0.1	18.0	1.0	0.53	82.0
2014-04-23	56770	21.7	2.0±0.2	1.9±0.2	< 0.3	11.1	5.4	3.26	−89.9
		43.4	1.4±0.1	1.3±0.1	0.43±0.03	6.8	2.67	1.64	−89.6
		86.8	1.4±0.2	1.2±0.1	0.45±0.05	15.9	1.39	0.79	−89.9
		129.3	1.0±0.3	0.9±0.3	0.15±0.04	19.6	0.9	0.54	−87.4
2014-09-01	56902	21.7	2.0±0.3	1.9±0.2	< 0.41	19.7	5.8	3.13	−67.2
		43.4	1.4±0.3	1.3±0.2	< 0.27	23.6	2.89	1.6	−67.3
		86.8	1.0±0.2	1.0±0.2	< 0.15	22.8	1.43	0.78	−70.7
2014-09-27	56928	21.7	1.8±0.2	1.8±0.1	0.83±0.06	10.2	5.29	3.25	−88.5
2014-10-29	56959	21.7	1.9±0.2	1.8±0.2	1.08±0.09	12.2	5.43	3.16	89.9
		43.4	1.4±0.1	1.3±0.1	0.55±0.04	6.7	2.72	1.59	89.7
		86.8	1.1±0.2	1.0±0.1	0.32±0.04	15.5	1.45	0.78	84.7
2014-11-28	56990	21.7	2.0±0.3	1.8±0.2	1.55±0.15	16.4	5.24	3.24	−87.8
		43.4	1.5±0.2	1.4±0.1	0.55±0.04	9.2	2.64	1.65	−79.5
		86.8	1.5±0.3	1.2±0.2	0.44±0.04	13.6	1.38	0.81	87.2

Table A.1 Continued.

Epoch (yyyy-mm-dd) (1)	MJD (2)	ν_{obs} (GHz) (3)	S_{ν} (Jy) (4)	S_{peak} (Jy/beam) (5)	d (mas) (6)	σ_{rms} (mJy/beam) (7)	B_{maj} (mas) (8)	B_{min} (mas) (9)	B_{PA} (deg) (10)
2014-12-26	57017	21.7	1.9±0.2	1.8±0.2	< 0.34	13.9	5.57	3.1	−76.1
		86.8	1.1±0.4	0.8±0.2	0.50±0.13	49.4	1.41	0.77	−74.7
2015-01-15	57037	21.7	1.8±0.2	1.7±0.1	1.3±0.1	10.8	5.56	3.16	86.8
		43.4	1.4±0.1	1.4±0.1	0.52±0.03	5.4	2.66	1.68	88.7
		86.8	1.3±0.3	1.1±0.2	0.43±0.06	23.1	1.41	0.79	−87.1
2015-03-26	57108	21.7	2.1±0.2	2.0±0.2	0.54±0.04	12.8	5.34	3.25	−85.5
		43.4	1.5±0.2	1.4±0.1	0.45±0.04	13.1	2.61	1.67	−84.8
		86.8	1.3±0.2	1.3±0.2	0.41±0.05	9.6	1.36	0.79	−85.0
		129.3	0.9±0.3	0.8±0.3	< 0.07	9.4	0.89	0.55	−82.4
2015-04-30	57142	21.7	2.0±0.3	2.0±0.2	< 0.35	15.9	5.49	3.12	89.0
		43.4	1.2±0.1	1.3±0.1	< 0.12	5.0	2.74	1.56	87.1
		86.8	1.1±0.2	1.0±0.1	0.17±0.02	19.6	1.44	0.75	88.7
2015-10-23	57318	21.7	1.8±0.3	1.7±0.2	< 0.4	17.7	5.79	3.07	−87.0
		43.4	1.5±0.2	1.4±0.1	0.59±0.04	7.5	2.78	1.59	86.7
		86.8	1.2±0.2	1.0±0.2	0.37±0.05	21.7	1.5	0.76	81.3
2015-11-30	57356	21.7	1.8±0.2	1.8±0.2	< 0.36	14.2	5.54	3.24	80.6
		43.4	1.5±0.2	1.4±0.1	< 0.17	10.0	2.73	1.64	81.5
		86.8	1.3±0.2	1.1±0.1	0.33±0.03	10.1	1.42	0.79	77.8
2015-12-28	57384	21.7	2.2±0.3	2.1±0.2	< 0.38	20.2	5.33	3.26	−89.5
		43.4	1.9±0.2	1.8±0.1	0.53±0.03	7.5	2.64	1.65	−88.5
		86.8	1.5±0.2	1.3±0.1	0.39±0.04	11.7	1.37	0.79	−89.7
		129.3	0.7±0.2	0.7±0.2	0.18±0.05	10.8	0.9	0.54	−88.3
2016-01-13	57401	21.7	2.2±0.2	2.2±0.2	0.77±0.05	10.2	5.72	3.19	79.1
		43.4	2.0±0.3	1.7±0.2	0.80±0.09	19.5	2.87	1.59	80.5
		86.8	1.5±0.2	1.2±0.1	0.45±0.04	11.2	1.48	0.77	79.8
		129.3	0.8±0.3	0.8±0.2	< 0.1	16.8	0.98	0.53	80.7
2016-03-01	57448	21.7	2.0±0.3	2.0±0.2	< 0.35	15.2	5.7	3.25	79.6
		43.4	1.7±0.2	1.5±0.1	0.65±0.05	9.5	2.81	1.65	82.6
		86.8	1.1±0.2	1.0±0.1	0.32±0.04	16.9	1.44	0.8	80.6

Table A.1 Continued.

Epoch (yyyy-mm-dd) (1)	MJD (2)	$\nu_{\rm obs}$ (GHz) (3)	S_ν (Jy) (4)	$S_{\rm peak}$ (Jy/beam) (5)	d (mas) (6)	$\sigma_{\rm rms}$ (mJy/beam) (7)	$B_{\rm maj}$ (mas) (8)	$B_{\rm min}$ (mas) (9)	$B_{\rm PA}$ (deg) (10)
		129.3	0.8±0.2	0.8±0.2	< 0.1	16.6	0.96	0.55	87.0
2016-04-24	57502	21.7	2.0±0.2	1.9±0.1	< 0.3	10.0	6.27	3.18	73.6
		43.4	1.6±0.2	1.4±0.1	0.70±0.06	8.5	3.15	1.58	73.8
		86.8	1.0±0.2	1.0±0.2	< 0.15	21.1	1.62	0.76	73.1
2016-10-18	57680	21.7	2.0±0.2	2.0±0.2	< 0.35	14.6	5.6	3.24	78.9
		43.4	1.6±0.2	1.5±0.1	0.65±0.05	9.8	2.77	1.63	78.2
		86.8	1.2±0.3	1.1±0.2	< 0.18	37.6	1.35	0.83	79.8
2016-11-27	57719	21.7	2.2±0.3	2.1±0.2	< 0.41	22.6	5.2	3.39	88.4
		43.4	1.3±0.4	1.3±0.3	< 0.53	68.2	3.67	1.63	67.9
		86.8	1.2±0.3	1.2±0.2	< 0.22	40.9	1.87	0.84	64.9
2016-12-28	57750	21.7	2.0±0.2	1.9±0.2	< 0.32	11.8	5.6	3.25	76.9
		43.4	1.6±0.2	1.5±0.1	0.67±0.05	7.1	2.83	1.63	75.4
		86.8	1.2±0.2	1.2±0.2	< 0.14	20.3	1.42	0.82	73.2

Appendix B

GMVA polarization images of the other sources in May 2015

Here we provide the GMVA polarization images of the other sources observed with 3C 84 in the same May 2015 session. For each figure, the panels show the source image (top), the (u, v)-coverage (bottom left), and the visibility amplitude distribution (bottom right). The mean observing epochs and the source names are shown in the source image panel. The total and polarized intensities are shown in contours and color scale, respectively. The electric vector position angles are shown with white bars. The contours start from a minimum level (which differs from image to image) and increase by factor 2. A negative contour of the same minimum level is shown in dashed lines. The source names, the minimum contour levels, and the peak values of the total intensities are provided in the captions. The restoring beams are shown by blue ellipses in the corner. The visibility data in the (u, v)-coverage and visibility amplitude distribution plots were binned in 30 sec for better illustration.

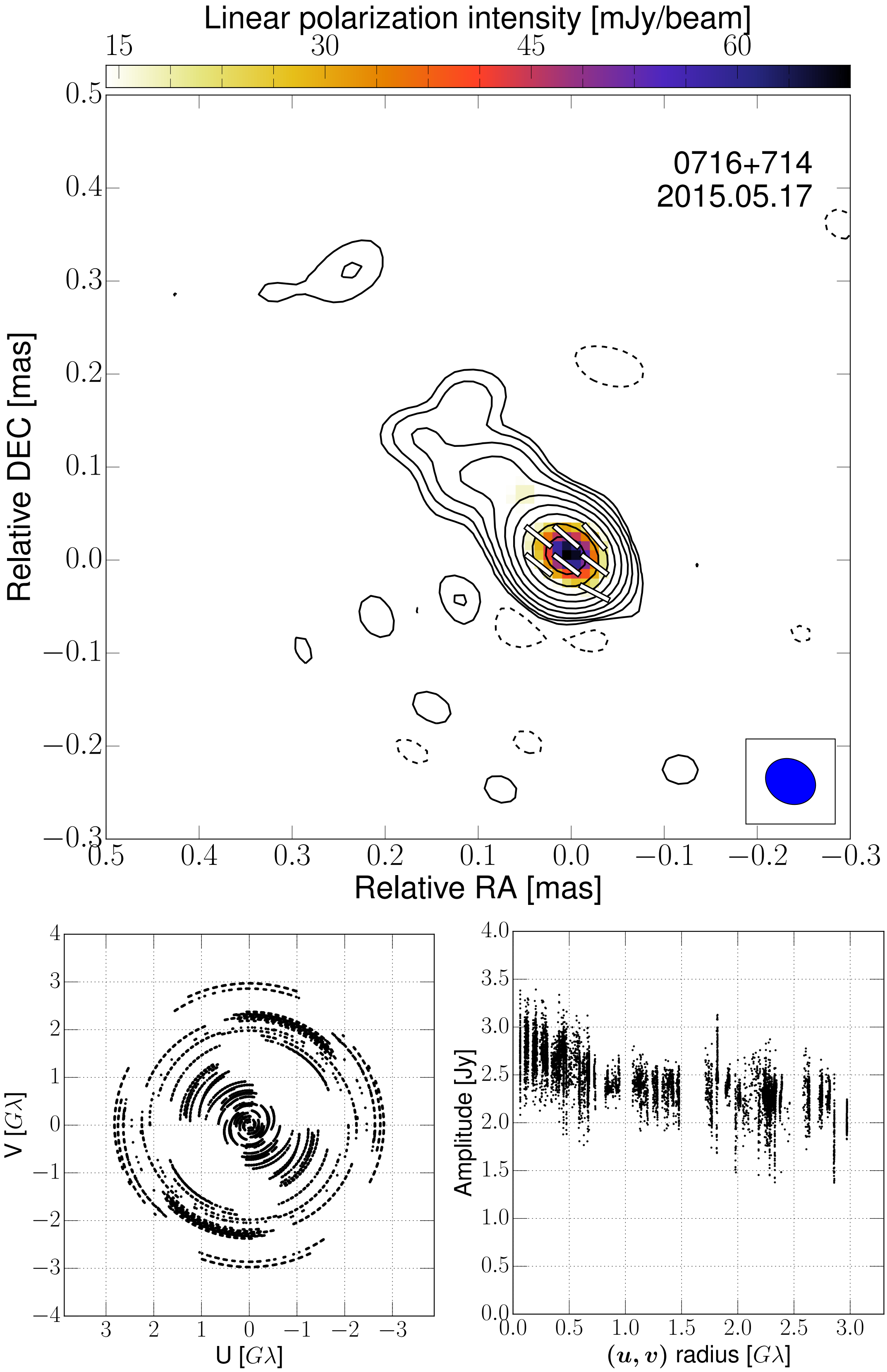

Fig. B.1 0716+714. Minimum contour level is 6 mJy/beam and the peak of the total intensity is 2.35 Jy/beam.

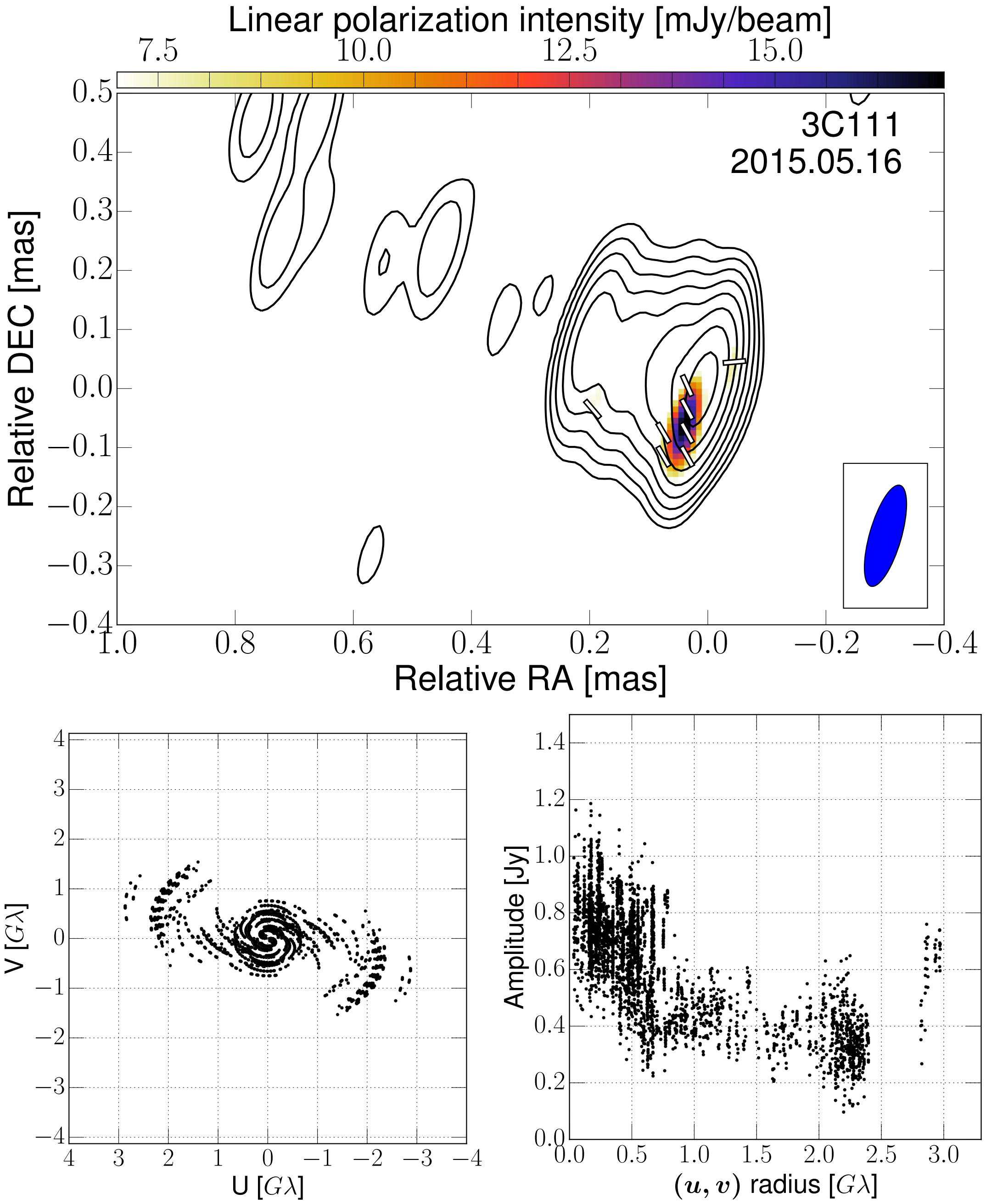

Fig. B.2 3C 111. Minimum contour level is 2.5 mJy/beam and peak of the total intensity is 0.47 Jy/beam.

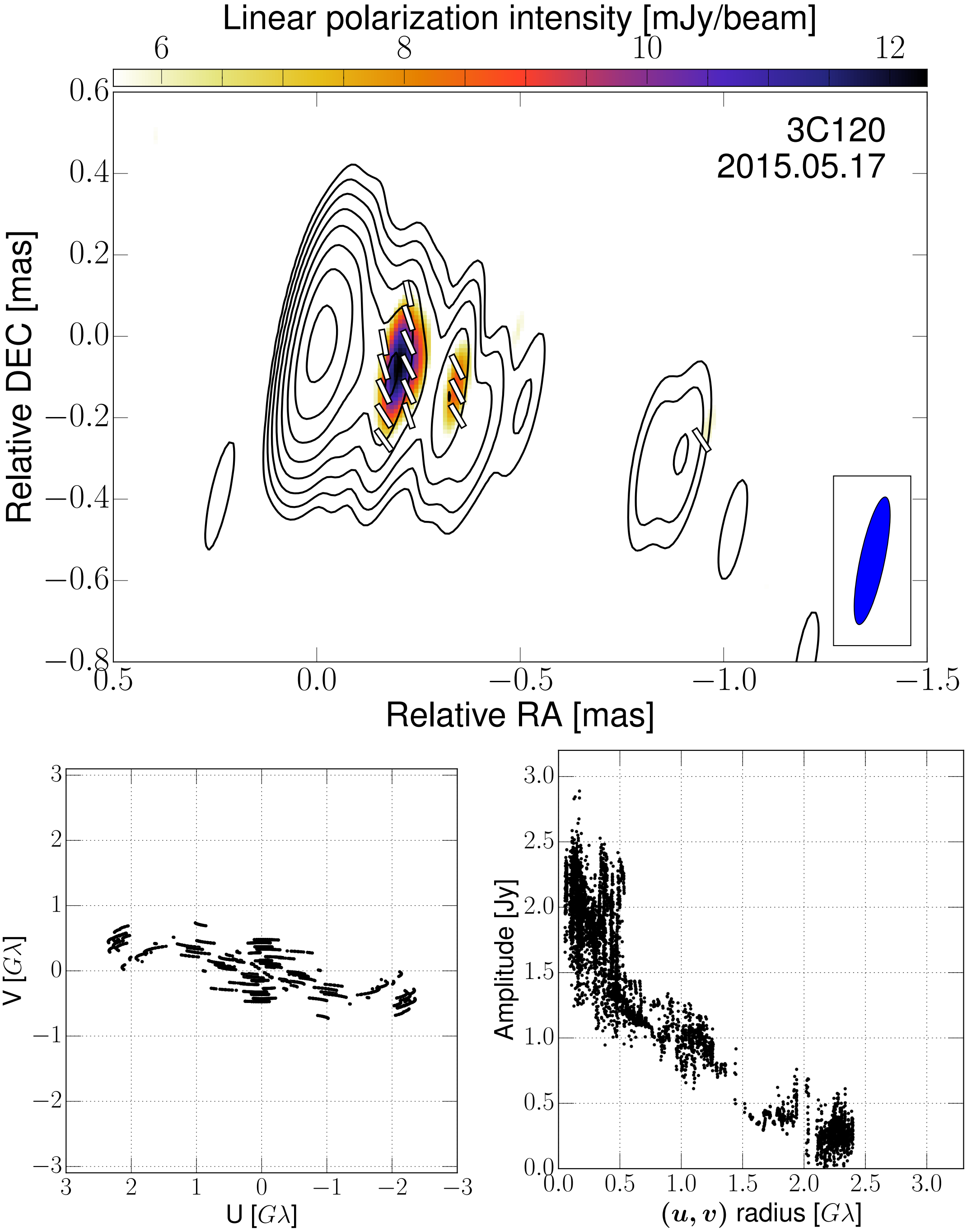

Fig. B.3 3C 120. Minimum contour level is 6.0 mJy/beam and peak of the total intensity is 0.98 Jy/beam.

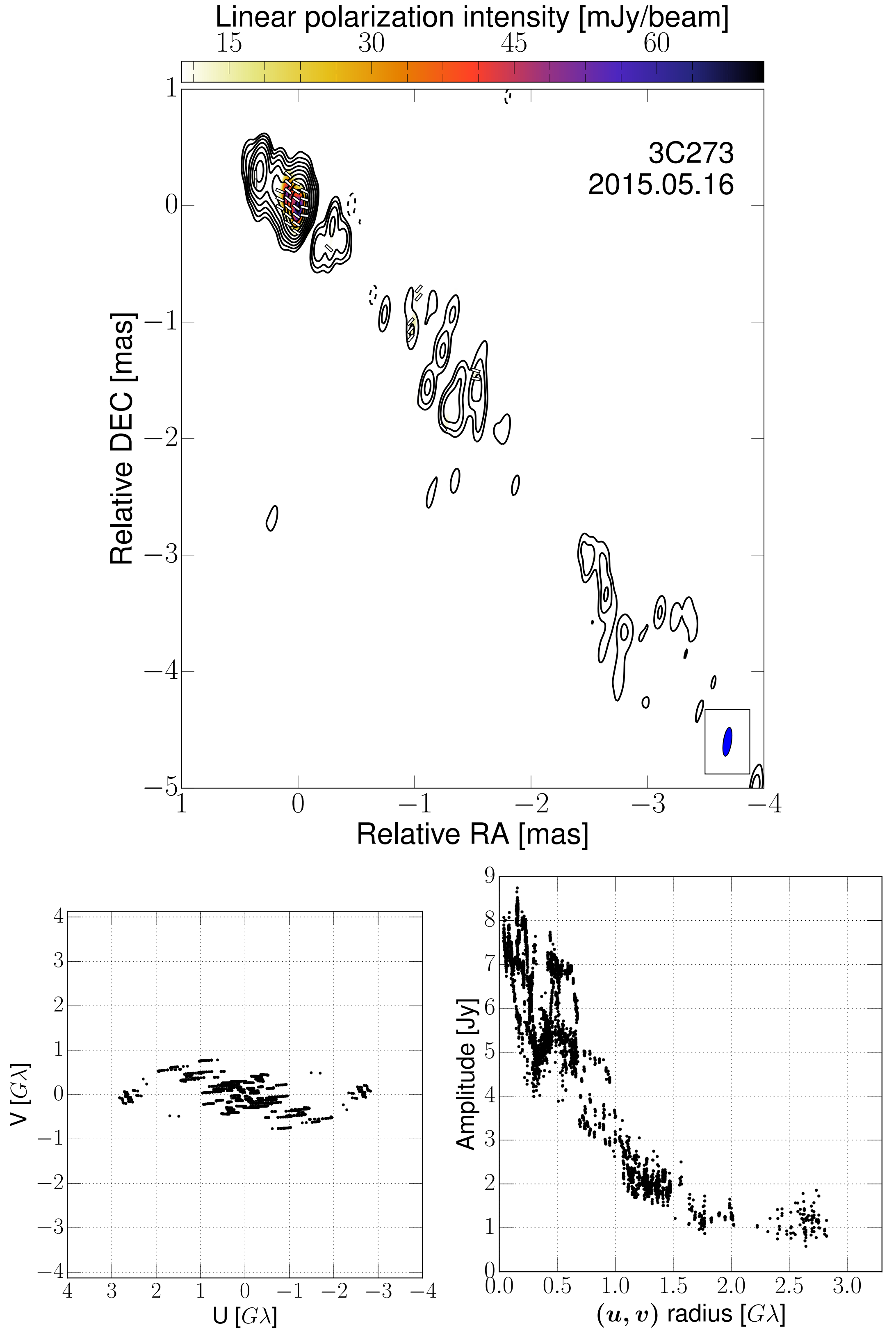

Fig. B.4 3C 273. Minimum contour level is 7.0 mJy/beam and peak of the total intensity is 3.88 Jy/beam.

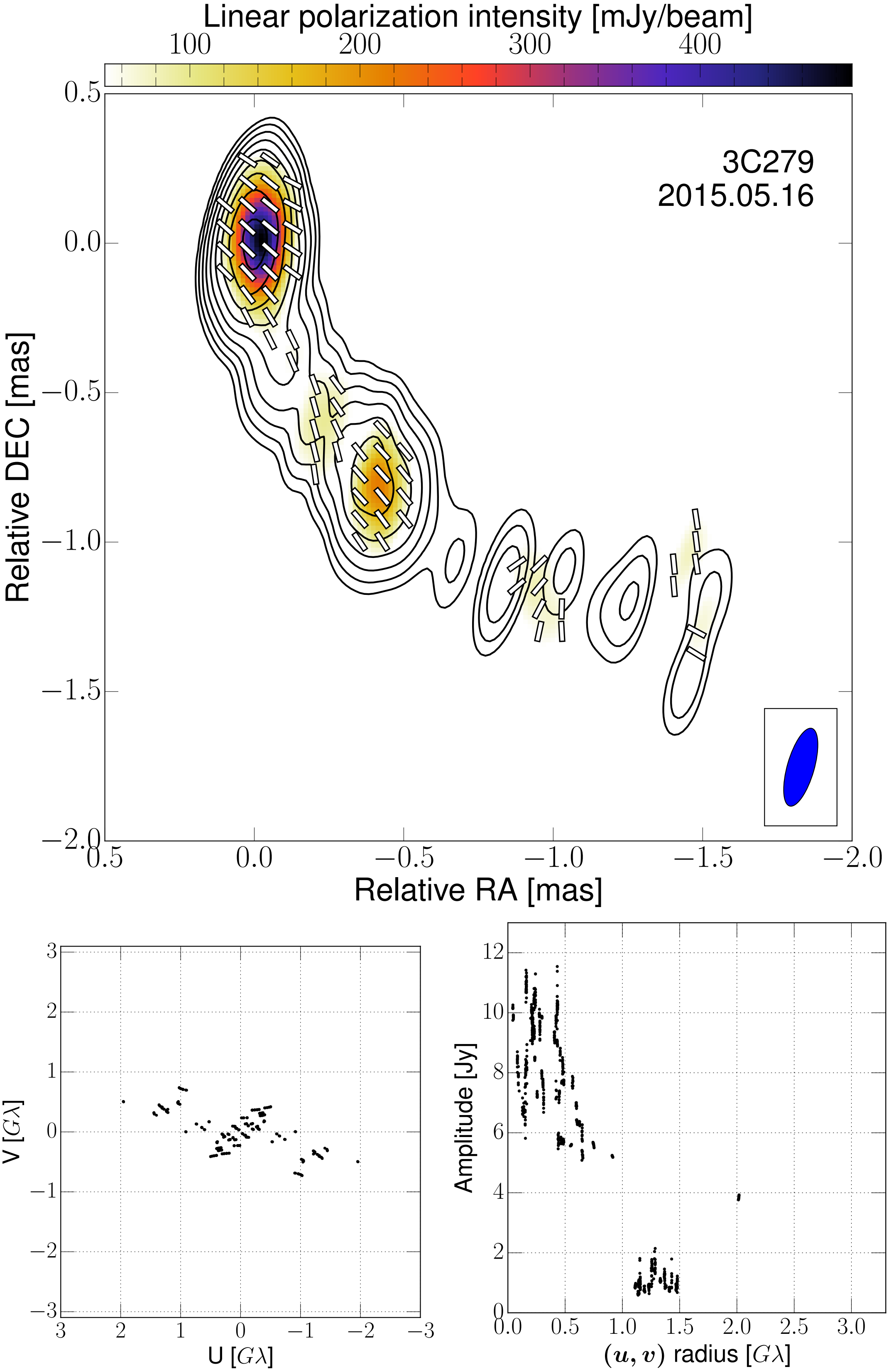

Fig. B.5 3C 279. Minimum contour level is 16 mJy/beam and peak of the total intensity is 5.05 Jy/beam.

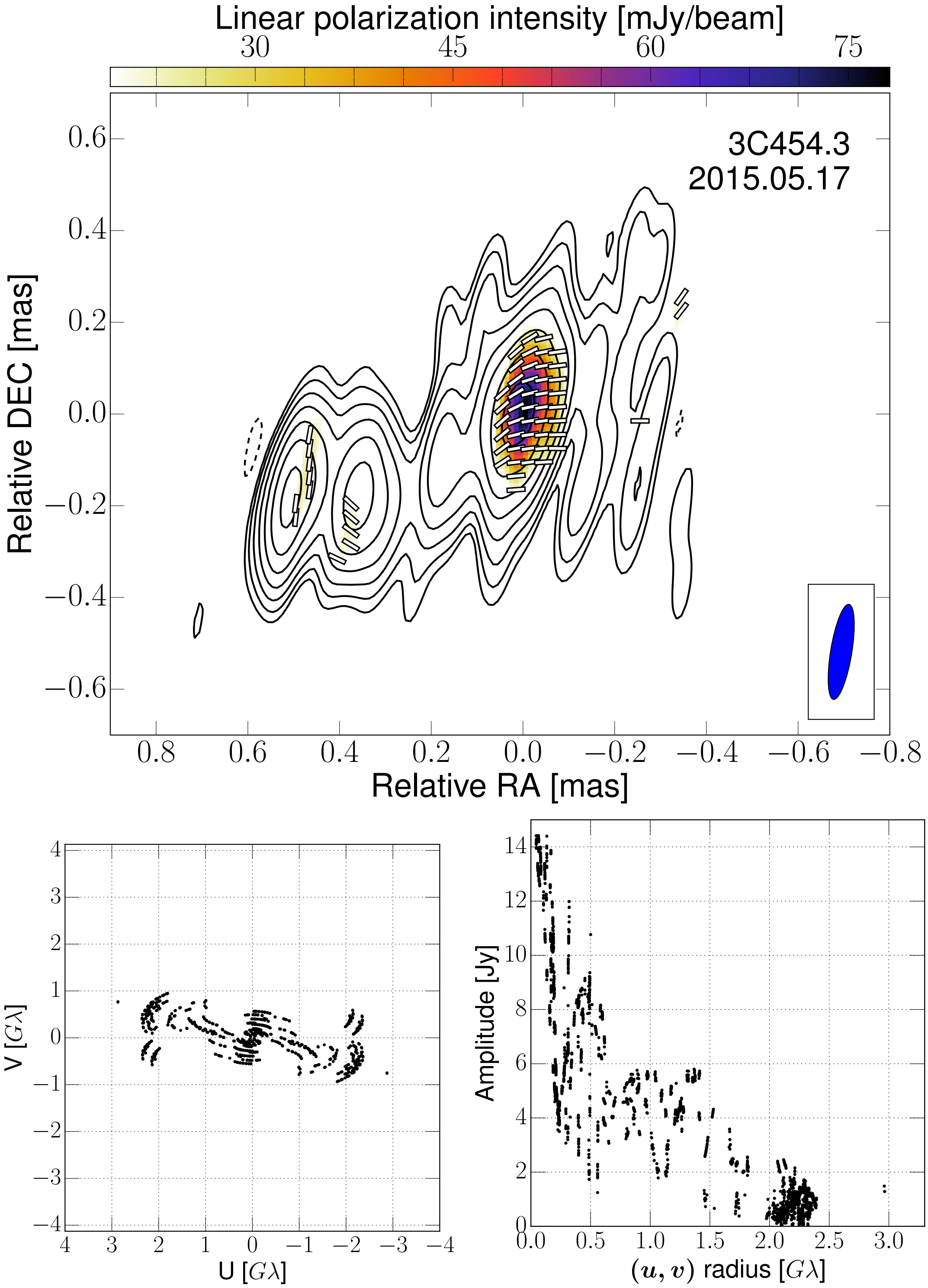

Fig. B.6 3C 454.3. Minimum contour level is 10 mJy/beam and peak of the total intensity is 1.67 Jy/beam.

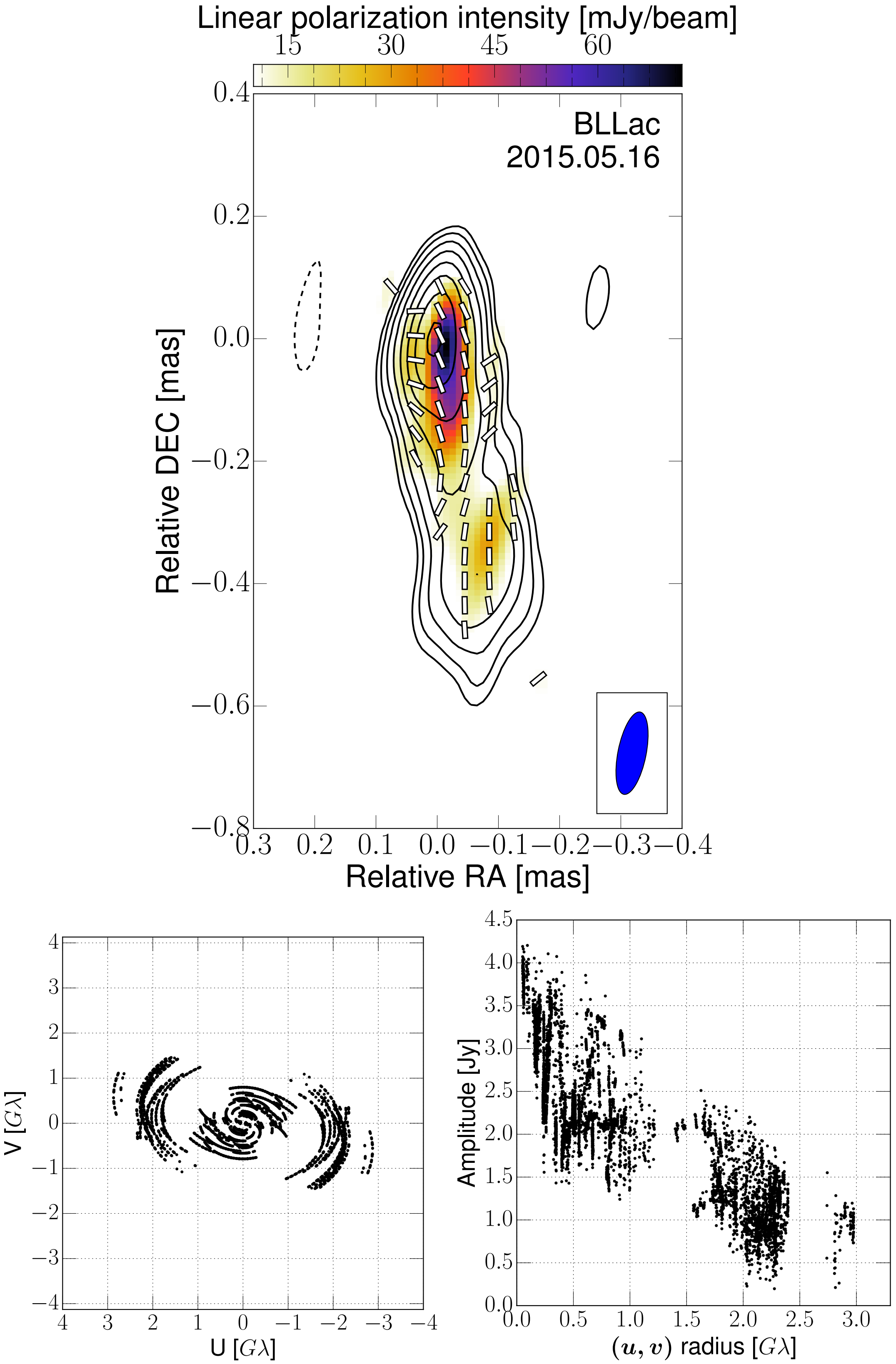

Fig. B.7 BL Lac. Minimum contour level is 12 mJy/beam and peak of the total intensity is 1.72 Jy/beam.

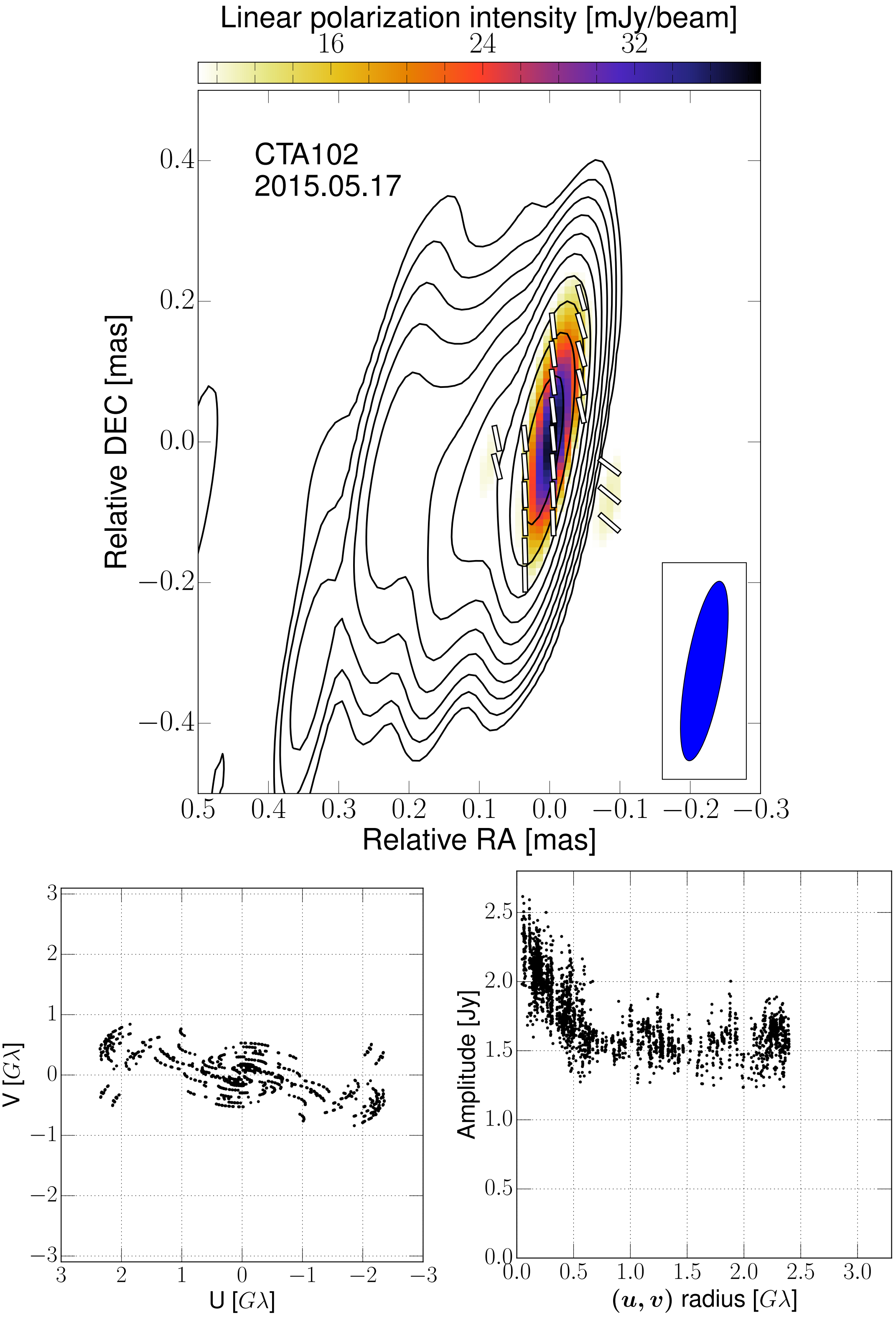

Fig. B.8 CTA 102. Minimum contour level is 2 mJy/beam and peak of the total intensity is 1.64 Jy/beam.

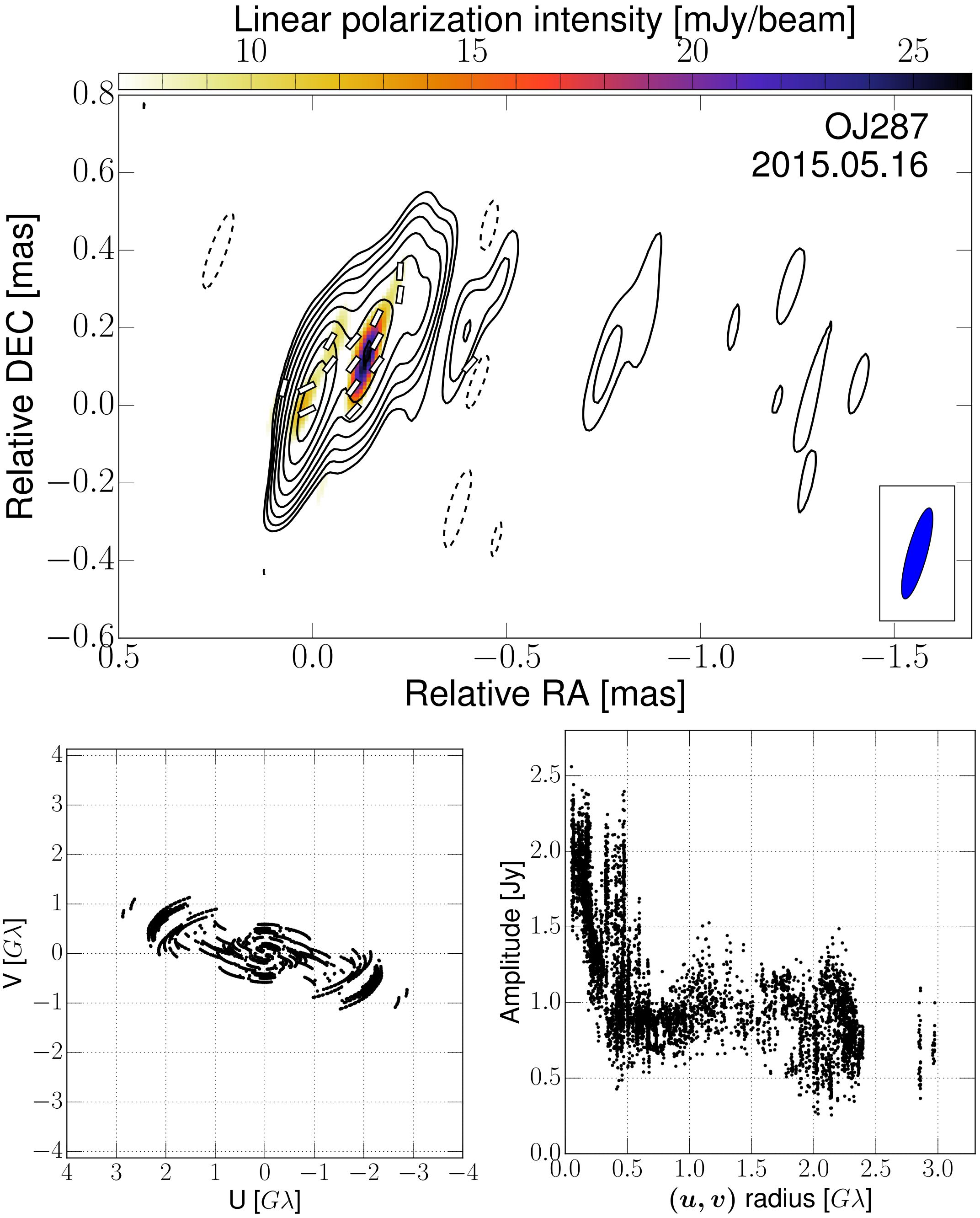

Fig. B.9 OJ 287. Minimum contour level is 5 mJy/beam and peak of the total intensity is 1.05 Jy/beam.

Appendix C

Multi-epoch VLBA 43 GHz total and linear polarization measurements of 3C 84

In Table C.1 we provide the results of the VLBI core polarization properties in the four different epochs of VLBA 43 GHz observations. The Stokes *I* core flux densities and the FWHM sizes during 2015 are listed in Table C.2.

Table C.1 Properties of the polarized components of 3C 84 obtained by polarization imaging at the four different IFs of the VLBA 43 GHz data. The columns show (1) the observing epoch, (2) the observing frequency at each IF, (3) the total flux, (4) the degree of linear polarization, and (5) the EVPA. The total flux was consistent across the frequency in each epoch and we report the measurement only for a single IF. We note that the time-variable total flux density of the polarized component is due to not only the variability but also the different positions of the polarization peak.

Epoch (1) [yyyy/mm/dd]	$\nu_{\rm obs}$ (2) [GHz]	S_ν^a (3) [Jy]	m_L (4) [%]	χ (5) [deg]
2015/04/11	43.0075	1.4 ± 0.1	0.73 ± 0.23	3 ± 10
	43.0875		0.76 ± 0.24	2 ± 10
	43.1515		0.61 ± 0.19	8 ± 10
	43.2155		0.32 ± 0.10	20 ± 10
2015/05/11	43.0075	2.0 ± 0.2	0.44 ± 0.14	$-(9 \pm 10)$
	43.0875		0.49 ± 0.16	$-(20 \pm 10)$
	43.1515		0.53 ± 0.17	$-(24 \pm 10)$
	43.2155		0.43 ± 0.13	$-(15 \pm 10)$
2015/07/02	43.0075	3.6 ± 0.4	0.37 ± 0.12	$-(5 \pm 10)$
	43.0875		0.40 ± 0.13	$-(22 \pm 10)$
	43.1515		0.67 ± 0.21	$-(26 \pm 10)$
	43.2155		0.47 ± 0.15	$-(23 \pm 10)$
2015/09/22	43.0075	2.8 ± 0.3	0.28 ± 0.09	$-(4 \pm 10)$
	43.0875		0.37 ± 0.10	6 ± 10
	43.1515		0.33 ± 0.11	$-(10 \pm 10)$
	43.2155		0.38 ± 0.12	$-(15 \pm 10)$

Table C.2 Stokes *I* core flux density (in Jy), the peak (in Jy/beam), and the core FWHM size (in mas) during 2015 measured from the archival VLBA 43 GHz data sets by the model-fitting analysis. A circular beam of 0.3 mas was used for all epochs.

Epoch [yyyy/mm/dd]	Flux [Jy]	Peak [Jy/beam]	FWHM size [mas]
2015/02/14	3.9 ± 0.7	3.6 ± 0.5	0.12 ± 0.01
2015/04/11	4.5 ± 0.6	4.1 ± 0.4	0.13 ± 0.01
2015/05/11	4.8 ± 0.7	4.4 ± 0.4	0.13 ± 0.01
2015/06/09	5.8 ± 0.6	5.2 ± 0.4	0.14 ± 0.01
2015/07/02	5.8 ± 0.6	5.2 ± 0.4	0.16 ± 0.01
2015/08/01	5.0 ± 0.5	4.5 ± 0.3	0.16 ± 0.01
2015/09/22	5.0 ± 0.6	4.4 ± 0.4	0.16 ± 0.01
2015/12/05	4.1 ± 0.5	3.7 ± 0.3	0.15 ± 0.01

Astronomy and Astrophysics
Editor in Chief: T. Forveille

T. Forveille
Astronomy & Astrophysics
Observatoire de Paris
61, avenue de l'Observatoire
75014 Paris, France

Tel.: 33 0(1) 43 29 05 41
Fax: 33 0(1) 43 29 05 57
e-mail: aanda.paris@obspm.fr
Web: http://www.aanda.org

merging
Annales d'Astrophysique
Arkiv for Astronomi
Bulletin of the Astronomical Institutes
of the Netherlands
Bulletin Astronomique
Journal des Observateurs
Zeitschrift fur Astrophysik
Bulletin of the Astronomical Institutes
of Czechoslovakia

Paris, February 18, 2019

Reprint Permission

Material:
Article by Kim, Lee, Hodgson et al. 2018, A&A, 610, L5
Article by Kim, Krichbaum, Lu et al. 2018, A&A, 616, 188
Article by Kim, Krichbaum, Marscher et al. 2019, A&A, in press (doi:10.1051/0004-6361/201832920)

To be used in:
PhD thesis, University of Cologne

Permission granted to:
KIM, Jae-Young
Department of Very Long Baseline Interferometry
Max Planck Institute for Radioastronomy
Auf dem Huegel 69, 53121 Bonn, Germany
E-mail : jykim@mpifr-bonn.mpg.de

I hold copyright on the material referred to above, and hereby grant permission for its use as requested herewith.

The article should be reproduced as a whole in a coherent fashion fully consistent with the version published in A&A.

Credit should be given as follows:
Credit: Author, A&A, vol, page, year, reproduced with permission © ESO.

Thierry Forveille
A&A Editor-in-Chief

Personal Acknowledgements

A number of important progresses have been made in the field of VLBI during the last recent years, including the operation of the space VLBI telescope RadioAstron, recent participation of the GBT and the phased ALMA in the GMVA, and the significantly expanded EHT array. It was more than just exciting not only to see these activities at the frontend of the research but also for being involved in the related projects directly or indirectly, thanks to the excellent research environment provided by the MPIfR. Therefore, my last three years as a PhD student was full of interesting and stimulating works. Of course, this implies that this thesis – which is largely based on the aforementioned works – would have not been completed without sincere helps from a number of people.

First of all, I would like to express my deepest gratitude to my thesis advisor Dr. Thomas P. Krichbaum. His deep knowledge and experiences, enthuasism in science, warm encouragements, and all the supports and advises always helped me to grow as a scientist. Without him, it would have not been possible to complete this PhD thesis. I deeply appreciate Prof. Dr. J. Anton Zensus for providing me the chance to work at the MPIfR within the framework of the IMPRS and all the supports for the research during the last years. I am also grateful to my PhD thesis advisory committee members, Prof. Dr. Andreas Eckart, Dr. Rusen Lu, and Prof. Dr. Eduardo Ros, who always provided their kind helps for the thesis whenever necessary. In particular, scientific discussions with Rusen helped me to become more familar with recent new techniques in the millimeter VLBI and come up with several new scientific ideas. I would like to give a special thank to Eduardo not only for reviewing this thesis but also for many other helps and advices during my PhD lifetime. Of course, I am also grateful to all the rest members of the VLBI group for not only sharing their knowledge and experiences but also making a good and friendly atmosphere in the VLBI group.

In addition, I also would like to acknowledge sincere help and support from the other collaborators and researchers as well; Prof. Alan P. Marscher and Dr. Svetlana Jorstad for giving me the chance to work for the GMVA monitoring project and for their helpful comments on the analysis and interpretation of the linear polarization in 3C 84, Dr. Iván Agudo for inviting me to the amazing POLAMI project and providing me the IRAM 30 m Telescope data, Prof. Sang-Sung Lee for kindly providing me the data from the ongoing KVN VLBI monitoring of M 87, and Dr. Nicholas R. MacDonald, Dr. Ioannis Myserlis, and Dr. Carolina Casadio for several fruitful discussions especially during the thesis writing period. Administrative support from Priv.-Doz. Dr. Rainer Mauersberger, Dr. Simone Pott, Ms. Beate Naunheim, Ms. Le Tran, Ms. Barbara Menten, and Ms. Sylvia Mertens was also essential. I also thank to my collaborators in Korea, especially Prof. Taehyun Jung, Prof. Sang-Sung Lee, Prof. Do-Young Byun, and Prof. Bong-Won Sohn for their invitations to KASI, kind welcoming, and friendly supports during my sporadic stay at there. It should be mentioned that modern astronomical observations, especially VLBI, involve a number of technicians and operators from the data aquisition to the data delivery to the researcher. Therefore, most of the data presented in this thesis would have not been available without their expertise and careful work.

I want to express my warm gratitude to the other PhD students and young researchers who are/were members of the VLBI group; in particular Mr. Roberto Angioni, Ms. Anne K. Baczko, Ms. Laura Vega-García, Dr. Dhanya G. Nair, Ms. Céline Chidiac, Ms. Thalia Traianou, Mr. Felix M. Pötzl, Dr. Jeff Hodgson, Dr. Bia Boccardi, Dr. Vassilis Karamanavis, Dr. Bindu Rani, Dr. Shoko Koyama, Dr. Florent Mertens, and Dr. Ioannis Myserlis for the delightful moments and precious memories during the last three years. Additional special thanks also go to Anne for her amazing job in helping the translation of the abstract into German and to Dhanya for her kind advices about the thesis submission process.

Finally, I would like to thank my parents and my sister from the bottom of my heart for their supports, lifelong love, encouragements, and for always being there. 항상 믿어주고 아낌없이 사랑을 주는 가족에게 감사의 말을 전하며 이 논문을 마칩니다.

Bonn, Monday 9th July, 2018

Funding, Data, and Software Acknowledgements

J.-Y. Kim is supported for this research by the International Max-Planck Research School (IMPRS) for Astronomy and Astrophysics at the University of Bonn and Cologne. This research has made use of data obtained with the Global Millimeter VLBI Array (GMVA), which consists of telescopes operated by the MPIfR, IRAM, Onsala, Metsahovi, Yebes, the Korean VLBI Network, the Green Bank Observatory and the Long Baseline Observatory (LBO). The VLBA is an instrument of the LBO, which is a facility of the National Science Foundation operated by Associated Universities, Inc. The data were correlated at the correlator of the MPIfR in Bonn, Germany. This work made use of the Swinburne University of Technology software correlator, developed as part of the Australian Major National Research Facilities Programme and operated under licence. This study makes use of 43 GHz VLBA data from the VLBA-BU Blazar Monitoring Program (VLBA-BU-BLAZAR; http://www.bu.edu/blazars/VLBAproject.html), funded by NASA through the Fermi Guest Investigator Program. This research has made use of data from the MOJAVE database that is maintained by the MOJAVE team (Lister et al., 2009). This paper makes use of the following ALMA data: ADS/JAO.ALMA#2011.0.00001.CAL. ALMA is a partnership of ESO (representing its member states), NSF (USA) and NINS (Japan), together with NRC (Canada), MOST and ASIAA (Taiwan), and KASI (Republic of Korea), in cooperation with the Republic of Chile. The Joint ALMA Observatory is operated by ESO, AUI/NRAO and NAOJ. J.-Y. Kim is grateful to all staff members in KVN who helped to operate the array and to correlate the data. The KVN is a facility operated by KASI (Korea Astronomy and Space Science Institute). The KVN operations are supported by KREONET (Korea Research Environment Open NETwork), which is managed and operated by KISTI (Korea Institute of Science and Technology Information). This research has made use of NASA's Astrophysics Data System. This research made use of Astropy, a community-developed core Python package for Astronomy (The Astropy Collaboration et al., 2018).

Erklärung

Ich versichere, dass ich die von mir vorgelegte Dissertation selbständig angefertigt, die benutzten Quellen und Hilfsmittel vollständig angegeben und die Stellen der Arbeit, einschließlich Tabellen, Karten und Abbildungen, die anderen Werken im Wortlaut oder dem Sinn nach entnommen sind, in jedem Einzelfall als Entlehnung kenntlich gemacht habe; dass diese Dissertation noch keiner anderen Fakultät oder Universität zur Prüfung vorgelegen hat; dass sie, abgesehen von unten angegebenen Teilpublikationen, noch nicht veröffentlicht worden ist sowie, dass ich eine solche Veröffentlichung vor Abschluss des Promotionsverfahrens nicht vornehmen werde. Die Bestimmungen der Promotionsordnung sind mir bekannt. Die von mir vorgelegte Dissertation ist von Prof. Dr. Andreas Eckart und Prof. Dr. J. Anton Zensus betreut worden.

______________	______________	______________________________
Ort	Datum	Unterschrift

Publications / Teilpublikationen

Kim, J.-Y., Krichbaum, T. P., Marscher, A. P., Jorstad, S.G., Agudo, I., Thum, C., Hodgson, J.A., MacDonald, N.R., Ros, E., Lu, R.-S., Bremer, M., de Vicente, P., Lindqvist, M., Trippe, S., and Zensus, J.A. 2019, *Spatially resolved origin of mm-wave linear polarization in the nuclear region of 3C 84*, A&A, 622, 196

Kim, J.-Y., Krichbaum, T. P., Lu, R.-S., Ros, E., Bach, U., Bremer, M., de Vicente, P., Lindqvist, M., and Zensus, J.A. 2018, *The limb-brightened jet of M 87 down to the 7 Schwarzschild radii scale*, A&A, 616, 188 (doi:10.1051/0004-6361/201832921)

Kim, J.-Y., Lee, S.-S., Hodgson, J.A., Algaba, J.-C., Zhao, G.-Y., Kino, M., Byun, D.-Y., Kang, S. 2018, *Long-term millimeter VLBI monitoring of M 87 with KVN at milliarcsecond resolution : nuclear spectrum*, A&A, 610, L5 (doi:10.1051/0004-6361/201732421)

Kim, J.-Y., Lu, R.-S., Krichbaum, T.P., Bremer, M., Zensus, J.A., Walker, R.C. 2016, *Resolving the Base of the Relativistic Jet in M87 at 6Rsch Resolution with Global mm-VLBI*, Galaxies, 4, 39 (doi:10.3390/galaxies4040039)

Lebenslauf

Persönliche Daten

Jae-Young Kim

Geburstdatum :	25. Februar 1988
Geburstsort :	Ulsan, Republik Korea
Staatsangehörigkeit :	Republik Korea

Anschrift

Max-Planck-Institut für Radioastrnomie
Auf dem Hügel 69
53121 Bonn
Deutschland
email : jykim@mpifr-bonn.mpg.de

Ausbildung

2015-2018	Doktorand an der Univeristät zu Köln und dem Max-Planck-Institut für Radioastronomie in Bonn Student der International Max Planck Research School (IMPRS) for Astronomy & Astrophyiscs wiss. Betreuer Prof. Dr. Andreas Eckart, Prof. Dr. J. Anton Zensus und Dr. Thomas P. Krichbaum Titel: *“High Spatial Resolution Millimeter VLBI Studies of the Neary Radio Galaxies M 87 and 3C 84”*
2013-2015	M.Sc. in Astronomie, Seoul National University, Republik Korea wiss. Betreuer Prof. Dr. Sascha Trippe Titel : *“A Study on Plasma-Physical Properties of Radio-Bright Nearby AGN with KVN and KaVA”*
2008-2010	Militärdienst, Ulsan, Republik Korea
2006-2013	B.Sc. in Astronomie, Seoul National University, Republik Korea
2003-2006	Bangeojin High School, Ulsan, Republik Korea